PROBING LOW-REDSHIFT GALAXIES USING QUASAR ABSORPTION LINES WITH AN EMPHASIS ON Ca II ABSORPTION

by

Gendith M. Sardane

B.S., University of Philippines, 2005

M.S., University of Florida, 2009

Submitted to the Graduate Faculty of

the Kenneth P. Dietrich School of Arts and Sciences in partial fulfillment

of the requirements for the degree of

Doctor of Philosophy

University of Pittsburgh

2015

UNIVERSITY OF PITTSBURGH

DIETRICH SCHOOL OF ARTS AND SCIENCES

PHYSICS AND ASTRONOMY DEPARTMENT

This dissertation was presented

by

Gendith M. Sardane

It was defended on

April 21, 2015

and approved by

David A. Turnshek, Professor and Chair, Dept. of Physics & Astronomy, UPitt

Sandhya M. Rao, Research Professor, Dept. of Physics & Astronomy, UPitt

Carles Badenes, Assistant Professor, Dept. of Physics & Astronomy, UPitt

Rupert A. C. Croft, Professor, Dept. of Physics, CMU

James A. Mueller, Associate Professor, Dept. of Physics & Astronomy, UPitt

Jeffrey A. Newman, Associate Professor, Dept. of Physics & Astronomy, UPitt

Dissertation Advisors: David A. Turnshek, Professor and Chair, Dept. of Physics & Astronomy, UPitt,

Sandhya M. Rao, Research Professor, Dept. of Physics & Astronomy, UPitt

PROBING LOW-REDSHIFT GALAXIES USING QUASAR ABSORPTION LINES WITH AN EMPHASIS ON Ca II ABSORPTION

Gendith M. Sardane, PhD

University of Pittsburgh, 2015

We searched for intervening CaII absorption in nearly 95,000 quasar spectra with i$\leq$20 from the Sloan Digital Sky Survey(SDSS) data releases DR7+DR9. Our identification of >400 CaII systems is the largest compilation of CaII absorbers in a blind search. Unlike other absorption line species with similar strengths, a single exponential profile is insufficient to describe the sensitivity-corrected CaIIλ3934 rest equivalent width distribution. Instead, two distributions are needed to describe the CaII absorbers, suggesting that there are at least two distinct absorber populations. The two populations can roughly be separated to lie above and below $W_0^{\lambda 3934} = 0.7$Å. Using this 0.7Å value to separate absorbers, we find from composite spectra that the mean dust content of the strong absorbers makes them nearly six times more reddened than the weak absorbers. Also, the mean element abundance ratios of the strong absorbers are intermediate to that of disk- and halo-type gas, while the abundance patterns of the weak absorbers are consistent with Milky Way halo-type gas. For absorbers with $z_{abs} \lesssim 0.4$ we identified associated galaxies in four cases using rare overlapping SDSS data. The four galaxies have impact parameters between 5-25kpc and luminosities between $\sim$0.1-1$L_r^\star$. The most reliable brightness profiles derived from stacked composite images reveal a more concentrated and steeper light profile for the stronger absorbers. The average luminosity-weighted impact parameter is $\approx$26kpc for strong absorbers, and $\approx$48kpc for weak absorbers.

We also conducted the first Hubble Space Telescope quasar absorption line study to search for absorbing gas in M31. While galaxies in the distant universe can normally be

probed with only one quasar sightline, this study of M31 utilized ten sightlines with impact parameters between 13-112kpc. Low- and high-ionization metal-line absorption systems arising in M31 were associated with its high velocity clouds and its disk and halo gas. However, contrary to the standard picture that metal-line absorption systems in quasar spectra arise in extended halos of galaxies, the four outermost sightlines showed no metal-line absorption to within our observational limits. Along sightlines where M31 MgII$\lambda\lambda$2796,2803 absorption was detected, the absorption was significantly weaker than that attributed to high-redshift galaxies at similar impact parameters.

TABLE OF CONTENTS

LIST OF TABLES

LIST OF FIGURES

PREFACE

This thesis would not have been possible without the mentorship and guidance of many people. First, I am grateful to my advisers Dave Turnshek and Sandhya Rao for giving me the chance to work with them, during a time they didn't plan on having a new student. Without their scientific insights, their careful and thorough review of every aspect of this work and their unparalleled support both personally and academically, this thesis would not have been possible. It is my pleasure and honor to be their student. I am specially thankful to Jeff Newman for his constructive critique of this work and for giving me useful suggestions in the statistical analysis of the absorber sample. I also thank the rest of the committee members: Carles Badenes, Rupert Croft and Jim Mueller for reviewing my work and your constructive comments. I thank Eric Monier for providing his list of DR7 MgII sample. I also thank Dan Nestor for making his pseudo-continuum fitter available. Finally, to Aris and Adalace, thank you for the inspiration.

1.0 INTRODUCTION

1.1 THE BIG PICTURE: THE FORMATION AND EVOLUTION OF GAS AND GALAXIES IN THE UNIVERSE

The modern-day dynamical model of the expanding Universe has it originating $\sim$ 13.7 billion years ago in a hot "big bang." The Universe is currently dominated by Dark Energy ($\sim$68%) and non-baryonic Dark Matter ($\sim$27%). Moreover, the remaining $\sim$5% is normal baryonic matter in the form of the chemical elements with which we are all familiar (Planck Collaboration XIII, 2015). While investigations of the nature of the mysterious Dark Energy and Dark Matter are among the most fundamental to our understanding of modern physics, significant advances in these areas are likely to require new theories and new instrumentation on new telescopes. However, observation of the remaining 5% of normal matter is, of course, possible with present-day technology. Indeed, past results based on observations of normal matter and the cosmic microwave background have led to the realization that Dark Energy and Dark Matter must exist.

As part of the standard model of cosmology, it is also known that as the Universe cools gravity will cause small perturbations to collapse and "halos" (clumps) of Dark Matter will form. Gas and galaxies will form and sink to the centers of these halos due to radiative processes. In this cosmic process gas initially collapses to form the first stars in galaxies, but the entire cosmic process entails many episodes of accretion of gas to form stars in galaxies, subsequent outflows (e.g., from supernovae in galaxies), and then new episodes of star formation in galaxies. Some galaxies will cluster and may merge with one another. Cosmic chemical evolution will occur. Since redshift equates to look-back time in an expanding Universe, this cosmic evolution can be studied by observing gas and galaxies as a function

of redshift.

This thesis primarily describes studies of gas as far back as 8.5 billion years ago. We use spectroscopy of bright background quasars to probe the foreground gas. In particular, Ca II absorbing gas is studied. Compared to other gas that can be studied, it is relatively rare. However, it is very important because it can be observed to redshift zero using ground-based telescopes, unlike most other species of absorbing gas, and a subset of Ca II absorbers are associated with molecular and dusty regions, which are known to be required conditions for star formation. Also, we apply our method to the "Great Spiral Galaxy in Andromeda (M31)" using other absorption species, which creates an important benchmark.

1.2 QUASARS AND QUASAR ABSORPTION LINES

Quasi-stellar objects, or quasars, are not only among the most distant objects detected, but are also among the most luminous astronomical sources known in the Universe. Quasars can generate enormous luminosities, $\sim 10 - 1000$ times the luminosities of bright normal spiral galaxies such as the Milky Way and M31, emanating from extremely compact nuclear regions about the size of the Solar System (< 1 light day). The high luminosities of quasars imply the important role that they play as cosmological probes, since they can be detected and identified at large distances. Quasars, therefore, present unique opportunities to probe the gaseous content of the Universe, since gaseous structures that are normally difficult to detect in emission leave their signatures as absorption lines in background quasar spectra.

In addition to the strong broad emission features intrinsic to the quasars themselves, much narrower absorption lines arising in intervening material along the quasar line-of-sight (LOS) are also found in most high-redshift quasar spectra. These absorption features contain information on the ionization, metal abundances, and kinematics of the gaseous interstellar medium (ISM), circumgalactic medium (CGM), and intergalactic medium (IGM) over a wide range of physical conditions and evolutionary stages at various redshifts.

As the detection of gaseous structures is independent of the luminosity of the absorbing medium, quasar absorption-line (QAL) spectroscopy can probe much greater depths than

traditional flux-limited imaging surveys. But the detection of these structures is subject to surface brightness limitations and $k-$corrections, and are biased towards the more luminous sources, especially at higher redshifts. Instead, the detection of gas in absorption is dependent on the cross-section of the absorbing material. Although luminosity biases are absent in QAL surveys, a different set of limitations apply such as dependence on quasar brightness, dust reddening bias, and adequate spectral resolution. A prominent limitation of QAL studies, however, lies in its normally one-dimensional spatial sampling nature — as pencil-beam sightlines towards background quasars.

Despite these limitations, the study of intervening absorption lines in the spectra of quasars has, nevertheless, become a powerful and unique method of deciphering the physical properties of otherwise invisible gaseous structures, where most of the Universe's baryons reside. In conjunction with galaxy surveys, QAL studies, in principle, provide a wealth of information useful for establishing a comprehensive understanding of the cosmological distribution and evolution of baryonic matter, and the formation and evolution of galaxies.

1.3 THE TECHNIQUE

A traditional study relating QALs to the gaseous environments of galaxies from which they originate begins with the detection of an intervening absorption-line system in a quasar spectrum. As shown in Figure 1.1, each parcel of gas along the LOS to a distant quasar selectively absorbs certain wavelengths of the continuum light from the quasar. Due to the expansion of the Universe, the wavelength that is observed in the spectrum is longer than the rest wavelength absorbed by the gas. The farther away the gas is, the longer it takes for the photons to reach earth. Since the photons are "locked" into the expansion of space, the longer the photons have traveled in time, the more they are stretched with the expanding space of the Universe. Hence, photons from the more distant universe appear at longer wavelengths, or are redshifted according to

$$\lambda_{obs} = (1 + z)\lambda_0 \tag{1.1}$$

where z is the redshift, and λ_0 and λ_{obs} are the vacuum rest and observed wavelengths of the transition, respectively.

Figure 1.2 depicts a typical one-dimensional quasar spectrum plotted in the observed optical wavelength frame. The quasar has an emission redshift $z_{em} = 3.0$. The quasar continuum and broad emission lines from H I, N V, Si IV, and C IV transitions are outlined by the red solid curve. The dashed red curve is the extrapolation of the quasar continuum blueward of Lyα emission. In this example, the absorption lines indicated by the green vertical lines are associated with an absorbing galaxy at $z_{abs} = 2.78$. The image shown in the top panel of Figure 1.2, taken from the Hubble Ultra Deep Field composite image, is marked to illustrate an example line-of-sight from a quasar to Earth.

Listed in Table 1.1 are the rest wavelengths and oscillator strengths of some of the common transitions seen in absorption in quasar spectra. Note that following spectroscopic convention, we refer to a transition of a neutral atom, X^0, as X I and a transition for the singly-ionized species, X^{+1}, as X II, etc. This list covers both high and low ionization lines. In §1.5, we will discuss the significance of these lines as key diagnostics of the different phases of the ISM, CGM, and IGM.

The rest wavelength of the transition and the wavelength coverage of the spectrograph determine the redshift range, or equivalently, the cosmic lookback time interval that can be probed by absorption lines, given a model of cosmology. The lookback time t_{LB} for an object at redshift z is given by

$$t_{LB} = t_H \int_0^z \frac{dz'}{(1+z')E(z')} \tag{1.2}$$

where $t_H = H_0^{-1}$ is the present Hubble time, and H_0 is the present Hubble constant. For the favored ΛCDM cosmology $E(z)$ is written as

$$E(z) = \frac{H(z)}{H_0} = [\Omega_M(1+z)^3 + (1-\Omega_M-\Omega_\Lambda)(1+z)^2 + \Omega_\Lambda] \tag{1.3}$$

where Ω_M and Ω_Λ are, respectively, the matter and dark energy density ratios relative to the critical density today. Current constraints indicate $\Omega_M = 0.317$, $\Omega_\Lambda = 0.683$ and $H_0 = 67.8$ km s^{-1} Mpc^{-1}, giving $t_H = 13.7$ Gyrs (Planck Collaboration XIII, 2015).

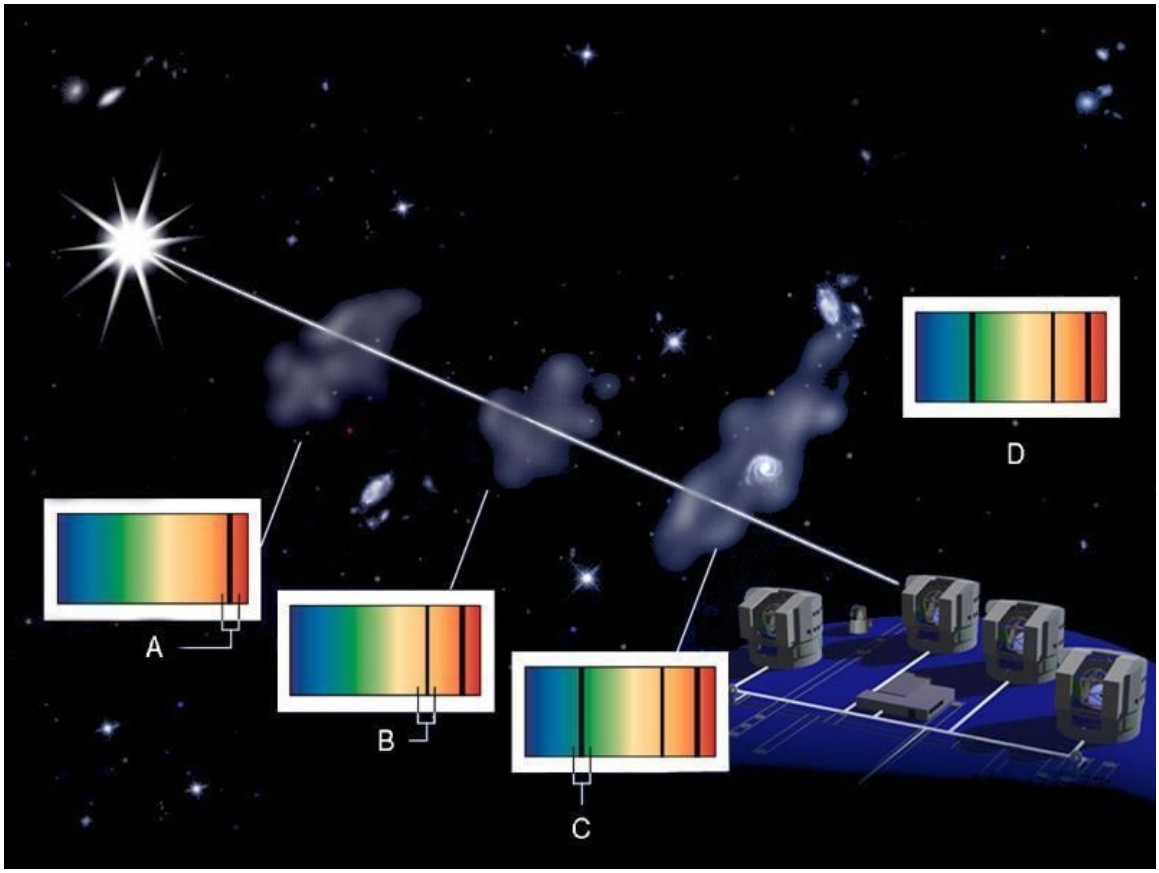

Figure 1.1: A schematic of a classic QAL study. Light from the distant background quasar is selectively absorbed by each intervening gaseous structure. Labeled "A," "B," and "C," the features from more distant sources are observed at redder wavelengths of the spectrum, as the photon is stretched according to Eqn. 1.1 due to the expansion of the Universe. Spectrum D is the resulting spectrum of the quasar as seen from Earth; spectra C, B, and A represent observations of gas at increasingly higher redshift. *Image credit: Ed Janssen, ESO*

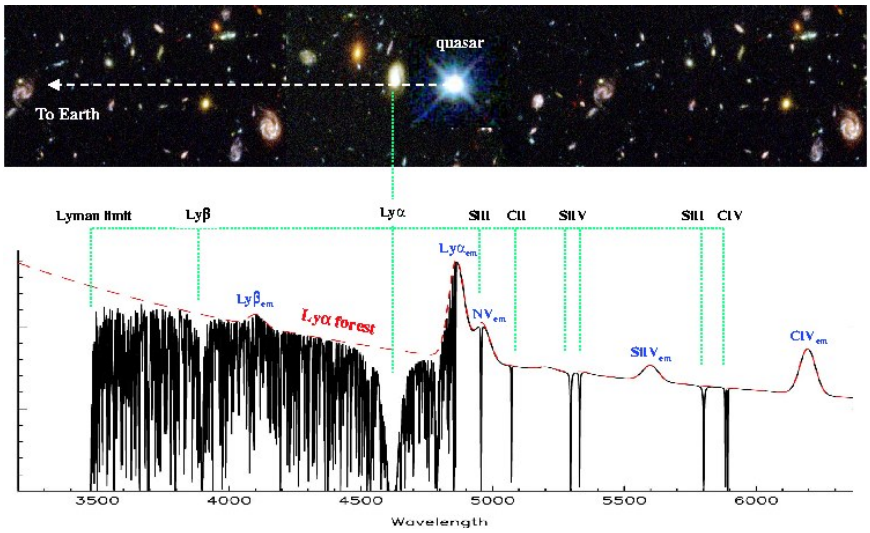

Figure 1.2: An example of a typical quasar spectrum at high redshift, $z_{em} = 3.0$, shown in the observed frame. The quasar continuum and broad emission lines are marked by the red curve; its extrapolation towards bluer wavelengths is indicated by the dashed red curve. The broad emission lines are from the C IV, Si IV, N V, Lyα and Lyβ transitions, redshifted by $1 + z_{em}$. The dense region blueward of the Lyα broad emission line is dominated by narrow H I Lyα absorption lines referred to as the "Lyα forest," caused by numerous intervening "clouds" of highly ionized gas in the IGM. The prominent intervening absorption features are associated with the absorption system at $z_{abs} = 2.78$, and are marked using green vertical lines. The absorption lines are due to high-ionization lines of C IV $\lambda\lambda$1548,1550 and Si IV $\lambda\lambda$1393,1402, and low-ionization lines of Si II λ1526, C II λ1334 and Si II λ1304. The broader absorption lines of neutral hydrogen, H I, are from the Lyα λ1216 and Lyβ λ1025 transitions. The broad Lyα profile is referred to as a damped Lyα line. Also identified for this system is the Lyman limit near 3500 Å, which is seen as a break in the spectrum due to absorption of photons with energies > 13.6 eV, which can ionize neutral hydrogen. An unrelated image marked to illustrate galaxies that intercept the quasar LOS is shown in the top panel. Image credit: Michael Murphy. Hubble Ultra Deep Field: NASA, ESA, S. Beckwith (STScI) and the HUDF Team.

Figure 1.3 shows the lookback time coverage on the linear vertical axis (with the redshift coverage on the right hand side vertical axis) for absorption lines that can be observed in quasar spectra using the *Sloan Digital Sky Survey (SDSS)* spectrograph. The gray boxes indicate the more ubiquitous QALs. The green box indicates the coverage for Ca II absorption, which is a much more rare QAL. As can be seen, Ca II has the largest lookback time interval, providing a coverage of ~ 8.8 Gyrs of cosmic history. Ca II is a doublet transition resulting from fine structure splitting the singly-ionized calcium, Ca^{+1}. This is the familiar Ca II H & K doublet first seen in the solar spectrum and in the interstellar medium of the Milky Way (e.g. West et al. 1985, Ben Bekhti et al. 2008). Unlike other QALs, the rest frame wavelength of the Ca II transition occurs in the optical at wavelengths 3934 Å and 3969 Å. This implies that Ca II has the advantage of being able to study the low-redshift Universe using ground-based telescopes. Note, especially, that with the Ca II transition and the SDSS spectrograph, we can observe more than 4 Gyrs of recent cosmic history that would otherwise be missed by surveys using the Mg II QAL. In this thesis, three chapters will be dedicated to understanding the statistical properties of Ca II absorbers from the ground-based *SDSS* survey, as well as their chemical abundances, dust, reddening, and the properties of associated galaxies.

1.4 THE ABSORPTION LINE PROFILE

The overall shape of an absorption line profile can be described by a Voigt function, which results from the convolution of a Lorentzian function with a Gaussian. The Lorentzian function describes the natural quantum mechanical broadening, which is a consequence of the finite life-time of excited atomic states within the absorbing gas. The Gaussian contribution results from the assumption of a Maxwellian velocity distribution of width characterized by the Doppler parameter, b, which in turn is related to the velocity dispersion of the gas, σ, $b = \sqrt{2}\sigma$. If the velocity is solely due to thermal motion then $b_{therm} = \sqrt{2k_BT/m}$, where k_B, m_{atom}, and T are the Boltzmann constant, atomic mass, and gas kinetic temperature, respectively. More generally, turbulent motion, usually assumed to be independent of the

Table 1.1: Common absorption transitions in quasar spectra and their oscillator strengths.

Transition	f_{osc}	λ_{rest}[Å]
Lyman Limit	-	911.8
Ly γ	0.0290	972.537
Ly β	0.0203	1025.762
Ly α	0.4164	1215.670
O VI 1031	0.1329	1031.9261
O VI 1037	0.0661	1037.6167
Si IV 1393	0.5280	1393.755
Si IV 1402	0.2620	1402.770
C IV 1393	0.1908	1548.195
C IV 1402	0.0952	1550.770
Fe II 2382	0.3200	2382.765
Fe II 2586	0.0691	2586.650
Fe II 2600	0.2390	2600.173
Mn II 2382	0.320	2576.877
Mn II 2586	0.2710	2594.499
Mn II 2586	0.1927	2606.462
Mg II 2796	0.6123	2796.352
Mg II 2803	0.3054	2803.531
Mg I 2852	1.8100	2852.964

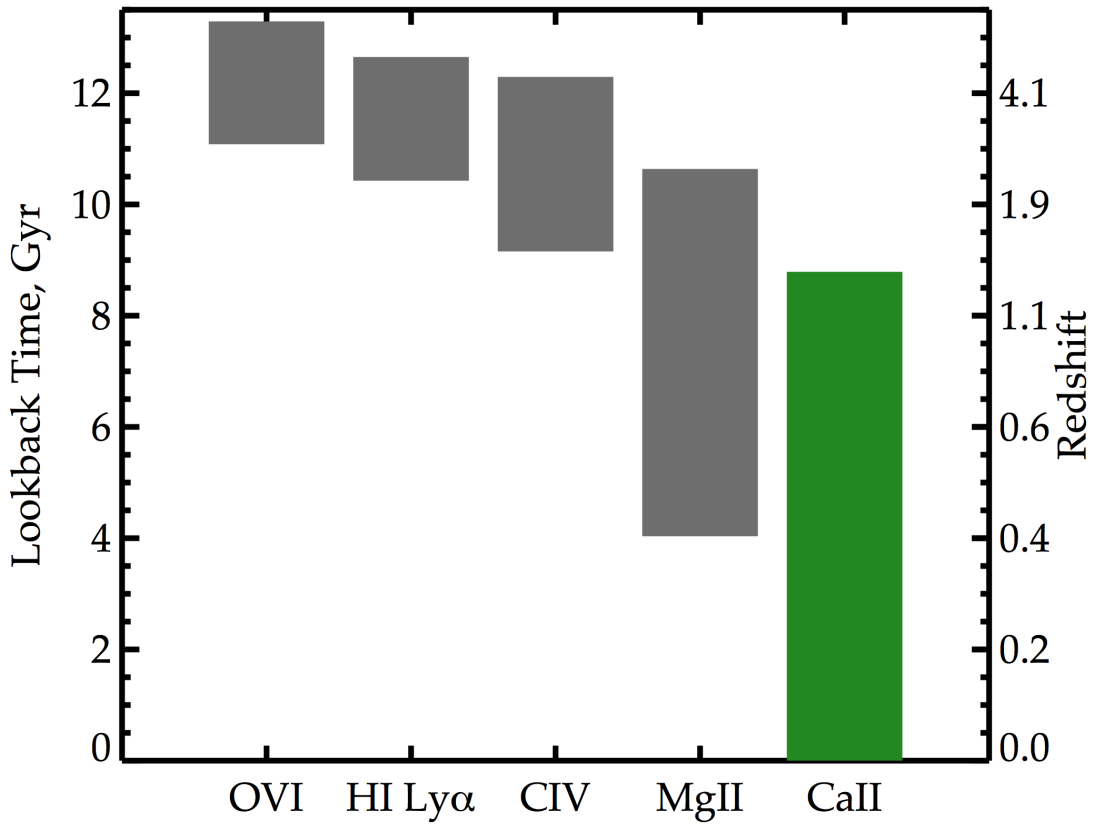

Figure 1.3: The lookback time coverage of various absorption lines observable with the SDSS spectrograph. The plot shows the lookback time on the left vertical axis (Eqn. 1.2) and the redshift on the right vertical axis. The coverage of the most common absorption lines are shown as gray boxes. The coverage of the much rarer Ca II transition, which covers more than ∼60% of cosmic history, is shown in green. Note, especially, that SDSS QAL surveys using the commonly detected transitions due to Mg II miss more than 4 Gyrs of the most recent cosmic history.

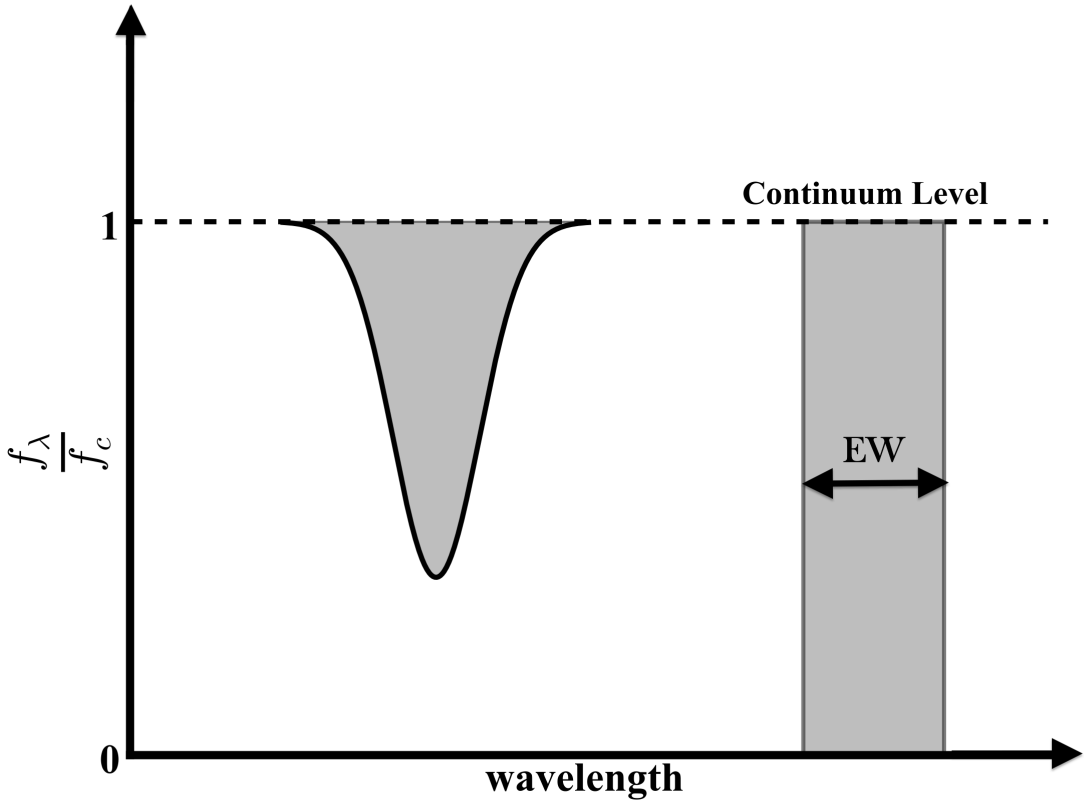

Figure 1.4: The equivalent width is a measure of the strength of an absorption line. It is defined by the amount of continuum that is absorbed. The area (gray-shaded region) of the absorption profile on the left is equal to the area of the rectangle on the right. The equivalent width is then defined as the width of the rectangle which completely absorbs the continuum.

thermal motion, is also present, so that the Doppler parameter becomes the quadrature sum of both kinematic components: $b = \sqrt{b_{therm}^2 + b_{turb}^2}$. Collisional broadening is often neglected due to the extremely rarified nature of the gas. Thus, in principle, the line profile is dominated by the Gaussian component near the line center, called the "Doppler core." As the Lorentzian component falls off more slowly than the Gaussian component with displacement from the line center, extended "damping wings" appear on the profile. See, for example, Petitjean (1998) and references therein for details on much of the discussion in this section.

The final measured absorption profile is the convolution of the Voigt line profile with the spectrograph's instrumental broadening profile, which is usually approximately Gaussian.

The strength of an absorption line is characterized by a single parameter called the rest equivalent width (REW), or W_0, which is a measure of any missing flux in the continuum. The parameter W_0 is independent of the intrinsic line profile or the instrumental broadening profile. By definition, W_0 is given by

$$W_0 = \frac{1}{1+z_{abs}} \int_{\lambda_1}^{\lambda_2} \Big(1 - \frac{I_\lambda}{I_c}\Big) d\lambda = \frac{1}{1+z_{abs}} \int_{\lambda_1}^{\lambda_2} \Big(1 - e^{-\tau_\lambda}\Big) d\lambda \tag{1.4}$$

where I_λ is the measured flux at wavelength λ, I_c is the interpolated continuum at λ, and τ_λ is the optical depth along the LOS, defined by the product of the column density, N, and the absorption coefficient, α_λ. Figure 1.4 graphically illustrates how W_0 is conceptualized and calculated.

The relationship between the gas column density and W_0 is known as the "curve of growth" (COG) for an absorption line. The COG consists of three distinct regimes:

- **Unsaturated:** A line is said to be "unsaturated" if it is sufficiently weak. In the optically thin limit where the line center optical depth is $\tau \ll 1$, the column density becomes linearly proportional to W_0, independent of b. This portion of the COG is also referred to as the *linear* portion of the COG. In this limit, W_0 gives an accurate determination of the column density, N, even if the line profile is unresolved. Physically, as more atoms are added to the absorbing gas, thereby increasing N, W_0 increases due to removal of more photons in the core of the line until the absorption profile saturates.
- **Saturated:** A line is saturated when the transmitted intensity at the core of the line

approaches zero. Essentially, no photons at the line center make it through the absorbing cloud. This occurs when the gas has a sufficiently large column of atoms or ions, but with negligible contribution from the damping wings of the Lorentzian profile. In this regime, with $\sim 2-3 \lesssim \tau \lesssim 10^3$, W_0 begins to grow as the product of b and $\sqrt{\ln(N/b)}$. This implies that W_0 varies very slowly with N, and therefore, is very insensitive to N. This regime is also called the *flat* or the *logarithmic* portion of the COG.

- **Damped:** In this regime, the Doppler core of the line is totally saturated, but the damping wings of the line profile provide some measurable partial transparency. This begins to occur at higher column densities, with $\tau > 10^{3-4}$. In this case, W_0 does not depend on b and it varies with N as $W_0 \propto \sqrt{N}$. Due to the presence of the prominent damping wings of line profiles in this regime, this regime is also called the *damped* or *square root* part of the COG. An example of a damped Lyα system was shown in Figure 1.2.

For some transitions, the absorbing level will have allowed transitions to two different excited states (u_1 and u_2) due to fine-structure splitting (Draine 2011). In the optically thin limit, i.e. in the linear regime of the COG, the ratio of the doublet equivalent widths, DR, simplifies to

$$DR = \frac{W_{0,2}}{W_{0,1}} \approx \frac{f_2 \lambda_2}{f_1 \lambda_2}, \tag{1.5}$$

where $W_{0,1}$, f_1 and λ_1 denote the rest equivalent width, oscillator strength, and rest wavelength for the state u_1, and similarly for u_2.

When the lines enter the saturated regime of the COG, the DR is approximately

$$DR \approx \left[1 + \frac{\ln[f_2\lambda_2/f_1\lambda_2]}{\ln[\tau_1/\ln 2]}\right]^{1/2}. \tag{1.6}$$

For many resonance doublet transitions, such as Mg II $\lambda\lambda 2796, 2803$, C IV $\lambda\lambda 1548, 1550$ and Ca II $\lambda\lambda 3934, 3969$, the rest wavelengths are separated by only a few Angstroms and the oscillator strengths have ratios $f_2/f_1 \approx 2$. In these cases, the doublet ratio is an indicator of the saturation level of the line. That is, an unsaturated line has DR ≈ 2, while a line that approaches complete saturation has DR ≈ 1.

1.5 INTERVENING QUASAR ABSORPTION LINE SYSTEMS

1.5.1 Hydrogen Systems

In the local universe, the neutral hydrogen phase is often studied using H I 21-cm emission using large radio telescopes. However, the collecting areas and radio receiver response of such telescopes are only large enough to usefully perform 21-cm surveys up to $z \sim 0.2$ (Lah et al. 2007). At higher redshifts, it is also possible to trace H I through 21-cm in absorption (e.g Kanekar et al. 2006, Gupta et al. 2009), but detections are rare due to the lack of bright background radio sources. Also, galaxies have low cross-sections to cold, neutral gas (Prochaska & Tumlinson 2009). For these reasons, the neutral gas content, especially of the high-redshift universe, is primarily surveyed using QALs.

Depending on the column density of the parcel of gas intercepted by the LOS to the background quasar, different types of H I absorption-line profiles, belonging to different regions of the COG arise. These profiles are shown in Figure 1.2, i.e., the weak, narrow absorption lines in the Lyα forest, the Lyman limit systems (LLS), and the damped Lyα absorption (DLA).

1.5.1.1 The Lyα Forest Systems. The thicket of narrow absorption lines blueward of the broad Lyα emission in Figure 1.2 are due to a multitude of intervening clouds containing trace amounts of neutral hydrogen, mostly with column densities $N_{\rm H\,I} \lesssim 10^{15}$ cm $^{-2}$. These hydrogen clouds are highly ionized with $n_{H^0}/n_{H^0+H^{+1}} \leq 10^{-4}$, and are kept at temperature $T \sim 3 \times 10^4$ K by photoionization heating from the intergalactic UV background light.

1.5.1.2 The Lyman Limit Systems. LLSs are optically thick at the H I Lyman limit (912 Å), and therefore have $N_{\rm H\,I} > 10^{17.2}$ cm^{-2}, which is required for a Lyman limit opacity $\tau_{LL} > 1$. In Figure 1.2, the LLS is identified by the drop in the continuum flux at 3500 Å, which is due to absorbing clouds at $z = 2.8$ that are optically thick to Lyman-limit photons at 912 Å. The energy dependence of the H I ionization cross section leads to a recovery of the flux at shorter wavelengths. LLS are tracers of a mix of ionized and neutral gas at

temperatures of $T \sim$ 1-4$\times 10^4$ K. LLS with $N_{\rm H\,I} > 10^{20.3}$ cm^{-2} are referred to as the DLAs.

1.5.1.3 The DLA Systems. These systems are intervening H I systems ($T \sim 1 - 10 \times 10^2 K$) with $\rm N_{H\,I} \geq 2 \times 10^{20}$ cm^{-2}. At such high column densities, there is a sufficient degree of self-shielding in the gas against UV background sources that the gas is essentially neutral. At $N_{\rm H\,I} \sim 10^{19}$ cm^{-2}, the damping wings of the Voigt profile become prominent, so that these profiles are resolved even with lower-resolution spectrographs (FWHM $\sim 5 - 10$ Å). Since the first survey for DLAs nearly three decades ago (Wolfe et al. 1986), it has been accepted that they contain the bulk of the neutral gas content of the universe (Lanzetta, Wolfe & Turnshek 1995; Rao, Turnshek & Nestor 2006), which may provide the neutral gas reservoirs for fuel for subsequent star formation.

1.5.2 Metal Lines Systems

In addition to the hydrogen absorption line systems listed above, absorption lines due to metal-line transitions are also frequently seen when the metal content of the gas is large enough. The most common of these are due to the low-ionization transitions, such as the Mg II $\lambda\lambda$2796, 2803 doublet and Fe II λ2586, Fe II λ2600 transitions, and high-ionization transitions from the resonance doublet transitions of O VI $\lambda\lambda$1031, 1037, Si IV $\lambda\lambda$1393, 1402 and C IV $\lambda\lambda$1548, 1550 with rest wavelengths indicated in Table 1.1. The ubiquity of these lines in a quasar spectrum is due to their significant cosmic abundances and oscillator strengths, f. Note that these lines are, for practical reasons, usually surveyed redward of the Lyα broad emission to avoid confusion with Lyα forest lines. The low-ionization lines are used to trace the physical conditions and kinematics of the warm neutral gas in the ISM/CGM/IGM at T $\sim 10^4$ K. High ionization lines such as C IV and Si IV, on the other hand, are used to trace the kinematics of the ionized IGM/CGM at temperatures roughly a few times 10^4 K. The even higher ionization lines of O VI trace the hot diffuse gas at $T \sim 10^6$ K.

1.5.2.1 The Low-Ionization Mg II Absorption Lines

The relatively long wavelengths of the Mg II doublet, coupled with their large oscillator strengths, make this doublet among the most studied metal quasar absorption lines in the literature (e.g. Lanzetta, Turnshek & Wolfe 1987, Steidel, Dickinson & Persson 1994, Nestor et al. 2005, Churchill et al. 2005, Quider et al. 2010, Zhu & Menard 2011; Rao et al. 2013; Seyffert et al. 2013). The doublet is easy to identify and traces the redshift regime $0.4 \lesssim z_{abs} \lesssim 2.4$ in SDSS quasar spectra (York et al. 2000). The tremendous increase in the number of quasars identified in the SDSS since the initial data release has resulted to the identification of more than 40,000 absorbers in the seventh data release (Zhu & Ménard 2013) which has since increased two-fold in the twelfth data release.

In Chapter 5, I will present results on the first ever use of quasar sightlines to probe the extended disk region of the great spiral galaxy in Andromeda, M31, our nearest large spiral galaxy neighbor. This is based on Hubble Space Telescope (HST) observations of Mg II in absorption.

1.5.2.2 The Low-Ionization Ca II Absorption Lines

As apparent in Figure 1.3 and Table 1.1, the transitions used in QAL studies almost all lie in the rest frame UV, so the absorbers are usually at moderate to high redshifts. Even with the large number of absorbers available from SDSS Mg II surveys, more than 60% of cosmic history is still largely inaccessible through SDSS spectroscopy. The option of using space-based facilities such as the HST to perform very large UV quasar absorption line surveys is problematic due to the limited availability of HST observing time. Thus, the general lack of metal-line absorbers at very low redshifts makes studies of galaxies in the vicinity of absorbers difficult.

However, the Ca II $\lambda\lambda$3934,3969 absorption doublet falls at optical wavelengths where large numbers of SDSS quasar spectra are now available. Ca II absorption is also rare, in part because it is found in cool neutral regions, which may contain molecules and dust (Wild & Hewett 2005; Wild et al. 2006; Wild et al. 2007; Nestor et al. 2008; Zych et al. 2009). In other words, the integrated cross section of Ca II absorbers on the sky is small. Despite the

low incidence of Ca II, this thesis has taken advantage of the huge number of existing SDSS quasar spectra. We use these to identify and compile the largest sample of Ca II absorbers to date. The advantage of our very low redshift sample is that Ca II absorption can be used as a tracer of cool gas in the vicinity of galaxies which cannot be detected at higher redshift. As will be described in §1.6, the three chapters of this thesis will cover the results on the search for, and analysis of, SDSS Ca II absorbers.

1.5.2.3 The High-Ionization Metal Lines

In addition to low-ionization metal lines, high-ionization QALs may also arise in quasar spectra. Common examples of these are the C IV and O VI resonance doublet transitions. Their relatively short rest wavelengths imply that they probe the intermediate to high redshift Universe in optical surveys. In the SDSS, C IV QALs probe $1.5 \lesssim z_{abs} \lesssim 4.5$, while the O VI QALs probe much higher redshifts, $2.7 \lesssim z_{abs} \lesssim 7.9$. Consequently, UV space-based studies with HST are often required for O VI studies at low redshift.

The C IV (e.g. Steidel 1990; Barlow & Tytler 1998; Schaye et al. 2003; Becker, Rauch & Sargent 2009; Cooksey et al. 2013) and O VI (e.g. Frank et al. 2010; Pieri et al. 2010a) transitions have been well studied primarily because they are relatively strong transitions of common metals. Only C IV can be observed redward of the Lyα forest. These absorbers are generally produced from regions of low density under a hard UV background (Muzahid et al. 2012). In addition to being observed in only high-ionization gas, observations have shown that highly ionized gas detected in C IV and O VI absorption are seen in DLAs (Lu et al. 1996; Ledoux et al. 1998; Wolfe & Prochaska 2000a; Fox et al. 2007), in sub-DLAs (Dessauges-Zavadsky et al. 2003; Péroux et al. 2003; Richter et al. 2005), and in LLSs (Bergeron et al. 1994; Kirkman & Tyler 1997, 1999). As one moves to lower columns of H I from the DLAs to LLSs, one samples progressively more remote and highly ionized regions of galaxy halos, with most gas in the LLSs lying outside the halo virial radius (Maller et al. 2003; Davé et al. 1999). Hence, these types of absorbers may be tracers of the low-density CGM and IGM, arising in the extended halos of galaxies or feedback zones from galactic outflows (Bergeron & Herbert-Fort 2005; Simcoe et al. 2006.)

1.6 ORGANIZATION

This thesis seeks to build upon quasar absorption-line studies that focus on the low-redshift Universe. First, in particular, Ca II QALs have up until now been under-represented due to their rarity, but nevertheless are important diagnostics of key physical gas properties such as gas density, degree of self-shielding, and dust content. Secondly, future UV spectroscopy of quasars behind the M31 galaxy can build upon the results presented in Chapter 5 by acquiring higher signal-to-noise and resolution spectra which will probe down to much weaker W_0. In particular, higher resolution can be used to better study gas kinematics relative to 21 cm emission measurements, and/or using a greater number of sightlines to probe various locations of a galaxy's extended halo and disk regions. The rest of the thesis is organized as follows.

Chapter Two: *Ca II Absorbers in the Sloan Digital Sky Survey: statistics*

This work has been published as Sardane, Turnshek & Rao 2014, MNRAS, 444, 1747.

Chapter Three: *Ca II Absorbers in the Sloan Digital Sky Survey: chemical abundances and dust*

This work is the second paper in the series of papers on Ca II absorbers in the SDSS, and has been published as Sardane, Turnshek, & Rao 2015, MNRAS, 452, 3192.

Chapter Four *Ca II Absorbers in the Sloan Digital Sky Survey: associated galaxies*

This work (Sardane, Turnshek & Rao) is the third and final paper in the series of papers on Ca II absorbers in the SDSS. This paper is in preparation for submission to MNRAS.

Chapter Five: *Probing the Extended Gaseous Regions of M31 with Quasar Absorption Lines*

This work has been published as Rao, Sardane, Turnshek, et al., 2013, MNRAS, 432, 866. I was responsible for the data reduction, measurement, and analysis of UV data from the *Cosmic Origins Spectrograph* on the HST for ten quasar sightlines through M31.

Chapter Six: Summary and Conclusions

This chapter summarizes the results of the various projects in this thesis, and outlines some goals both for future projects and those that are already underway.

2.0 Ca II ABSORBERS IN THE SLOAN DIGITAL SKY SURVEY: STATISTICS

The contents of this chapter have been published in Sardane, Turnshek and Rao, 2014, *Monthly Notices of the Royal Astronomical Society*, 444, 1747 - 1758.

2.1 INTRODUCTION

A successful and complete theory of galaxy formation and evolution must not only explain the properties of the luminous components of galaxies, but also account for the properties, kinematics, and evolution of gaseous structures associated with them. Quasar absorption lines (QALs) are an extremely powerful probe of the physical properties and kinematics of the gas in galactic, intergalactic and circumgalactic environments. Since the detection of gaseous structures in absorption is independent of the luminosity of the absorbing medium, quasar spectroscopy has been crucial in providing a wealth of information on the distribution and evolution of matter in the Universe. Without the selection bias caused by galaxy brightness and surface brightness limitations, one can identify structures that are fainter than what traditional imaging studies allow. QAL studies have resulted in the identification of a gamut of intervening gaseous absorbers from the coolest molecular clouds detected in H_2 (e.g., Noterdaeme et al. 2008) to the predominantly neutral regions identified as H I damped Lyman alpha systems (DLAs) and low-ionization Mg II absorbers (e.g., Noterdaeme et al. 2012, Rao, Turnshek, & Nestor 2006, Quider et al. 2011, Seyffert et al. 2013), as well as hot ionized plasma in the extended halos of galaxies (e.g., Werk et al. 2014). The resonance transitions for the most common atoms and ions fall in the rest-frame ultraviolet

(UV). Consequently, the QALs used to explore and make identifications of these various gaseous components have often concentrated on absorbers at moderate to high redshifts where these lines fall at wavelengths accessible to optical ground-based telescopes. Given available time allocations, the option of using space-based telescopes such as the Hubble Space Telescope (HST) to perform large UV QAL surveys is impractical, expensive, and unrealistic. Consequently, large statistical studies of absorption line systems and the gaseous components of low-redshift galaxies that they trace are lacking.

One particular class of absorber, which falls at optical wavelengths at low redshift, is that traced by the Ca II H & K doublet, i.e. Ca II $\lambda\lambda 3934, 3969$. It is a resonance doublet transition of singly ionized calcium from the ground state with rest-frame wavelengths $\lambda = 3934.78$ Å (Ca II K) and $\lambda = 3969.60$ Å (Ca II H). The energy required to photoionize the neutral Ca atom is 6.11 eV. However, the energy required to photoionize Ca^+ is only 11.87 eV, a value that is slightly less than the ionization potential of H I. Thus, Ca^+ may not be the dominant ionization state of calcium. Moreover, Ca is a highly refractory element, being among the most depleted in the interstellar medium (Savage and Sembach 1996; Wild and Hewett 2005; Wild, Hewett & Pettini 2006). Thus, Ca II is a rare class of absorber, which nevertheless is an important diagnostic of key physical properties of the gas such as its density, degree of self-shielding, and dust content. To emphasize this point, we further note that detailed spectroscopic studies of the astrophysical properties of Ca II absorbers (e.g. Zych et al. 2009, Richter et al. 2011, Crighton at al. 2013) reveal that they exhibit a variety of neutral hydrogen column densities, sometimes exhibit H_2, have a range of dust to gas ratios, and are sometimes associated with environments which give rise to high-ionization metal lines.

Ca II absorption has been proposed to arise in environments where some fraction of the dust grains has been destroyed, and the fraction of Ca in the gas phase enhanced due to shocks driven by supernovae associated with recent star-formation (Routly & Spitzer 1952). More recent studies of a handful of Ca II absorbers (Wild & Hewett 2005; Wild, et al. 2006; Wild, Hewett & Pettini 2007; Nestor et al. 2008; Zych et al. 2007; Zych et al. 2009) indicate that Ca II systems with $W_0^{\lambda 3934} \gtrsim 0.2$ Å preferentially reside in dense, dusty, neutral, metal-rich, H_2-bearing environments — the reservoirs for subsequent star-formation.

Intervening Ca II absorption associated with low-redshift galaxies were detected in quasar

spectra early in the history of QAL spectroscopy. See Blades (1988) for a summary of early detections. The first systematic attempt to establish the extent of Ca II absorption in present-day galaxies was carried out by Morton, York & Jenkins (1986). Their search, which used seven background quasars, was unable to detect any absorption above their sensitivity limits at projected galactocentric distances of $\sim 10 - 300$ kpc. Subsequent work by Bowen et al. (1991) and Bowen (1991) using background quasars found to be fortuitously close to $z \lesssim 0.1$ foreground galaxies suggested that Ca II absorption occurring beyond ~ 20 kpc from a galaxy's center is relatively weak, with Ca II K rest frame equivalent widths $W_0^{\lambda 3934} \lesssim 0.2$ Å, and distributed non-homogeneously around the galaxies. They detected a single Ca II system with $W_0^{\lambda 3934} \approx 0.6$ Å and within ~ 10 kpc from a galaxy's center. They suggested that Ca II absorption may arise from material deposited through galaxy interactions. In addition, results on the extent of Ca II absorbers have been discussed in the literature (e.g. Ben Bekhti et al. 2008, Richter et al. 2011) in terms of being distant analogs of the intermediate and high velocity clouds in the halo of the Milky Way, as they appear to trace neutral and partly ionized gas clouds in the halos and circumgalactic environments of galaxies.

Recent measurements (Zhu & Menard 2013) of the average density profile of Ca II gas around galaxies out to ~ 200 kpc using cross-correlation analysis of the positions of $\sim 10^6$ foreground galaxies with $\sim 10^5$ background quasars in the Sloan Digital Sky Survey (SDSS) concluded that most of the Ca II in the Universe is in circum- and intergalactic environments, and that the Ca II content in galaxy halos is larger for galaxies with higher stellar mass and star formation rates.

Studies of the extent of rare Ca II absorbers around galaxies will, therefore, place important empirical contraints on models for the existence of cool gas in the extended regions of galaxies. This includes models of cold accretion (e.g. Dekel & Birnboim 2006, Kereš et al. 2009, Stewart et al. 2011, and references therein); and models relying on radiation pressure driving from massive clusters followed by ram pressure driving from SNe (e.g, Nath & Silk 2009, Murray et al. 2011, Sharma & Nath 2012, and references therein), which can launch cool gas out beyond 50 kpc. These processes have implications for the fueling and evolution of galaxies (Davé, Oppenheimer & Finlator 2011; Davé, Finlator & Oppenheimer 2011, and references therein); cold accretion fuels star formation, while resulting feedback

and outflows quench it. Furthermore, such studies are useful in understanding trends in the colors, luminosities, morphologies and orientations of galaxies, as well as the dust-content and metal-enrichment of the IGM/CGM. Since Ca II can be detected in ground-based surveys down to $z = 0$, the lowest redshift Ca II systems allow for detailed studies of the absorbers and their host galaxy environments.

In this paper, we present the results from the largest sample of Ca II $\lambda\lambda 3934, 3969$ absorbers ever compiled. In a blind survey of roughly $95,000$ quasar spectra from the Seventh and Ninth Data Release of the SDSS (SDSS-DR7, DR9), we identified 435 Ca II doublets with $W_0^{\lambda 3934} \geq 0.16$ Å. The wavelength coverage of the SDSS spectrum allows us to probe the redshift interval $z < 1.34$, which corresponds to ~ 8.9 Gyr of cosmic history. More importantly, of all the ionic transitions commonly observed in SDSS spectra, only Ca II provides ground-based access to the low redshift regime of $z < 0.34$, which is equivalent to 4 Gyrs of cosmic history. This work, which primarily aims to present a statistical description of Ca II systems in low-resolution SDSS spectra, is the first in a series of chapters exploring the properties of these rare absorbers. Follow-up analysis on their chemical and dust depletion properties, and their connection to potential host galaxies, will be discussed in forthcoming chapters in the series.

The paper is organized as follows: In §2.2 we describe the data reduction process: the continuum fitting and line-finding algorithms, the selection criteria we imposed, and tests for systematic biases. We then present our main results in §2.3, where we derive the absorber rest equivalent width (REW) parametrization and evolution and the absorber redshift number density and its evolution, along with results on Ca II doublet ratios and how the incidence of Ca II absorbers compares with that of Mg II absorbers. In §2.4, we discuss evidence for two populations of Ca II absorbers. We summarize and present our conclusions in §2.5. Throughout the paper, we assume a standard ΛCDM cosmology with $H_0 = 71$ km s^{-1}Mpc^{-1}, $\Omega_M = 0.27$, and $\Omega_\Lambda = 0.73$ (Spergel et al. 2007; Komatsu et al. 2011).

2.2 THE SDSS Ca II CATALOG

From its early beginnings, the SDSS (York et al. 2000) has been pivotal in advancing moderate resolution quasar absorption line spectroscopy by providing a huge increase in the number of quasar spectra available for absorption line surveys. Spectroscopy from the SDSS-I/II data releases has resulted in over 100,000 quasar spectra in the seventh data release (Schneider et al. 2010). The spectra were obtained using a pair of similar multi-object fiber spectrographs mounted on a dedicated 2.5-m wide-field telescope. Each spectrograph has 640 three-arcsecond-diameter fibers, with a combined spectral coverage of $3800 - 9200$ Å. More recently, the ninth data release provided an additional $\sim 80,000$ quasar spectra (Ahn et al. 2012; Pâris et al. 2012) from ~ 1.5 years of data from the SDSS-III Baryon Oscillation Spectroscopic Survey (BOSS, Schlegel et al. 2007; Dawson et al. 2013). The improved BOSS spectrograph (Smee et al. 2013) has 1000 two-arcsecond-diameter fibers, and has an extended wavelength coverage of $3600 - 10,400$ Å. Both the SDSS and BOSS spectrographs have approximately the same resolution ranging from 1500 at 3800 Å to 2500 at 9000 Å.

In this work, we utilize the most recent entries found in the SDSS DR7 and DR9 quasar catalogs of Schneider et al. (2010) and Pâris et al. (2012), respectively. The SDSS spectral coverage corresponds to an absorption redshift interval of $z < 1.34$ in the Ca II λ3934 absorption line. We confined our search for Ca II absorption lines in the BOSS data set to redshifts $z < 1.34$ even though the BOSS quasar spectra have redshift coverage up to $z = 1.64$.

2.2.1 Quasar Sample Selection

In order to ensure adequate signal-to-noise ratios, we restricted the quasar sample to SDSS fiber magnitudes of $i < 20$, and to minimize the incidence of galaxies that have been misidentified as quasars, we only considered quasars with $z_{em} \geq 0.1$. In addition, we searched for Ca II at wavelengths greater than 6000 km s^{-1} redward of the quasar Ly-α emission line. The quasar with the highest redshift in our sample has $z_{em} = 6.0$. We used the catalogs compiled by Shen et al. (2011) for SDSS DR7, and extended by Pâris et al. (2012) for SDSS DR9, to exclude broad absorption line quasars from our search. Altogether, 94,114

quasar spectra were useful for the search of the Ca II absorption doublet. The distribution of emission redshifts, z_{em}, of the quasar sample is shown in Figure 2.1. The distribution has a mean of $< z_{em} >= 1.4$.

2.2.2 Data Reduction

The construction of our Ca II absorber sample closely follows the methods adopted for the construction of the University of Pittsburgh SDSS Mg II catalog described in Nestor et al. (2005), Rimoldini (2007), and Quider et al. (2011). Quite generally, our data reduction proceeds three-fold as follows: (1) automated quasar processing, (2) visual inspection of the automatically flagged doublet candidates, and (3) measurement of the line strengths of the doublets that passed the stringent visual inspection.

The automated processing procedure consisted of two stages, i.e., the pseudo-continuum normalization and the search for Ca II doublets. A combination of cubic splines and Gaussians were employed to determine the pseudo-continuum fit, which included both the true continuum as well as the broad emission features. In Figure 2.2, we show an example spectrum with the pseudo-continuum fit overplotted in red. For the vast majority of spectra, the continuum-fitter worked quite well, even in regions of poor signal-to-noise ratios. The error in the normalized flux is derived by dividing the flux error array by the fitted continuum. We do not propagate any errors in the continuum fit to determine the normalized error array. However, we will later show that a 20% error in continuum level determination is not the dominant source of uncertainty; given the relatively small number of detected systems, statistical Poisson errors are still the major source of uncertainty.

All normalized spectra were then searched for Ca II absorption using a line-finding algorithm that flags possible Ca II candidate doublets based on the doublet separation and line significance levels. To isolate a sample of intervening absorbers, we only accepted candidates that were separated in velocity by at least 6000 km s^{-1} from the quasar emission redshift, and from $z = 0$. Thus, biases that could arise due to an over-density of absorbers in the vicinity of quasar environments and the Milky Way, respectively, were minimized.

All candidate doublets were then visually inspected to check for satisfactory continuum

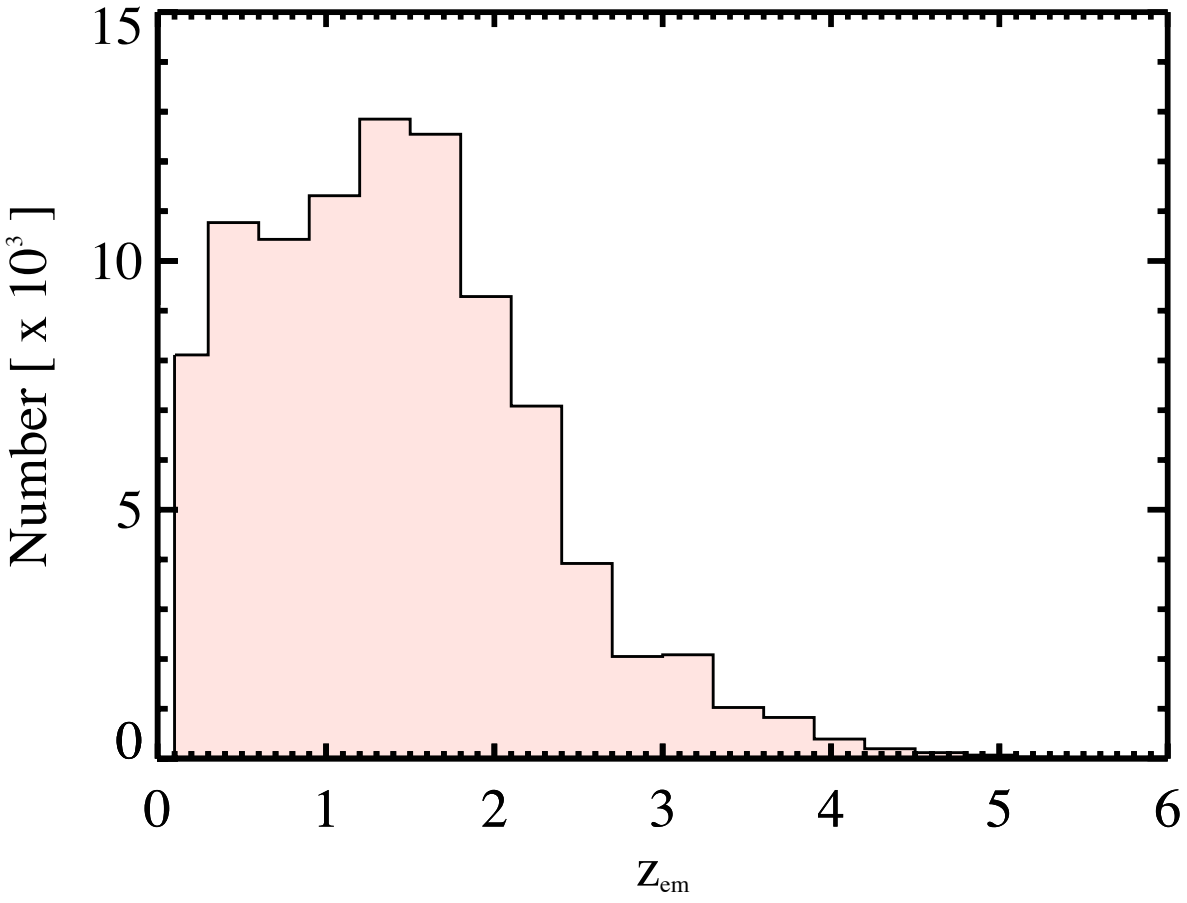

Figure 2.1: The distribution of emission redshifts of the SDSS quasars, with magnitudes $i < 20$ and $z_{em} \geq 0.1$, used to search for the Ca II $\lambda\lambda 3934, 3969$ absorption doublet. The distribution has a mean of $< z_{em} >= 1.4$, and a maximum redshift of $z_{em} = 6.0$.

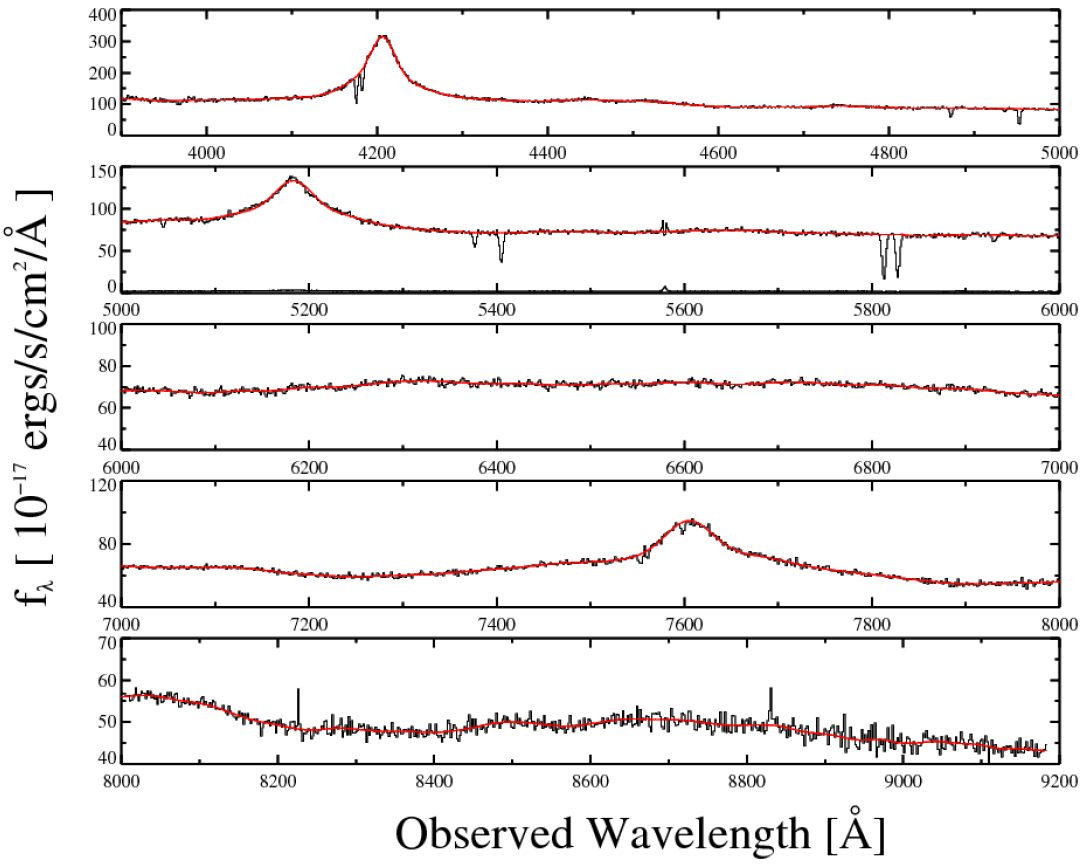

Figure 2.2: An example quasar spectrum with the psuedo-continuum fit overplotted in red. In this example, $z_{em} = 1.720$, and the median error is $\sim 2.6\%$ of the flux.

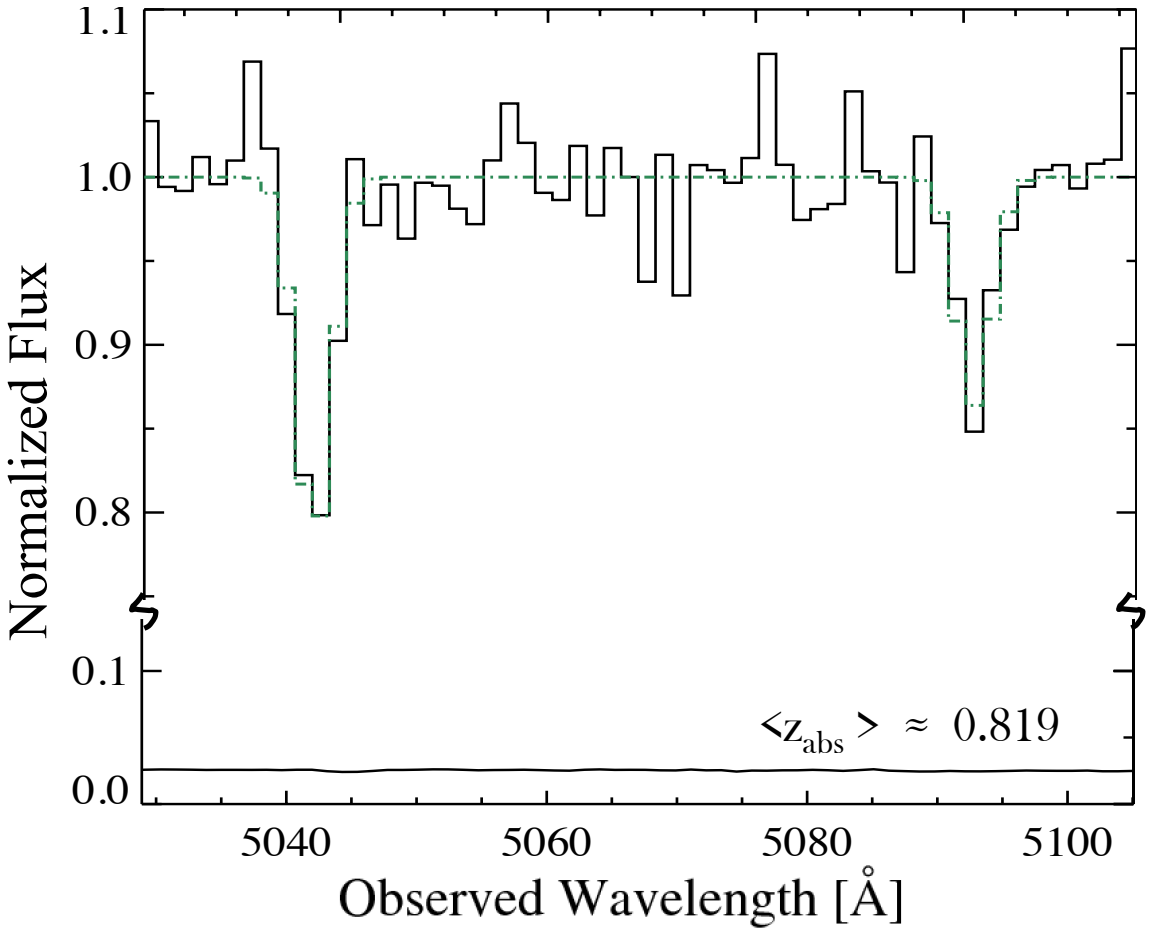

Figure 2.3: An example Ca II absorber system at $z_{abs} = 0.819$. The green dot-dash curve is a double Gaussian profile that was fit simultaneously to both members of the doublet. Note that to emphasize the feature, as well as its error array, the spectrum is truncated between $\sim 0.1 - 0.8$ in normalized flux units.

fits, blends, and potential false detections due to the presence of absorption lines at other redshifts that could mimic the Ca II profile. We further note that we painstakingly examined each absorption feature flagged by the line-finding routine and retained systems after eliminating every other possibility. In order to identify a Ca II system, we required the detection of the λ3934 line *and* the λ3969 doublet partner. We required a 5σ minimum level of significance for the λ3934 line and a 2.5σ minimum level of significance for the λ3969 doublet partner. From their oscillator strengths, $f = 0.682$ for the λ3934 line and $f = 0.330$ for the λ3969 line (Kramida et al. 2013), the secondary λ3969 line is expected to be roughly half as weak as the primary λ3934 line in the unsaturated regime. We measured the doublet REWs, $W_0^{\lambda3934}$ and $W_0^{\lambda3969}$, by fitting unresolved Gaussian profiles to both lines simultaneously, with full width half maxima (FWHM) given by the resolution of the SDSS spectrograph. Candidates with doublet ratios (DRs) that were outside the physically allowed range of $1.0 - \sigma_{DR} \leq W_0^{\lambda3934}/W_0^{\lambda3969} \leq 2.0 + \sigma_{DR}$ were eliminated. The error in the doublet ratio, σ_{DR}, was estimated assuming Gaussian uncertainties. The redshift of an absorber was determined from the weighted average of the wavelength centroids of the two fitted doublet Gaussian profiles. Figure 2.3 shows an example absorber that passed our selection cuts.

The survey sightline coverage, or sensitivity function, is shown in Figure 2.4 as a function of absorber redshift and minimum detectable REW threshold, W_0^{min}. The corresponding SDSS wavelength coverage is indicated by the top axis. The sightline coverage is the total number of lines of sight with sufficient signal-to-noise ratio to detect the λ3934 Å line with $W_0^{\lambda3934} \geq W_0^{min}$ at a $\geq 5\sigma$ level of significance, *and, at the same time,* detect the λ3969 Å line at a $\geq 2.5\sigma$ level of significance. We emphasize that in order to be included in the accounting of the total survey path, a single redshift pixel and its corresponding doublet pixel position must have sufficient signal-to-noise ratios to detect the doublet pair at significance levels of 5σ and 2.5σ, respectively, and to detect both lines within the physically allowable doublet ratio range of $1.0 - \sigma_{DR} \leq W_0^{\lambda3934}/W_0^{\lambda3969} \leq 2.0 + \sigma_{DR}$. [1] The strongest possible λ3969 absorption line is given by a profile with $DR = 1.0$, therefore, a pixel is rejected from the redshift path if a saturated $W_0^{\lambda3969}$ line, where $W_{0,min}^{\lambda3934} = W_{0,min}^{\lambda3969}$, cannot be detected at this

[1] We note that no previous survey for absorption line doublets has imposed as stringent a doublet-finding criterion as employed here. Past surveys imposed a significance cut only on the stronger member of the doublet.

position with a significance level of at least 2.5σ. The sensitivity function for our survey is given by Equation 2.1:

$$g(W_0^{\lambda 3934}, z) = \sum_{i=1}^{N_{LOS}} H(z - z_{min(i)}) H(z_{max(i)} - z) \times H[W_0^{\lambda 3934} - 5\sigma_0(z)] H[W_0^{\lambda 3969} - 2.5\sigma_0(z)] \tag{2.1}$$

where the sum is over the total number of lines of sight, N_{LOS}, and H is the Heaviside function. Using λ_{min} and λ_{max} to indicate the wavelength limit of each quasar spectrum, we write the minimum (maximum) redshift coverage, z_{min} (z_{max}), for each quasar spectrum as

$$z_{min} = \begin{cases} 0.02 & \text{if } \lambda_0 \geq \lambda_{min} \\ \lambda_{min}/\lambda_0 - 1 & \text{if } \lambda_0 < \lambda_{min} \end{cases} \tag{2.2}$$

$$z_{max} = \begin{cases} z_{em} - 0.02 & \text{if } \lambda_0(1 + z_{em}) < \lambda_{max} \\ \lambda_{max}/\lambda_0 - 1 & \text{if } \lambda_0(1 + z_{em}) \geq \lambda_{max}. \end{cases} \tag{2.3}$$

The prominent deep feature in Figure 2.4 occurring near absorber redshift $z \sim 0.5$ (6000 Å) is due to the SDSS dichroic (Schneider et al. 2010). The conspicuous absorption features redward of $z \sim 0.8$ are due to strong night sky lines in many spectra. Taking into account the line significance of both members of the Ca II doublet in calculating redshift path results in the doubling of narrow dips seen in Figure 2.4, as one might expect.

Integrating the sensitivity function of Figure 2.4 over the allowed redshift interval for Ca II, as determined by each SDSS spectrum, gives the cumulative path length of the survey, $g(W_0^{min})$, as a function of REW threshold W_0^{min}. The solid black curve shown in Figure 2.5 effectively describes the sensitivity of the survey to the measurement of a given strength of the λ3934 line. For example, a λ3934 line with REW $W_0^{\lambda 3934} \geq 1.0$ Å can only be detected in roughly half of the total available sightlines. The cumulative path length of the survey then asymptotes to 94, 114 lines of sight at large REWs. The dash-dot black curve depicts the decrease in the cumulative path that would result from a (conservatively chosen) 20% error in the continuum fit, added to the flux error array in quadrature. The difference between

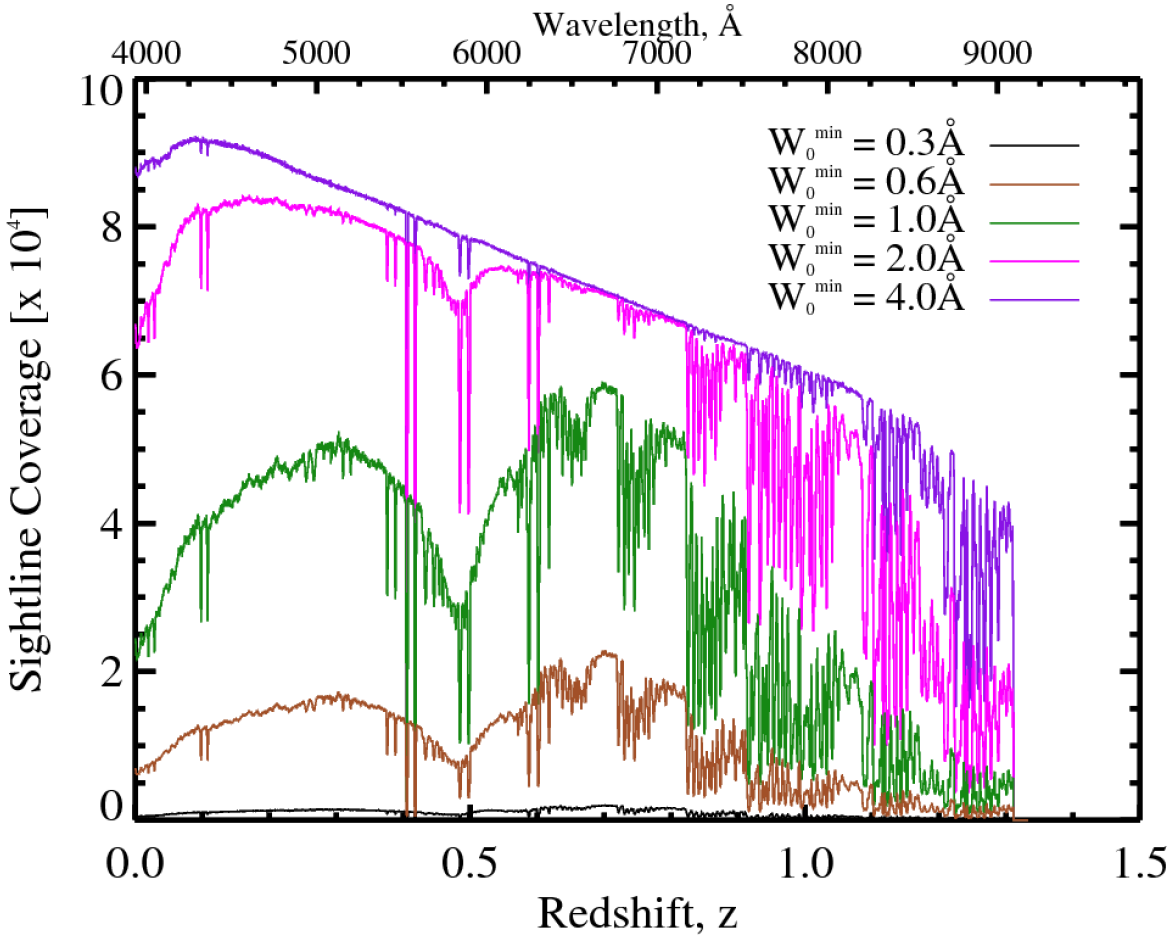

Figure 2.4: Sightline coverage for the Ca II survey in the SDSS DR7+DR9 as a function of absorber redshift and REW threshold: $W_0^{\rm min} = 0.3, 0.6, 1.0, 2.0, 4.0$ Å. This gives the total number of lines of sight with sufficient signal-to-noise ratio to detect at least a saturated Ca II doublet at the 5σ,2.5σ significance levels. See text. The wide, deep feature near $z = 0.5$ is due to the SDSS dichroic. The sharp narrow dip in the middle of the dichroic is from the prominent O I λ5578 night sky line. The series of sharp declines redward of z $\approx$ 0.8 are the due to strong night sky lines. The additional constraint on the λ3969 line in Eq. 2.1 results in the doubling of narrow dips.

the two paths peaks at 8% at $W_{min,0}^{\lambda 3934} = 0.2$ Å, decreases to 2% at $W_{min,0}^{\lambda 3934} = 1.0$ Å, and to 0.04% at $W_{min,0}^{\lambda 3934} = 6.0$ Å.

2.2.3 Monte Carlo Simulations to Determine False Positives and Systematics

We ran Monte Carlo simulations of the absorber catalog to test the efficiency of our detection routine and identify possible biases and systematic effects. Prior to the simulations, we masked out all detected Ca II systems from their respective spectra, and used the edited spectra for the simulations instead. Using the observed distributions for the absorption redshift, $W_0^{\lambda 3934}$, and FWHM of the absorbers, and a uniformly distributed doublet ratio, we generated 10,000 Ca II doublets and inserted them into randomly-selected spectra. Approximately 7300 of these appeared in regions of spectra with sufficient signal-to-noise ratio that met our criteria for detection. We then ran the entire data pipeline and recovered 97.7% of these simulated doublets. Thus, we may have missed a maximum of 10 doublets in our search. In addition, no Ca II doublet that was not in the input list was falsely included in the output list of the simulation.

2.3 RESULTS

2.3.1 The $W_0^{\lambda 3934}$ Distribution

We identified 435 Ca II doublets with $W_0^{\lambda 3934} \geq 0.160$ Å and $z \lesssim 1.34$. The first few entries of our Ca II catalog are presented in Table 2.1. The table is available in its entirety online. The observed $W_0^{\lambda 3934}$ distribution is shown in Figure 2.6. The strongest system we found has $W_0^{\lambda 3934} = 2.573$ Å, while the weakest system has $W_0^{\lambda 3934} = 0.163$ Å. The distribution has a mean of $< W_0^{\lambda 3934} >= 0.769$ Å and a spread of $\sigma = 0.393$ Å. Combining the observed distribution from Figure 2.6 with the cumulative path length in Figure 2.5, we obtain the sensitivity-corrected distribution for $W_0^{\lambda 3934}$, shown as the binned data points in Figure 2.7. The errors are determined using Poisson statistics. Similar to what has been found for other classes of QAL systems, the REW distribution rises with decreasing REWs. However, the

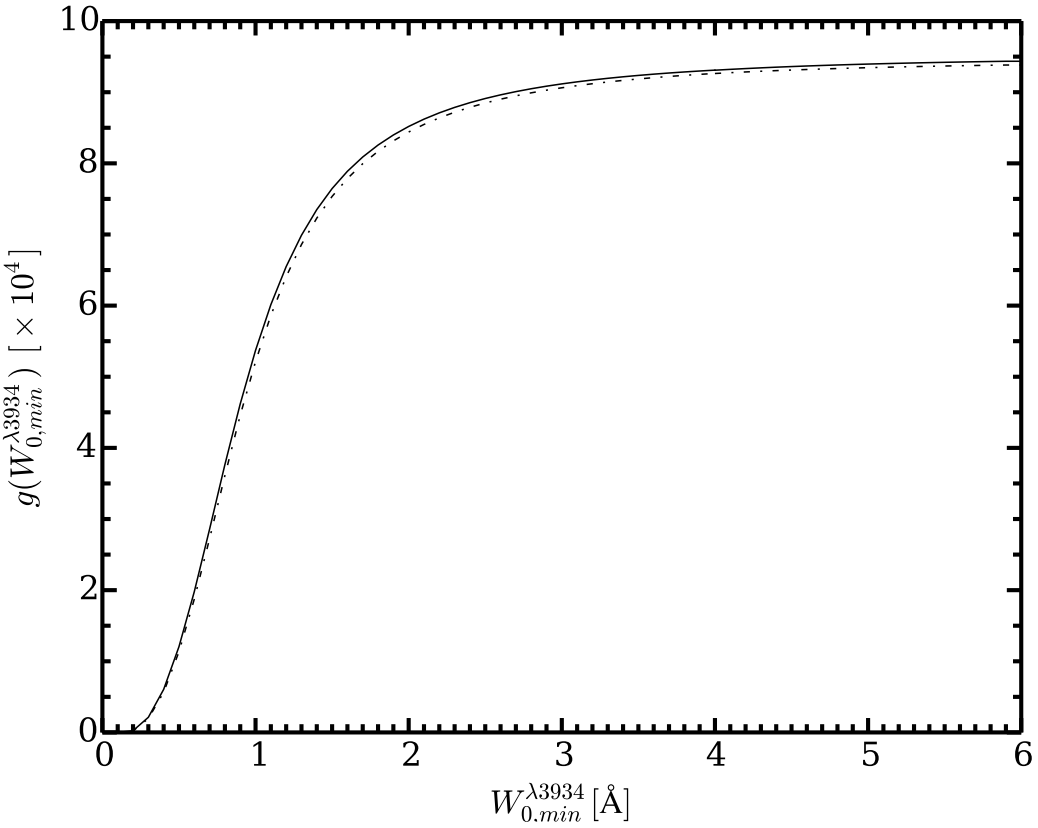

Figure 2.5: The cumulative pathlength, $g(W)$, as a function of REW threshold is shown here as the black solid curve. The decrease in the path due to an additional 20% uncertainty in the pseudo-continuum fit added in quadrature is shown by the black dash-dot curve. The difference between the two cumulative path lengths peaks at 8% at $W_{0,min}^{\lambda 3934} = 0.2$ Å, decreases to 2% at $W_{0,min}^{\lambda 3934} = 1.0$ Å, and to 0.04% at $W_{min,0}^{\lambda 3934} = 6.0$ Å.

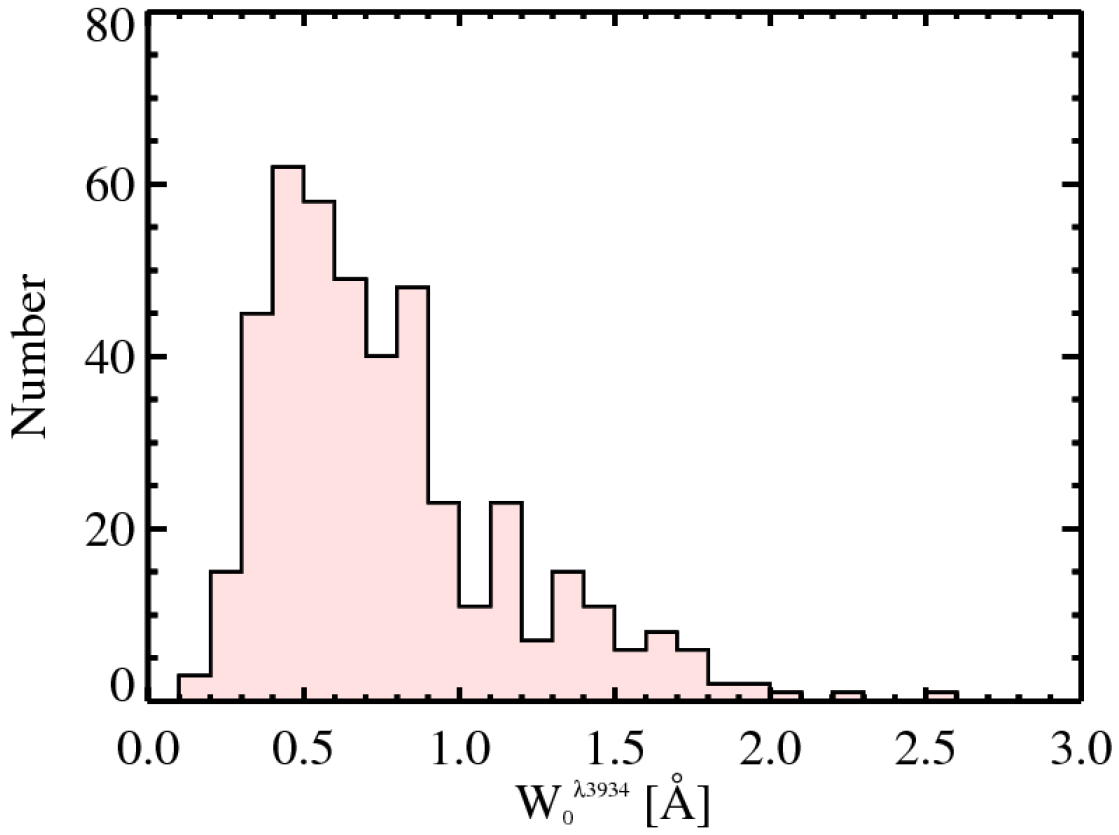

Figure 2.6: The observed REW distribution for $W_0^{\lambda 3934}$. The distribution has a mean of 0.769Å and a spread of 0.393 Å. Measured REWs range from 0.163 Å $\leq W_0^{\lambda 3934} \leq$ 2.573 Å.

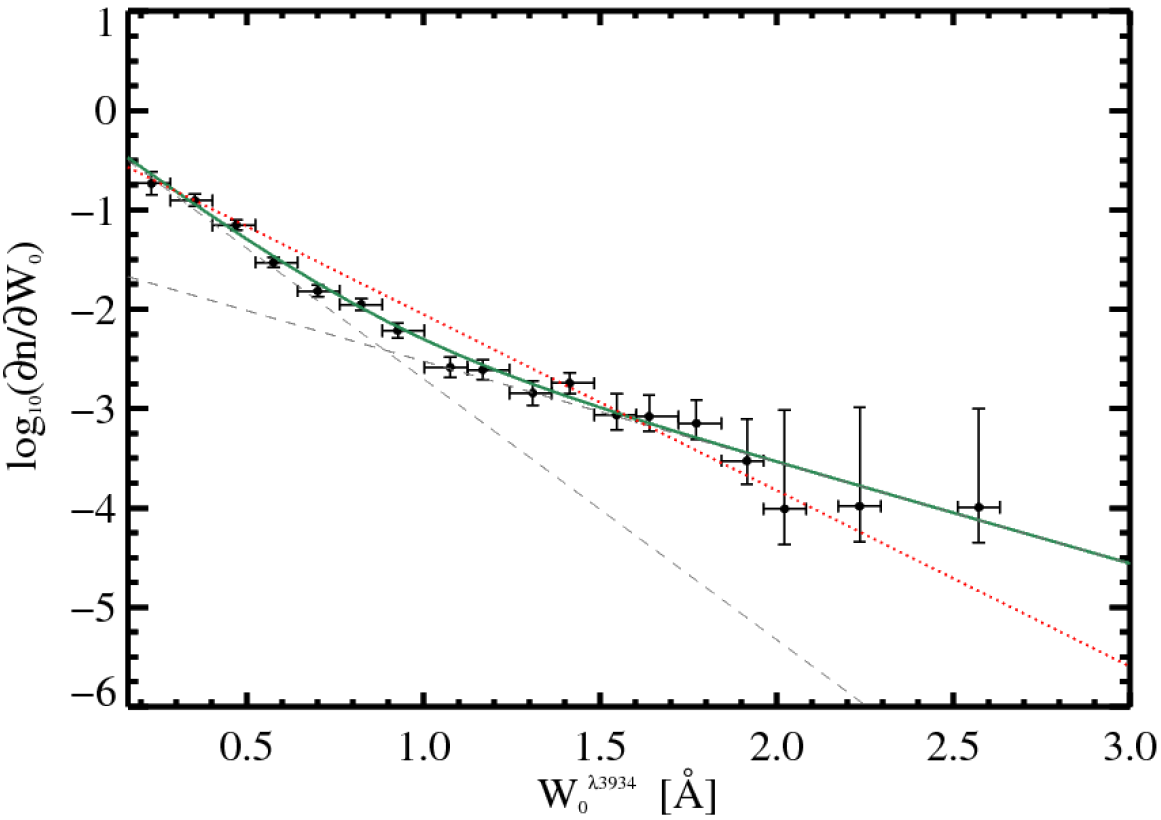

Figure 2.7: The sensitivity-corrected $W_0^{\lambda 3934}$ distribution. The double exponential model, Equation 2.4, that maximizes the likelihood to the unbinned data, is shown in green. The two single-exponential components of Equation 2.4 are plotted as grey dashed lines. The maximum likelihood fit using a single exponential model is shown as the red dotted line.

Table 2.1: The Ca II Sample[a]

Quasar	SDSS g mag	z_{em}	z_{abs}	$W_0^{\lambda3934}$ (Å)	$\sigma(W_0^{\lambda3934})$ (Å)	$W_0^{\lambda3969}$ (Å)	$\sigma(W_0^{\lambda3969})$ (Å)
J001214.19−095922.9	19.44	1.262	0.6901	0.773	0.137	0.412	0.112
J001444.02−000018.5	17.95	1.550	0.0277	0.326	0.056	0.201	0.055
J002940.02+010528.5	17.83	1.388	0.3732	0.302	0.059	0.213	0.060
J004130.97+024222.5	18.81	2.308	0.7095	0.720	0.143	0.370	0.120
J004800.50+022514.9	18.96	2.160	0.5982	0.594	0.101	0.297	0.096

[a] The table is available in its entirety in the Appendix.

data clearly show a change in the slope of the distribution near $W_0^{\lambda3934} \approx 0.9$ Å. The best-fit single exponential function, determined using a maximum likelihood estimate (MLE) on the unbinned data, is clearly a poor fit as shown by the red dotted line in Figure 2.7. Therefore, we used a double-exponential function, written as the sum of weak and strong components, to obtain a satisfactory fit. Equation 2.4 parametrizes the model with two characteristic REWs, $W^\star_{wk}$ and $W^\star_{str}$, and two normalization constants, $N^\star_{wk}$ and $N^\star_{str}$, for the weak and strong components, respectively. [2]

$$\frac{\partial n}{\partial W_0^{\lambda3934}} = \frac{N^\star_{wk}}{W^\star_{wk}} e^{-\frac{W_0^{\lambda3934}}{W^\star_{wk}}} + \frac{N^\star_{str}}{W^\star_{str}} e^{-\frac{W_0^{\lambda3934}}{W^\star_{str}}} \tag{2.4}$$

The resulting fit parameters are $N^\star_{wk} = 0.140 \pm 0.029$ and $W^\star_{wk} = 0.165 \pm 0.020$Å for the weak component, and $N^\star_{str} = 0.024 \pm 0.020$ and $W^\star_{str} = 0.427 \pm 0.101$Å for the strong component. The solid green curve shows this best-fit double exponential function MLE fit to the unbinned data. The dashed grey lines are the two individual components; from this fit, we determined that the change in slope occurs at $W_0^{\lambda3934} = 0.88$Å.

[2] In this context, we use the terms "weak" and "strong" to refer to the two components of the observed $W_0^{\lambda3934}$ distribution. Thus, this usage does not intend to provide a formal definition of whether an individual Ca II absorber should be considered weak or strong.

We evaluated the Akaike Information Criterion (AIC) for both the single and double exponential fits, and obtained $AIC = 46$ and $AIC = 11$ for the two fits, respectively. The AIC is a measure of the quality of the candidate models relative to each other (Liddle 2007). It is based on information entropy and quantifies the trade-off between goodness of fit and complexity (i.e., the number of parameters) of the model. Given a set of candidate models, the model with the smallest AIC value has the strongest support. Thus based on the AIC values above, the data are significantly better represented by the double exponential fit. The existence of a change in slope and the success of the double exponential model may be interpreted as evidence for the existence of more than one class of Ca II absorber. We will address this possibility further in §2.4.

2.3.1.1 Redshift Evolution of $\partial n/\partial W_0$ We now investigate the redshift evolution of the REW distribution, $\partial n/\partial W_0$. We binned the data into three redshift subsamples, with each z_{abs} interval having roughly the same number of absorbers. The results are shown in Figure 2.8. The solid green curves show the MLE fit to the unbinned data. For comparison, the single exponential fits are shown as red dashed lines. The subsample in the lowest redshift bin shows the most prominent departure from a single exponential fit. While the other two subsamples still show some hints of a change in slope, it is less apparent given the increasing size of the error bars at larger $W_0^{\lambda 3934}$. The AIC values in each subsample suggest that the single exponential model is still less favored, although the degree of support has decreased in the higher-redshift subsamples. Thus, we cannot discount the possibility of the persistence of multiple populations across the different redshifts.

In Figure 2.9 we plot the resulting double exponential model parameters $W^{\star}_{wk}$ and $W^{\star}_{str}$, and $N^{\star}_{wk}$ and $N^{\star}_{str}$, as a function of the mean z_{abs} in each subsample. The result for the entire Ca II sample is shown as the open data points, plotted at a z_{abs} that is slightly offset from the median for clarity. These plots clearly show that there is no evidence for evolution in the shape of the exponenial distributions for either the weak or strong components of the fit. In addition, Kolmogorov-Smirnov (KS) tests are also consistent with no evolution.

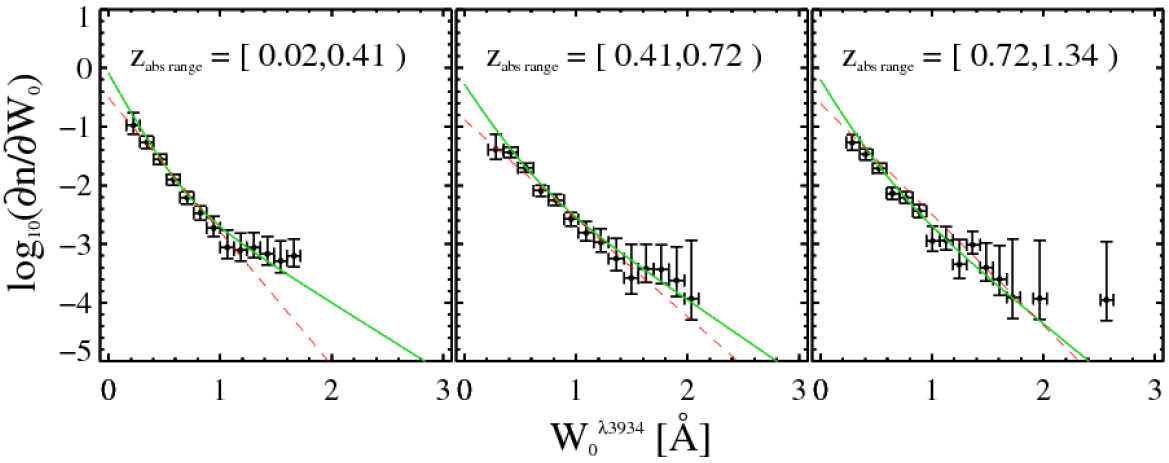

Figure 2.8: The sensitivity-corrected $W_0^{\lambda 3934}$ distribution binned into three redshift intervals. The double exponential model (Equation 2.4) that maximizes the likelihood to the unbinned data is shown in green. The single exponential fit is shown as the red dashed line. The single exponential model is less favored over the double exponential model in all redshift intervals.

2.3.2 The Ca II Absorber Redshift Distribution

The observed absorber redshift distribution is shown in Figure 2.10. As mentioned previously, SDSS spectra can be used to search for Ca II at redshifts $z_{abs} \lesssim 1.34$, equivalent to a lookback time of $t_{LB} \sim 8.9$ Gyrs, or $\gtrsim 60\%$ of our cosmic history. The observed distribution has a mean redshift of $< z_{abs} >= 0.579$, and standard deviation of $\sigma_{z_{abs}} = 0.296$. The distinct drop in sensitivity near $z \sim 0.5$ is mainly due to the SDSS dichroic.

The redshift number density, $\partial n/\partial z$, or the incidence of lines that have $W_0^{\lambda 3934}$ larger than a specified threshold W_0^{min} over some redshift interval, is given by

$$\left.\frac{\partial n}{\partial z}\right|_{W_0 > W_0^{min}} = \sum_{\substack{W_{0,i} > W_{0,min} \\ z_i \in (z, z+dz)}} \frac{1}{g(W_{0,i}, z_i) dz} \tag{2.5}$$

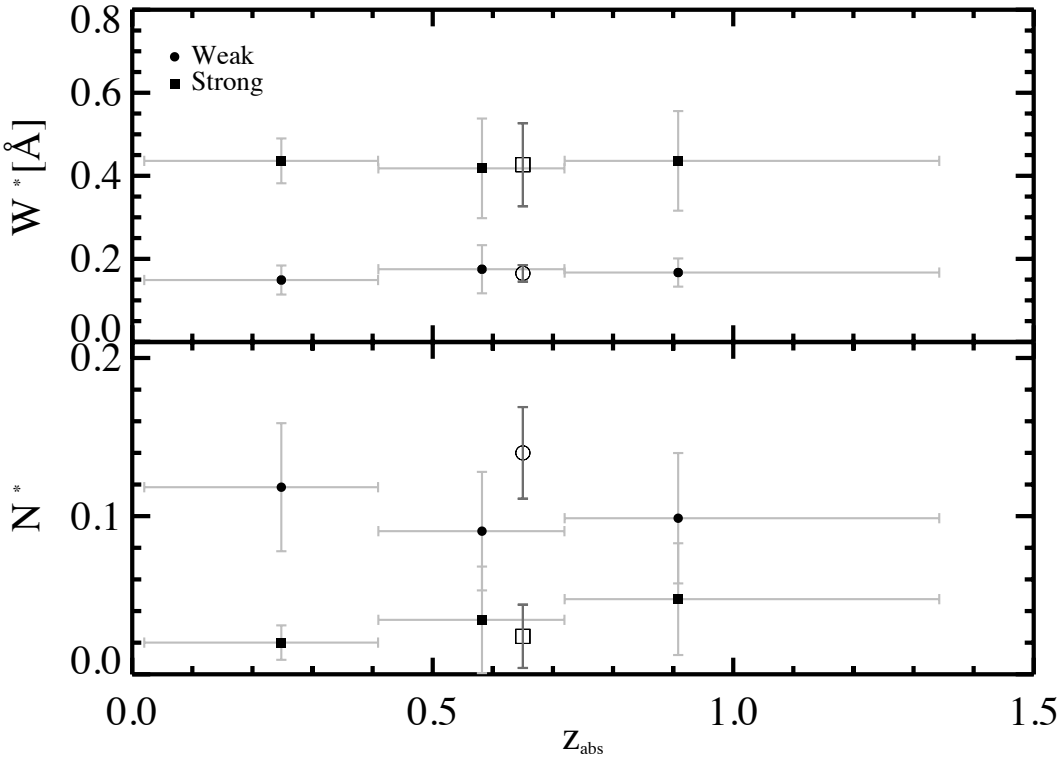

Figure 2.9: *Top:* The MLE characteristic REWs, $W^{\star}$, for the weak (filled circles) and strong (filled squares) components, in the three redshift ranges shown in Figure 2.8. The error bars and bin sizes are shown in grey. The $W^{\star}$ parameters imply a lack of redshift evolution in the slopes of each component. *Bottom:* The MLE normalizations for the two-component fit, which within the errors, are also consistent with no evolution. For reference, we have plotted the results for the entire sample as open circles and squares, which for clarity, are plotted at a location slightly offset from the median z_{abs}.

whose variance is given by

$$\sigma^2 = \sum_{\substack{W_{0,i} > W^0_{min} \\ z_i \in (z, z+dz)}} \left(\frac{1}{g(W_{0,i}, z_i) dz} \right)^2 . \tag{2.6}$$

We reiterate that one can ignore the errors in $g(W, z)$ since the dominant contribution to the error budget comes from the number counts, as discussed in §2.2.2. The incidence of absorption lines represents the product of the integrated number density of absorbers per co-moving volume and their effective cross section. Figure 2.11 shows the Ca II incidence for various equivalent width thresholds, $\mathrm{W}_0^{\mathrm{min}} = 0.3, 0.6, 1.0, 1.5$ Å. In each panel, the data are binned to have approximately equal numbers of systems. In each panel, the dash-dot lines show the no-evolution curves (NECs) predicted by the standard cosmology (Equation 2.7):

$$\frac{dn}{dz} = n_0 \frac{(1+z)^2}{\sqrt{\Omega_M (1+z)^3 + \Omega_\Lambda}} \tag{2.7}$$

The normalization, n_0, has been adjusted to minimize the sum of squared deviations of the binned data points from the curve. For $W_0^{\lambda 3934} \geq 0.3$ Å, the normalization constant, which is also the extrapolated incidence at $z = 0$, is $n_0 = 0.017 \pm 0.001$. Except for the case where $W_0^{\lambda 3934} \geq 1.5$ Å, the data are consistent with the NEC at better than the 99.9% confidence level.

In Table 2.2, we compare our results on the Ca II incidence with earlier results. The Wild et al. (2006) study used the SDSS-DR3 and required the simultaneous detection of Mg II absorption at $\geq 6\sigma$ significance for the λ2796 line. On the other hand, Richter et al. (2011) used high-resolution VLT/UVES data and required the detection of other transitions such as Na I, Mg II and Fe II. Note the difference in the number of systems detected. As summarized in Table 2.2, and the accompanying table notes, our results are consistent with the Wild et al. (2006) results, while the Richter et al. (2011) incidence is ~ 2 times larger.

2.3.3 The Ca II Doublet Ratio

For transitions with different oscillator strengths (e.g., absorption doublets), a measured doublet ratio (DR) is an important indicator of the degree of saturation of an absorption

Table 2.2: The Ca II incidence comparisons

Reference	$W_{0,min}^{\lambda3934}$ (Å)	num. sys.	z_{min}	z_{max}	$\langle z_{abs} \rangle$	$\partial n/\partial z$
Wild et al. (2006)	0.5	31	0.84	1.3	0.95	0.013[a]
Richter et al. (2011)	0.015	23	0.00396	0.47439	0.35	0.117 ± 0.044[b]
This work	0.16	435	0.02	1.34	0.58	0.078 ± 0.006

[a] For comparison, using Eq. (7) and our best-fit n_0 for $W_{0,\rm min}^{\lambda3934} = 0.5$ Å, our results give $\partial n/\partial z = 0.014 \pm 0.001$ at $\langle z_{\rm abs} \rangle = 0.95$.

[b] Using the Richter et al. (2011)-reported average redshift path, we derive $\partial n/\partial z \approx 0.09$ at $\langle z_{abs} \rangle \approx 0.22$ for the 8 (out of 23) detections with $W_0^{\lambda3934} \geq 0.16$ Å in the Richter et al. (2011) sample. For comparison, using Eq. (7) and our best-fit n_0 for $W_{0,\rm min}^{\lambda3934} = 0.16$ Å, we get $\partial n/\partial z = 0.051 \pm 0.003$ at $\langle z_{abs} \rangle = 0.22$.

line. The equivalent widths of weak unsaturated lines provide direct measurements of column densities. For strong, saturated doublets, such as Mg II $\lambda\lambda2796, 2803$ and Fe II $\lambda\lambda2586, 2600$, equivalent width measurements are more appropriately related to gas velocity spreads. The observed Ca II DRs ($W_0^{\lambda3934}/W_0^{\lambda3969}$) for our sample range from ~ 2 for completely unsaturated systems to ~ 1 for completely saturated systems. The left panel in Figure 2.12 shows the DR distribution for our sample. It has a mean of ~ 1.7 and a spread of $\sigma_{DR} \sim 0.4$. Hence, the Ca II doublets are, on average, between the two extreme possible values. The right panel in Figure 2.12 shows $W_0^{\lambda3969}$ versus $W_0^{\lambda3934}$ and includes the errors on these observed values, with the dash-dot lines bounding the physically allowed DR ranges, as in the left panel. Figure 2.13 shows the DRs as a function of redshift, along with the propagated DR errors assuming Gaussian error distributions. There is no detectable evolution in the DR distribution.

2.3.4 The Ca II versus Mg II Incidence

To make appropriate comparisons of the Mg II incidence to that of Ca II, we first determine which of the Ca II systems in our sample have confirmed Mg II measurements. We made use of the data available from the University of Pittsburgh SDSS DR4 Mg II Catalog (Quider et al.

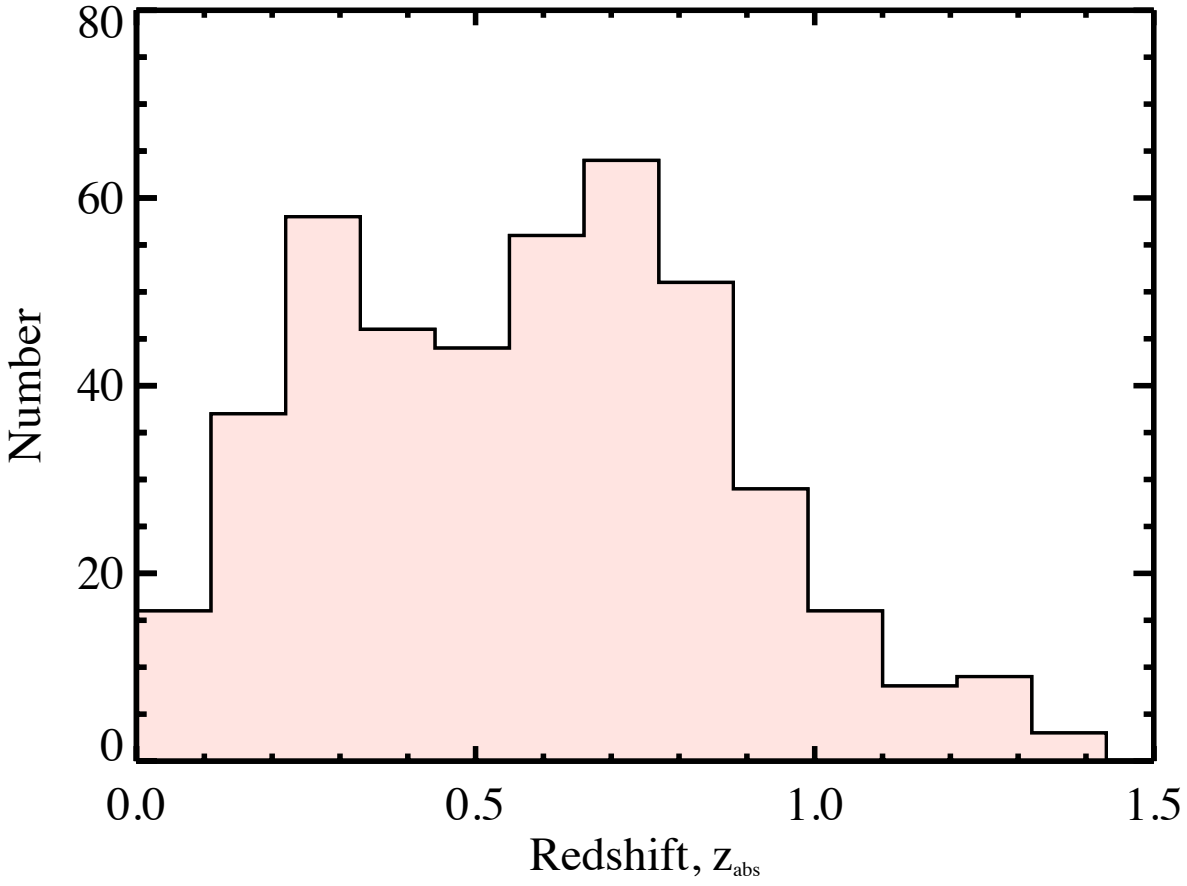

Figure 2.10: The observed absorber redshift distribution shown in bins of $\Delta z = 0.1$, with mean $z_{abs} = 0.579$ and standard deviation $\sigma = 0.296$. The poor SNR of SDSS spectra near $z_{abs} \sim 0.5$, due to the SDSS dichroic, causes the decrease in the number of detected Ca II systems that pass our selection criteria at this redshift.

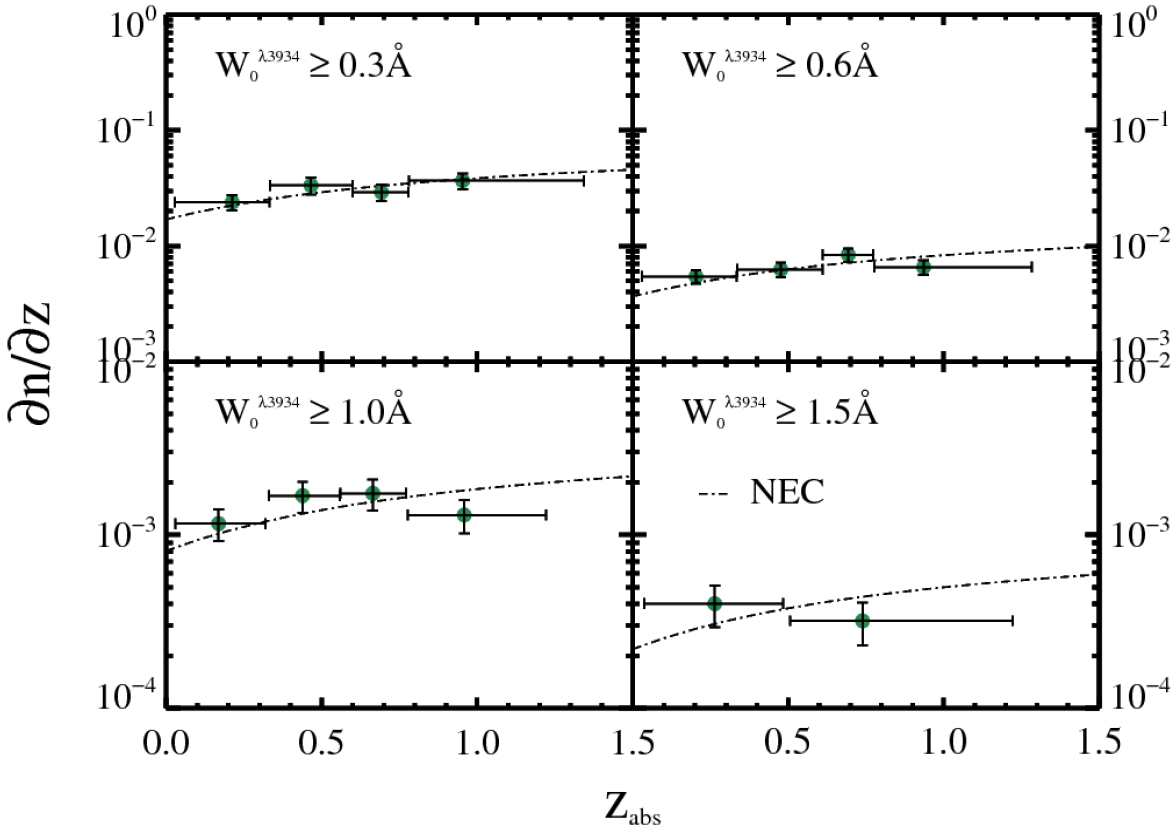

Figure 2.11: The Ca II redshift number density as a function of the lookback time, t_{LB}, for various REW thresholds $W_0^{\lambda 3934} \geq W_0^{min}$. The errors are determined using Poisson statistics. The bin sizes are such that there are approximately equal numbers of systems in each bin. The no-evolution curves (NEC) are shown as dash-dot lines. The NECs are normalized to minimize the sum of squared deviations of the binned data from the curve. With the exception of the $W_0^{\lambda 3934} \geq 1.5$ Å sample, the NECs are consistent with the data at a $> 99.9\%$ significance level. The $W_0^{\lambda 3934} \geq 1.5$ Å sample has too few data points to allow for a meaningful interpretation.

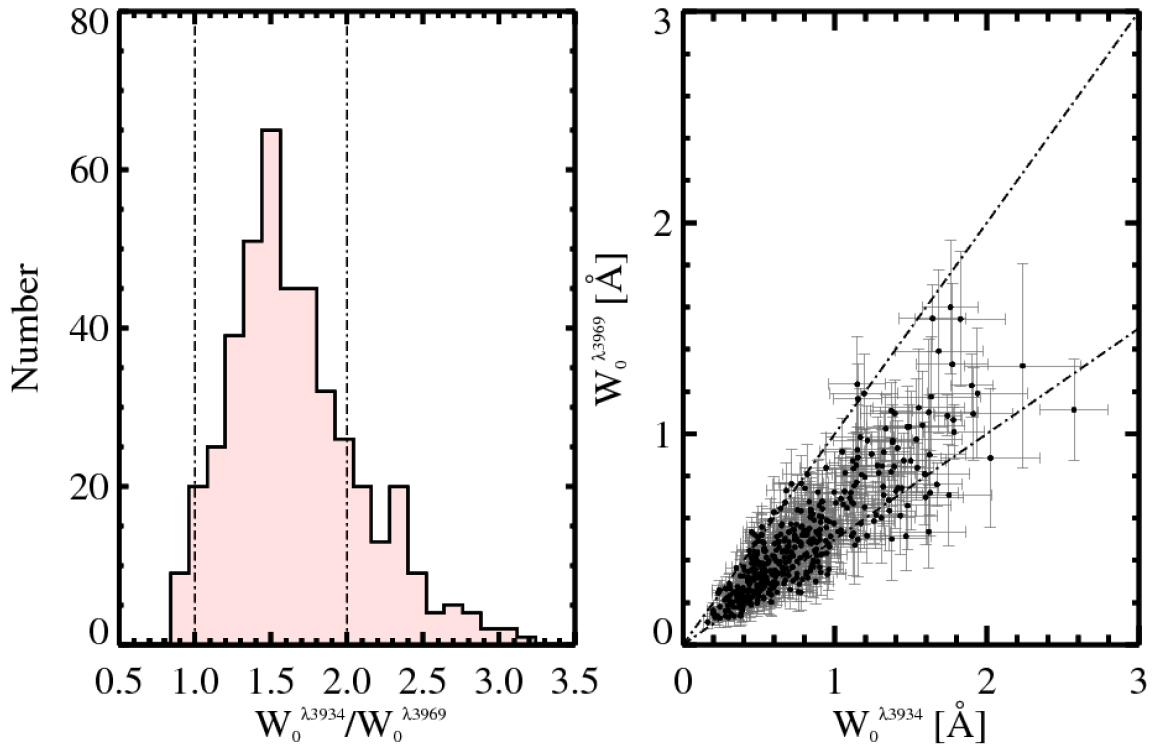

Figure 2.12: *Left:* The distribution of doublet ratios, $W_0^{\lambda3934}/W_0^{\lambda3969}$, for the Ca II sample. The dash-dot lines mark the limits of 1.0 for completely saturated systems and 2.0 for completely unsaturated systems. Values above and below these limits are due to poorer signal-to-noise ratio data. Our sample is not dominated by either extreme DR values. *Right:* $W_0^{\lambda3969}$ vs. $W_0^{\lambda3934}$.

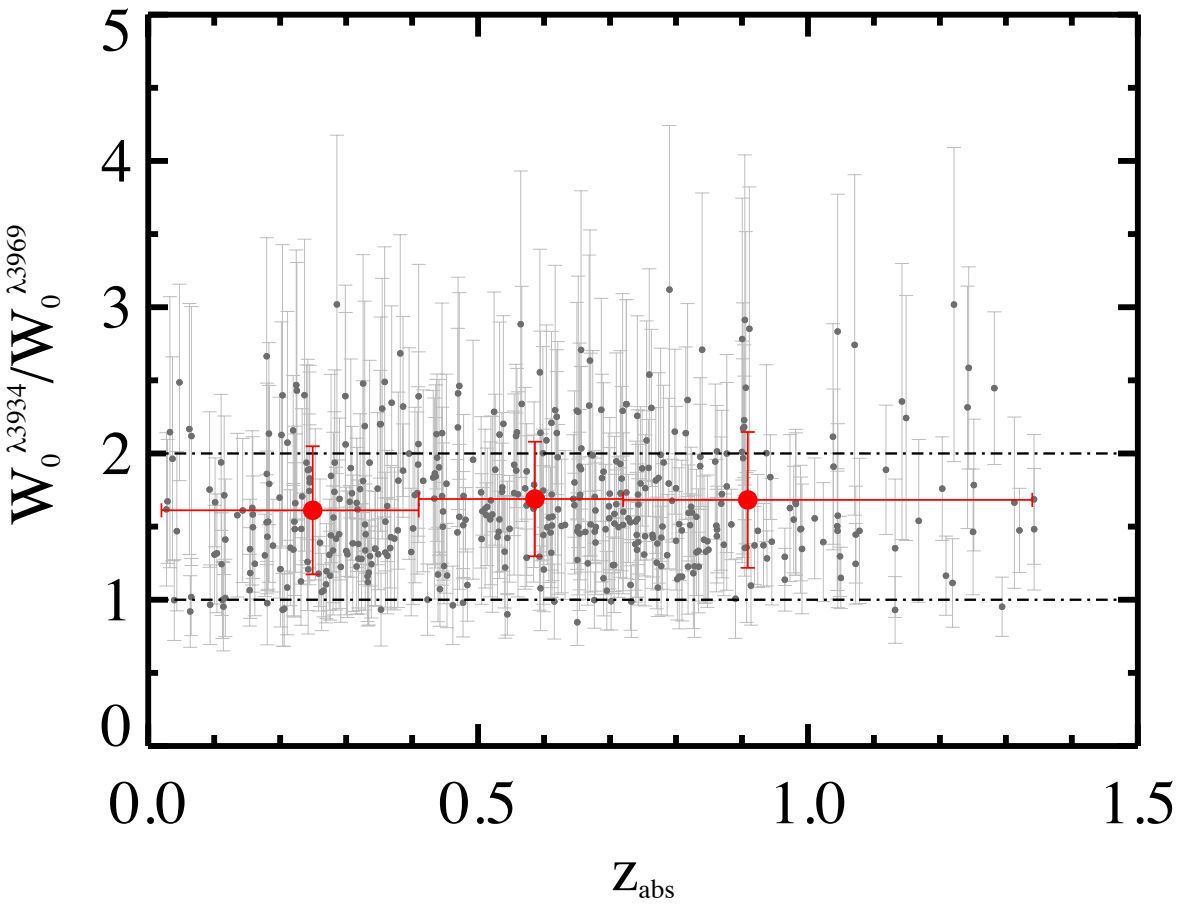

Figure 2.13: The $W_0^{\lambda 3934}/W_0^{\lambda 3969}$ doublet ratio as a function of redshift. There is no detected redshift evolution in the doublet ratio.

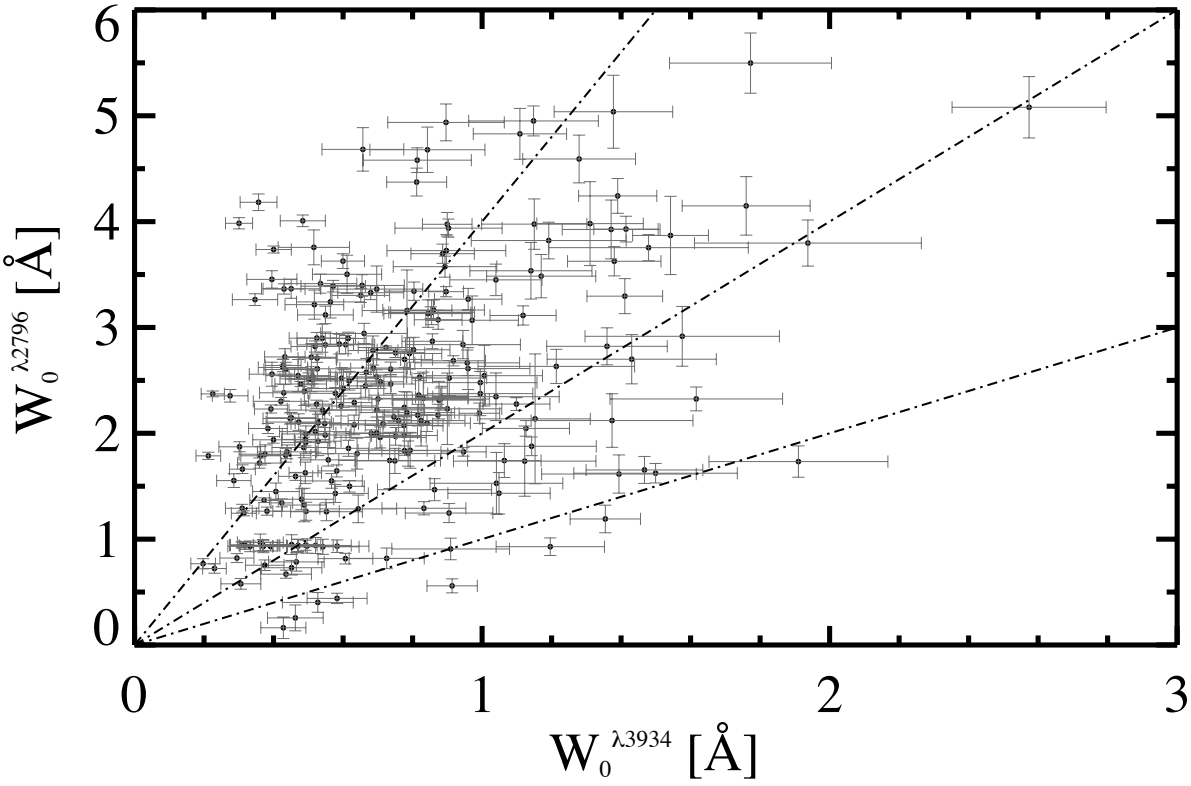

Figure 2.14: $W_0^{\lambda 2796}$ versus $W_0^{\lambda 3934}$ for the 251 Ca II systems in our sample with detected Mg II. See text. There is a correlation between the REWs of Mg II and Ca II, albeit with a large spread, but a sharp lower bound. The three dash-dot lines have $W_0^{\lambda 2796}/W_0^{\lambda 3934} = [1.0, 2.0, 4.0]$.

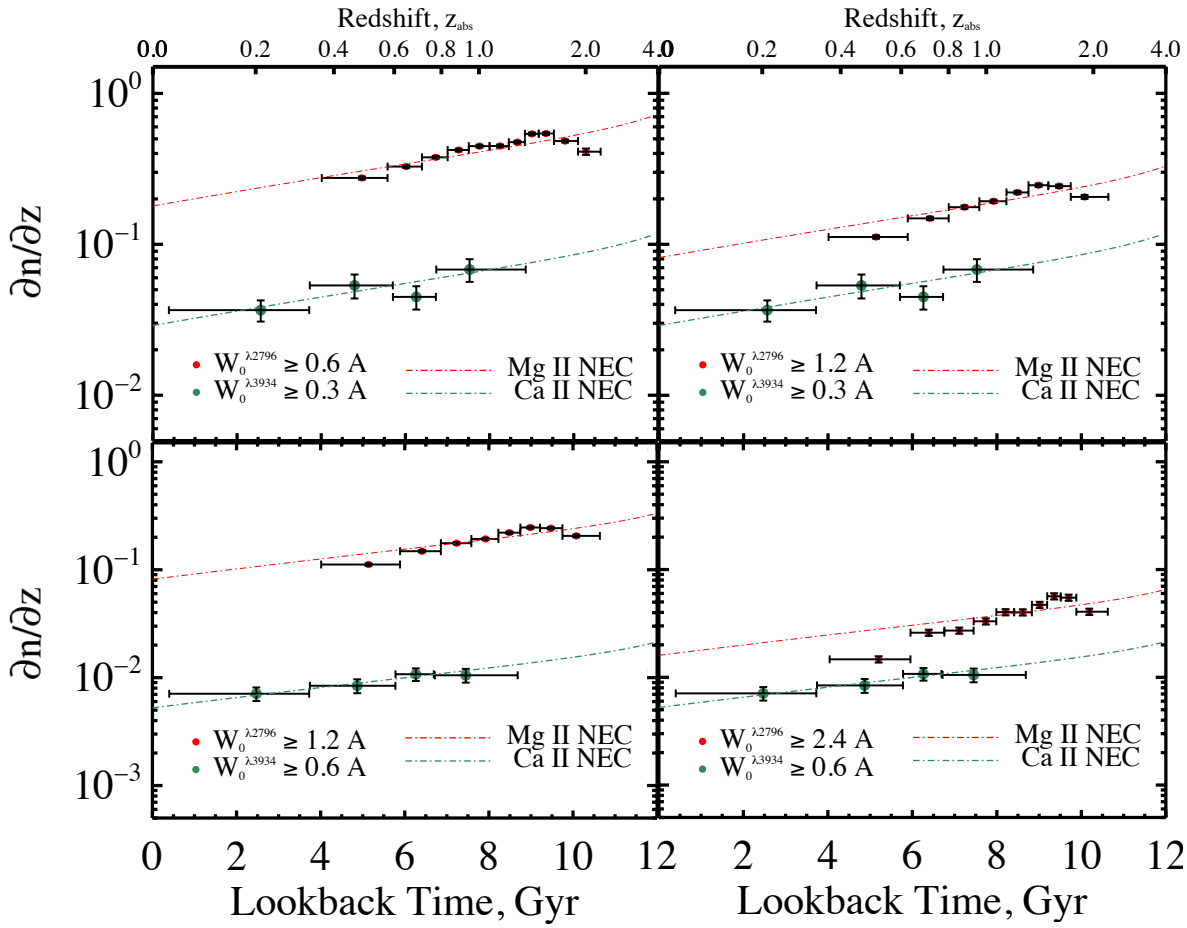

Figure 2.15: Ca II incidence as a function of z_{abs} across various $W_0^{\lambda 3934}$ thresholds. The no-evolution curve is shown as dash-dot lines. The errors are propagated using Poisson statistics.

2011), extended up to SDSS DR7 (E. Monier, private communication). In total, the extended Mg II catalog contains over 29,000 doublets, which includes an additional $\sim 13,000$ unique Mg II systems from SDSS DR7. The Quider et al. (2011) Mg II sample was selected based on 5σ and 3σ significance cuts for $W_0^{\lambda 2796}$ and $W_0^{\lambda 2803}$, respectively. A similar doublet ratio cut of $1.0-\sigma_{DR} \leq W_0^{\lambda 2796}/W_0^{\lambda 2803} \leq 2.0+\sigma_{DR}$ was also imposed to construct the final catalog. For absorbers from SDSS DR9, we measured the strengths of the Mg II doublets, and made the appropriate cuts. Note that to find Mg II, the Ca II system must be at $z_{abs} \gtrsim 0.4$. However, detecting the corresponding Mg II lines also depends on the quasar emission redshift and the SNR of the spectrum at the predicted Mg II location. Lines that fell in the Lyα forest were not measured. After implementing the required selection cuts, we have 251 Ca II-Mg II systems. The results are shown in Figure 2.14. We see a positive correlation between the strengths of the two lines, albeit with a spread that is quite large. However, the distribution does appear to have a sharp lower bound. The three dash-dot lines have $W_0^{\lambda 2796}/W_0^{\lambda 3934} = [1, 2, 4]$.

We also performed the reverse search where we looked for Ca II lines corresponding to Mg II systems from DR7 in the $0.4 \leq z \leq 1.34$ redshift interval. Only 3% of Mg II systems were found to have Ca II, confirming that it is rare to identify Ca II in quasar absorption-line surveys.

We now compare the incidence of Ca II absorbers to the more common Mg II systems. In Figure 2.15, the incidence of Ca II is shown as the green data points using the following REW thresholds: $W_0^{\lambda 3934} \geq 0.3$Å shown on the top panels, and $W_0^{\lambda 3934} \geq 0.6$Å shown by the bottom panels. The Mg II incidence is shown in red. The errors are derived using Poisson counting statistics. Within each panel, we binned the data so that each point has roughly the same number of systems. Note that these are plotted against t_{LB} in the linear scale instead of z_{abs} in order to highlight the length of cosmic time that Mg II cannot trace using SDSS spectra. Motivated by the observed ratios in Figure 2.14, we have chosen the following Mg II-Ca II ratios: $W_0^{\lambda 2796}/W_0^{\lambda 3934} = [2, 4]$ for this comparison. For both absorbers, the NECs were normalized to minimize the sum of the squares of the residuals. The resulting fits are consistent with the data at $\gtrsim 99\%$ confidence level for both absorbers at all REW thresholds. The Ca II incidence is in a sense similar to Mg II in that the gaseous cross sections do not show evidence for evolution at $z_{abs} > 0.4$, and with this new result from Ca II, we extend the

same conclusions down to $z = 0$. Figure 2.15 also underscores the rareness of Ca II absorbers relative to Mg II. More specifically, in the left panels of Figure 2.15, where $W_0^{\lambda 2796} = 2W_0^{\lambda 3934}$, the incidence of Ca II is roughly a factor of ~ 10 times smaller. At the larger REW ratios (right panels), as the number of stronger Mg II absorbers becomes rare, this fraction drops to a factor of ~ 3 to 4.

2.4 INVESTIGATING THE POSSIBILITY OF TWO Ca II ABSORBER POPULATIONS

The $W_0^{\lambda 3934}$ distribution shown in Figure 2.7 reveals a break in $\partial n/\partial W_0^{\lambda 3934}$ at $W_0^{\lambda 3934} = 0.88$ Å. The need for a strong and a weak component to adequately fit the overall distribution (Equation 4) suggests that we should investigate trends which might further reveal the properties of these components. Below we search for identifiable trends based on: (1) the $W_0^{\lambda 3934}$ value and Ca II DR, and (2) the $W_0^{\lambda 3934}$ value and the Mg II-to-Ca II ratio ($W_0^{\lambda 2796}/W_0^{\lambda 3934}$).

2.4.1 Trends Between $W_0^{\lambda 3934}$ and Ca II DR

Here we explore the possible role of the Ca II DR in isolating the two components of the $W_0^{\lambda 3934}$ distribution. To do this we divide the entire Ca II sample into four subsamples of roughly equal size based on their DRs and $W_0^{\lambda 3934}$ values. This can be accomplished by making divisions above and below DR $= 1.5$ and $W_0^{\lambda 3934} = 0.7$ Å. Note that these values lie close the the mean doublet ratio of the entire sample and the location of the break in Figure 2.7.

In Figure 2.16, we plot the sensitivity-corrected $W_0^{\lambda 3934}$ distributions for the four defined subsamples. The resulting four distributions can now be accurately parametrized by single exponential functions. The best-fit single exponential functions to the unbinned data are shown as dash-dot lines. All four single exponential functions fit the data in their corresponding subsamples at a better than 99% confidence level. Moreover, the MLE slopes for both subsamples with $W_0^{\lambda 3934} < 0.7$ Å (left panels) are consistent with the $W_{wk}^{\star}$ value

for the overall sample to within the errors, and the MLE slopes for both subsamples with $W_0^{\lambda 3934} \geq 0.7$ Å (right panels) are consistent with the $W_{str}^{\star}$ value to within the errors. Also, dividing the entire sample at DR=1.5 into two subsamples yielded the same two component distribution specified in Equation 4 to within the errors.

Thus, at the accuracy of our data, the Ca II DR alone does not play a role in separating the Ca II absorbers into two populations. A series of KS tests were also performed and found to support this conclusion.

2.4.2 Trends Between $W_0^{\lambda 3934}$ and $W_0^{\lambda 2796}/W_0^{\lambda 3934}$

For almost all Ca II absorbers with redshifts $z > 0.4$ we have information on the corresponding Mg II absorption. Therefore, we can explore if Mg II information can be used to isolate the two components of the $W_0^{\lambda 3934}$ distribution. From past work we know that Mg II absorption doublets found in SDSS surveys are generally saturated (Quider et al. 2011). As explained in §2.3.3, this means that Mg II rest equivalent widths are more representative of low-ionization gas velocity spreads rather than Mg^+ column densities. However, the Ca II doublet is generally unsaturated or only partially saturated, so to some degree the Ca II rest equivalent widths must be representative of Ca^+ column densities.

In Figure 2.17 we plot the two observed $W_0^{\lambda 2796}/W_0^{\lambda 3934}$ ratio histograms for Ca II absorbers with $W_0^{\lambda 3934} < 0.7$ Å and $W_0^{\lambda 3934} \geq 0.7$ Å. This separation value is the same as the one used in §2.4.1 and is again motivated by our desire to roughly equalize the number of systems in each of the two subsamples. There are ~ 120 absorbers in each subsample.

By using this $W_0^{\lambda 3934}$ separation value and including Mg II information, we produced Figure 2.17, which shows the Ca II absorbers to be a bimodal population, with the weaker Ca II absorbers having a larger (on average) and wider spread in $W_0^{\lambda 2796}/W_0^{\lambda 3934}$ than the stronger Ca II absorbers. A KS-test renders the two distributions inconsistent with one another at a $> 99\%$ confidence level. This bimodality provides supporting evidence that stronger and weaker Ca II absorbers (i.e., absorbers with relatively higher and lower Ca^+ column density values) may be different populations. We note that with the exception of a few data points, the Mg II absorbers associated with the Ca II absorbers have saturated

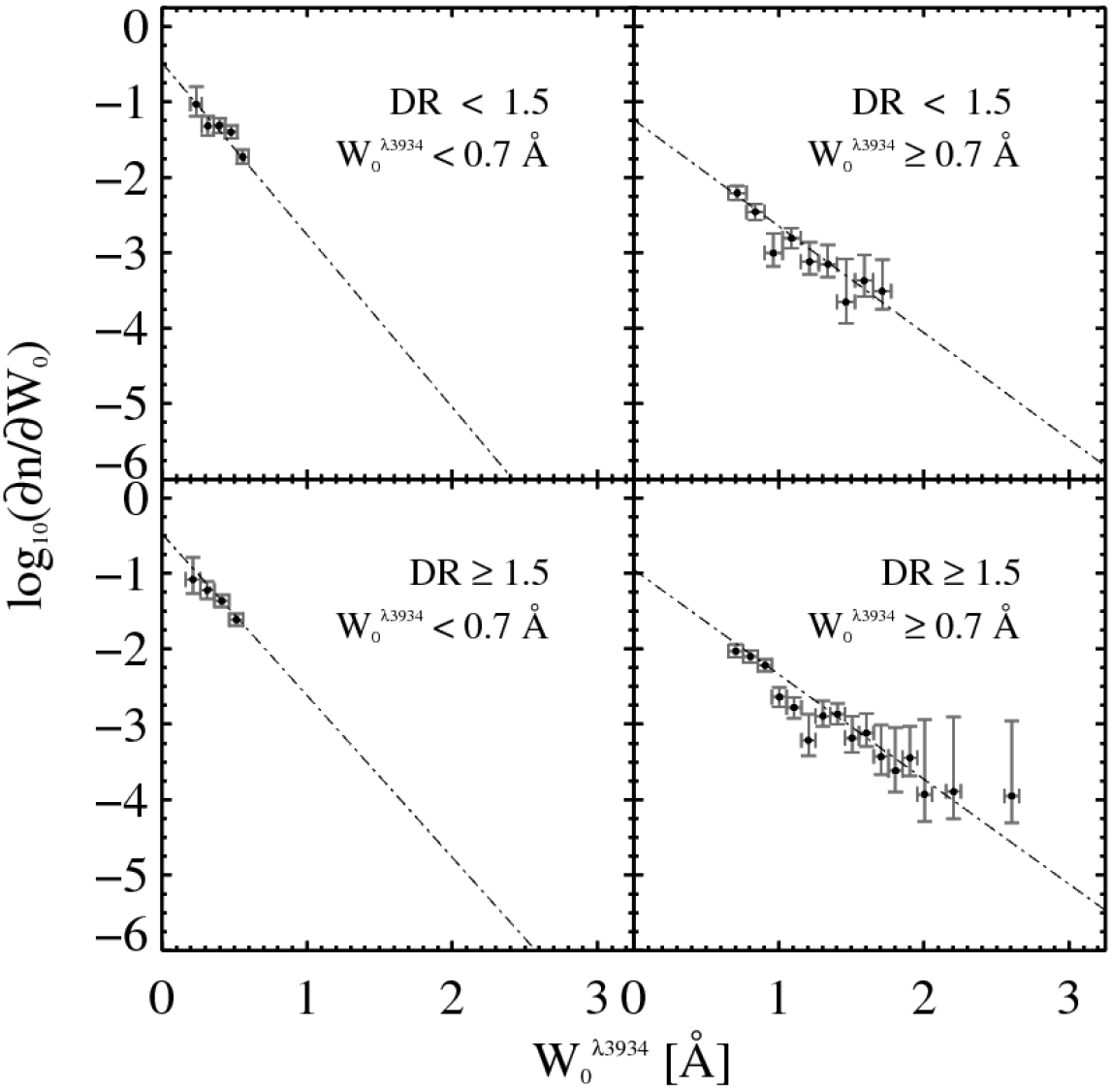

Figure 2.16: The sensitivity-corrected equivalent width distributions for four roughly equal subsamples of Ca II absorbers divided according to Ca II DR and $W_0^{\lambda 3934}$. The dash-dot lines are the MLE single power-law fits.

doublets, which means that $W_0^{\lambda 2796}$ values are indicative of gas velocity spreads. See Figure 2.17 and its caption for color-coded data points (online version only) on Mg II doublet ratios and some additional explanation.

Finally, in Figure 2.18 we show that for those Ca II absorbers with Mg II information, it is possible to separate the $W_0^{\lambda 3934}$ distribution shown in Figure 2.7 into two single power-law distributions over the entire range of $W_0^{\lambda 3934}$ values. This is done by forming two subsamples divided at $W_0^{\lambda 2796}/W_0^{\lambda 2803} = 1.8$, but in this case the subsamples are not approximately of equal size.

The slope of the steeper distribution is found to be consistent with the slopes of the weak component of the distribution in Figure 2.7 and the top-left and bottom-left panels of Figure 2.16 (i.e with $W_0^{\lambda 3934} < 0.7$ Å). Similarly, the flatter red distribution is also consistent with the corresponding results for the strong systems in Figures 2.7 and 2.16.

2.5 SUMMARY, CONCLUSIONS AND OUTLOOK

We have presented the results of a blind survey for intervening Ca II absorption-line systems using $\sim 95,000$ quasar spectra from the seventh and ninth data release of the SDSS. Our results represent the largest compilation of Ca II absorbers to date. The rest wavelengths of the Ca II$\lambda\lambda 3934, 3969$ doublet resonance transition allow us to probe redshifts $z \lesssim 1.34$, which corresponds to the most recent ~ 8.9 Gyrs of the history of the Universe. Ca II absorbers are considerably more rare than Mg II absorbers. However, it is notable that with the orginal SDSS spectrograph, Mg II absorbers at $z \lesssim 0.4$ are not accessible. Therefore, studies of Ca II absorbers in quasar spectra are the only absorption-line systems which are generally accessible with SDSS spectra at $z \lesssim 0.4$, which is equivalent to the past ~ 4.3 Gyrs of cosmic time. Consequently, within the SDSS spectral window Ca II presents a unique opportunity for ground-based studies of cool, metal-rich gas around galaxies at the lowest redshifts, and such studies can help constrain models for the existence of cool gas in the extended gaseous halos of galaxies.

Our blind survey resulted in the identification of 435 Ca II absorbers at rest equivalent

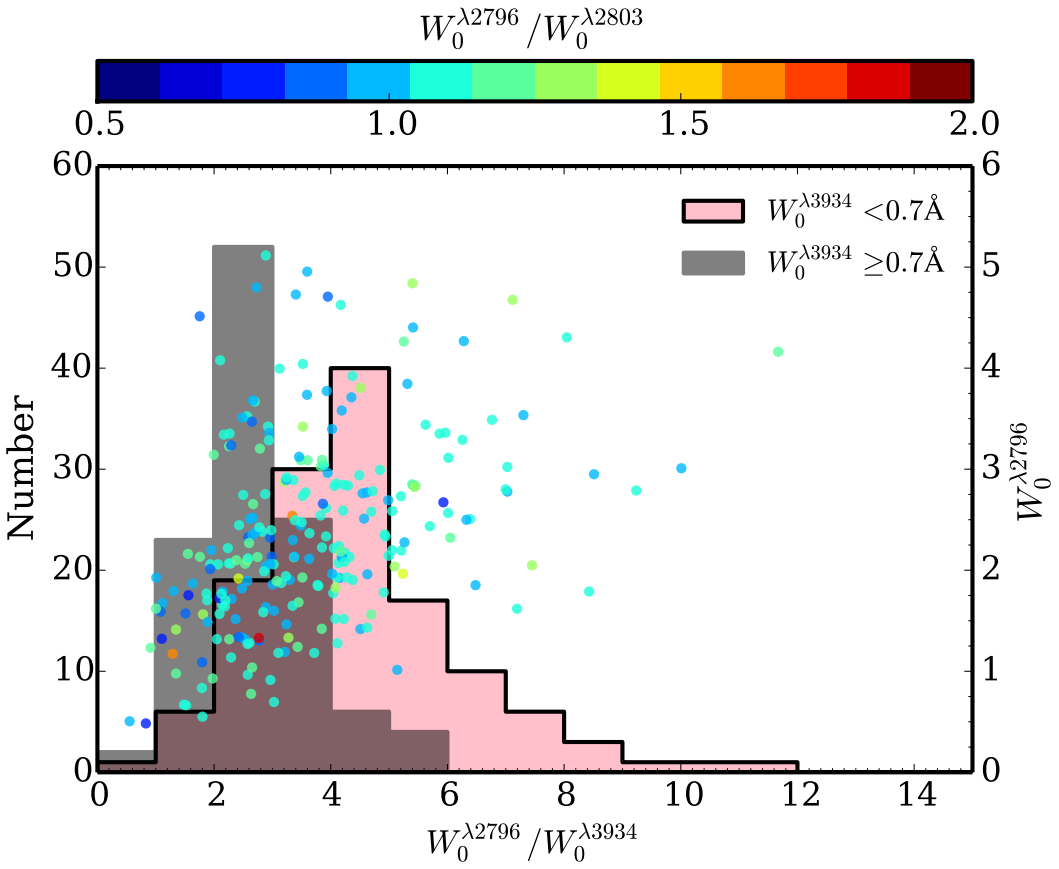

Figure 2.17: The bimodal distribution of the $W_0^{\lambda2796}/W_0^{\lambda3934}$ ratio for the weak and strong Ca II absorbers divided at $W_0^{\lambda3934} = 0.7$ Å. Note that we also plot $W_0^{\lambda2796}$ (right y-axis) as a function of $W_0^{\lambda2796}/W_0^{\lambda3934}$ (x-axis); these data points are color-coded (online version only) according to the top color bar to show the saturation level of the Mg II doublet.

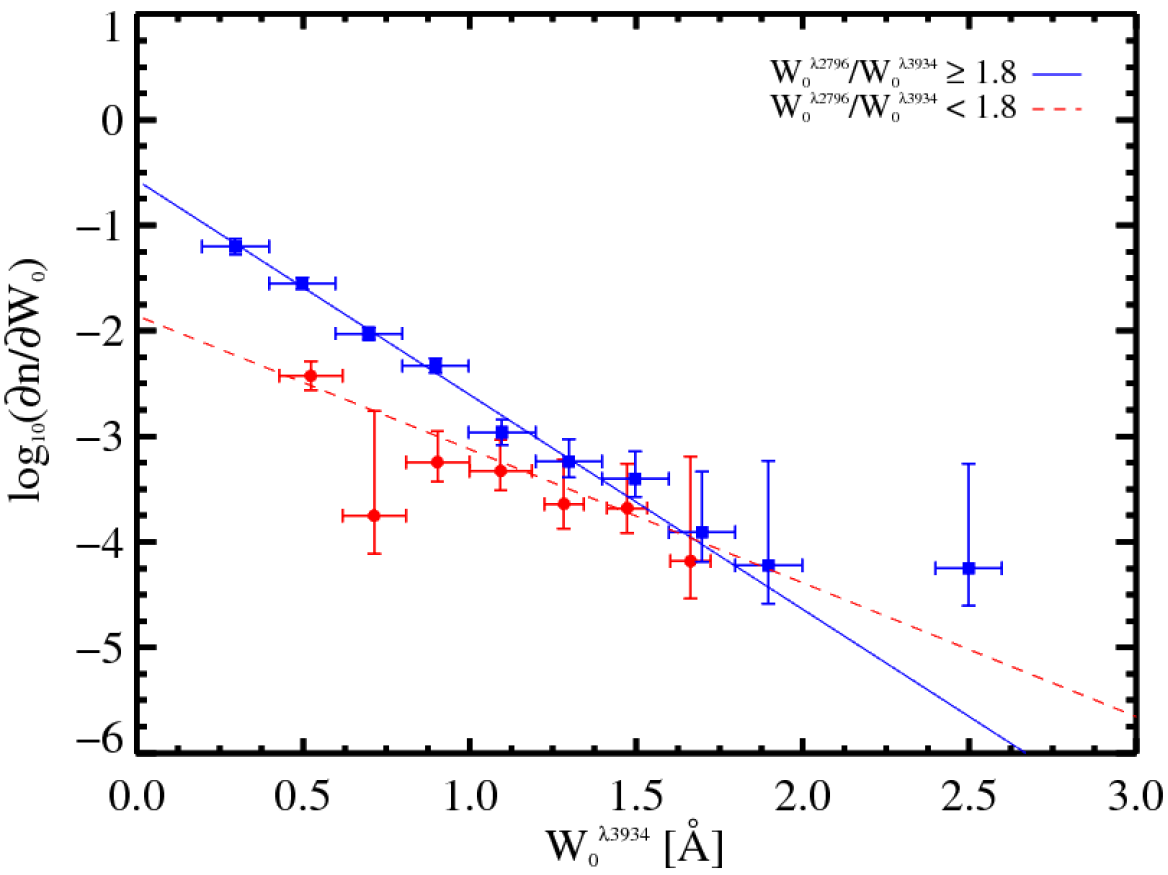

Figure 2.18: The sensitivity-corrected equivalent width distributions for two subsamples of Ca II absorbers separated at $W_0^{\lambda2796}/W_0^{\lambda3934} = 1.8$. The separation into two single-power-law fits is clear. The blue squares and red circles represent the subsamples with a $W_0^{\lambda2796}/W_0^{\lambda3934}$ ratio greater than and less than 1.8, respectively. The solid blue and dashed red lines are the best-fit single-exponential MLE fits to the unbinned distributions.

width significance levels $\geq 5\sigma$ for $W_0^{\lambda 3934}$ and $\geq 2.5\sigma$ for $W_0^{\lambda 3969}$, within the physically-allowable doublet ratio range, i.e., $1-\sigma_{DR} \leq W_0^{\lambda 3934}/W_0^{\lambda 3969} \leq 2+\sigma_{DR}$. Of these detections, 251 Ca II absorbers at $z \gtrsim 0.4$ were found to have associated Mg II absorption, which is essentially all of them.

The sensitivity-corrected $W_0^{\lambda 3934}$ distribution cannot be fitted by a single-component exponential function, but a two-component exponential function describes the data well. We find $\partial n/\partial W_0^{\lambda 3934} = (N^\star_{wk}/W^\star_{wk})exp(-W_0^{\lambda 3934}/W^\star_{wk}) + (N^\star_{str}/W^\star_{str})exp(-W_0^{\lambda 3934}/W^\star_{str})$, with $N^\star_{wk} = 0.140\pm0.029$, $W^\star_{wk} = 0.165\pm0.020$ Å, $N^\star_{str} = 0.024\pm0.020$, and $W^\star_{str} = 0.427\pm0.101$ Å. This suggests that the Ca II absorbers are composed of at least two distinct populations (Figure 2.7).

The Ca II absorber incidence was found to not evolve in the standard cosmology, implying that the product of integrated Ca II absorber cross section and their comoving number density has remained roughly constant over the last ~ 8.9 Gyrs.

The normalization of the no-evolution curve, which is also the incidence extrapolated to $z = 0$, is $n_0 = 0.017 \pm 0.001$ for the sample with $W_0^{\lambda 3934} \geq 0.3$ Å.

Furthermore, we have demonstrated that the incidence of Ca II absorbers relative to the more common Mg II absorbers in quasar spectra is about 3 to 10 times smaller, depending on the REW threshold used for the comparison (Figure 2.15).

Finally, we performed some investigations to determine if we could use available Ca II absorber properties, specifically doublet ratio and Mg II information, to isolate the "weak" and "strong" populations of Ca II absorbers. While it was not possible to do this using the Ca II doublet ratio, we did find that Mg II information could be used to isolate the two populations (Figures 2.17 and 2.18).

Clearly, there are numerous important issues that could be investigated using the Ca II absorbers identified in this survey. For example, questions such as: (1) How do we explain the observed incidence and cross section ratio between Mg II and Ca II absorbers in terms of the ionization, abundance, and dust depletion properties of the two types of absorbers? (2) How do the Ca II absorbers fit into our current understanding of galaxies and their evolution? (3) What are the host galaxies of Ca II absorbers and what is the characteristic spatial distribution of absorption around the host galaxies? (4) And what is the physical origin of

the two-component Ca II $W_0^{\lambda 3934}$ distribution? We will explore these issues in the succeeding chapters.

3.0 Ca II ABSORBERS IN THE SLOAN DIGITAL SKY SURVEY: ELEMENT ABUNDANCES AND DUST

The contents of this chapter have been published in Sardane, Turnshek and Rao, 2015, *Monthly Notices of the Royal Astronomical Society*, 452, 3192-3208.

3.1 INTRODUCTION

Determination of element abundances, dust properties, and the overall chemical histories of the gaseous environments of galaxies is needed for an improved understanding of galaxy formation and evolution. The gaseous environments of galaxies include their interstellar medium (ISM) as well as surrounding circumgalactic medium and intergalactic medium (CGM and IGM). A broad goal is to constrain how galaxies convert their gas into stars, and the feedback (outflow) mechanisms that are at play in polluting the gas surrounding galaxies in the context of the observed galaxy stellar populations. Here we consider what can be learned from a study of the properties of intervening gas giving rise to Ca II absorption seen in the spectra of background quasars. The statistics of these absorbers, as derived from an analysis of SDSS quasar spectroscopy, were recently presented in Sardane, Turnshek & Rao (2014). Some of the properties of galaxies associated with them, derived from SDSS images, will be presented in Sardane, Turnshek & Rao (2015). In this chapter, we use SDSS spectroscopy to constrain results on relative element abundances and dust in Ca II absorbers.

Quasar absorption line (QAL) spectroscopy is a unique probe of the evolution of galaxies and their gaseous components, from the coolest molecular clouds to the hotter ionized gaseous halos (Foltz et al. 1988; Lu et al. 1996; Ledoux et al. 1998; Wolfe & Prochaska 2000a;

Petitjean et al. 2000; Ledoux, Srianand & Petitjean 2002; Ledoux, Petitjean & Srianand 2003; Cui et al. 2005; Srianand et al. 2005; Petitjean et al. 2006; Fox et al. 2007; Tripp et al. 2008; Thom & Chen 2008; Noterdaeme et al. 2008; 2010; Prochaska et al. 2011; Tumlinson et al. 2011a; Crighton et al. 2013; Stocke et al. 2014; Lehner et al. 2014; Savage et al. 2014). Due to the rest-frame UV location of the resonance transitions most relevant for QAL studies, such studies have traditionally concentrated on probing the gaseous absorbers and their environments at high redshifts. As a result, the paucity of identified gaseous structures at very low redshift naturally creates a gap in our understanding of how galaxies and their gaseous environments evolve from high redshift to the present. Moreover, cosmological dimming, which reduces the surface brightness of astronomical sources by $(1+z)^4$, makes it more difficult to identify and characterize the galaxies that could host the absorbers at high redshift.

One rare class of QAL system that is not as well studied and understood as others is the one identified using the resonance doublet transition of singly ionized calcium: Ca II $\lambda\lambda 3934, 3969$. However, although its incidence makes it rare, the advantage of studying the Ca II QAL doublet is that it can be observed from $z \sim 1.4$ all the way down to the present epoch using the large number of optical ground-based quasar spectra obtained by the Sloan Digital Sky Survey (SDSS) (Schneider et al. 2010; Ahn et al. 2012).

Recently, we harnessed the statistical power of the SDSS to assemble the largest catalog of these rare Ca II absorbers (Chapter 2). This search, which utilized $\sim 95,000$ quasar sightlines from the Seventh (DR7) and Ninth (DR9) data releases of the SDSS, resulted in the compilation of 435 Ca II absorbers. As described in Chapter 2, the detections were based on $\geq 5\sigma$ and $\geq 2.5\sigma$ rest equivalent width significance threshholds for the strong and weak members of the Ca II doublet, respectively. A constraint on the doublet ratio was also employed to remove "unphysical" profiles, as dictated by the theoretical ratio of the doublet oscillator strengths.

In Chapter 2 we demonstrated that after accounting for sensitivity corrections, a single power-law fit is insufficient to describe the $\lambda 3934$ rest equivalent width, $W_0^{\lambda 3934}$, distribution. More specifically, a two-component exponential distribution is required to fit the data satisfactorily. This result is somewhat surprising based on analysis of much larger samples of

more ubiquitous QAL systems such as Mg II (e.g., Nestor, Turnshek & Rao 2005, Seyffert et al. 2013, and Zhu & Menard 2013) and C IV (Cooksey et al. 2013). For these QAL systems, a single exponential function suffices to characterize their W_0 distributions at $W_0 \gtrsim 0.1$ Å. For Ca II absorbers the need for a two-component distribution persists across all observed redshifts, which is strong statistical evidence for *at least* two distinct populations.

A preliminary investigation of the nature of the two-component fit suggested that there was a bimodality in the distribution of Mg II-to-Ca II ratios (i.e., $W_0^{\lambda 2796}/W_0^{\lambda 3934}$) with a separation above and below $W_0^{\lambda 3934} \sim 0.7$ Å. However, there was no evidence that the Ca II doublet ratio, which is an indicator of saturation, could be used to distinguish between the two absorber populations.

Using the statistical sample from Chapter 2, this work will explore the chemical abundances and dust-extinction properties of the Ca II absorbers. In particular, we will exploit the power of spectral stacking to form various composite spectra which will be analyzed to infer chemical abundance ratios and dust-extinction properties for various subsamples. This will allow us to characterize and distinguish between two different Ca II absorber populations as implied by their statistical properties.

The Chapter is organized as follows. In §3.2 we give a brief description of our SDSS Ca II absorber catalog that was presented in Chapter 2. In §3.3 we discuss notable individual systems in the Ca II catalog. In §3.4 we derive the composite properties of the Ca II absorber full sample and subsamples in the context of their element abundance ratios and dust-extinction properties. We then discuss the implications of these results and how they explain the existence of two different populations of Ca II absorbers in §3.5. In §3.6 we summarize our results and conclusions.

3.2 THE SDSS CA II ABSORBER CATALOG

The sample of Ca II absorbers used in this analysis is derived from our Chapter 2 catalog. It consists of 435 Ca II absorbers with $W_0^{\lambda 3934} \geq 0.16$ Å, compiled using over 95,000 quasar spectra with SDSS magnitudes $i < 20$ from the SDSS data releases DR7 (Abazajian et al.

2009; Schneider et al. 2010) and DR9 (Ahn et al. 2012; Pâris et al. 2012). Data from DR7 and DR9 were obtained using two nearly identical spectrographs, the SDSS spectrograph and the Baryon Oscillation Spectroscopic Survey (BOSS) spectrograph, respectively. The BOSS spectrograph (Smee et al. 2013), which was designed to target higher-redshift quasars for the BOSS project (Schlegel et al. 2007; Dawson et al. 2013), is an improved version of the SDSS spectrograph. The SDSS spectrograph covers the wavelength range of $3800 - 9200$ Å, while the BOSS spectrograph has extended wavelength coverage in both the blue and the near-infrared, and covers $3600 - 10,400$ Å. The resolutions of both spectrographs are essentially the same, ranging from ~ 1500 at 3800 Å to ~ 2500 at 9000 Å.

To identify the Ca II absorbers, splines and Gaussians were used to fit a quasar spectrum's so-called pseudo-continuum, which consists of the "true" continuum plus the broad emission lines. As indicated previously, the absorbers were selected based on 5σ and 2.5σ significance thresholds for the $\lambda3934$ and $\lambda3969$ lines, respectively, and a doublet ratio (DR)[1] constraint of $1 \leq \mathrm{DR} \leq 2$ to within the measurement errors, which is the range of physically-allowable doublet ratios between saturated ($\mathrm{DR} = 1$) and completely unsaturated ($\mathrm{DR} = 2$) absorption lines.

3.3 PROPERTIES OF SOME INDIVIDUAL CA II ABSORBERS IN THE CATALOG

In the limit of an absorption line in the optically thin regime, the optical depth is independent of the Doppler parameter, so a measurement of its equivalent width translates reliably into a column density measurement. Hence, for weak, unsaturated resonance transitions at rest-frame wavelength, λ_0, and oscillator strength, f, the column density, N, is approximately a linear function of the rest equivalent width, W_0,

$$N \approx 1.13 \times 10^{20} \ \frac{W_0}{\lambda_0^2 f} \tag{3.1}$$

where N is in atoms cm^{-2} and W_0 and λ_0 are in Å (Draine 2011).

[1]The doublet ratio is defined here as $\mathrm{DR} = \mathrm{W}_0^{\lambda3934}/\mathrm{W}_0^{\lambda3969}$.

In QAL studies of high-N(H I) systems, which generally applies to the Ca II absorbers, it is common to use this relation to derive total element column densities from weak, low-ionization, unsaturated lines due to, e.g., Zn II, Cr II, Fe II, and Mn II. Self-shielding generally ensures that the low-ionization metallic elements will be the dominant ionization state. Therefore, we will employ this method to infer some of the properties of individual Ca II absorbers, and we will also take advantage of this in the §3.4 analysis using composite spectra. These assumptions are theoretically justified, and departures should be small for the elements we consider (e.g., Viegas 1995; Vladilo et al. 2001; Prochaska & Wolfe 2002). In cases where there is evidence for a non-negligible degree of saturation, we will report lower limits on derived column densities.

Under these assumptions, we derive abundance ratios of special sightlines that have high enough redshift and signal-to-noise ratios to permit spectral coverage and reliable measurements of interesting weak absorption features. In keeping with standard practice, the reported abundance ratios are relative to solar (Asplund et al. 2009), i.e., the abundance ratio of element X relative to element Y will be given relative to solar values:

$$[X/Y] \equiv \log[N(X)/N(Y)] - \log[N(X)/N(Y)]_{\odot} \tag{3.2}$$

For absorbers with $z_{abs} \gtrsim 0.9$, the UV Zn II-Cr II rest-frame region of the spectrum falls into the SDSS optical wavelength window. The Ca II sample consists of ~ 70 systems with $z_{abs} \gtrsim 0.9$. However, due to increasingly poor signal-to-noise ratios in the blue region of many SDSS spectra, and the unfortunate blending of the Zn II-Cr II region with Lyα forest lines or other unrelated metal lines, the useful sample where Zn II-Cr II can be studied in Ca II absorbers is reduced to a dozen systems. Since zinc is only mildly refractory, its abundance ratio relative to more strongly depleted elements such as chromium, titanium, and iron is of primary importance for characterizing the depletion properties of the gas. Pettini, Boksenberg & Hunstead (1990) were the first to use Zn II as a metallicity indicator in QAL systems.

The Zn II-Cr II region has a rest-frame wavelength interval $2026 - 2066$ Å. For the usable spectra we infer the column densities of Cr and Zn from four Cr II transitions and two Zn II transitions. The first of these is a feature at $\lambda 2026$ which is a blend due to three

transitions: a Zn II line, a weak Mg I line, and a very weak Cr II line. Another feature at λ2062 is a blend of Cr II and Zn II. The two additional transitions for Cr II are at λ2056 and λ2066.

Deblending the features in the Zn II-Cr II region at SDSS resolution can be done by making use of known oscillator strength ratios for an element's ionic transition. For example, for the feature at λ2026 the equivalent widths of Mg I λ2026 and Cr II λ2026 were taken to be 32 and 23 times smaller than the observed equivalent widths of the unblended Mg I λ2852 and Cr II λ2056 lines, resepctively. The remaining absorption can then be attributed to Zn II λ2026.[2] Generally, since the oscillator strength of Cr II λ2026 is quite small relative to Zn II λ2026, its contribution to the λ2026 feature is negligible.

Similarly, the feature at λ2062 due to Zn II and Cr II can be deblended by taking the Cr II λ2062 equivalent width to be half of the sum of the Cr II λ2056 and Cr II λ2066 equivalent widths, with the remainder due to Zn II λ2062. The corresponding errors are then propagated in quadrature. The reported column densities are the error-weighted average values inferred from each transition. The results on the column densities for Zn^+, Cr^+, Fe^+ and Mn^+ are summarized in Table 3.1, where the column density for Fe^+ is inferred from the weak lines of Fe II $\lambda\lambda$2249, 2260 and the column density for Mn^+ is inferred from the weak lines of Mn II $\lambda\lambda\lambda$2576, 2594, 2606.

For the Ca II absorbers in Table 3.1, Figure 3.1 shows the abundance ratios [X/Zn], where X = [Cr, Fe, Mn], as filled circles versus $W_0^{\lambda 3934}$. Cr, Fe, and Mn are known to be highly refractory, while Zn is not. Hence, an indication of the degree of depletion of Cr, Fe, and Mn onto dust grains can be inferred from these abundance ratios. Results from previous investigations of Ca II absorbers (open symbols) known to be damped Lyα absorbers (DLAs) and subDLAs at $z \sim 1$ are also included in Figure 3.1 for comparison. These data are due to Wild, Hewett & Pettini (2006)[3], Nestor et al. (2008), and the Zych et al. (2009) VLT/UVES and Keck/HIRESb datasets. Consistent with previous results, these refractory

[2] In some systems comparisons of Mg I λ2852 to Mg II $\lambda\lambda$2796, 2803 suggest that Mg I λ2852 may be approaching saturation, but neglecting this does not introduce a significant uncertainty.

[3] Wild et al. (2006) abundance ratios were derived from composite spectra constructed from 37 Ca II absorbers from SDSS DR3+DR4. One of their results was for their entire sample, while two additional result were presented for "High" and "Low" $W_0^{\lambda 3934}$ values on either side of their median $W_0^{\lambda 3934} = 0.68$ Å value. Our results from composite spectra in this study are presented in §3.4 and §3.5.

elements are all seen to be depleted relative to Zn. While the depletion levels are fairly typical, nucleosynthetic processes can yield departures of -0.3 to -0.1 in [Fe/Zn] (Prochaska & Wolfe 2002). The depletion levels are seen to vary over a range of values, suggestive of a significant range in dust-to-gas ratios in these sightlines and/or environments. Although a large scatter is present, the results suggest that depletion increases with increasing $W_0^{\lambda 3934}$, which is generally consistent with previous findings.

Table 3.1: Cr^+, Zn^+, Fe^+, and Mn^+ column densities of Ca II absorbers derived from the equivalent widths of detectable weak transitions. The Ca II absorbers all lie in the redshift interval $0.87 \lesssim z_{abs} \lesssim 1.21$. The column densities of the various low-ionization elements are derived as described in the text.

Quasar	z_{abs}	$W_0^{\lambda 3934}$ (Å)	$W_0^{\lambda 3969}$ (Å)	log $N(Cr^{+1})$	log $N(Zn^{+1})$	log $N(Fe^{+1})$ (atoms cm^{-2})	log $N(Mn^{+1})$]
J014717+125808	1.039	0.484 ± 0.065	0.253 ± 0.066	13.36 ± 0.08	12.08 ± 0.05	14.40 ± 0.04	12.07 ± 0.03
J081053+352224	0.877	0.509 ± 0.074	0.254 ± 0.078	13.30 ± 0.15	12.84 ± 0.10	14.61 ± 0.04	12.31 ± 0.04
J233917-002943	0.967	0.475 ± 0.095	0.439 ± 0.111	13.62 ± 0.08	12.42 ± 0.18	···	12.39 ± 0.07
J112932+020422	0.965	0.632 ± 0.051	0.489 ± 0.063	13.09 ± 0.09	11.97 ± 0.41	14.30 ± 0.04	11.93 ± 0.04
J172739+530229	0.945	0.590 ± 0.094	0.422 ± 0.112	13.43 ± 0.13	12.49 ± 0.19	14.50 ± 0.06	12.15 ± 0.04
J094145+303503	0.938	1.118 ± 0.095	0.872 ± 0.104	13.45 ± 0.12	12.34 ± 0.06	14.62 ± 0.08	12.21 ± 0.03
J100000+514416	0.907	0.896 ± 0.168	0.660 ± 0.216	13.34 ± 0.21	12.59 ± 0.12	14.53 ± 0.40	12.36 ± 0.13
J162558+313911	0.906	0.813 ± 0.156	0.332 ± 0.130	13.63 ± 0.07	12.58 ± 0.10	14.96 ± 0.27	12.46 ± 0.04
J153503+311832	0.904	0.524 ± 0.045	0.387 ± 0.044	12.87 ± 0.08	11.90 ± 0.12	14.16 ± 0.07	11.84 ± 0.04
J114658+395834	0.900	0.381 ± 0.042	0.137 ± 0.045	13.86 ± 0.02	12.09 ± 0.02	14.23 ± 0.02	11.93 ± 0.02
J141615+365537	1.204	0.696 ± 0.086	0.396 ± 0.063	13.19 ± 0.11	11.89 ± 0.27	···	12.09 ± 0.83
J213408+043611	1.118	0.804 ± 0.085	0.426 ± 0.089	12.68 ± 0.13	11.96 ± 0.06	14.28 ± 0.08	11.97 ± 0.11

The Na I $\lambda\lambda$5891,5897 absorption transitions can be observed with the SDSS spectrograph for absorbers with $z_{abs} \lesssim 0.6$. With the BOSS spectrograph the coverage is extended to $z_{abs} \lesssim 0.7$. For absorbers in the Ca II catalog, measurements of Na I are possible for 213 systems. However, due to signal-to-noise limitations, which is particularly severe for many of the Na I lines since they occur close to the red limit of SDSS/BOSS spectra, only 31 Ca II absorbers had $\geq 2\sigma$ Na I detections. The results are summarized in Table 3.2. However, based on the observed doublet ratios, 23 of the measurements indicate some degree of saturation, and so most of the results are given as lower limits on Na^+ column densities. For the remaining eight, Eq. 3.1 was employed to derive the Na^+ column densities.

Galactic ISM studies show that Na^+ to Ca^+ column density ratios span about four orders of magnitude, ranging from $\sim +2.5$ to ~ -1.5 dex (Routly & Spitzer 1952; Siluk & Silk 1974; Welty et al. 1996), which is mainly due to substantial differences in the depletion of Ca onto dust grains. Large ratios occur in cold, dense and quiescent clouds, whereas the smaller values can be attributed to environments where no significant depletion has yet occurred or where some Ca has been returned to the gas phase due to shocks, such as those in warm and/or high velocity clouds.

Finally, we note that our Ca II catalog has two cases where the Ca II and Na I lines have doublet ratios which are clearly indicative of lines in the unsaturated regime. Both of these have $W_0^{\lambda 3934} < 0.6$Å, and in those cases we calculate the Na^+/Ca^+ column density ratios to be -0.36 ± 0.06 dex and -0.04 ± 0.10 dex. These values fall within the range that is typical of the diffuse, warm neutral medium in the Milky Way, where $T = 10^2 - 10^4$ K and $n_H \leq 10$ atoms cm^{-3} (Crawford 1992; Welty et al. 1996; Richter et. al 2011).

3.4 PROPERTIES OF Ca II ABSORBERS FROM COMPOSITE SPECTRA

Here we explore the composite properties of the Ca II absorbers by considering the 435 Ca II absorbers in the Chapter 2 catalog. We form two types of composite spectra. The first type is one constructed by median-combining continuum-normalized spectra. Element abundances will be inferred from this type of composite spectrum. The second type is formed using the

Table 3.2: Measurements of Na I $\lambda\lambda$5891,5897 doublet rest equivalent widths for Ca II absorbers with $z_{abs} \lesssim 0.7$. The table is ordered in terms of increasing z_{abs}. For weak unsaturated lines, we derive the Na^0 column densities as described in the text. For Na I profiles with doublet ratios approaching saturation, lower limits on $N(Na^0)$ are reported.

Quasar	z_{abs}	$W_0^{\lambda 3934}$ (Å)	$W_0^{\lambda 3969}$ (Å)	$W_0^{\lambda 5891}$ (Å)	$W_0^{\lambda 5897}$ (Å)	log $N(Na^{+1})$ (atoms cm^{-2})
J155752+342140	0.114	0.598 ± 0.102	0.628 ± 0.168	0.527 ± 0.165	0.380 ± 0.154	$\geq$ 12.54
J075031+192754	0.18	0.437 ± 0.084	0.447 ± 0.098	0.580 ± 0.123	0.380 ± 0.097	$\geq$ 12.55
J091958+111152	0.182	1.105 ± 0.212	0.720 ± 0.168	0.407 ± 0.138	0.569 ± 0.144	$\geq$ 12.66
J085917+105509	0.183	0.92 ± 0.108	0.431 ± 0.115	0.277 ± 0.098	0.209 ± 0.103	$\geq$ 12.28
J114339+073105	0.189	0.632 ± 0.098	0.462 ± 0.080	0.420 ± 0.089	0.180 ± 0.095	12.29 ± 0.09
J142536-001702	0.22	1.111 ± 0.094	0.515 ± 0.079	0.181 ± 0.091	0.150 ± 0.093	$\geq$ 12.13
J085045+563618	0.225	0.532 ± 0.071	0.219 ± 0.073	1.226 ± 0.121	1.068 ± 0.099	$\geq$ 12.96
J082312+264415	0.253	0.633 ± 0.103	0.383 ± 0.102	0.673 ± 0.165	0.398 ± 0.154	12.59 ± 0.08
J165743+221149	0.266	1.642 ± 0.221	1.546 ± 0.158	1.838 ± 0.176	1.060 ± 0.200	$\geq$ 13.02
J124300+204246	0.277	1.488 ± 0.126	1.034 ± 0.101	1.716 ± 0.145	0.957 ± 0.120	$\geq$ 12.97
J085010+593118	0.282	0.279 ± 0.043	0.160 ± 0.044	0.310 ± 0.054	0.194 ± 0.067	$\geq$ 12.27
J102935-012138	0.29	0.351 ± 0.067	0.208 ± 0.055	0.177 ± 0.084	0.240 ± 0.118	$\geq$ 12.31
J152800+535223	0.316	0.541 ± 0.056	0.325 ± 0.080	0.475 ± 0.147	0.186 ± 0.108	12.33 ± 0.13
J161649+415416	0.321	0.397 ± 0.067	0.226 ± 0.054	0.369 ± 0.086	0.201 ± 0.089	12.30 ± 0.09
J105640+013941	0.348	1.318 ± 0.213	0.749 ± 0.185	2.040 ± 0.433	1.710 ± 0.436	$\geq$ 13.02
J130811+113609	0.349	1.068 ± 0.121	0.815 ± 0.119	1.646 ± 0.157	1.734 ± 0.195	$\geq$ 12.97
J161018+042631	0.363	0.293 ± 0.054	0.225 ± 0.055	0.391 ± 0.153	0.365 ± 0.092	$\geq$ 12.27
J162957+423051	0.378	0.734 ± 0.146	0.498 ± 0.148	0.885 ± 0.224	0.942 ± 0.207	$\geq$ 12.89
J081336+481302	0.437	0.619 ± 0.042	0.290 ± 0.047	2.073 ± 0.359	0.515 ± 0.252	$\geq$ 12.87
J212727+082724	0.439	0.535 ± 0.104	0.456 ± 0.089	0.238 ± 0.096	0.080 ± 0.091	$\geq$ 12.31
J104923+012224	0.472	0.582 ± 0.054	0.236 ± 0.057	3.322 ± 0.462	2.644 ± 0.439	$\geq$ 13.19
J143614+105905	0.478	0.833 ± 0.121	0.551 ± 0.107	0.752 ± 0.135	0.448 ± 0.134	12.64 ± 0.06
J015701+135503	0.484	1.760 ± 0.184	1.599 ± 0.318	2.652 ± 0.322	2.838 ± 0.277	$\geq$ 13.37
J125244+642103	0.512	1.099 ± 0.096	0.696 ± 0.076	1.518 ± 0.824	2.189 ± 1.119	$\geq$ 12.99
J083553+154139	0.531	1.064 ± 0.106	0.726 ± 0.117	3.377 ± 0.911	1.320 ± 0.962	13.08 ± 0.12
J132803+352152	0.532	0.679 ± 0.095	0.439 ± 0.096	0.186 ± 0.098	0.244 ± 0.110	$\geq$ 12.30
J074816+422509	0.558	0.314 ± 0.036	0.148 ± 0.030	0.290 ± 0.104	0.321 ± 0.122	$\geq$ 12.44
J004800+022514	0.598	0.594 ± 0.101	0.297 ± 0.096	1.324 ± 0.282	0.560 ± 0.328	12.78 ± 0.10
J132657+405018	0.611	0.723 ± 0.080	0.548 ± 0.078	1.149 ± 0.152	0.683 ± 0.147	$\geq$ 12.82
J160343+244836	0.656	0.723 ± 0.080	0.548 ± 0.078	0.957 ± 0.277	0.612 ± 0.259	12.76 ± 0.09

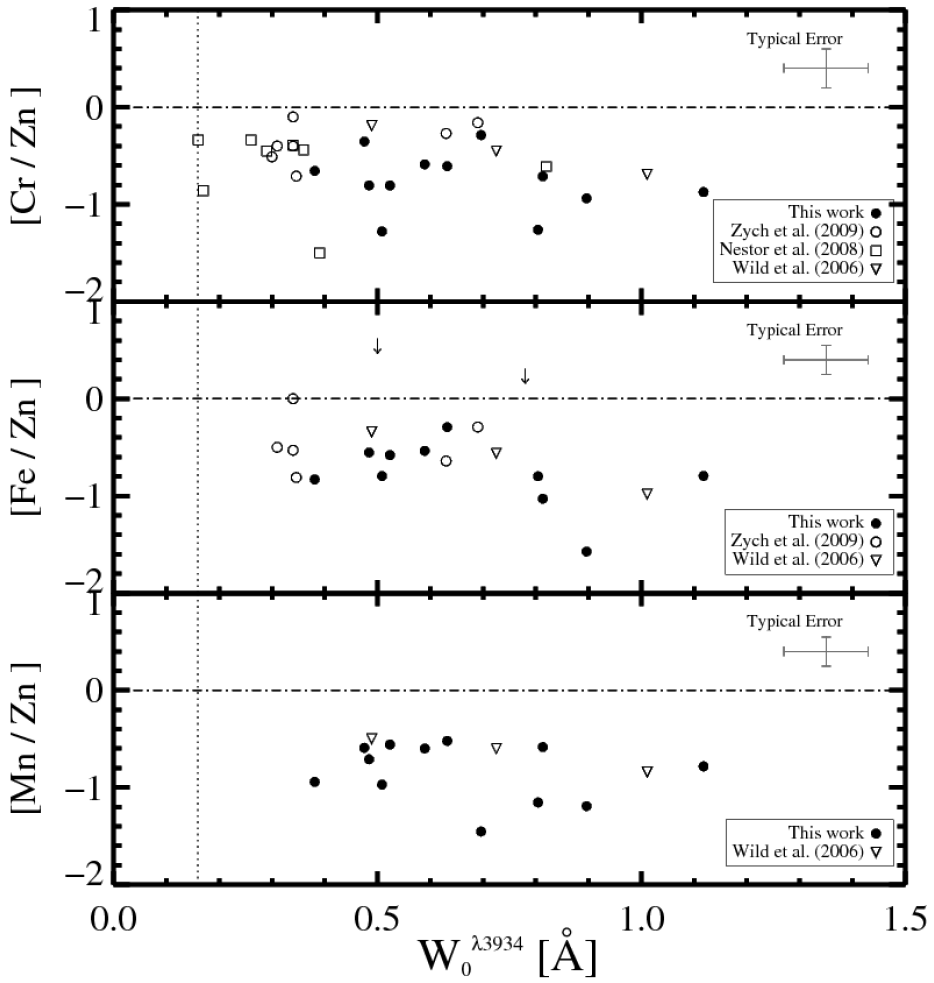

Figure 3.1: The reliable abundance ratio measurements for a dozen individual Ca II absorbers (Table 3.1) in our sample (filled circles) in comparison to results reported in other studies (open symbols). *Top panel:* The abundance ratio [Cr/Zn] vs. $W_0^{\lambda 3934}$, determined as explained in the text. *Center panel:* The abundance ratio [Fe/Zn] vs. $W_0^{\lambda 3934}$, as inferred from Fe II $\lambda\lambda 2249, 2260$. The downward arrows are upper limits from Zych et al. (2009). *Bottom panel:* The abundance ratio [Mn/Zn] vs. $W_0^{\lambda 3934}$, as inferred from Mn II $\lambda\lambda\lambda 2576, 2594, 2606$. Typical errors are shown in the upper right of all three panels. Note that the three Wild et al. (2006) data points are for their low-$W_0^{\lambda 3934}$, full sample, and high-$W_0^{\lambda 3934}$ composites. The reader is referred to §3.4 (Tables 3.6 and 3.7) and §3.5 (Figure 3.12) for our composite results. All three abundance ratio results show a trend of increasing depletion with increasing $W_0^{\lambda 3934}$, although the spread in [X/Zn] is large. The dotted vertical line in the figure marks the lowest values of the Ca II rest equivalent width detection threshold from Chapter 2, i.e., $W_0^{\lambda 3934} = 0.16$ Å. The dash-dot horizontal lines mark the solar reference level for no depletion.

geometric mean of unnormalized flux spectra (e.g., York et al. 2006, Vanden Berk et al. 2001). From this type of composite we will measure the overall extinction and reddening characteristics of the Ca II absorbers. This is done using unabsorbed quasar spectra that are matched (in emission redshift and i-band magnitude) to the Ca II absorber quasar spectra.

We form these two types of composites for our full sample and four different subsamples, which are subsets of the full sample. The rationale behind choosing the criteria to define the four subsamples was given in Chapter 2. In particular, Chapter 2 showed the existence of two populations of Ca II absorbers that could be separated based upon the bimodality in the distribution of $W_0^{\lambda 2796}/W_0^{\lambda 3934}$ ratios, with the separation occurring at $W_0^{\lambda 3934} = 0.7$ Å. We also found that the change in slope of the $W_0^{\lambda 3934}$ distribution occurred at $W_0^{\lambda 2796}/W_0^{\lambda 3934} = 1.8$. (See Figures 2.17 and 2.18 of Chapter 2.) Therefore, we define the four subsamples as systems with $W_0^{\lambda 3934} < 0.7$Å and ≥ 0.7Å, and those with $W_0^{\lambda 2796}/W_0^{\lambda 3934} < 1.8$ and ≥ 1.8. The results we derive from the full sample are primarily discussed in this section, while the results from the four subsamples are primarily discussed in §3.5.

3.4.1 Normalized Composite Spectra

The stacking procedure begins by shifting all 435 normalized spectra to the Ca II absorber rest frame. To facilitate wavelength registration before doing this, we start by rebinning the spectra into a finer sub-pixel grid, the size of which is about one-tenth of the original pixel size. The spectra were then combined to build two types of normalized composite spectra, a median composite and an inverse-variance-weighted composite. We find essentially no significant difference in the absorption rest equivalent width measurements of the two types. Since the median is a robust measure of central tendency, we have chosen to use the median-combined spectra for the normalized composites (e.g. Vanden Berk et al. 2001; Pieri et al. 2010). The error in the composite flux is estimated using normal error propagation. Our errors are appropriately smaller than those reported for the SDSS sample of Wild et al. (2006), consistent with our increase in sample size relative to theirs. The final stack is then rebinned to 2-pixels per resolution element and then smoothed over two pixels for display purposes only. We summarize the number of spectra that contributed to the various regions

of the composite spectra in Table 3.3. We emphasize that when forming the composites, we used all available spectra at all redshifts. This means, for example, that the Zn II - Cr II region only includes data at $z > 0.85$ (50 spectra in the full sample), whereas the Ca II region includes all data down to redshifts near zero (435 spectra in the full sample). This is justified because there is no evidence for redshift evolution and we wish to minimize errors in all spectral regions; the Ca II composite spectral regions are statistically the same above and below $z = 0.85$.

Figure 3.2 shows the full sample normalized composite spectrum, which was formed using all 435 SDSS Ca II absorber spectra identified in Chapter 2. Figures 3.3-3.6 are the normalized composite spectra for the four subsamples (see §3.5 discussion). The error array of the full sample composite spectrum ranges between ∼1.4% and ∼ 6.5% of the flux. The red vertical lines mark the rest-frame locations of the absorption features that are typical of those identified in QAL studies. The wavelength coverage of the various spectra in the Ca II absorber rest frame allows access to absorption features that lie between and include Si II λ1808 and Na I $\lambda\lambda$5891,5897. Note that the stack includes absorber rest frame wavelengths down to ∼ 1700 Å, but we do not attempt to measure any QALs at $\lambda \lesssim 1750$ Å because of potential errors in the continuum placement at the (noisy) blue end of SDSS spectra.

Clearly seen in the normalized composite spectrum are the transitions of low-ionization lines such as Zn II, Cr II, Ni II, Ti II, Fe II, Mn II Mg II, Mg I and Na I, as well as the higher-ionization transitions due to Al III. In the individual SDSS spectra most of these transitions are too weak, and/or located in spectral regions with too poor signal-to-noise, to identify them. In the Zn II-Cr II region at shorter wavelengths, the composite is derived from only ∼ 50 out of > 400 spectra, and thus it exhibits poorer signal-to-noise characteristics; on the other hand, at the longer wavelengths the Na I region composite is comprised of ∼ 200 spectra. In Figure 3.2 we only label those features with $\geq 2\sigma$ detections to avoid crowded labeling. We measure the rest equivalent widths by fitting Gaussian profiles to each feature, with the constraint that features have a minimum line width set by the resolution of the SDSS/BOSS spectra. The rest equivalent widths of the various QAL transitions are summarized in Table 3.4. For those lines which do not pass the 2σ detection limit, we report 2σ upper limits. Composite results for the full sample and four subsamples are given in

Table 3.4. There is a ∼30% improvement in the measured absorption rest equivalent width errors in the Zn II - Cr II region (Table 3.4) in comparison to the earlier study of Wild et al. (2006).

3.4.2 Column Densities and Element Abundance Ratios in Ca II Absorbers from their Composite Spectra

Column densities derived using Eq. 3.1 for the weak, unsaturated absorption lines in the full sample composite and the four subsample composites are reported in Table 3.5 along with their 1σ uncertainties. The reported results are generally variance-weighted averages of column densities determined from accessible unsaturated transitions of the ion, similar to the results reported in §3.3. We only provide results when significance levels are $\geq 2\sigma$, otherwise, 2σ upper limits are reported. The limit for N(Fe^0) was derived from the 2σ rest equivalent width upper limit of Fe I λ2484, since it has the strongest oscillator strength among the Fe I transitions in our coverage. The N(Fe^{+1}) value was obtained using the weak lines of Fe II λ2249, λ2260.

The doublet ratios of Ca II and Na I indicate that both may be partially saturated so we assign lower limits on their column densities. These column densities are consistent with those reported by previous authors using ∼10 times fewer systems (e.g., Wild et al. 2006, Nestor et al. 2008, Zych et al. 2009). However, none of these studies have sampled much of the $W_0^{\lambda 3934} \gtrsim 0.7$ Å regime.

As in §3.3 we assume that the low-ionization column densities reported in Table 3.5 represent the dominant ionization state due to self-shielding and that no significant ionization corrections are needed. The solar abundance ratios relative to Zn and Fe, i.e., [X/Zn] and [X/Fe], are then tabulated in Table 3.6 and Table 3.7, respectively. The ratios relative to Zn can reveal depletion of elements on to dust grains relative to solar abundances, while ratios relative to Fe can show important enhancements (see below).

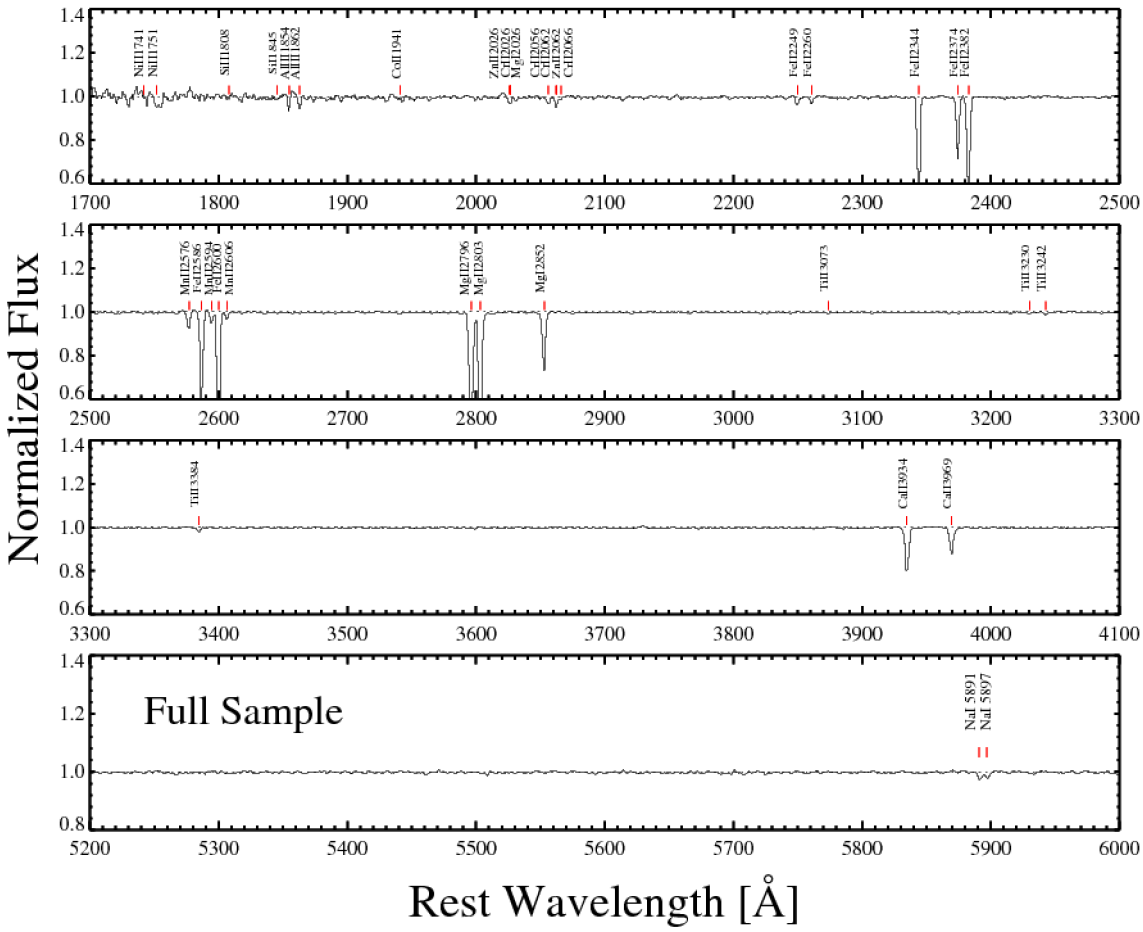

Figure 3.2: The median-combined normalized composite spectrum of the full sample of Ca II absorbers in the Paper I and Chapter 2 catalog. To facilitate accurate wavelength registration, each spectrum in the composite has been shifted to the rest frame of the Ca II absorber prior to stacking using a finer subpixel grid. Details are provided in the text. Red vertical lines mark absorption features that are significant at the $> 2\sigma$ level. The rest equivalent width measurements and 2σ upper limits of QALs associated with the Ca II absorption in this spectrum are summarized in Table 3.4.

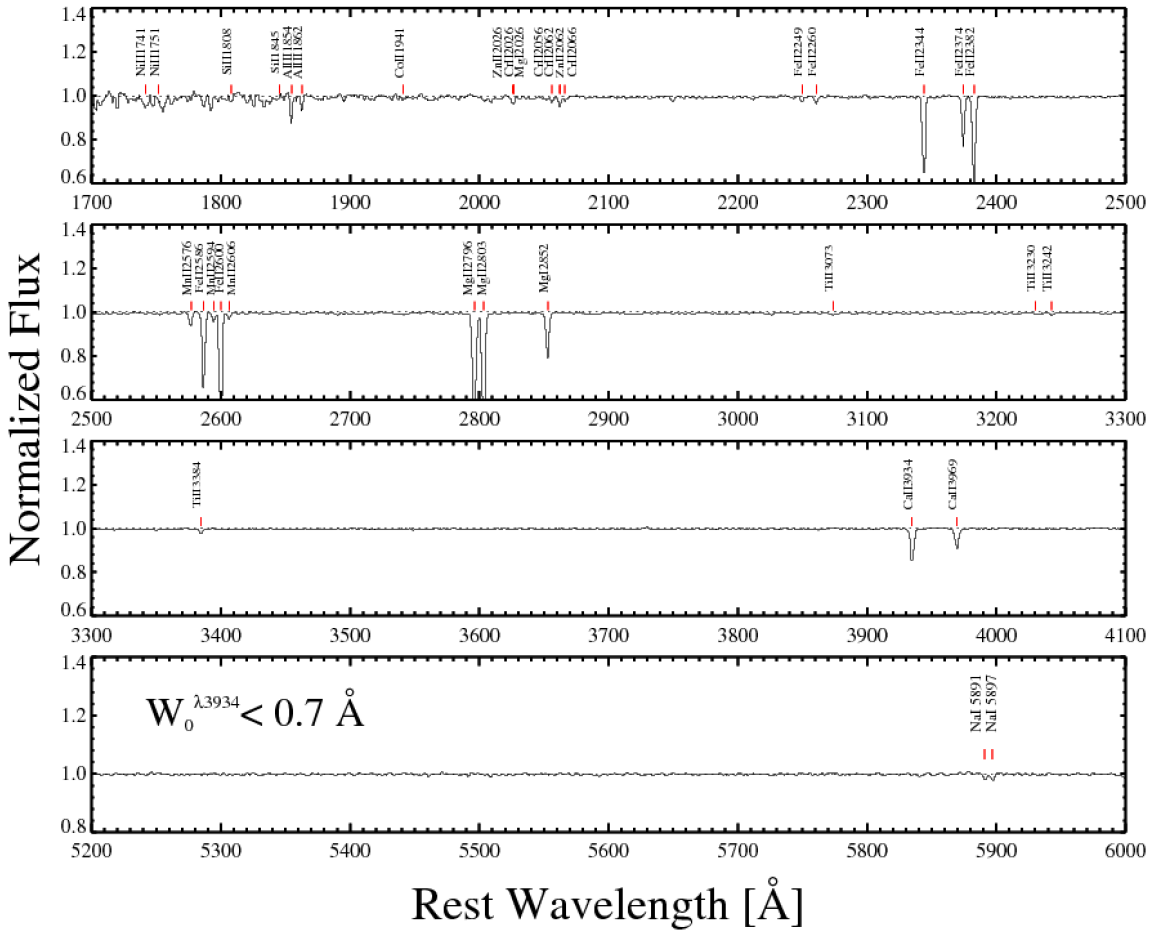

Figure 3.3: Same as Fig. 3.2 but for the sample of Ca II absorbers with $W_0^{\lambda 3934} < 0.7$ Å.

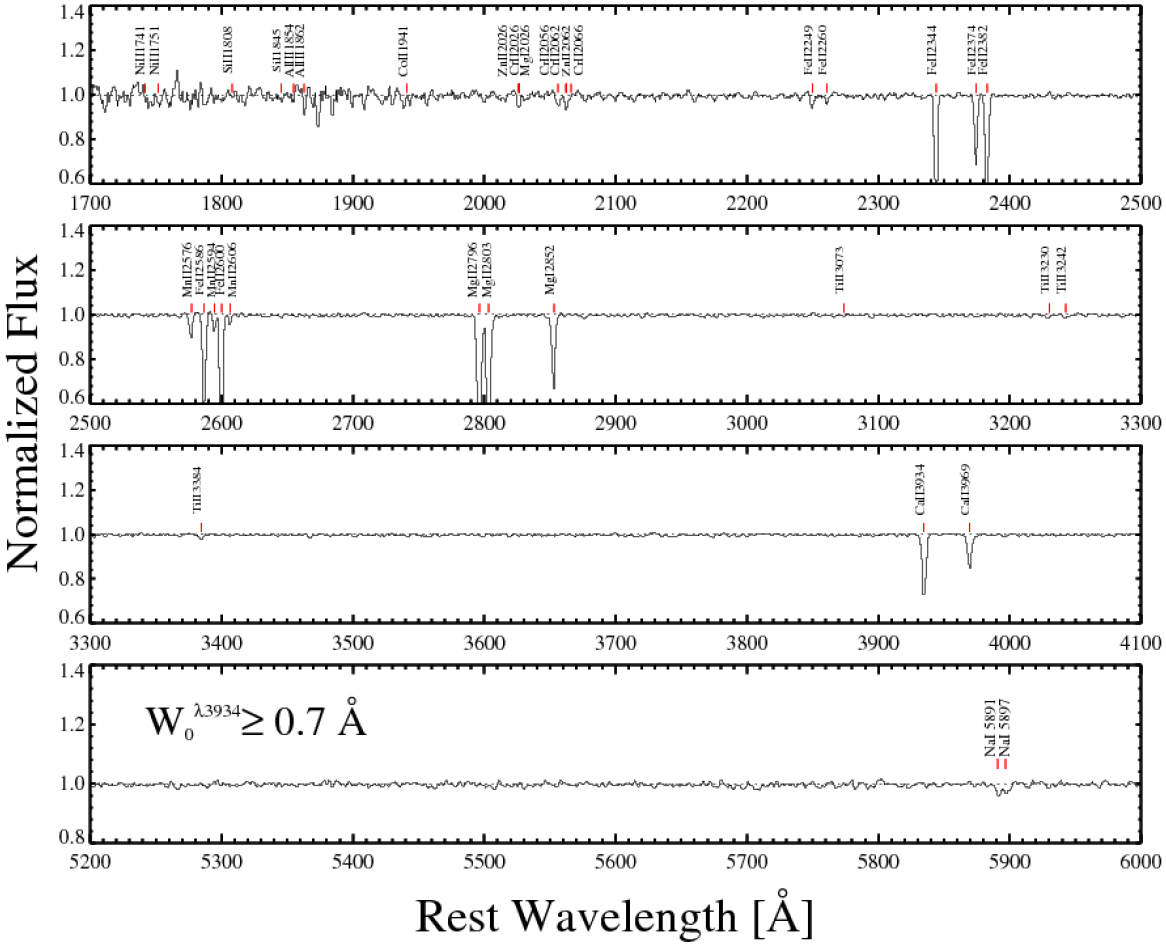

Figure 3.4: Same as Fig. 3.2 but for the sample of Ca II absorbers with $W_0^{\lambda 3934} \geq 0.7$ Å.

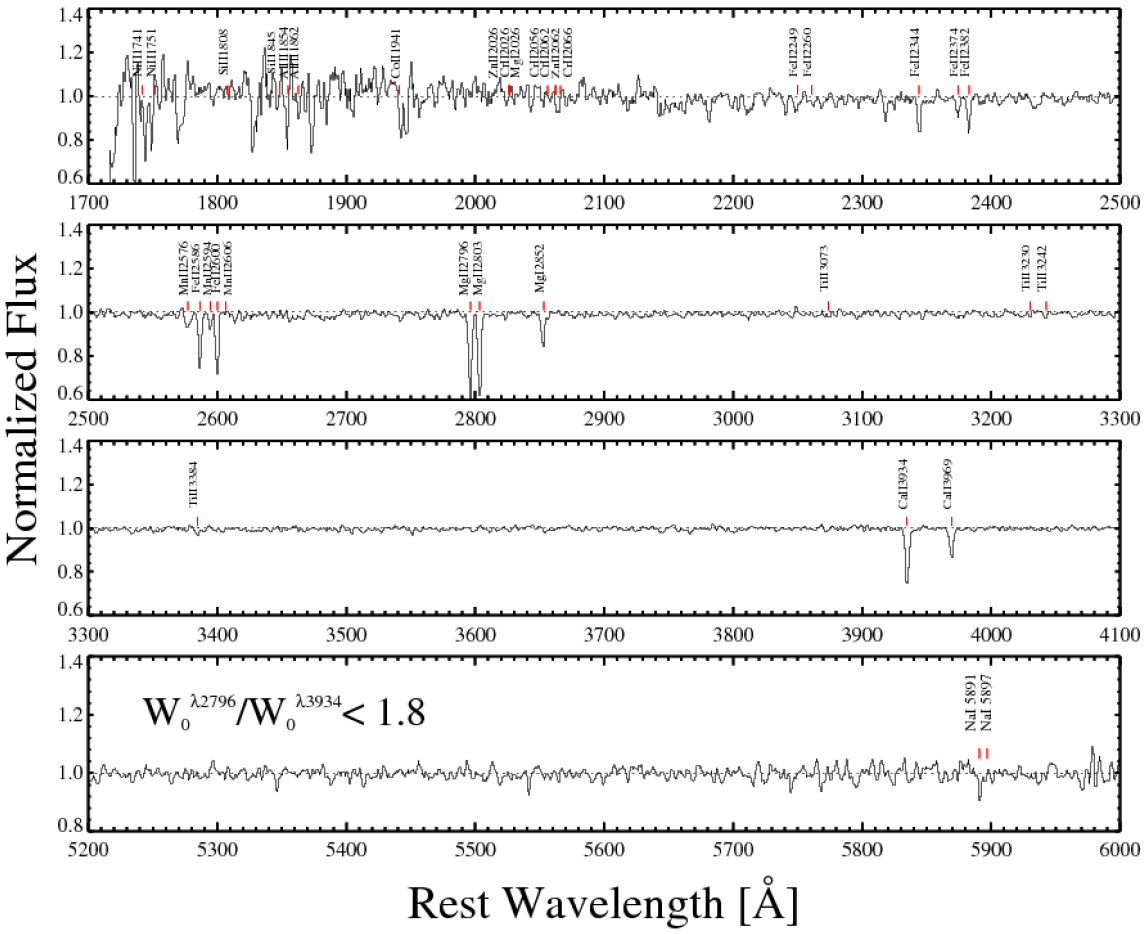

Figure 3.5: Same as Fig.3.2 but for the sample of Ca II absorbers with $W_0^{\lambda 2796}/W_0^{\lambda 3934}$ <1.8.

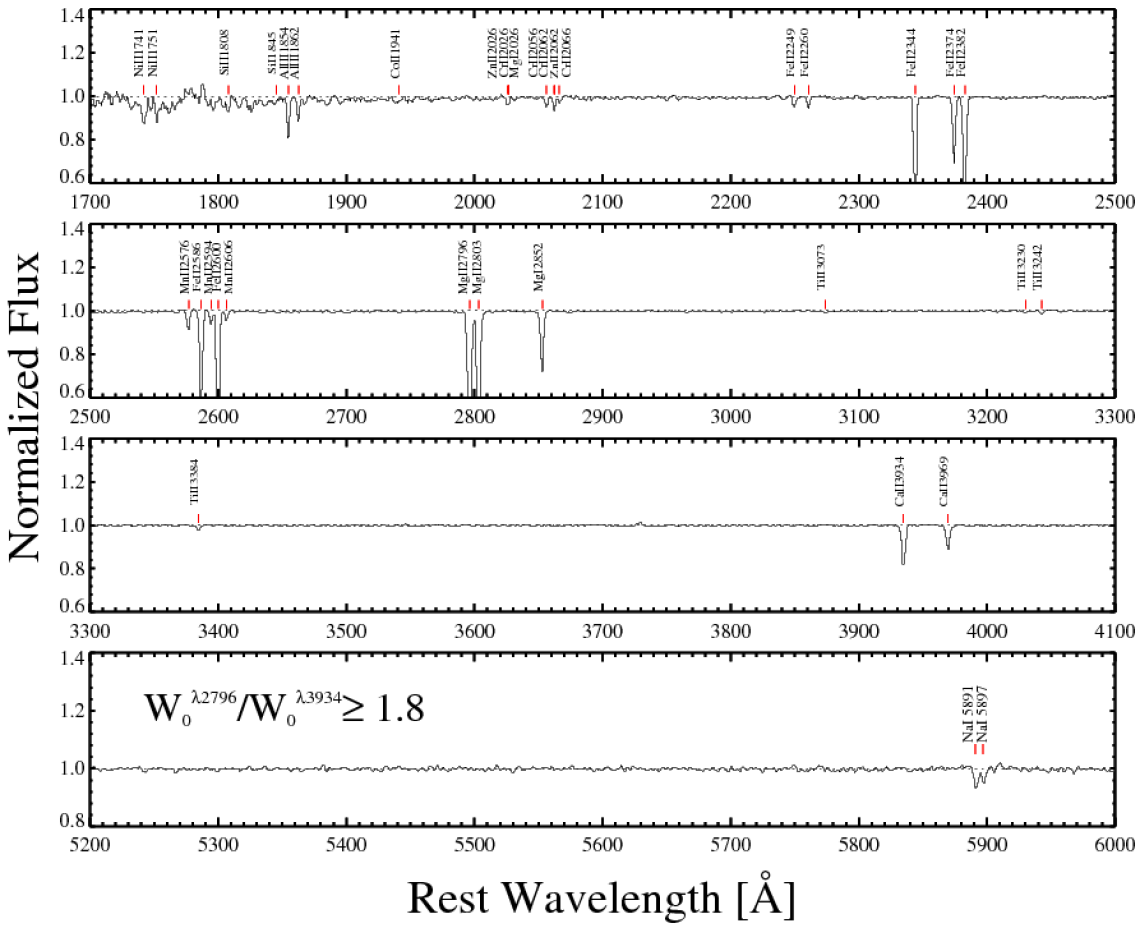

Figure 3.6: Same as Fig. 3.2 but for the sample of Ca II absorbers with $W_0^{\lambda 2796}/W_0^{\lambda 3934} \geq 1.8$.

Table 3.3: The number of individual spectra included in the various regions of the final normalized composite spectra (§4.1). When forming fluxed composites (§4.4), approximately 10% of these individual spectra were excluded due to an inadequate non-absorber match.

Region	Full Sample	$W_0^{\lambda 3934} < 0.7$Å	$W_0^{\lambda 3934} \geq 0.7$Å	$W_0^{\lambda 2796}/W_0^{\lambda 3934} < 1.8$	$W_0^{\lambda 2796}/W_0^{\lambda 3934} \geq 1.8$
Zn II- Cr II	50	29	21	4	40
Fe II λ2249	141	82	59	7	124
Mn II	229	128	101	21	189
Ti II	375	202	173	29	223
Ca II	435	233	202	31	223
Na I	223	126	97	12	59

Table 3.4: Rest equivalent width (REW, W_0) measurements off five different normalized composite spectra, including the composite spectrum formed using the full sample of 435 Ca II absorber spectra. The rationale behind forming four additional composite spectra by dividing the full sample into subsamples is explained in the text.

Line	REW (Å)				
...	Full Sample	$W_0^{\lambda 3934} < 0.7$Å	$W_0^{\lambda 3934} \geq 0.7$Å	$W_0^{\lambda 2796}/W_0^{\lambda 3934} < 1.8$	$W_0^{\lambda 2796}/W_0^{\lambda 3934} \geq 1.8$
Ni II 1741	0.133 ± 0.039	0.107 ± 0.029	0.054 ± 0.022	...	0.130 ± 0.025
Ni II 1751	0.081 ± 0.031	0.060 ± 0.026	0.034 ± 0.018	...	0.059 ± 0.021
Si II 1808	0.155 ± 0.029	0.160 ± 0.024	0.151 ± 0.028	≤ 0.437	0.159 ± 0.019
Al III 1854	0.424 ± 0.029	0.378 ± 0.031	0.525 ± 0.031	≤ 0.348	0.512 ± 0.019
Al III 1862	0.286 ± 0.024	0.322 ± 0.026	0.363 ± 0.034	≤ 0.399	0.315 ± 0.020
Fe II 1901	≤ 0.028	≤ 0.032	≤ 0.044	≤ 0.322	≤ 0.040
Ti II 1910	≤ 0.040	0.084 ± 0.020	≤ 0.050	≤ 0.223	0.067± 0.017
Co II 1941*	0.094 ± 0.020	0.063 ± 0.022	≤ 0.184	≤ 0.323	0.083 ± 0.017
Co II 2012*	≤ 0.058	≤ 0.028	≤ 0.082	≤ 0.344	0.066 ± 0.010
Zn II 2026†	0.142	0.070	0.103	≤ 0.205	0.079
Cr II 2026†	0.004	0.003	0.004	≤ 0.005	0.005
Mg I 2026†	0.023	0.019	0.029	≤ 0.015	0.026
Cr II 2056	0.084 ± 0.014	0.082 ± 0.010	0.085 ± 0.021	≤ 0.303	0.100 ± 0.015
Cr II 2062	0.056 ± 0.010	0.063 ± 0.010	≤ 0.024	≤ 0.309	0.074 ± 0.010
Zn II 2062	0.069 ± 0.022	0.058 ± 0.018	0.157 ± 0.029	≤ 0.146‡	0.072 ± 0.016
Cr II 2066	0.028 ± 0.015	0.044 ± 0.011	≤ 0.048	≤ 0.181	0.048 ± 0.012
Cd II 2145	≤ 0.028	≤ 0.034	≤ 0.038	≤ 0.158	≤ 0.024
Fe I 2167	≤ 0.013	≤ 0.038	≤ 0.044	≤ 0.125	≤ 0.022
Fe II 2249	0.126 ± 0.012	0.090 ± 0.012	0.108 ± 0.019	0.097 ± 0.023	0.130 ± 0.010
Fe II 2260	0.115 ± 0.011	0.110 ± 0.011	0.096 ± 0.017	0.099 ± 0.036	0.136 ± 0.009
Fe II 2344	1.140 ± 0.009	0.976 ± 0.009	1.260 ± 0.016	0.391 ± 0.034	1.269 ± 0.008
Fe II 2374	0.751 ± 0.009	0.618 ± 0.009	0.819 ± 0.016	0.148 ± 0.042	0.840 ± 0.008
Fe II 2382	1.398 ± 0.009	1.279 ± 0.009	1.475 ± 0.015	0.486 ± 0.043	1.635 ± 0.007
Fe I 2463	≤ 0.020	≤ 0.020	≤ 0.032	≤ 0.080	≤ 0.017
Fe I 2484	≤ 0.020	≤ 0.020	≤ 0.032	≤ 0.084	≤ 0.017
Fe I 2501	≤ 0.020	≤ 0.020	≤ 0.030	≤ 0.098	≤ 0.017
Si I 2515	≤ 0.022	≤ 0.022	≤ 0.030	≤ 0.080	≤ 0.017
Fe I 2523	≤ 0.020	≤ 0.020	≤ 0.022	≤ 0.078	≤ 0.017
Mn II 2576	0.226 ± 0.010	0.183 ± 0.010	0.299 ± 0.017	0.236 ± 0.037	0.237 ± 0.008
Fe II 2586	1.115 ± 0.008	0.954 ± 0.008	1.247 ± 0.013	0.711 ± 0.034	1.239 ± 0.006
Mn II 2594	0.164 ± 0.009	0.137 ± 0.010	0.197 ± 0.014	0.181 ± 0.036	0.171 ± 0.008
Fe II 2600	1.472 ± 0.008	1.321 ± 0.008	1.616 ± 0.013	0.770 ± 0.030	1.641 ± 0.007
Mn II 2606	0.104 ± 0.009	0.100 ± 0.010	0.115 ± 0.013	0.109 ± 0.022	0.123 ± 0.008
Mg II 2796	1.940 ± 0.008	1.785 ± 0.008	2.068 ± 0.013	1.235 ± 0.027	2.283 ± 0.006
Mg II 2803	1.803 ± 0.008	1.595 ± 0.007	2.054 ± 0.013	1.175 ± 0.027	2.065 ± 0.006
Mg I 2852	0.742 ± 0.007	0.614 ± 0.008	0.919 ± 0.012	0.474 ± 0.027	0.818 ± 0.006
Fe I 2967	≤ 0.016	≤ 0.018	≤ 0.028	≤ 0.074	≤ 0.015
Fe I 3021	≤ 0.016	≤ 0.018	≤ 0.028	≤ 0.069	≤ 0.015
Ti II 3073	0.039 ± 0.008	0.039 ± 0.009	0.036 ± 0.014	0.057 ± 0.018	0.032 ± 0.007
Ti II 3230	0.035 ± 0.006	0.035 ± 0.006	0.048 ± 0.009	0.045 ± 0.019	0.030 ± 0.005
Ti II 3242	0.046 ± 0.008	0.050 ± 0.007	0.052 ± 0.014	0.068 ± 0.020	0.052 ± 0.006
Ti II 3384	0.082 ± 0.007	0.091 ± 0.006	0.089 ± 0.014	0.111 ± 0.017	0.079 ± 0.006
Fe I 3720	≤ 0.016	≤ 0.016	≤ 0.026	≤ 0.079	≤ 0.032
Ca II 3934	0.703 ± 0.006	0.493 ± 0.006	1.012 ± 0.010	0.885 ± 0.024	0.636 ± 0.006
Ca II 3969	0.418 ± 0.006	0.312 ± 0.006	0.572 ± 0.011	0.470 ± 0.023	0.378 ± 0.006
Ca I 4227	≤ 0.018	≤ 0.018	≤ 0.028	≤ 0.060	≤ 0.015
Na I 5891	0.118 ± 0.013	0.079 ± 0.012	0.194 ± 0.039	0.235 ± 0.053	0.269 ± 0.020
Na I 5897	0.089 ± 0.011	0.074 ± 0.009	0.182 ± 0.033	≤ 0.104	0.174 ± 0.018

* Tentative detections

† Blended. The deblending procedures were as outlined in Nestor et al. (2003). Cr II λ2026 and Mg I λ2026 are predicted strengths.

‡ Upper limit inferred using the 2σ upper limit for Cr II+Zn II.

Table 3.5: Metal-line column densities derived from the normalized composite spectra.

	log N [atoms per cm^2]				
Ion	Full Sample	$W_0^{\lambda 3934} < 0.7$Å	$W_0^{\lambda 3934} \geq 0.7$Å	$W_0^{\lambda 2796}/W_0^{\lambda 3934} < 1.8$	$W_0^{\lambda 2796}/W_0^{\lambda 3934} \geq 1.8$
Si^{+1}	15.39 ± 0.08	15.40 ± 0.07	15.38 ± 0.08	···	15.40 ± 0.05
Al^{+2}	13.44 ± 0.09	13.36 ± 0.09	13.51 ± 0.07	≤ 13.54	13.49 ± 0.06
Zn^{+1}	12.89 ± 0.05	12.63 ± 0.07	12.82 ± 0.06	≤ 13.35	12.69 ± 0.06
Cr^{+1}	13.32 ± 0.05	13.33 ± 0.04	13.07 ± 0.12	≤ 13.93	13.41 ± 0.04
Fe^{+1}	15.12 ± 0.03	15.01 ± 0.03	15.05 ± 0.05	15.03 ± 0.09	15.13 ± 0.02
Mn^{+1}	13.01 ± 0.01	12.94 ± 0.02	13.00 ± 0.02	12.94 ± 0.05	13.04 ± 0.01
Ti^{+1}	12.42 ± 0.03	12.44 ± 0.02	12.41 ± 0.06	12.55 ± 0.05	12.41 ± 0.03
Fe ^{0}	≤ 11.82	≤ 11.82	≤ 12.02	≤ 12.30	≤ 12.20
Ca^{+1}	≥ 12.97	≥12.84	≥13.11	13.02 ± 0.01	≥12.87
Na ^{0}	≥ 11.83	≥11.71	≥12.14	≥12.06	≥12.17

For the full sample, the results are generally consistent with DLA absorber populations over a range of redshifts (e.g., Turnshek et al. 1989, Pettini et al. 1999, Prochaska & Wolfe 2002, Ledoux, Bergeron & Petitjean 2002, Prochaska et al. 2003, Akerman et al. 2005, Kulkarni et al. 2005, Battisti et al. 2012), and with the ratios seen in individual Ca II absorbers in the literature (e.g., Zych et al. 2009, Richter et al. 2011). Similar abundance ratios are also seen in metal-strong DLAs (MSDLAs), which are classified as those DLAs with $\log N(Zn^+) \geq 13.15$ or $\log N(Si^+) \geq 15.95$ (Herbert-Fort et al. 2006), though the metal column densities of the Ca II absorbers are significantly lower than these values. The abundance ratios relative to Zn also approximately match the abundances ratios of the SMC as measured toward the star Sk 155 (Welty et al. 2001).

The wavelength coverage of the Ca II absorber spectra permits the detection of both Fe-peak (e.g., Cr, Mn, Fe) and α-capture elements (e.g., Si, Ca, Ti). It is generally thought that the Fe-peak and α-capture elements are synthesized in the lead-up to Type II supernovae events over timescales $< 10^7$ years, whereas Fe-peak elements are also synthesized through Type Ia supernovae events occurring over $10^8 - 10^9$ years. Hence, studying the abundance of α-elements relative to Fe-peak elements provides clues to the chemical and star-formation patterns of the absorber. Furthermore, since different elements display various affinities to dust, one can also characterize the absorber depletion patterns. But disentangling the degeneracy between depletion and chemical enrichment is often difficult (e.g. Lauroesch et al. 1996, Lu et al. 1996, Prochaska & Wolfe 2002, Vladilo 2002, Dessauges-Zavadsky, Prochaska & D'Odorico 2002, Welty & Crowther 2010). However, some constraints on the two effects can still be inferred from comparisons of various abundances against each other (Prochaska & Wolfe 2002; Herbert-Fort et al. 2006). An enhanced [Ti/Fe] generally implies a Type II enrichment pattern, while an enhancement of [Si/Fe] suggests a population that is strongly depleted by dust. The [Ti/Zn] ratio is generally not a clear tracer of depletion, and using it would likely under-estimate the extent of depletion; however, the [Ti/Zn] ratio we observe for the Ca II absorbers does hint at some level of depletion of Ti on to dust grains. The enhancements of [Si/Fe], [Zn/Fe], and [Si/Ti] all unanimously indicate strong depletions in the typical Ca II absorber (Prochaska & Wolfe 2002).

Table 3.6: Elemental abundances relative to Zn for the various (sub)samples of Ca II absorbers. The determinations are derived using the methods discussed in the text.

	[X/Zn]				
X	Full Sample	$W_0^{\lambda 3934} < 0.7$Å	$W_0^{\lambda 3934} \geq 0.7$Å	$W_0^{\lambda 2796}/W_0^{\lambda 3934} < 1.8$	$W_0^{\lambda 2796}/W_0^{\lambda 3934} \geq 1.8$
Cr	-0.63 ± 0.06	-0.38 ± 0.08	-0.88 ± 0.13	$\cdots$	-0.36 ± 0.09
Si	-0.37 ± 0.11	-0.17 ± 0.09	-0.45 ± 0.13	$\cdots$	-0.24 ± 0.09
Mn	-0.75 ± 0.06	-0.56 ± 0.06	-0.75 ± 0.06	≥ -1.49	-0.51 ± 0.09
Ti	-0.85 ± 0.06	-0.58 ± 0.06	-0.86 ± 0.08	≥ -1.19	-0.66 ± 0.06
Fe	-0.70 ± 0.06	-0.56 ± 0.08	-0.77 ± 0.09	≥ -1.26	-0.50 ± 0.09
Ni	-0.45 ± 0.11	-0.34 ± 0.13	-0.87 ± 0.16	$\cdots$	-0.37 ± 0.14

Table 3.7: Elemental abundances relative to Fe for the various (sub)samples of Ca II absorbers. The determinations are derived using the methods discussed in the text.

	[X/Fe]				
X	Full Sample	$W_0^{\lambda 3934} < 0.7$Å	$W_0^{\lambda 3934} \geq 0.7$Å	$W_0^{\lambda 2796}/W_0^{\lambda 3934} < 1.8$	$W_0^{\lambda 2796}/W_0^{\lambda 3934} \geq 1.8$
Cr	$+0.06 \pm 0.06$	$+0.17 \pm 0.05$	-0.12 ± 0.13	$\leq +0.76$	$+0.14 \pm 0.04$
Si	$+0.25 \pm 0.09$	$+0.38 \pm 0.07$	$+0.32 \pm 0.10$	$\cdots$	$+0.26 \pm 0.06$
Mn	-0.04 ± 0.03	-0.01 ± 0.04	$+0.02 \pm 0.06$	-0.02 ± 0.10	-0.01 ± 0.02
Ti	-0.16 ± 0.04	-0.02 ± 0.04	-0.09 ± 0.08	$+0.07 \pm 0.10$	-0.16 ± 0.03
Zn	$+0.70 \pm 0.09$	$+0.56 \pm 0.09$	$+0.77 \pm 0.09$	$\leq +1.26$	$+0.50 \pm 0.09$
Ni	$+0.21 \pm 0.11$	$+0.21 \pm 0.11$	-0.10 ± 0.15	$\cdots$	$+0.13 \pm 0.08$

3.4.3 Limits on Electron Densities in Ca II Absorbing Gas

The improvement in signal to noise which results when forming composite spectra allows us to derive some constraints on the electron density of the absorbing gas. Under ionization equilibrium, the balance between a neutral element X and a singly ionized element X^+ is

$$\frac{n(X^+)}{n(X^0)} = \frac{\Gamma}{\alpha(T)n_e} \tag{3.3}$$

where n(X) denotes the volume density of X, Γ is the photoionization rate of X to X^+, α is the temperature-dependent recombination coefficient to form X^0 from X^+, and n_e is the electron density. For gas of uniform density this can also be expressed using column densities by replacing $n(X)$ and $n(X^+)$ with the column densities $N(X)$ and $N(X^+)$, respectively (e.g., Prochaska, Chen & Bloom 2006). In principle, constraints on n_e could be obtained using observations of Fe, Ca, and Mg transitions. However, except for Mg I, no transitions from a neutral atom are observed at $\geq 2\sigma$ in the composite. Also, the Ca II and Mg II doublet ratios show some indications of saturation. Therefore, the most conservative way to place constraints on n_e is to use column density results derived from the observed Fe II lines and the absence of observed Fe I. These column density results are reported in Table 3.5.

The frequency integral of the product of the Fe photoionization cross section (Verner et al. 1996) and the local UV background (Mathis, Mezger, & Panagia 1983) yields $\Gamma = 1.9 \times 10^{-10}$ s^{-1}. The total (radiative+dielectronic) recombination coefficient for Fe^{+1} is $\alpha = 7.2 \times 10^{-13}$ cm^3 s^{-1} at T= 10^4 K (Mazzotta et al. 1998; Verner 1999). Using the measurements of the $N(Fe^0)/N(Fe^{+1})$ ratio inferred from Table 3.5 yields a 2σ upper limit of $n_e \lesssim 0.1$ cm^{-3} for the full sample and weak absorber subsample, and $n_e \lesssim 0.3$ cm^{-3} for the strong absorber subsample. The electron density upper limit of our full Ca II absorber sample is in good agreement with higher-quality observations of individual absorbers by Nestor et al. (2008) and Zych et al. (2009). Such limits on n_e may imply hydrogen densities suitable for molecular gas (Zych et al. 2009; Nestor et al. 2008; Srianand et al. 2005).

3.4.4 Dust in Ca II Absorbing Gas

The average extinction and reddening of Ca II absorbing gas can be derived by forming composites using the geometric mean of unnormalized flux spectra. This is done for the full sample of Ca II absorbers and the four subsamples. The approach we take to form these composites is similar to the one taken in York et al. (2006). That is, when we construct a composite using Ca II absorber flux spectra, we also construct an unabsorbed reference composite.

Specifically, we define a non-absorber match for every Ca II absorber in the sample. The match is determined using the quasar SDSS i-band magnitude and emission redshift z_{em}. To find a match, we formed a list of all SDSS quasars up to DR9 with $z_{em} > 0.1$ and $i < 20$ mag. We then eliminated those quasars with known intervening Mg II absorption (Quider et al. 2010; Monier et al., in prep, *private communication*), Ca II absorption (Chapter 2), or broad absorption lines (Shen et al. 2011). A tentative match between a Ca II absorber spectrum and an unabsorbed quasar spectrum is then determined by finding an unabsorbed quasar that lies closest to the absorbed quasar in $\Delta i/<i> -\Delta z_{em}/<z_{em}>$ space, where Δi and Δz_{em} represent differences between the absorbed and matching unabsorbed quasar properties.

Initial matches are accepted for those with $|\Delta i| \leq 0.20$ and $|\Delta z_{em}| \leq 0.01$ since we found it especially important to have similar emission features in both spectra. However, we also visually inspected initial matches for any missed absorption transitions because their presence in the unabsorbed list has the potential to cause extra extinction/reddening in the "unabsorbed" quasar spectrum and affect our analysis. In addition, we checked for other issues such as broad intrinsic Fe II emission in the matched unabsorbed quasar spectra, which may lead to significant unmatched broad features in individual absorbed and unabsorbed spectra.

When these types of problems occurred, we removed the quasar from the unabsorbed quasar list and re-ran the matching process until a satisfactory match was found. In the end, we found that it was not possible to find a suitable match with $|\Delta i| \leq 0.2$ and $|\Delta z_{em}| \leq 0.01$ for 41 of our Ca II absorbers, which is $\sim 10\%$ of our full sample. We did accept seven of

those 41 since the matches were not too discrepant. Figure 3.7 illustrates the distribution of Δi and Δz_{em} for our final matches. Red points mark the seven closer outliers which just missed matching our search criteria but were included. Figure 3.8 illustrates an example case of an individual Ca II absorber and its match. Fifty per cent of the final matches are within $|\Delta i| \leq 0.014$ mag and $|\Delta z_{em}| \leq 0.001$, and the median and average values of the distributions of Δi and Δz_{em} are indistinguishable from zero. Thus, in the end, the numbers of spectra used to form the flux composite spectra were less than those used to form the normalized composite spectra (Table 3.3). Yet we point out that, even with these precautions, forming a normalized composite is an inherently more robust process because undulations in the pseudo-continuum due to both weak and strong emissions are fitted and removed by the normalization, but this does not happen when forming a flux composite. This is most troublesome when the number of individual spectra forming a flux composite at the shortest rest wavelengths becomes small.

To assess extinction and reddening we are interested in comparing the Ca II absorber fluxed composite continuum (which is in the rest frame of the absorber) to the unabsorbed reference continuum. To this end, we constructed the composites for our extinction analysis by taking the geometric mean of those Ca II absorbed spectra which have suitable unabsorbed matches, hence we used 401 sets of absorbed-unabsorbed spectra. A quasar continuum generally follows a power-law and the geometric mean of a set of power-law spectra preserves the average power-law index. Therefore, this is an appropriate method to use to determine the average extinction law, which is also likely to be similar to a power-law.

To form a fluxed composite each Ca II absorbed quasar spectrum and its match were shifted to the absorber rest frame after rebinning to a wavelength scale that was one-tenth of the original pixel size in order to make the registration of spectra accurate. The final composites were then rebinned to a wavelength scale of 1 Å per pixel in the rest frame. The standard deviation, $\sigma_{\lambda,g}$, in the geometric mean is given by

$$\ln \sigma_{\lambda,g} = \sqrt{\frac{1}{N}\sum_{i=1}^{N}\left[\ln\left(\frac{f_{\lambda,i}}{\mu_{\lambda,g}}\right)\right]^2} \tag{3.4}$$

where $\mu_{\lambda,g}$ is the geometric mean of N fluxes and $f_{\lambda,i}$ are the individual spectrum fluxes as

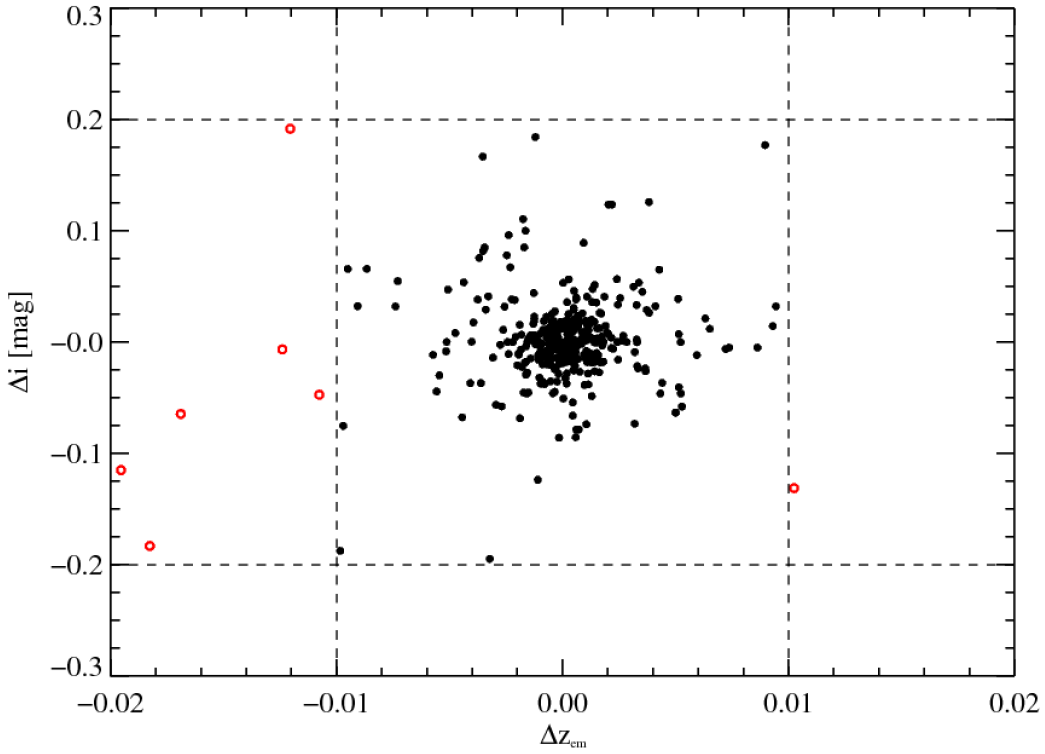

Figure 3.7: The Δi - Δz_{em} space for the final Ca II absorber and non-absorber matches. The dashed lines depict our initial match search box criteria. Suitable matches were found for 401 absorbers including the near matches shown as red open circles which we used.

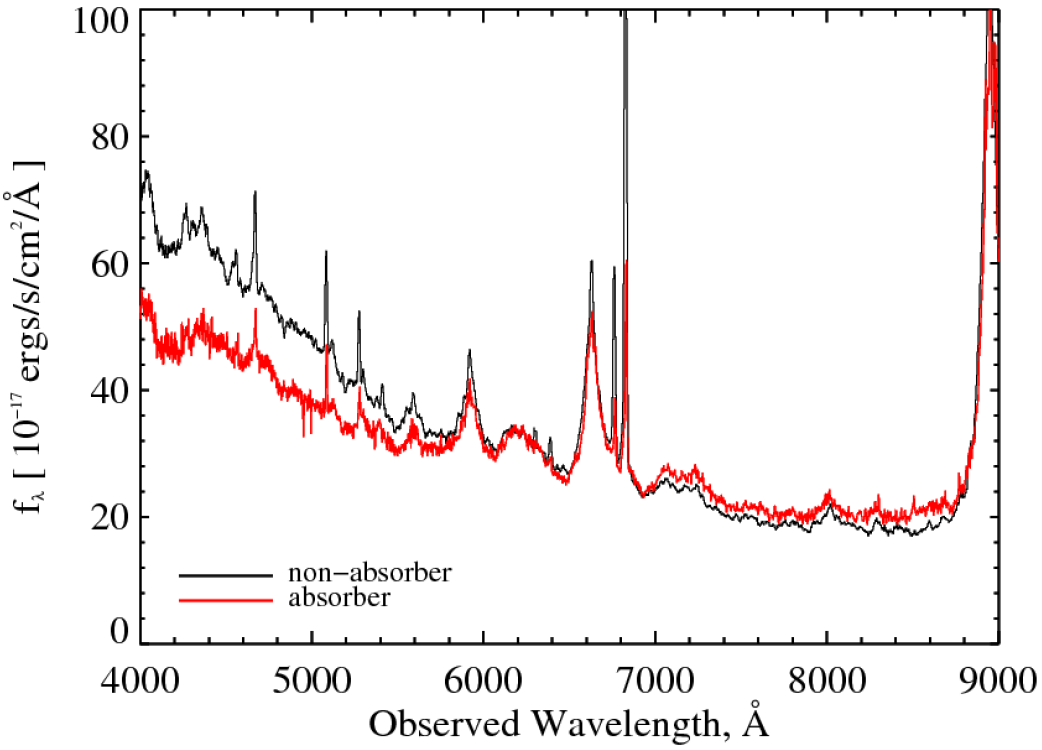

Figure 3.8: An example Ca II absorber spectrum and its non-absorber spectrum match. In this case $|\Delta i| = 0.01$ and $|\Delta z_{em}| = 0.001$.

a function of wavelength (Kirkwood 1979). The top panel of Figure 3.9 shows the matched composites for the full sample, with the Ca II absorber sample in red and the unabsorbed reference sample in blue. Figures 3.10-3.11 illustrate this in the four subsamples (see §3.5 discussion.) The errors in the full sample composite typically lie in the range $1.8-2.2\times10^{-17}$ ergs cm^{-2} s^{-1} Å^{-1} level. Prominent absorption features from transitions of Fe II, Mg II, Mg I, and Ca II are clear in the Ca II absorber composite. The bottom panel shows the flux ratios between the absorbed and unabsorbed composites. Overlaid are extinction model fits to the data: the magenta dashed line shows a LMC-like dust model (Gordon et al. 2003), the solid green line shows a SMC-like model (Gordon et al. 2003), and the dashed-dot cyan lines show a standard Milky Way (MW) model (Fitzpatrick 1999). All fits have been made over a wavelength range $\geq$ 2500 Å to ensure more uniform noise characteristics across the wavelength range when performing the fits; absorption lines were masked out when making the fits.

In Table 3.8 we summarize the modeled or observed absorbed-to-unabsorbed flux ratios at $\lambda_{rest} = 2200$ Å, $\mathcal{R}$, and color excesses, $E(B-V)$, for the full sample and four subsamples. For the full sample the observed $\mathcal{R}$ is 0.83, which is best matched by either the LMC or SMC; the color excess is inferred to be $E(B-V) \approx 0.03$. Over the fitted range ($\lambda > 2500$ Å) the LMC and SMC models are nearly indistinguishable, while the MW dust law is definitely ruled out. As can be seen from Figures 3.10 and 3.11, due to a combination of smaller sample sizes and/or lower extinction, ruling out the MW extinction law becomes difficult for all subsamples except the $W_o^{\lambda3934} \geq 0.7$ Å subsample. Wild et al. (2006) concluded that an LMC extinction law applied to the Ca II sample of absorbers that they studied, however, with a color excess that is two to five times higher. Nevertheless, the results presented here are consistent with earlier studies that the strong Ca II absorbers are among the dustiest absorber systems, and are likely to be DLAs (Wild et al. 2006; Zych et al. 2009). We also note for comparison that an SMC-like extinction curve with $E(B-V) < 0.02$ mag has been inferred using DLA and Mg II samples (Murphy & Liske 2004; York et al. 2006; Vladilo, Prochaska & Wolfe 2008).

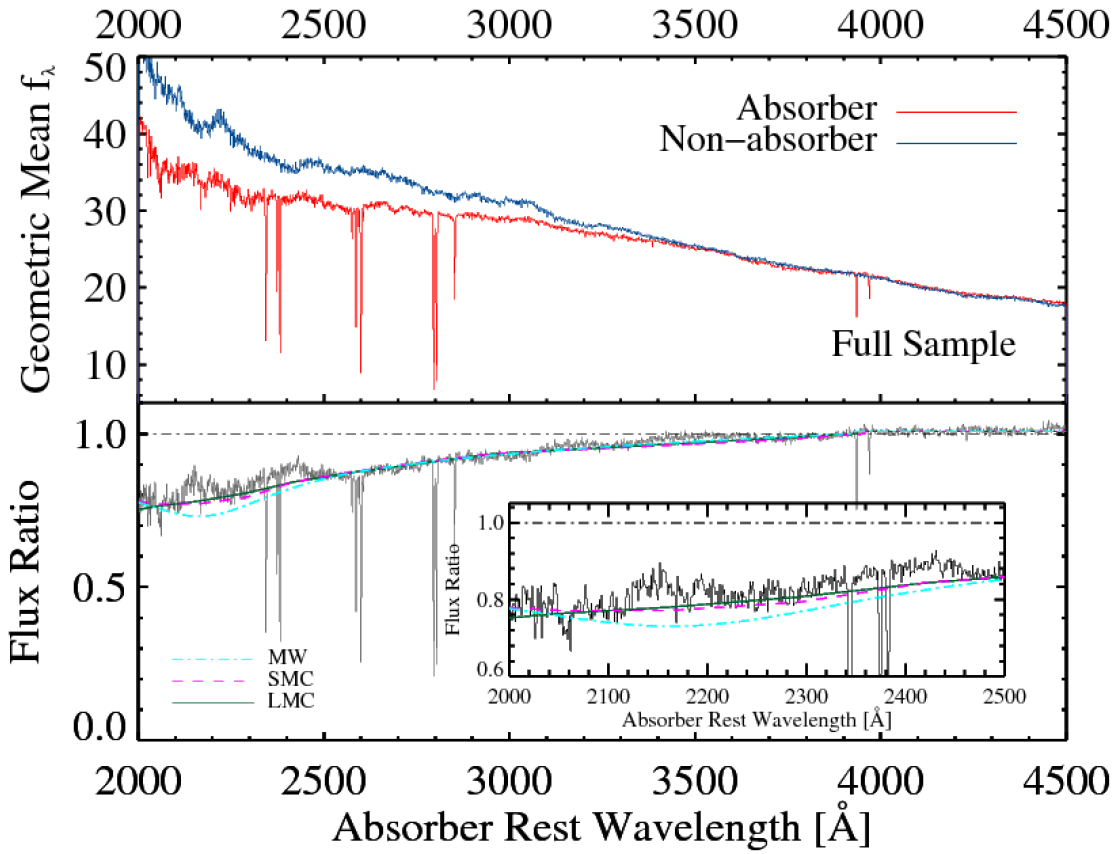

Figure 3.9: *Top:* The geometric mean rest-frame composites for the Ca II absorbers (red) and the unabsorbed reference sample (blue) derived using the full sample. Clearly visible in the absorber composite are the narrow absorption lines from Fe II, Mg II, Mg I, and Ca II. *Bottom:* The ratio of the absorber composite to the unabsorbed reference composite. Least-squares fits of dust models derived from the LMC (dashed line in magenta), SMC (solid line in green), and Milky Way (MW) (dashed-dot line in cyan) are also shown. The LMC and SMC dust laws both provide good fits to the observe extinction, with $E(B-V) \approx 0.03$. The LMC and SMC fits are nearly indistinguishable.

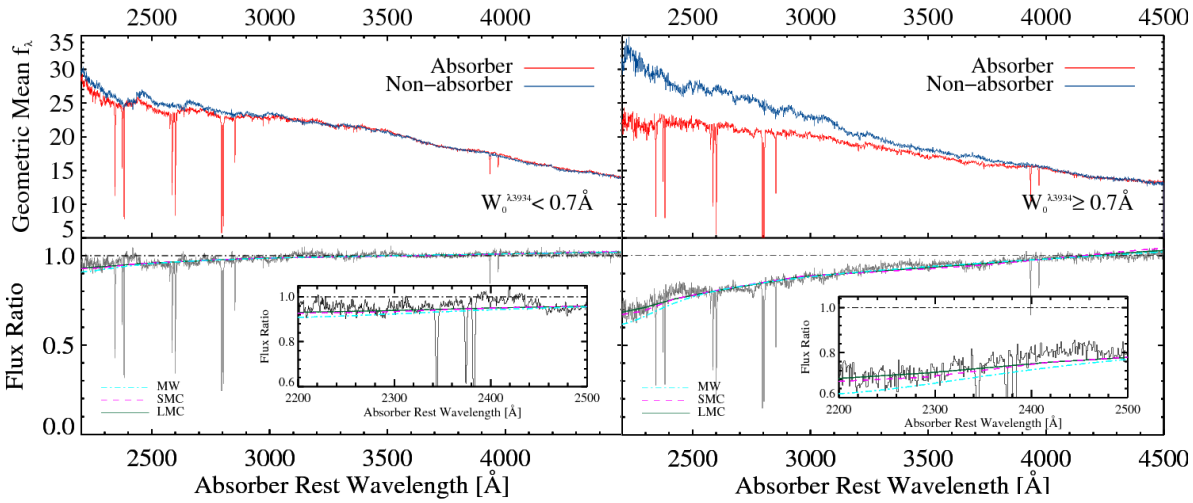

Figure 3.10: Same as Figure 3.9, but showing the results for the $W_0^{\lambda 3934} < 0.7$ Å subsample (left side) and $W_0^{\lambda 3934} \geq 0.7$ Å subsample (right side).

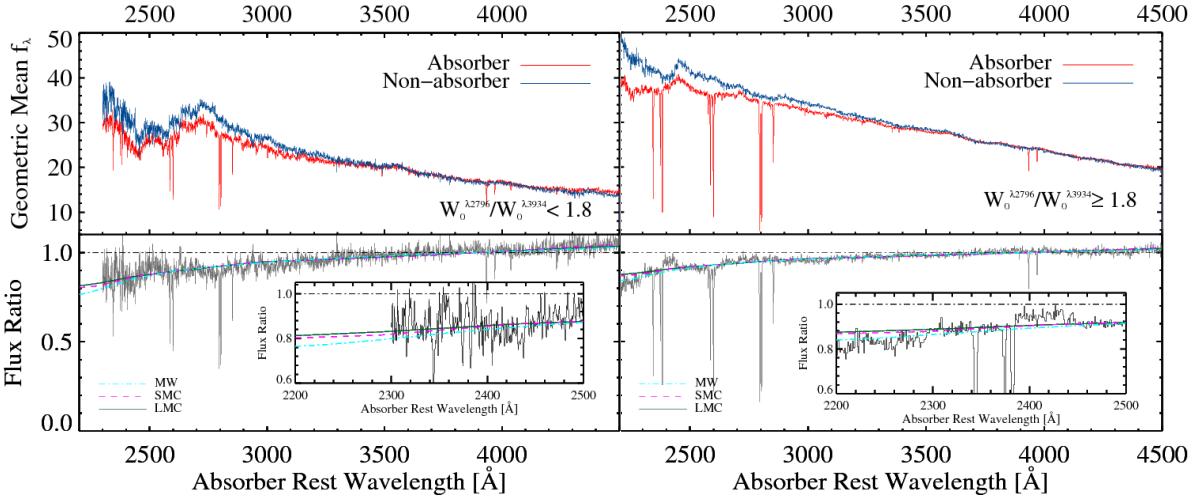

Figure 3.11: Same as Figure 3.9, but showing the results for the $W_0^{\lambda 2796}/W_0^{\lambda 3934} < 1.8$ subsample (left side) and $W_0^{\lambda 2796}/W_0^{\lambda 3934} \geq 1.8$ subsample (right side).

3.5 IMPLICATIONS OF THE RESULTS FOR CA II ABSORBER POPULATIONS USING THE SUBSAMPLES

As indicated at the beginning of §3.4, in Chapter 2 we found that while Ca II absorbers are rare, they are unlikely to represent a single type or population of absorber. The $W_0^{\lambda 3934}$ distribution requires a two-component exponential to satisfactorily fit the data, hinting at the existence of at least two distinct populations. This persists across our survey redshift interval, $z_{abs} \lesssim 1.4$. Upon further analysis of the Ca II survey data, it was also shown that when the Mg II properties of these Ca II absorbers are taken into account, it is possible to more clearly separate the Ca II absorbers into two populations at the $> 99\%$ confidence level. In this section we investigate whether the chemical and dust depletion properties of subsamples of Ca II absorbers are consistent with the statistical evidence for two populations.

To do this, we divide the full sample into four subsamples, and we analyze the subsamples in the same way we analyze the full sample as discussed in §3.4. The tabulations of results and the figures on subsamples are in Tables 3.3-3.7 and Figures 3.3-3.6 and 3.10-3.11. Recall (Chapter 2 and §3.4) that we divide the full sample as follows. Two subsamples were formed by separating the full sample at $W_0^{\lambda 3934} = 0.7$ Å, which results in ~ 200 Ca II absorbers in each. This is also the separation which exhibits the maximum difference between two populations from KS tests. We also form two more subsamples by separating the full sample at $W_0^{\lambda 2796}/W_0^{\lambda 3934} = 1.8$, but only 29 Ca II absorbers have $W_0^{\lambda 2796}/W_0^{\lambda 3934} < 1.8$. Finally, we note that we also performed an analysis by dividing the $W_0^{\lambda 3934}$ distribution into four subsamples of equal size. This produces results that are consistent with dividing the $W_0^{\lambda 3934}$ distribution into two subsamples, but with appropriately larger errors, as expected. We determined that there was not anything reliable to be learned by pursuing this.

Figures 3.3 and 3.4 show the normalized composite spectra of the two subsamples of Ca II absorbers separated at $W_0^{\lambda 3934} = 0.7$ Å. The measurements of the equivalent widths are reported in Table 3.4. The corresponding ionic column densities derived from unsaturated lines of Cr II, Zn II, Fe II, Ni II, and Mn II are tabulated in Table 3.5. Estimates on the abundance ratios relative to Zn and Fe are inferred in Tables 3.6 and 3.7, assuming no ionization corrections. The results clearly indicate that the two subsamples separated at

$W_0^{\lambda 3934} = 0.7$ Å reveal the existence of two broadly defined populations of Ca II absorbers in terms of their element abundance ratios and depletion measures, although there is likely some cross-mixing between the two populations given the crude way they were separated. However, the two subsamples formed by separating the full sample at $W_0^{\lambda 2796}/W_0^{\lambda 3934} = 1.8$ do not allow us to draw a similar type of conclusion because only 29 Ca II absorbers have $W_0^{\lambda 2796}/W_0^{\lambda 3934} < 1.8$ and only five spectra contribute to the flux composite below ~ 2300 Å, which compromises the accuracy of this particular measurement. Results from the $W_0^{\lambda 2796}/W_0^{\lambda 3934} \geq 1.8$ subsample are very similar to $W_0^{\lambda 3934} < 0.7$ Å results.

Figures 3.10 and 3.11 illustrate the extinction and reddening results for the four subsamples. A tabulation of observed results and best-fit extinction laws are given in Table 3.8.

Figure 3.12 shows the log of the abundance ratios of Si, Mn, Cr, Fe, Ni, and Ti relative to Zn, as measured with respect to solar values. The elements on the x-axis are ordered left-to-right in increasing condensation temperatures. Filled symbols are Galactic abundance measurements for the halo (green squares), cold disk (brown circles), and warm disk (red diamonds) obtained from the compilations of Welty et al. (1999). The halo + disk (blue triangles) abundances are taken from Savage & Sembach (1996). Measurements pertaining to Ca II absorbers with $W_0^{\lambda 3934} < 0.7$ Å are shown as filled green circles while those with $W_0^{\lambda 3934} \geq 0.7$ Å are blue asterisks; results for Ca II absorbers with $W_0^{\lambda 2796}/W_0^{\lambda 3934} \geq 1.8$ are shown as filled orange triangles and are seen to be very similar to the $W_0^{\lambda 3934} < 0.7$ Å results; the $W_0^{\lambda 2796}/W_0^{\lambda 3934} < 1.8$ results are not shown due to their poor accuracy. We also draw attention to Figure 3.1, which includes our individual Ca II absorber results and results from earlier work.

The stronger Ca II absorber subsample ($W_0^{\lambda 3934} \geq 0.7$ Å) is seen in Figure 3.12 to be similar to the halo + disk component in terms of both chemical enrichment and element depletions on to dust grains. This conclusion is consistent with both the best-fit LMC or SMC dust extinction laws for our stronger Ca II absorber subsample (right panel of Figure 3.10). This is our most heavily reddened subsample, with an absorbed-to-unabsorbed flux ratio at 2200 Å of $\mathcal{R} = 0.73$ (Table 3.8). A MW extinction law is clearly ruled out for the stronger Ca II absorber subsample. However, the weaker Ca II absorber subsample ($W_0^{\lambda 3934} < 0.7$ Å)

is seen to have chemical enrichment and element depletion characteristics of the warm halo component, and there is much less reddening due to dust extinction (left panel of Figure 3.10 and Table 3.8), with $\mathcal{R} = 0.95$. Calculating the optical depths from the flux ratios indicates that the stronger Ca II absorbers are nearly six times more reddened than the weaker absorbers.

In comparison to expected nucleosynthetic effects and the errors in our measurements, Figure 3.12 reveals that depletion of elements to form dust grains is the dominant physics observed in the Ca II absorber normalized composite spectra; studies of the details of nucleosynthetic processes are probably better accomplished using high-resolution, high signal-to-noise observations of individual Ca II absorbers. In particular, Figure 3.12 shows that elements with larger condensation temperatures have generally greater depletion levels (Field 1974), and indicates a clear progression of increasing depletions, consistent with moving from halo regions toward cooler disk regions. The differences likely provide clues on the physical processes that transport and form/destroy gas and dust in the ISM and CGM of galaxies. The depletion patterns may be indicative of severe destruction of dust grains in the halo clouds than in the disk clouds, which may result from either more frequent or more severe shocking of the halo clouds compared with disk clouds (Savage & Sembach 1996), as supported by direct comparisons of the halo cloud abundances with those in strongly shocked environments (Jenkins & Wallerstein 1996).

We should add some comments about depletion results for Ca II absorbers from other authors. Using a smaller sample, Wild et al. (2006) compared the depletion patterns of refractory elements (Mn, Cr, Fe, and Ti) to that of the warm and cold disks of the MW; they formed two subsamples separated at $W_0^{\lambda 3934} = 0.68$ Å. Consistent with our findings, their results show that the depletion pattern for Ca II absorbers is inconsistent with that of the cold disk of the MW. They also find that Ca II absorbers with $W_0^{\lambda 3934} > 0.68$ Å have depletions that approach or exceed those of the warm disk of the MW. In comparison, we find weaker depletion levels for our strong Ca II absorbers compared to the MW's warm disk phase and, as shown in Figure 3.12, our results are consistent with halo+disk-like depletions. Results from Nestor et al. (2008) indicate that the [Cr/Zn] ratios for their sample of 22 Ca II absorbers (of which 16 are subDLAs and six are DLAs) are similar to the values seen along

sightlines sampling the MW halo. The more recent study by Zych et al. (2009) found similar results, as inferred from the [Fe/Zn] ratios of their sample of 19 Ca II absorbers. We note, however, that the Ca II absorber sample from both studies consisted of weak absorbers. In particular, the Nestor et al. (2008) sample has only a single absorber with $W_0^{\lambda 3934} > 0.7$ Å, while Zych et al. (2009) has three. Thus, our conclusions on the depletions for the weak absorbers generally agree with earlier results.

From the analysis of depletion measures and velocity profiles of 19 Ca II absorbers ($W_0^{\lambda 3934} > 0.2$ Å), Zych et al. (2009) suggested that there might be two distinct scenarios giving rise to Ca II absorbers, with one being a low-impact-parameter sightline passing through a quiescent galaxy disk, and the other being a sightline passing through more disturbed and complex environments such as outflows, mergers, or galaxy clusters. Moreover, Richter et al. (2011) concluded that the majority of their sample of 23 Ca II absorbers (with $W_0^{\lambda 3934} \lesssim 0.8$ Å) trace neutral and partly ionized gas in clouds in the halos and circumgalactic environments of galaxies. Hence, the two-population picture for Ca II absorbers is apparent even with smaller data sets. Our results on chemical depletion and reddening suggest that stronger absorbers are likely to be associated with low impact parameter, disk-like environments, while the weaker absorbers are likely to be associated with larger impact parameter environments more typical of galactic halos. We will explore this further in Chapter 4.

Finally, we emphasize again that previous studies of the stronger Ca II absorption systems have been very limited until now. In the future it will be important to explore the properties of individual Ca II absorbers (especially the stronger ones) with high-resolution spectroscopy in order to measure their kinematics and better characterize their chemistry.

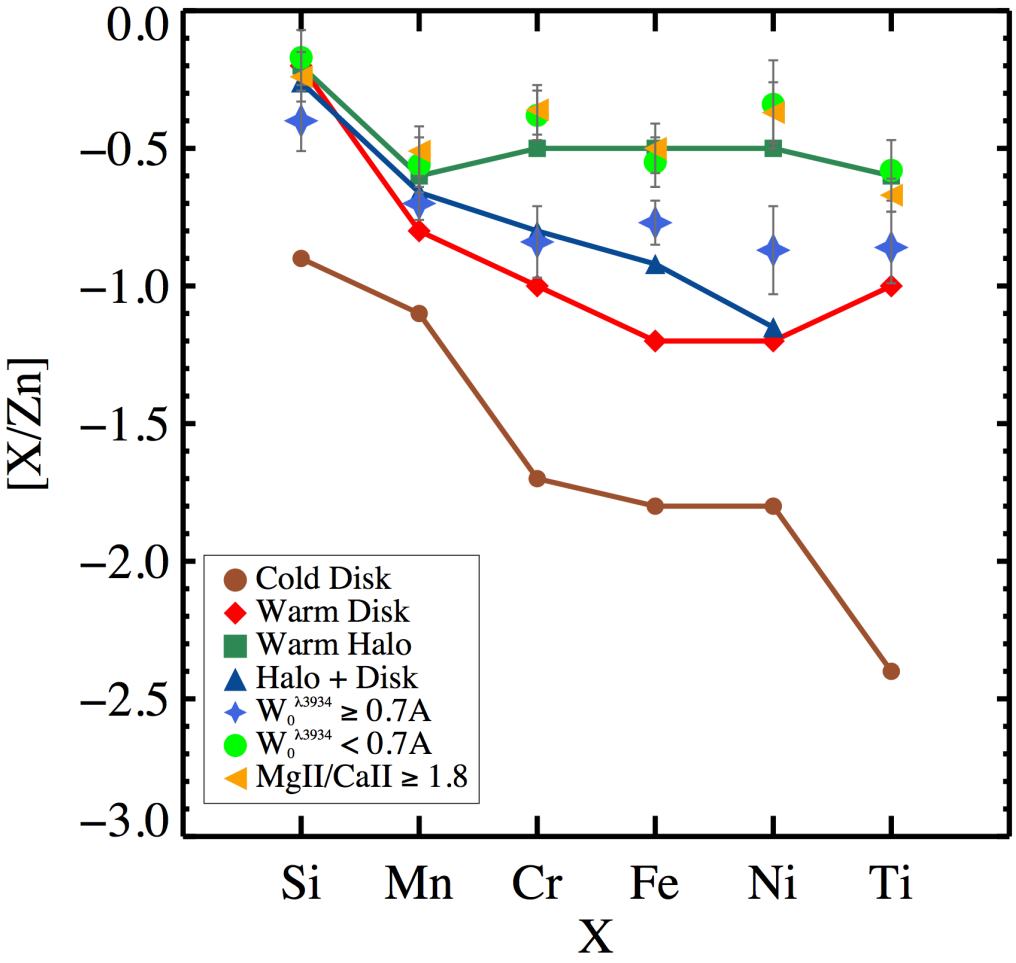

Figure 3.12: Element abundance ratios relative to Zn for three Ca II absorbers subsamples: (1) $W_0^{\lambda 3934} < 0.7$ Å, (2) $W_0^{\lambda 3934} \geq 0.7$ Å, (3) and $W_0^{\lambda 2796}/W_0^{\lambda 3934} \geq 1.8$. The Ca II absorber subsample with $W_0^{\lambda 2796}/W_0^{\lambda 3934} < 1.8$ is not shown because of the small number of absorbers (and large error bars) that pertain to this subsample. The elements are arranged in order increasing condensation temperature. For comparison, and as described in the text, also shown are abundance ratio compilations for cold disk gas, warm disk gas, disk + halo gas, and warm halo gas (Welty et al. 1999; Savage & Sembach 1996).

Table 3.8: Results on extinction and reddening for the full sample and four subsamples of Ca II absorbers. Parameters are given for the best-fit LMC, SMC, and MW extinction laws applied to the fluxed Ca II absorber composite spectra, relative to the unabsorbed reference composite spectra, at $\lambda_{rest} \geq 2500$ Å. The parameter $\mathcal{R}$ is the absorbed-to-unabsorbed flux ratio at 2200 Å. For the Ca II absorber (sub)samples $\mathcal{R}$ is observed. For the best-fit extinction models $\mathcal{R}$ is predicted.

	Full Sample		$W_0^{\lambda 3934} < 0.7$Å		$W_0^{\lambda 3934} \geq 0.7$Å		$W_0^{\lambda 2796}/W_0^{\lambda 3934} < 1.8$		$W_0^{\lambda 2796}/W_0^{\lambda 3934} \geq 1.8$	
Dust Law	$E(B-V)$	$\mathcal{R}$	$E(B-V)$	$\mathcal{R}$	$E(B-V)$	$\mathcal{R}$	$E(B-V)$	$\mathcal{R}$	$E(B-V)$	$\mathcal{R}$
...	[mag]	...	[mag]	...	[mag]	...	[mag]	...	[mag]	...
LMC	0.029	0.80	0.011	0.93	0.048	0.67	0.029	0.80	0.018	0.87
SMC	0.024	0.81	0.009	0.93	0.040	0.69	0.024	0.81	0.015	0.87
MW	0.026	0.75	0.010	0.90	0.043	0.62	0.025	0.77	0.016	0.84
Ca II Sample	-	0.83	-	0.95	-	0.73	-	...	-	0.83

3.6 SUMMARY AND CONCLUSIONS

We have used statistical results on the 435 Ca II absorbers identified in SDSS quasar spectra (Chapter 2) to derive results on their element abundance ratios and dust properties. In contrast to earlier studies, this new large sample includes a large number ($\approx$ 200) of $W_0^{\lambda3934} \geq 0.7$ Å Ca II absorbers at redshifts $z_{abs} < 1.4$. We present results on a number of individual Ca II absorption systems in Tables 3.1 and 3.2. More importantly, by median-combining > 400 normalized spectra for the full sample and four subsamples, we have formed high signal-to-noise normalized composite spectra and used them to detect (or place limits on) low-ionization metal lines due to Si II, Fe II, Co II, Zn II, Cr II, Fe I, Si I, Mn II, Mg II, Mg I, Ni II, Ti II, Ca II and Na I, as included within the redshifted spectral coverage of the SDSS spectrograph. These have been used to investigate element abundance ratios in Ca II absorbers. We also formed Ca II absorber fluxed composite spectra and matching unabsorbed fluxed composite spectra of the full sample and four subsamples to investigate extinction and reddening in Ca II absorbers.

We tested a hypothesis put forth in Chapter 2. Namely, that the sensitivity-corrected $W_0^{\lambda3934}$ distribution of Ca II absorbers follows a shape that is suggestive of at least two populations of Ca II absorbers, separated at $W_0^{\lambda3934} = 0.7$ Å. We therefore hypothesized that analysis of two subsamples divided at $W_0^{\lambda3934} = 0.7$ Å would allow us to reveal the nature of these two populations, and this turned out to be the case. We also showed in Chapter 2 that by using information on Mg II in Ca II absorbers we could statistically infer the presence of two populations divided at $W_0^{\lambda2796}/W_0^{\lambda3934} = 1.8$, but unfortunately only 29 Ca II absorbers are in the subsample with $W_0^{\lambda2796}/W_0^{\lambda3934} < 1.8$, so we could not make an accurate comparison of these other two subsamples using this criterion.

Because of our findings, in what follows we will refer to the $W_0^{\lambda3934} \geq 0.7$ Å absorbers as the strong Ca II absorbers, and the $W_0^{\lambda3934} < 0.7$ Å absorbers as the weak Ca II absorbers.

Analysis of the element abundance ratios derived for Si, Mn, Cr, Fe, Ni, and Ti relative to Zn using normalized composite spectra indicate that the abundance pattern of the strong Ca II absorbers is intermediate between disk- and halo-type gas (see Figure 3.12). The results indicate more significant depletions of the highly refractory elements of Cr, Fe, Ni, and Ti in

the strong Ca II absorbers. In addition, independent of the absorption line analysis, which was based on normalized composites, an investigation of the extinction and reddening in the strong Ca II absorbers using the ratio of the absorbed-to-unabsorbed composite fluxed spectra shows that they are a significantly reddened population of absorbers, with the absorbed-to-unabsorbed composite flux ratio at $\lambda_{rest} = 2200$ Å being $\mathcal{R} \approx 0.73$ and $E(B-V) \approx 0.046$, consistent with a LMC or SMC dust law (right hand panel of Figure 3.10 and Table 3.8). Our data do not allow us to distinguish between an LMC versus SMC reddening law.

At the same time, we showed that the weak Ca II absorbers have an abundance pattern typical of halo-type gas with less depletion of the highly refractory elements of Cr, Fe, Ni, and Ti (also Figure 3.12). Again independent of the absorption line analysis, we find that the weak Ca II absorbers are nearly six times less reddened than the strong Ca II absorbers, with $\mathcal{R} \approx 0.95$ and $E(B-V) \approx 0.011$ (left hand panel of Figure 3.10 and Table 3.8).

Thus, the results of this analysis have confirmed the hypothesis that at least two populations of Ca II absorbers exist, consistent with the statistical evidence in Chapter 2. Thanks to the high-signal-to-noise composite spectra, we were able to identify the striking differences in the element abundance ratios, depletion patterns, and dust extinction and reddening properties of the two populations of Ca II absorbers divided at $W_0^{\lambda 3934} = 0.7$ Å. In Chapter 4 we will explore the association between Ca II absorbers and galaxies.

4.0 Ca II ABSORBERS IN THE SLOAN DIGITAL SKY SURVEY: GALAXIES

4.1 INTRODUCTION

Chapter 4 is the third in a series of papers based on our survey for Ca II $\lambda\lambda 3934, 3969$ absorption-line systems in the Seventh and Ninth data releases of the Sloan Digitial Sky Survey (SDSS; Schneider et al. 2010; Ahn et al. 2012). In the first paper, Sardane, Turnshek & Rao (2014; hereafter Paper I; also thesis Chapter 2), we discussed details of the survey and presented our sample of 435 Ca II absorbers. The survey covered the redshift range $z < 1.34$ and included rest equivalent widths $W_0^{\lambda 3934} \geq 0.16$ Å. We also required that the stronger line of the doublet be detected at a $\geq 5\sigma$ level of significance and, at the same time, the weaker line be detected at a $\geq 2.5\sigma$ level of significance. We presented evidence for the existence of two distinct populations of Ca II absorbers. We found that the $W_0^{\lambda 3934}$ rest equivalent width distribution is better represented by a double exponential function rather than a single component, with a change in slope occurring at $W_0^{\lambda 3934} \approx 0.7 - 0.9$ Å and the weaker systems showing a steeper rise towards lower values of $W_0^{\lambda 3934}$. In the second paper, Sardane, Turnshek, & Rao (2015; hereafter Paper II; also thesis Chapter 3), we performed a spectral stacking analysis of Ca II absorbers that were divided into two roughly equal-sized subsamples with $W_0^{\lambda 3934}$ less than and greater than 0.7 Å. We found a significant difference in the dust-reddening and abundance patterns between the two composites; the strong absorbers with $W_0^{\lambda 3934} \geq 0.7$ Å are a factor of six times more reddened, and hence significantly more dusty, than the weak absorbers. The abundance pattern of weak systems was found to be consistent with Milky Way halo-type material (Savage & Sembach 1998). On the other hand, the stronger systems are more complex, with a composite abundance

pattern that is intermediate between disk and halo-type gaseous material.

In this chapter of the thesis, which is the third paper in the series, we present our results on the properties of galaxies associated with Ca II absorbers using imaging data from the SDSS. We first describe the properties of the galaxies that have been directly identified in the SDSS images as the most likely absorber. We then use an image stacking analysis (e.g., similar to Zibetti et al. 2007) to derive the surface brightness profiles of the light in the vicinity of the quasar sightlines with Ca II absorbers, which allows us to infer average differences in galaxy properties between the two populations of absorbers.

Prior to our work, Zych et al. (2009) had identified galaxies associated with Ca II absorbers that had $W_0^{\lambda 3934} \geq 0.2$ Å from imaging and spectroscopic observations using the FORS2 spectrograph on the Very Large Telescope. Their study consisted of a sample of five Ca II absorbers identified in the SDSS at redshifts $z_{abs} < 0.5$. In contrast to our survey for Ca II described in Paper I, their selection criteria required a line significance of $\geq 4\sigma$ for the λ3934 line and $\geq 1\sigma$ for the λ3969 line. A $\geq 6\sigma$-Mg II or $\geq 1\sigma$-Na I detection was also required. They found that these absorbers are associated with galaxies that are luminous ($L \sim L^{\star}$), have substantial star-formation, are metal rich ($Z \sim Z_{\odot}$), and have impact parameters $\lesssim 24$ kpc. K-band imaging of 30 strong Ca II absorber host galaxies at $z \sim 1$ by Hewett & Wild (2007) showed similar results. The absorbers were found to be preferentially luminous with a mean impact parameter of 24 kpc and a filling factor of only 10%. No associated galaxy was detected for approximately a third of the absorbers. However, the physical origin of these absorbers remains unclear, and includes a wide range of possibilities from very extended disks of luminous galaxies to associated dwarf galaxy neighbors, outflows, or cannibalism of tidal debris by smaller galaxies. A recent cross-correlation analysis of foreground galaxies with background quasars in the SDSS resulted in the suggestion that, for edge-on galaxies, bipolar outflows induced by star-formation is largely responsible for producing Ca II in the halos of galaxies (Zhu & Menard 2013). Furthermore, several authors have suggested that Ca II absorbers with $W_0^{\lambda 3934} \gtrsim 0.2$ Å may be a subclass of damped Lyman alpha (DLA) systems with higher neutral gas densities (Wild, Hewett & Pettini 2006; Nestor et al. 2008). Other investigations have indicated, however, that Ca II systems exhibit a variety of neutral hydrogen column densities, sometimes bearing H_2, have a range of dust-to-gas ratios and are

sometimes associated with environments giving rise to high-ionization metal lines (Zych et al. 2007; Richter et al. 2011; Crighton et al. 2013).

Having assembled the largest catalog of Ca II absorbers to date, we are now able to determine their properties in a statistically meaningful way. In Paper I we presented the rest equivalent width and redshift distribution of the absorbers. Paper II described their dust reddening and abundance patterns. And here in Paper III we present some results on the properties of the galaxies that are associated with the Ca II absorbers. The paper is organized as follows. In §4.2 we give a brief description of the Ca II absorber catalog, as well as the non-absorber samples used to form reference or control images for an image stacking analysis. In §4.3 we present some galaxies that are likely to host some of the absorbers. These are SDSS galaxies for which spectroscopic data are available and whose redshifts match those of the absorbers. Details on the image stacking technique, the construction of the image composites, the derivation of light profiles, and the inferred luminosity-weighted mean impact parameter of galaxies associated with Ca II absorbers are described in §4.4. In §4.5 we present our conclusions and discuss the implications of our results.

Hereafter, we refer to absorbers with $W_0^{\lambda 3934} < 0.7$ Å as "weak" Ca II absorbers, and those with $W_0^{\lambda 3934} \geq 0.7$ Å as "strong" absorbers. Throughout this paper we assume standard ΛCDM cosmological parameters of $\Omega_m = 0.27$, $\Omega_\Lambda = 0.73$, and $H_0 = 71$ km s^{-1} (Spergel et al. 2007; Komatsu et al. 2011).

4.2 THE DATA

4.2.1 The Ca II Absorber Catalog

The sample of Ca II absorbers that we use in this paper is derived from the catalog presented in Paper I. In this section, we briefly describe the Ca II dataset. The catalog consists of 435 Ca II absorbers identified from a search of over 95,000 quasar spectra from the Seventh (SDSS DR7, Shen et al. 2011) and Ninth (SDSS DR9, Pâris et al. 2012) data releases of the SDSS. Ca II absorption can be detected at redshifts $0 < z < 1.34$ in SDSS quasar spectra, tracing

back more than 8.5 Gyrs of cosmic time. The spectra of all quasars brighter than $i = 20$ mag were normalized using a pseudo-continuum and then searched for the Ca II$\lambda\lambda$3934, 3969 doublet feature. A positive detection was defined in terms of the significance levels of the strengths of the two absorption lines and the value of the doublet ratio. Specifically, under these criteria the rest equivalent widths (REWs) of accepted Ca II doublets had be significant at a $\geq 5\sigma$ significance level for the stronger line, λ3934, and at a $\geq 2.5\sigma$ significance level for the weaker line, λ3969. The doublets also needed to satisfy the doublet ratio (DR) criterion, which requires them to be within the physically allowed range of $1.0-\sigma_{DR} \leq DR \leq 2.0+\sigma_{DR}$. Profiles with $DR = 1$ are said to be fully saturated, in which case the REWs are sensitive to the velocity spread of the gas, while those with $DR = 2$ are fully unsaturated, in which case the strengths are proportional to the Ca^+ column density of the gas. Furthermore, only systems with a separation greater than 6000 km s^{-1} longward of the Lyα emission line were accepted into the catalog.

4.2.2 The Reference Non-Absorber Quasar Sample

In order to define a control sample for our image stacking analysis, we also needed to select a sample of quasars which had no absorbers detected in their spectra. This set of non-absorber quasar fields serves as a baseline for establishing background levels. The non-absorbers were selected using the matching algorithm described in York et al. (2006) and adopted in Paper II to compile our non-absorber set. In brief, each quasar in the absorber set is matched with a quasar containing no absorbers by minimizing the difference in their SDSS i magnitudes and emission redshifts, z_{em}. We refer the reader to Paper II for a complete discussion of the matching process. In this analysis, we use the same sample of absorber-non-absorber pairs as defined for the Paper II analysis.

4.3 DIRECT DETECTION OF ABSORBING GALAXIES

In this section, we present results from an examination of SDSS $r-$band images of quasar fields with the lowest redshift Ca II absorbers. We restricted the search to quasar fields with $z_{abs} \leq 0.4$ in order to concentrate on galaxies that lie within the primary redshift range of galaxies explored by the SDSS. The Ca II absorber sample has approximately 150 systems at redshifts $z \leq 0.4$. Of these, only 4 galaxies had spectroscopic redshifts that matched the redshift of the Ca II absorption systems and were within a search radius of 100 kpc from the quasar sightline. A primary reason for there being so few matches is the fact that spectroscopic fibers are placed at a minimum of 55 arcsec apart on any single SDSS plate. Thus, spectroscopic data for targets separated by less than 55 arcsec can exist only in overlapping plate regions. We were fortunate to have found 4 matches.

The properties of the absorbers and identified galaxies are tabulated in Table 4.1. Absolute magnitudes are calculated using K-corrections obtained as in Blanton & Roweis (2007), which uses the stellar population synthesis models of Bruzual & Charlot (2003) and the nebular emission-line models of Kewley et al. (2001). Ratios of the absolute luminosities of the galaxies relative to $L^\star$ were obtained using $M^\star$ values from Montero-Dorta & Prada (2009). In Figure 4.1, the Ca II absorption features are shown along the top row, with the Ca II absorption redshifts indicated on each panel. Solid red vertical lines indicate the location of the Ca II doublets. The second row shows the SDSS r-band postage-stamp images of the quasar-galaxy pairs. The blue arrows mark the location of the galaxies, while the red arrows point to the quasars. The images are labeled A through D to correspond to the row labels in Table 4.1. The galaxies, which have redshifts in the range $0.047 < z < 0.242$, have generally small impact parameters that range between 5 and 25 kpc. Galaxies A, B, and C are emission-line, star-forming galaxies according to the classification scheme in the SDSS database. At $z = 0.4$ 100 kpc corresponds to ~ 18.4 arcsec. The spectra of the four galaxies are shown in Figure 4.2.

The nature of the fourth galaxy, labeled D, is ambiguous. Here, we have a bright nuclear region embedded in an extended, low-surface brightness, fuzzy structure. The spectrum reveals that the galaxy is early-type, but with weak emission lines blended. Accounting

for K-corrections and using the de Vaucouleurs model magnitude tabulated in the SDSS photometric table, the luminosity of the spherical nuclear component (see Figure 4.1) is $6L^{\star}$. But the fiber and point spread function (PSF) magnitudes give a luminosity of $0.8L^{\star}$. It is likely that the model magnitude of this object is confused due to its blended morphology, giving the light profile an erroneously larger spread. We also note that this particular galaxy can be found in the Galaxy Zoo dataset (Lintott et al. 2011) with a morphology classification of "uncertain". Given the images and the spectrum, we suspect that this galaxy is a blend of two separate, but physically close structures, possibly a dwarf companion to the larger early-type galaxy dominating the spectrum. It is unlikely that the nuclear component is the absorber host. The absorber is more likely to be associated with the much fainter extended region, from which the weak emission lines seen in the spectrum of this object are likely to originate. We also note that upon adjusting the image contrast for this object as shown in Figure 4.3, we see signatures of what appear to be spiral arms and an additional faint nuclear component. The green arrow points to the possible spiral arm-like structure and the magenta arrow shows the location of a separate nuclear component. If this low-surface brightness galaxy is indeed the absorber, we estimate its physical extent to be ~ 96 kpc. Due to the ambiguity of the nature of the galaxy associated with this absorber, we have left the magnitudes and colors in Table 4.1 blank.

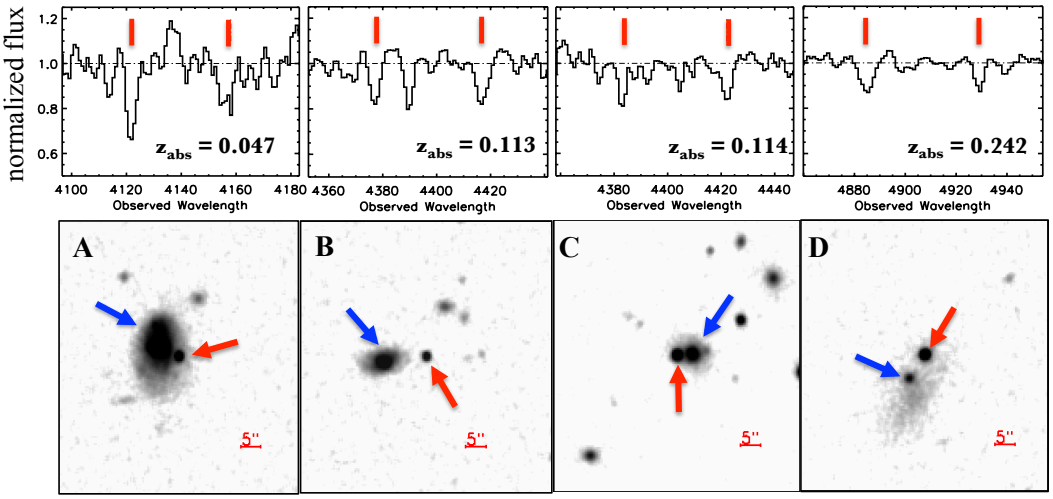

Figure 4.1: The luminous, low-impact parameter galaxies associated with Ca II absorption arranged in order of increasing redshift from left to right. See Table 4.1 for absorption and galaxy properties. *Top Row:* The Ca II absorption lines detected in the spectra of the four quasars. The absorber redshifts are indicated. Pairs of red vertical lines identify the two lines of the Ca II doublet. *Bottom Row:* Postage-stamp SDSS r-band images of the quasar fields corresponding to the Ca II absorbers in the top panel. Red arrows mark the location of the quasar, while blue arrows point to the location of the galaxy that has a spectroscopic redshift that matches that of Ca II. The scale of the image is also shown.

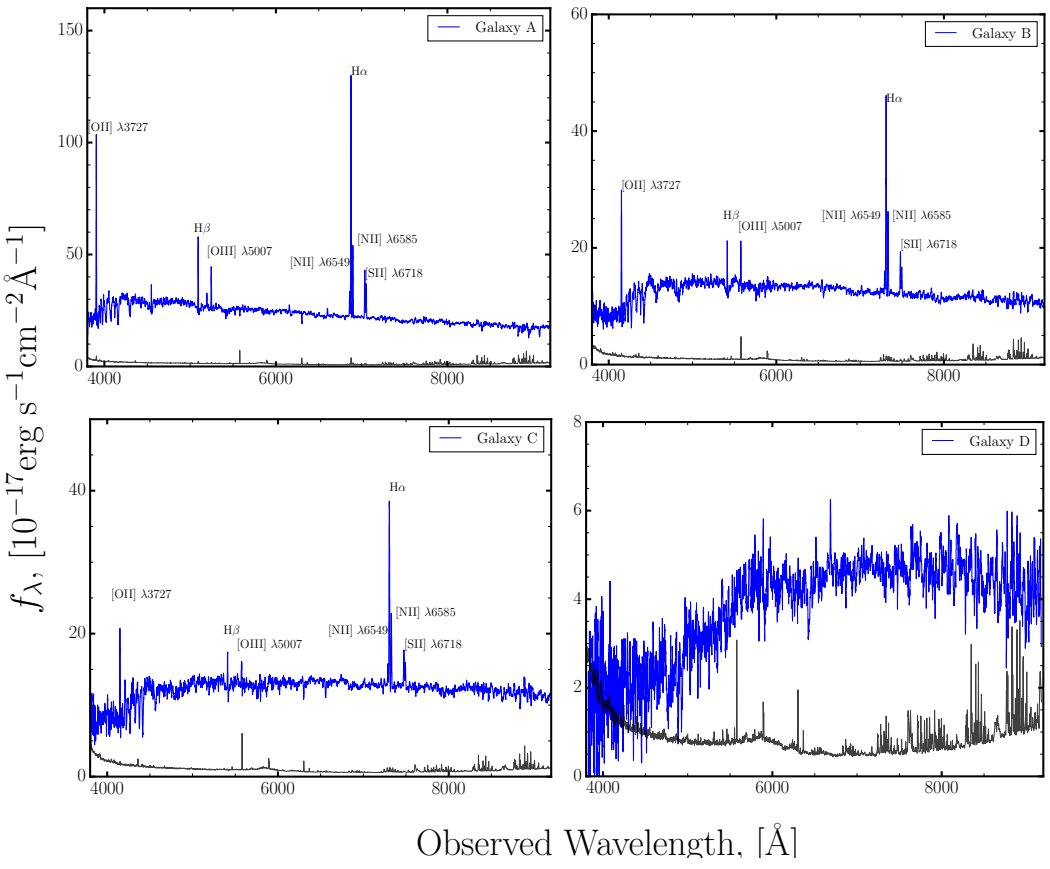

Figure 4.2: The SDSS spectra, shown in blue, of the four galaxies identified at the same redshift as the Ca II absorbers. For display purposes, the spectra are smoothed over five pixels. The error arrays are shown in black and prominent emission lines are labeled where applicable.

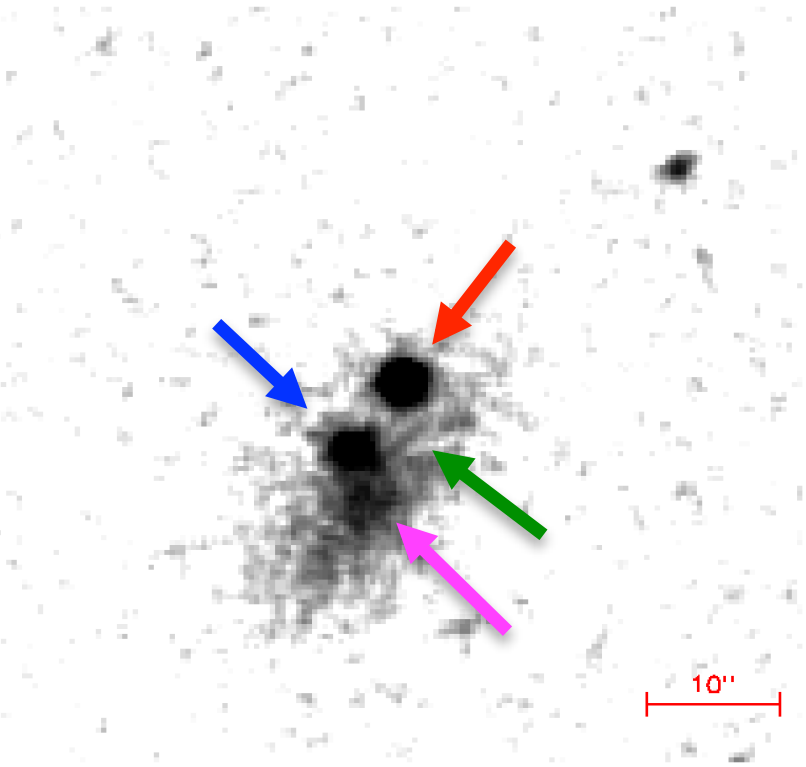

Figure 4.3: Galaxy D shown with enhanced contrast in comparison to Figure 4.1, revealing what appears to be a portion of a spiral arm (green arrow), and a faint nuclear component (magenta arrow).

Table 4.1: The four SDSS spectroscopic galaxies identified in the SDSS. A few percentage of Ca II absorbers identified in Sardane et al. (2014) are found to be associated to low-luminousity, low-impact parameter galaxies.

IAU Name	Image	z_{abs}	$W_0^{\lambda 3934}$	$W_0^{\lambda 3934}$	b	b	m_r	g-r	M_r	Luminosity	type
...	Label	...	Å	Å	arcsec	kpc	mag	mag	mag	$L^\star$	
J114719+522923	A	0.0475	1.327 ± 0.269	0.601 ± 0.173	5.4	5.0	18.8	0.37	-17.8	0.1	Starburst
J123401+002427	B	0.1125	0.518 ± 0.097	0.519 ± 0.097	10.3	21.3	19.4	0.64	-20.0	0.2	Star-Forming
J155752+342142	C	0.1140	0.598 ± 0.102	0.628 ± 0.168	3.7	7.7	18.1	0.57	-21.3	0.9	Star-forming
J141746+162512	D	0.2416	0.603 ± 0.110	0.479 ± 0.092	12.5	25.4	-	-	-	-	-

4.4 IMAGE STACKING ANALYSIS

4.4.1 Selection of the Images Used in the Composites

As shown by Zibetti et al. (2007) for Mg II absorbers, the approach of image stacking is an efficient way to statistically detect the excess of surface brightness around absorbed quasars relative to unabsorbed ones. The excess in the stacked light profile is assumed to be produced by galaxies associated with the absorbing systems. More specifically, this approach allows one to measure the spatial distribution of the light of the absorbing galaxies, from which the luminosity-weighted impact parameter distribution of the galaxies associated with the gaseous absorption can be derived. In this section, our goal is to uncover any differences in the surface brightness profiles between strong and weak Ca II absorbers that could provide more clues to the nature of the Ca II absorber populations.

We now describe the selection of images that will be included in the composite. The stacking and subsequent analysis are carried out using g as well r band images. We used the corrected (calibrated and sky-subtracted) imaging fields downloaded from the SDSS DR9 Science Archive Server (SAS) in SDSS-III FITS file format. Each SDSS field is 2048 $\times$ 1489 pixels, corresponding to $13' \times 10'$, and is uniquely identified by a run, camera column, and field number designation. We restrict our stacks to the absorber redshift ranges $0.2 \leq z_{abs} \leq 0.4$ and $0.4 < z_{abs} \leq 0.65$, which are large enough to include a statistically significant number of absorbers, yet small enough that the difference in pixel scales at the low and high redshift ends did not require unreasonably large rebinning at the lowest redshifts. Each SDSS image was examined for its quality within a 350 kpc radius around the quasar at the redshift of the absorber. Fields which contained highly saturated stars and large foreground galaxies that have negligible chance of being the galaxy at the redshift of the absorber were eliminated from the list to be stacked, since light from these sources overwhelmingly dominated these images. Each field was also required to have a minimum, uninterrupted area of 700$\times$700 square kpc, so that differences in depth and/or image quality of adjoining plates, if the quasar was near the edge of a plate, could be avoided.

The measurement of excess light in stacked images encounters sources of noise that come

Table 4.2: Number of fields included in the stacks.

z_{abs}	Number of Fields		
	$W_0^{\lambda 3934} < 0.7$ Å	$W_0^{\lambda 3934} \geq 0.7$ Å	Non-absorber
0.20 - 0.40	29	27	50
0.40 - 0.65	32	33	49

from intrinsic photon noise, the noise from foreground and background galaxies and foreground stars, and noise from the quasar light itself (Zibetti et al. 2007). The intrinsic photon noise is fixed by the number of images that are stacked and their depth. The contribution from background and/or foreground sources unrelated to the absorbers is somewhat alleviated by masking these sources out from the images. Appropriate subtraction of the quasar PSF can drastically reduce the contribution from the quasar itself. Implementation of these techniques is described in the following subsections.

4.4.2 Quasar PSF Subtraction

In very high signal-to-noise ratio images, such as stacked images, the quasar PSF can be detected out to angular distances of a few tens of arcseconds and can, therefore, contribute a non-negligible fraction of the azimuthally averaged surface brightness (SB). In order to suppress this contribution, the SB distribution of the quasar is estimated from high signal-to-noise ratio PSFs of bright, unsaturated, stars in the same field. For each quasar, the PSF is empirically determined using bright ($r < 18.0$ mag), unsaturated stars found in the same $10' \times 13'$ SDSS field as the quasar. Suitable PSF stars were those flagged with clean photometry in the SDSS PhotoObj tables (i.e., CLEAN = 1) and tagged as primary objects (i.e., MODE = 1), identifying the best version of an object observed multiple times.

To ensure that the quasar and the PSF star were observed under similar detector and sky (seeing) conditions, both of them were required to be identified with the same CAMCOL and RUN numbers. Candidate PSF stars too close to an edge were eliminated. Two-dimensional Gaussians were fit to PSF stars with magnitudes $15 \leq m_r \leq 18$, which were then scaled to the intensity amplitude of the quasar and subtracted with the centroid at the location of the quasar. The quality of the PSF subtraction was visually examined, and fields with unsatisfactory PSF subtractions were eliminated. We then divided the sample into weak and strong Ca II absorber samples. Table 4.2 summarizes the number of fields that were ultimately included in the stacks.

4.4.3 Masking Algorithm

We used the SDSS SAS catalog of sources to identify stars in each quasar field that needed to be masked. Galaxies identified to have a negligible likelihood of being associated with the absorber, based on the availability of reliable redshift (photometric and spectroscopic) information, were also masked out. Galaxies brighter than 3L*, equivalent to an absolute magnitude $M_r = -22.7$ and $M_g = -21.5$, at the redshift of the absorber were masked out. Figure 4.4 shows the corresponding apparent magnitudes as a function of redshift for $3L^\star$. For simplicity, we used square masks of uniform size that were 5" and 7" on a side to mask out stars and galaxies, respectively. Each pixel in the mask was assigned a brightness value equal to the median pixel value of the entire $13' \times 10'$ SDSS field containing the quasar sightline. Occasionally, a bright star overwhelmed a field, in which case that sightline was not included in the stack.

We note that we supplemented our source list using catalogs generated by the source extraction software **SExtractor** (ver. 2.5.0; Bertin & Arnouts 1996). All sources detected at a significance level 1.5σ above the local background over a minimum area of 10 pixels were cataloged. The quasar PSF was subtracted prior to running the source detection software.

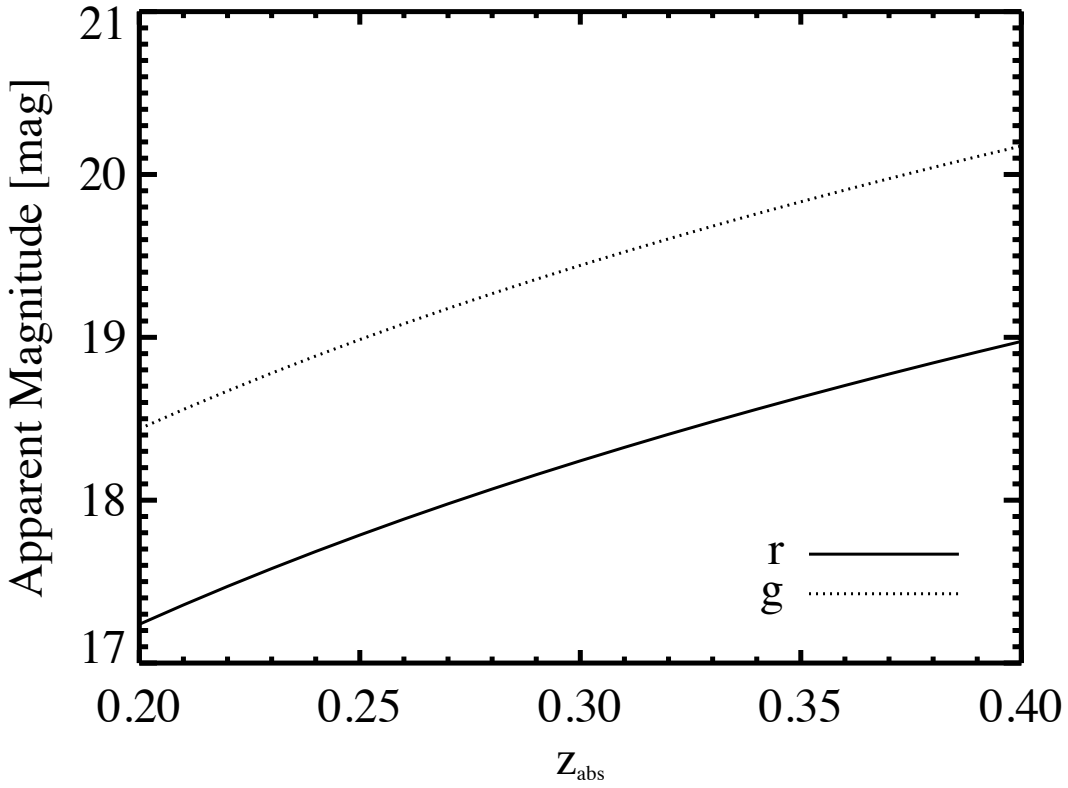

Figure 4.4: Apparent magnitude thresholds equivalent to $3L^{\star}$ as a function of absorber redshift for the SDSS r and g filters.

4.4.4 Construction of the Image Composites and Light Profiles

Prior to stacking the PSF-subtracted images, each field was rescaled to the same physical scale at the redshift of the absorber, z_{abs}. The resulting pixel scale for each field was set at 2 kpc per pixel, and rescaled to conserve the total flux of an object. Corresponding non-absorber fields (§4.2.2) were also rescaled in the same manner, as if an absorber existed at the z_{abs} of its matching absorber field. The final composite images only included unmasked regions of individual images. The intensity of each pixel in the stacked image was calculated as the simple average over the all individual unmasked pixels. The uncertainties in the final composite images were estimated using a jackknife method, where for a given sample of N quasar fields, the stacking is repeated N times, leaving out a different field each time. The variance in each pixel from these N realizations of the stack is multiplied by N-1 to get the sample variance (e.g., Zibetti 2007).

Figure 4.5 shows the 600 $\times$ 600 kpc^2 regions for our resulting stacks, projected at z_{abs} and centered around the quasar, for the redshift range $z_{abs} = [0.20, 0.40]$. As noted by the labels, the top row is for the r-band composites and the bottom row is for the g-band composites. The left column shows the weak Ca II absorber stacks, whereas the strong Ca II absorber stacks are shown in the right column. The corresponding 600$\times$600 kpc^2 regions for the non-absorber stacks are shown in Figure 4.6. Note that the non-absorber matches for the strong and weak absorbers are statistically similar, therefore we combined them into a single non-absorber sample. The surface brightness levels in units of apparent magnitudes per square kpc are shown above each panel. Similarly, we show the corresponding composites in Figures 4.7 and 4.8 for the redshift interval $z_{abs} = [0.40, 0.65]$.

By construction, the central pixel of each stack has zero intensity since the PSF was scaled to the quasar peak intensity before subtraction. For these stacks, which consist of a small number of fields, individual sources are sometimes visible. Note that in both absorber and non-absorber composites, the appearance of these individual sources are less apparent in the g-band than in the r-band, as the SDSS images go deeper in r than in g. Sources farther away from the center of the field can be attributed to light from background/foreground sources, which were likely to be too faint to pass the detection cuts from the SDSS and/or

SExtractor constraints, and hence were not masked out. However, we suspect that these should become less apparent as more individual images are added to the stack. The excess seen near the quasar sightline appears to be more extended and is more likely to be related to galaxies associated with absorbers themselves. Though not as dramatic in extent as the absorber stacks, the non-absorber intensity maps show a slight excess which can be seen by eye within the ∼10 kpc radius around the quasar. Zibetti et al. (2007) suggested that such an excess around reference quasars might be attributed to light physically associated with the quasar's host galaxy. This systematic additive contribution to the light profiles is more apparent with low-redshift quasars. For quasars at high redshifts, $z_{em} \gtrsim 1.5$, the light from the host galaxy would drop below detection limits, so would not show this excess (Zibetti et al. 2007).

Analysis of the surface brightness distribution of the excess light around absorbed quasars in Figures 4-7 can be used to measure the radial light profiles, allowing us to infer the spatial distribution of galaxies for the Ca II absorbers as probed by quasar sightlines. Specifically, we extract one-dimensional surface brightness profiles in circular annuli surrounding the quasar sightlines. The accuracy of our quasar PSF subtraction enables us to probe only up to a minimum radius of 7 kpc from the quasar sightline at $0.20 \leq z_{abs} < 0.40$. The spacing between subsequent apertures is chosen to progress geometrically.

To establish the background light profile levels at $0.20 \leq z_{abs} < 0.40$, we first show in Figure 4.9 the surface brightness profiles as a function of the distance from the quasar sightline for the non-absorber quasar fields, with the g-band composite on the left and the r-band on the right. A slight increase in the surface brightness ($\lesssim 0.5$ mag per kpc^2) closer to the quasar sightline can be seen, but consistent with the overall noise levels. This is plausibly consistent with excess light coming from the host galaxies of low-z quasars.

The profiles for the surface brightness for the absorber fields, subdivided into weak and strong Ca II absorber components, as a function of the projected distance from the quasar from 7-300 kpc is shown two different ways. In the first, we assume a constant background level per square kpc using the results in Figures 4.9 and 4.10. In the second, we subtract the non-absorber reference images. For each of these profiles, the distribution of light is modeled as a power-law distribution of order n where r is the distance from the quasar sightline in

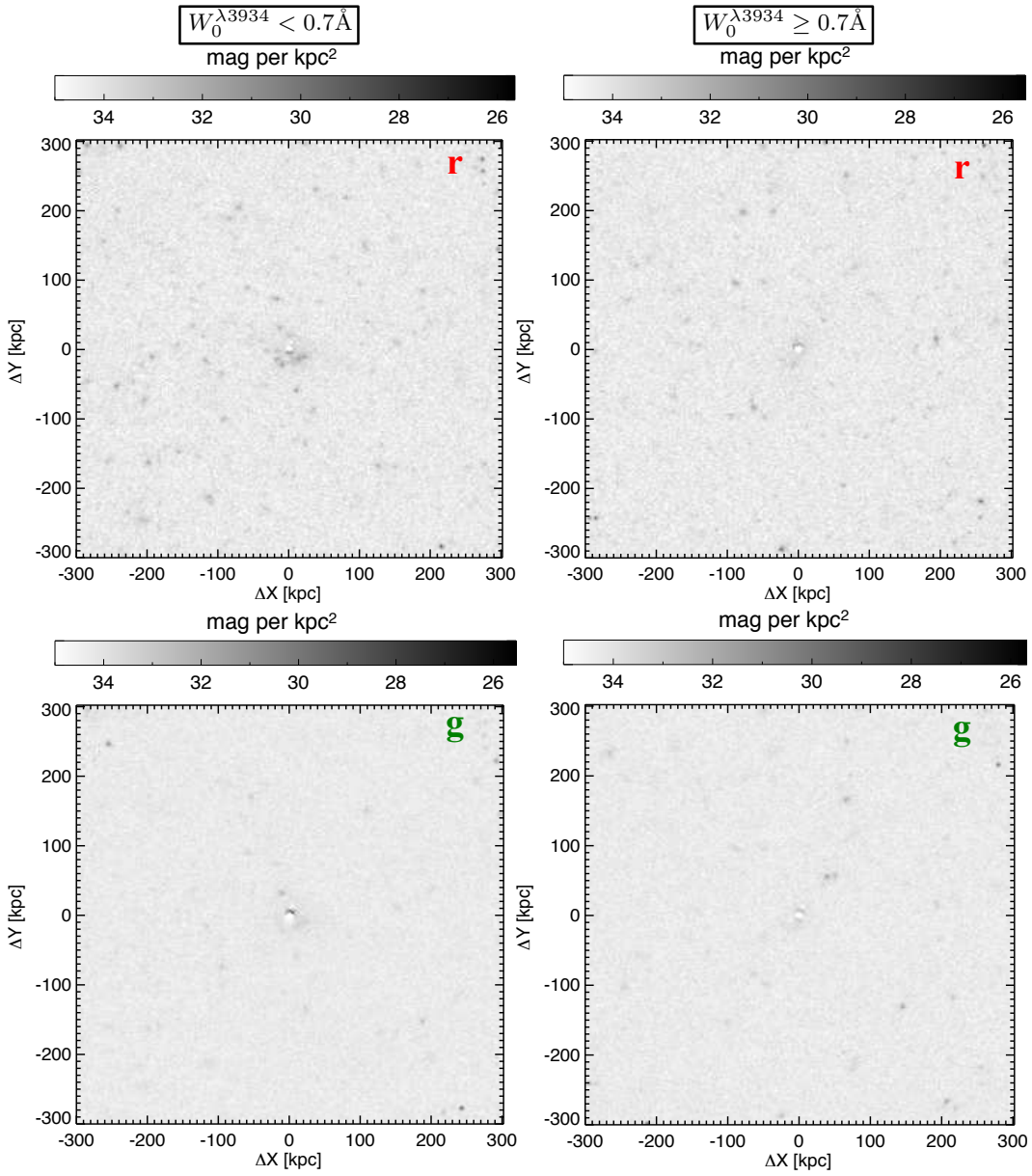

Figure 4.5: The 600×600 kpc^2 quasar PSF-subtracted image composites for the Ca II absorber sample with absorption redshifts from 0.20 to 0.40. The subtracted quasar is at the center of the image. As the labels indicate, the top row shows the composites constructed from the SDSS r-band images, while the bottom row shows the g-band composite images. The left panels are for the absorbers with $W_0^{\lambda 3934} < 0.7$Å, and the right panels are for $W_0^{\lambda 3934} \geq 0.7$Å absorbers.

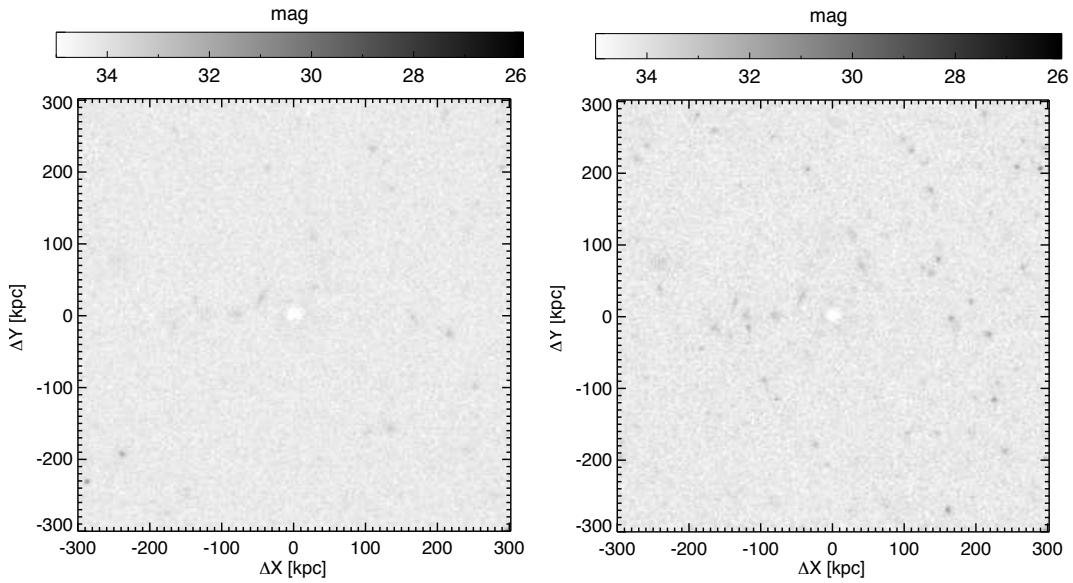

Figure 4.6: The 600×600 kpc^2 quasar PSF-subtracted image composites for the non-absorber quasar matches centered on the quasar. The matched absorber redshifts span the range $0.20 \leq z_{abs} \leq 0.40$. *Left:* The SDSS g-band non-absorber composite. *Right:* The SDSS r-band non-absorber composite.

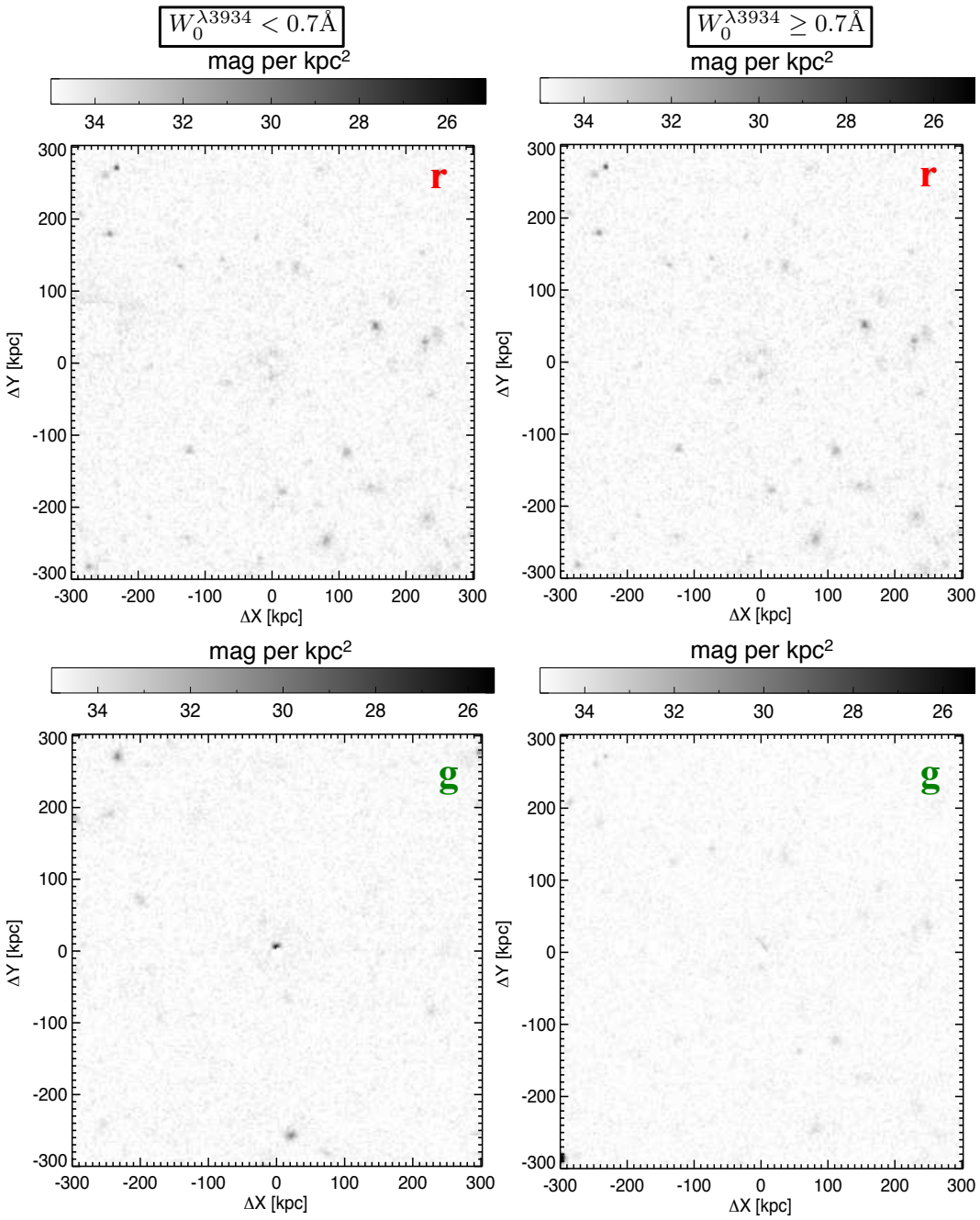

Figure 4.7: The 600×600 kpc^2 quasar PSF-subtracted image composites for the Ca II absorber sample with absorption redshifts from 0.40 to 0.65. The subtracted quasar is at the center of the image. The top rows show the composites constructed from the SDSS r-band composite images, while the bottom rows show the g-band composite images. The left panels are for the absorbers with $W_0^{\lambda3934} < 0.7$Å, and the right panels are for $W_0^{\lambda3934} \geq 0.7$Å absorbers. Noise from foreground and background sources are still apparent in this redshift range due to the small number of fields.

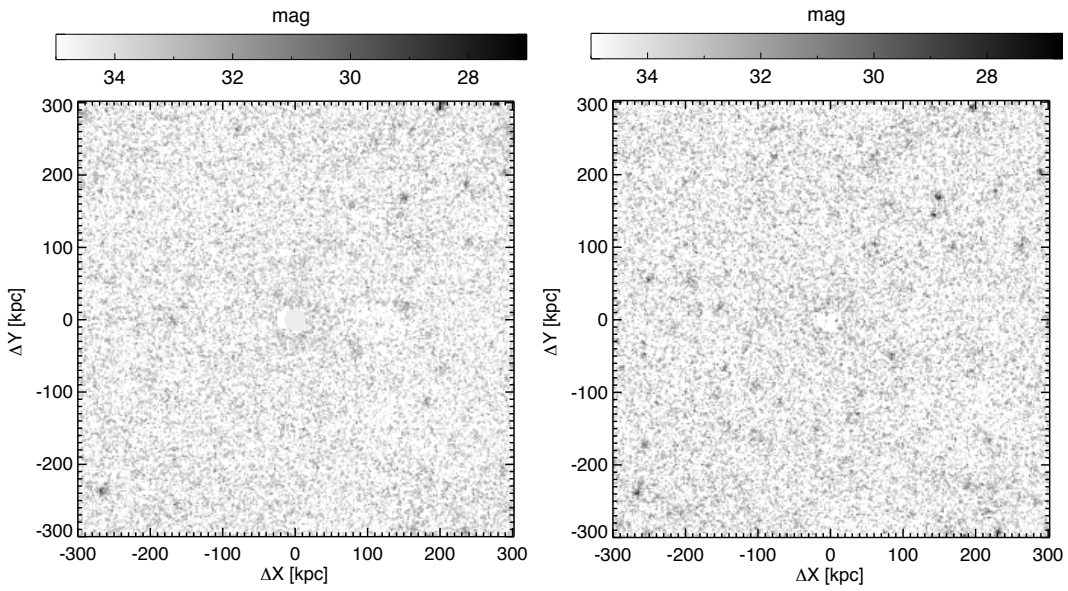

Figure 4.8: The 600×600 kpc^2 quasar PSF-subtracted image composites for the non-absorber quasar matches centered on the quasar. The matched absorber redshifts span the range $0.40 \geq z_{abs} \geq 0.65$. *Left:* The SDSS g-band non-absorber composite. *Right:* The SDSS r-band non-absorber composite.

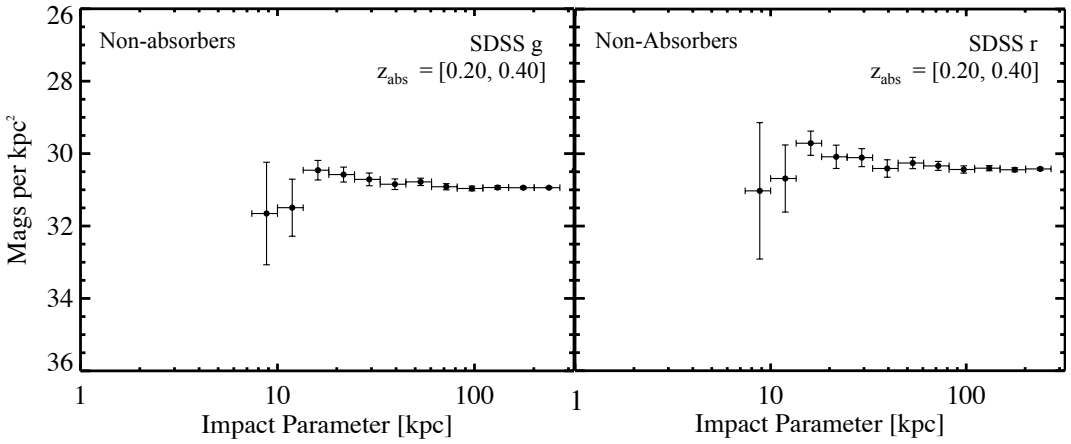

Figure 4.9: The radial surface brightness profiles centered around the quasar for the non-absorber image composites shown in Figure 4.6 for the redshift range $0.20 \leq z_{abs} < 0.40$. The left panel is for the g-band image composite and the right panel is for r-band composite. These relatively flat profiles will be used to infer the constant background level when deriving the surface brightness profiles for the composites of Figure 4.5.

kpc, as shown in Eqn.4.1:

$$I(r) = Ar^{\alpha}. \tag{4.1}$$

The first moment of the light distribution is then

$$R_1 = \frac{\int_{7kpc}^{100kpc} I(r) r^2 dr}{\int_{7kpc}^{100kpc} I(r) r dr} \tag{4.2}$$

where R_1 is the luminosity-weighted average impact parameter of Ca II absorbing galaxies, with small values indicating more centrally concentrated light profiles. We summarize the results of the profile fitting and the corresponding R_1 values in Table 4.3. In both bands, strong systems tend to have steeper power-laws than weaker absorbers, as shown in Table 4.3. This result is consistent with that found by Zibetti et al. (2007) for Mg II absorbers,

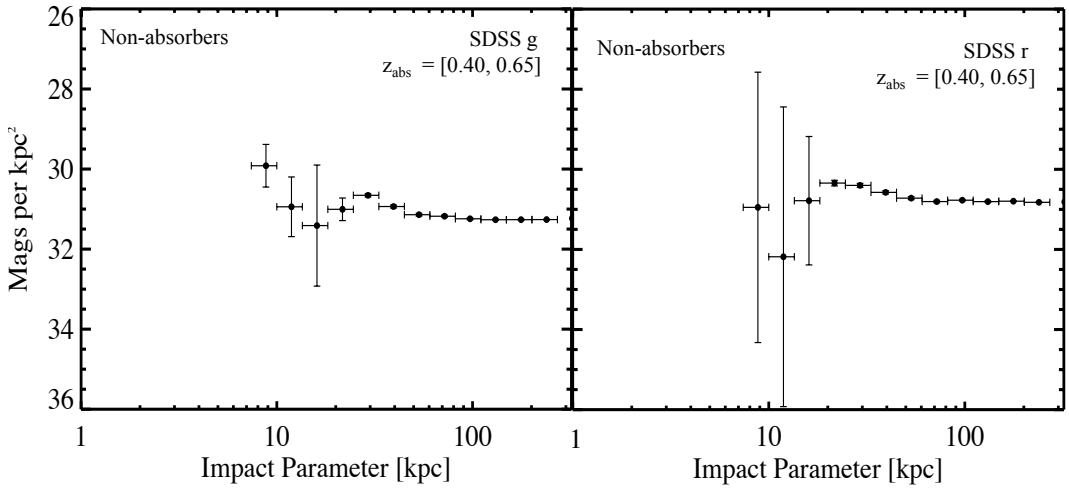

Figure 4.10: The radial surface brightness profiles centered around the quasar for the non-absorber image composites shown in Figure 4.6 for the redshift range $0.40 \leq z_{abs} \leq 0.65$. The left panel is for the g-band image composite and the right panel is for r-band composite. These relatively flat profiles will be used to infer the constant background level when deriving the surface brightness profiles for the composites of Figure 4.9.

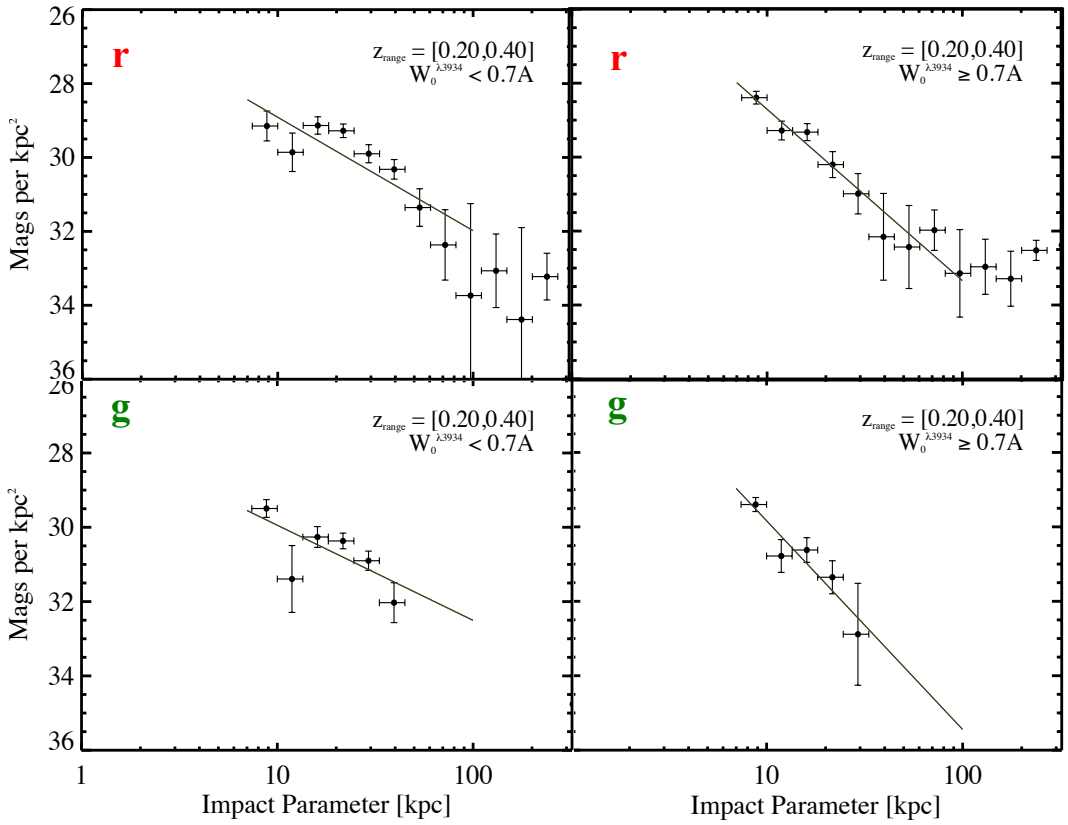

Figure 4.11: The radial brightness profiles from 7-300 kpc for the composites in the redshift range $0.20 \leq z_{abs} < 0.40$ (Figure 4.5) after subtraction of a constant background of 31.0 and 30.5 mags per kpc^2, respectively, in the g and r bands. The left panels are for the absorbers with $W_0^{\lambda 3934} < 0.7$ Å, and the right panels are for the absorbers with $W_0^{\lambda 3934} \geq 0.7$ Å. The top panels show the radial r-band surface brightness profiles, and the bottom panels show for the g-band profiles. The solid lines correspond to the best-fit power-law of Eq. 4.1 from 7 kpc to 100 kpc. The results of the fit and effective impact parameter R_1 values are summarized in Table 4.3.

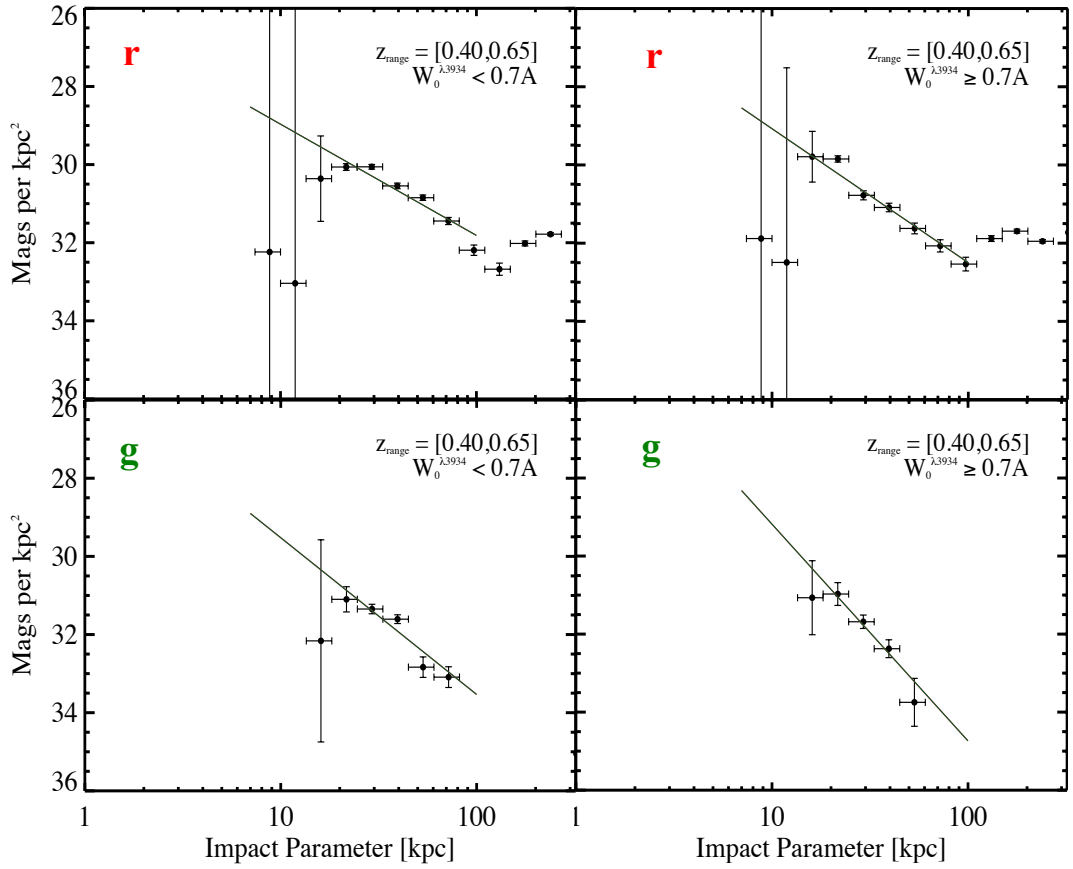

Figure 4.12: The radial brightness profiles from 7-300 kpc for the composites in the redshift range $0.40 \leq z_{abs} < 0.65$ (Figure 4.7) after subtraction of a constant background of 31.3 and 31.0 mags per kpc^2, respectively, in the g- and $r-$ bands. The left panels are for the absorbers with $W_0^{\lambda 3934} < 0.7$ Å, and the right panels are for the absorbers with $W_0^{\lambda 3934} \geq 0.7$ Å. The top panels show the radial r-band surface brightness profiles, and the bottom panels show for the g-band profiles. The solid lines correspond to the best-fit power-law of Eq. 4.1 from 7 kpc to 100 kpc. The results of the fit and effective impact parameter R_1 values are summarized in Table 4.3.

i.e., the R_1 values for the strong absorbers are smaller, indicating more concentrated light profiles.

We show in Figures 4.11 and 4.12 the surface brightness profiles as a function of the impact parameter from $\sim$ 7-300 kpc for the redshift bins z_{abs} = [0.20, 0.40] and z_{abs} = [0.40, 0.65], respectively. For these profiles, we have assumed a constant surface brightness background (Table 4.3). As indicated by the figure labels and corresponding to the order of the intensity maps of Figure 4.5, the left and right columns indicate the weak and strong Ca II absorber subsamples, respectively. The top and bottom rows indicate the corresponding filters. The solid lines show the fit to the profiles using Eqn. 4.1, which models the distribution of light as a power-law of order n of the impact parameter r. The fits are performed over the impact parameter range from 7-100 kpc by minimizing the sums of the residuals. The results are summarized in Table 4.3.

The results from the second background subtraction method are shown in Figures 4.13 and 4.14 for the surface brightness profiles for the redshift bins z_{abs} = [0.20, 0.40] and z_{abs} = [0.40, 0.65], respectively. These were obtained by direct subtraction of the reference images of Figures 4.6 and 4.8 from the absorber frames Figure 4.5 and 4.7. The parameters of the power-law fits, Eqn. 4.1, and characteristic mean impact parameter R_1 are given in Table 4.4. It is quite apparent that this method of subtraction results in steeper, albeit more noisy, profiles for the strong Ca II absorber subsample. Nevertheless, both methods show that strong Ca II absorbers, on average, have a more concentrated light distribution than the weak systems. Moreover, both methods are in agreement that for the weak absorbers the characteristic R_1 is within 40-50 kpc for both redshift bins and filters. On the other hand, the light profiles for the strong systems show a wider range in R_1, but for the more reliable direct background subtraction method, $R_1 \sim 20 - 30$ kpc. Similar conclusions were drawn by Zibetti et al. (2007) in a study of Mg II absorbers using 2800 images from the SDSS, spanning the redshift range from $\sim$ 0.4 - 1.0. For Mg II absorbers, the average characteristic R_1 is $\sim$ 40 kpc for the high-W_0 systems ($W_0^{\lambda 2796} > 1.5$Å), and increases to $\sim$60 kpc for the weaker systems ($W_0^{\lambda 2796} \sim 0.8 - 1.0$Å).

Table 4.3: Summary of results of the brightness profiles analysis via image stacking in the SDSS r and g bands, showing the slopes of the power-law profiles of Eq. 4.1. As described in the text, we assume a constant background to derive the final brightness profiles. The results show that the strong systems have significantly compact light profiles compared to the weak counterparts.

z_{abs}	$W_0^{\lambda 3934} < 0.7$Å		$W_0^{\lambda 3934} \geq 0.7$Å		
range	α	R_1 [kpc]	α	R_1 [kpc]	Filter
0.20 - 0.40	-1.21 ± 0.14	$49.9\ ^{2.4}_{2.6}$	-1.85 ± 0.20	$37.7^{3.8}_{3.7}$	r
0.20 - 0.40	-1.11 ± 0.18	$51.5\ ^{3.1}_{3.3}$	-2.24 ± 0.45	$30.1^{8.3}_{6.9}$	g
0.40 - 0.65	-1.14 ± 0.06	$51.1\ ^{1.0}_{1.0}$	-1.37 ± 0.08	$46.9^{1.6}_{1.6}$	r
0.40 - 0.65	-1.60 ± 0.19	$42.5\ ^{3.7}_{3.7}$	-2.22 ± 0.37	$31.0^{6.7}_{5.8}$	g

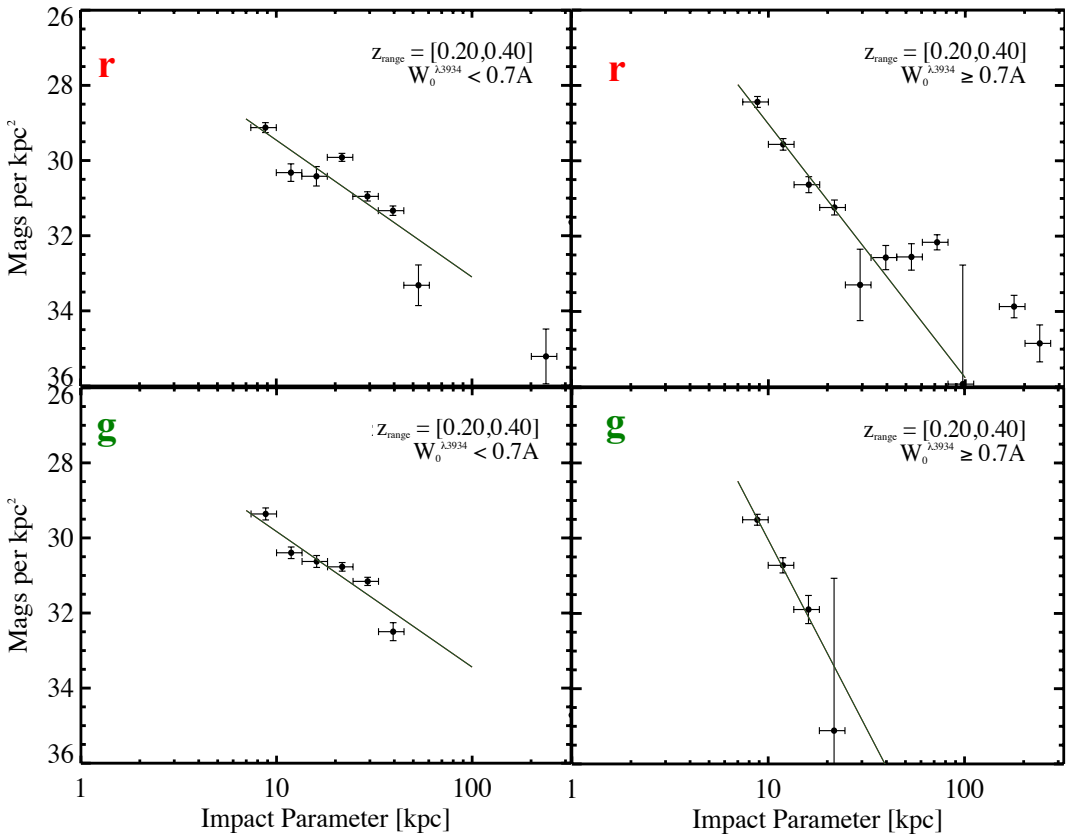

Figure 4.13: The radial brightness profiles from 7-100 kpc for the composites in the redshift range $0.20 \leq z_{abs} < 0.40$ (Figure 4.5) obtained by direct subtraction of the unabsorbed composite in Figure 4.6. The left panels are for the absorbers with $W_0^{\lambda 3934} < 0.7$ Å, and the right panels are for $W_0^{\lambda 3934} \geq 0.7$ Å. The top panels show the radial r-band surface brightness profiles, and the bottom panels show for the g-band profiles. The solid lines correspond to the best-fit power-law of Eq. 4.1 from 7 kpc to 100 kpc. The results for the fit and the effective impact parameter R_1 values are summarized in Table 4.4.

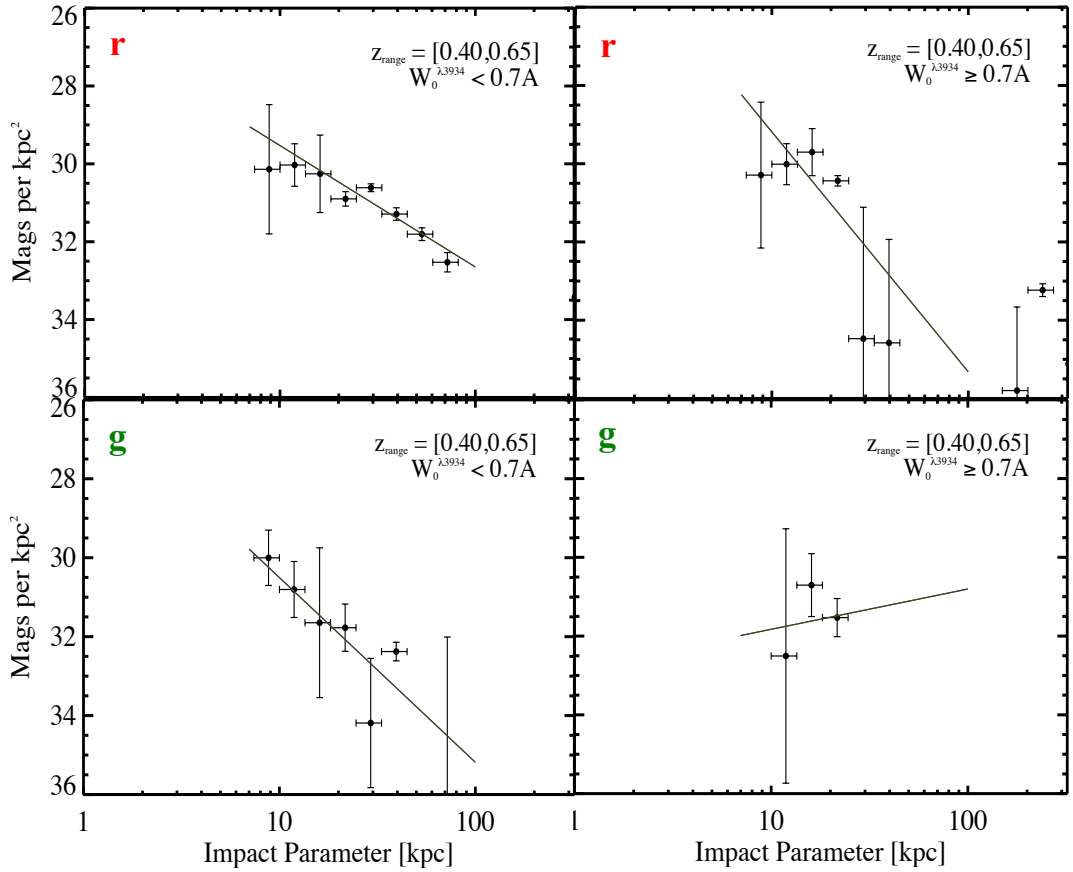

Figure 4.14: The radial brightness profiles from 7-100 kpc for the composite images in the redshift range $0.40 \leq z_{abs} \leq 0.65$ (Figure 4.7) obtained by direct subtraction of the unabsorbed composite in Figure 4.6. The left panels are for the absorbers with $W_0^{\lambda 3934} <$ 0.7 Å, and the right panels are for $W_0^{\lambda 3934} \geq 0.7$ Å. The top panels show the radial r-band surface brightness profiles, and the bottom panels show for the g-band profiles. The solid lines correspond to the best-fit power-law of Eq. 4.1 from 7 kpc to 100 kpc. The results of the fit and effective impact parameter R_1 values are summarized in Table 4.4.

Table 4.4: Summary of results of the brightness profiles analysis via image stacking in the SDSS r and g bands, showing the slopes of the power-law profiles of Eqn. 4.1. These results were derived by direct subtraction of the reference non-absorber composites of Figures 4.13 and 4.14 from the corresponding absorber composite frames in Figures 4.6 and 4.8. The results are in agreement with the general results of Table 4.3 in that the strong systems have steeper slopes, and hence more compact light profiles compared to the weak counterparts.

z_{abs}	$W_0^{\lambda 3934} < 0.7$Å		$W_0^{\lambda 3934} \geq 0.7$Å		
range	α	R_1 [kpc]	α	R_1 [kpc]	Filter
0.20 - 0.40	-1.46 ± 0.09	$45.3\ ^{1.4}_{1.7}$	-2.70 ± 0.19	$23.7^{2.6}_{2.3}$	r
0.20 - 0.40	-1.44 ± 0.11	$45.5\ ^{2.2}_{2.1}$	-4.01 ± 0.50	$13.0^{2.6}_{1.6}$	g
0.40 - 0.65	-1.24 ± 0.09	$49.3\ ^{1.6}_{1.5}$	-2.56 ± 0.18	$25.5^{2.8}_{2.5}$	r
0.40 - 0.65	-1.52 ± 0.54	$44.1\ ^{10.2}_{9.7}$	···	···	g

4.5 SUMMARY AND DISCUSSION

This is the third in a series of papers investigating the properties of Ca II absorbers identified in moderate-resolution SDSS quasar spectra. The redshift range over which Ca II absorbers can be studied in SDSS optical spectra ($0 < z < 1.34$) allows us to study them over the most recent 8.5 Gyrs of our cosmic history. The ability to study Ca II absorbers at the lowest redshifts makes them unique, as the rest wavelengths of more common QAL transitions lie in the UV. For example, in SDSS spectra, Mg II can only be studied down to redshift $z = 0.4$. However, the incidence of Ca II absorption in quasar spectra is much more rare in comparison to Mg II, which makes performing a survey to discover a large number of them challenging.

In Paper I (Chapter 2 of this thesis) we described our SDSS survey for Ca II, which resulted in the identification of 435 Ca II absorbers, and we characterized their statistical properties, which included evidence for the existence of at least two populations of absorbers, e.g., based on the need for a two-component fit to model their $W_0^{\lambda 3934}$ distribution. Among the various possibilities we considered, the simplest was the proposal that "weak Ca II absorbers" with $W_0^{\lambda 3934} < 0.7$ Å might have different astrophysical properties than "strong Ca II absorbers" with $W_0^{\lambda 3934} \geq 0.7$ Å. Owing to the nature of our evidence, if two populations do exist, one would expect the populations to be mixed near $W_0^{\lambda 3934} \approx 0.7$ Å.

In Paper II (Chapter 3 of this thesis) we investigated element abundance ratios and dust in the weak and strong absorbers using their composite spectra. We found that the weak Ca II absorbers had element abundance ratios typical of halo-type gas, whereas the strong Ca II absorbers had element abundance ratios typical of a mix of halo- and disk-type gas. Moreover, while both populations of Ca II absorbers showed evidence for dust in the form of element depletions and the reddening they caused, the strong Ca II absorbers showed nearly six times more reddening than the weak Ca II absorbers. The reddening was found to be consistent with either LMC- or SMC-type extinction laws, but a MW-type extinction law was ruled out.

In this Chapter, we investigated the galaxy populations associated with the weak and strong Ca II absorbers using SDSS imaging data. We identified four galaxies along quasar sightlines that had SDSS spectroscopic redshifts that matched the Ca II absorber redshifts

(Figures 4.1-4.3 and Table 4.1). The fact that matches required spectroscopic data for both the quasar and the nearby galaxy meant that these could only be found using rare, overlapping, plates, which resulted in the serendipitous identification of only four galaxies. The four absorbers have rest equivalent widths and redshifts lying in the intervals $W_0^{\lambda 3934} = [0.48, 1.3]$ Å and $z_{abs} = [0.04, 0.24]$. The four associated galaxies have impact parameters and luminosities lying in the intervals $b = [5, 25]$ kpc and $L = [0.1, 0.9]$ L^*. The identification and luminosity of one galaxy is unclear, but the three others are clearly star-forming galaxies, exhibiting strong hydrogen Balmer emission lines as well as emission from [O II], [O III], [N II], and [S II] (Figure 4.2). We also investigated the population of galaxies associated with the Ca II absorbers by stacking and forming composite images. These investigations were necessarily statistical in nature, since we did not utilize any spectroscopic galaxy redshifts, but simply inferred their properties by assuming that any excess galaxy light above the background had $z = z_{abs}$. The background-subtracted composite images, which covered the redshift intervals $z_{abs} = [0.20, 0.40]$ and $[0.40, 0.65]$, revealed excess light along the Ca II absorber quasar sightlines (Figures 4.11-4.14). We found that the strong Ca II absorbers had a more concentrated and steeper light profile than the weak Ca II absorbers. The first moments of the excess light distributions were used to derive the luminosity-weighted impact parameters, R_1, for the weak and strong absorbers. If we average the various r-band and g-band results (Tables 4.3 and 4.4) in the most reliable $z_{abs} = [0.20, 0.40]$ interval, the weak Ca II absorbers have $R_1 \approx 48$ kpc, while the strong Ca II absorbers have $R_1 \approx 26$ kpc.

Thus, the results from Chapters 2-4 give rise to a consistent picture. The two-component rest equivalent rest distribution (Chapter 2, Paper 1) was the first clue indicating two absorber populations. The strong Ca II absorbers were then shown to have metal abundance ratios and dust properties consistent with a contribution from disk- and halo-type gas, whereas the weak Ca II absorbers show properties consistent with only halo-type gas; the strong Ca II absorbers contain nearly six times more dust than weak Ca II absorbers, which puts them among the most dusty quasar absorbers (Chapter 3, Paper 2). The metal abundance ratio and dust results lead to the expectation that typical strong Ca II absorbers might have smaller impact parameters than typical weak Ca II absorbers. And indeed, in this third paper of the series, the strong Ca II absorbers were found to have associated galaxies with

typical luminosity-weighted impact parameters of ≈ 26 kpc, which is $\sim 54\%$ of the impact-parameter (or $\sim 29\%$ of the cross-sectional area) that characterizes the weak Ca II absorbers. Thus, the various derived observables are qualitatively correlated as might be expected.

But while the combination of results leads to a consistent picture, the results also raise a number of issues which should be investigated into the future. As discussed in these last three Chapters, previous results on Ca II absorbers have provided evidence that a significant fraction of them contain high column densities of neutral as well as molecular gas and dust conducive to star-formation. Ultimately direct measurements of H I column densities, H_2 column densities, and depletions on to dust grains in a significant subsample of Ca II absorbers are needed to study this and better understand the Ca II absorber populations. At the same time, our results show that much of this gas lies at large impact parameters, typically ranging between $20-60$ kpc, and there appear to be cases where an associated absorbing galaxy can not be identified to very faint levels within ~ 100 kpc. This provides important clues about inflows, outflows, and chemical enrichment in the extended circumgalactic regions surrounding galaxies and possibly the intergalactic medium. The existence of such regions far away from the centers of galaxies would also require theoretical explanation.

Therefore, these new results raise a number of issues which should be investigated into the future. As discussed in this series of papers, previous results on Ca II absorbers have provided evidence that at a significant fraction of them contain high column densities of neutral gas, and also molecular gas conducive to star-formation. Ultimately direct measurements of H I and H_2 column densities in a significant subsample of Ca II absorbers are ideally needed to confirm this. At the same time, our results show that much of this gas lies at large impact parameters, typically ranging between $20-60$ kpc, predominately from galaxies with dwarf-like or near dwarf-like luminosities. This provides important clues about inflows, outflows, and chemical enrichment in the extended circumgalactic regions surrounding this under-luminous galaxy population.

5.0 PROBING THE EXTENDED GASEOUS REGIONS OF M31 WITH QUASAR ABSORPTION LINES*

The contents of this chapter have been published in the paper by Rao, Sardane, Turnshek, et al., 2013, *Monthly Notices of the Royal Astronomical Society*, 432, 866 - 885.

5.1 INTRODUCTION

The standard paradigm for metal-line absorption systems in quasar spectra is that they arise in the extended gaseous halos/disks of galaxies well beyond their observable optical radii. However, with the exceptions afforded by gravitationally-lensed quasars, rarely is there more than one sightline passing in the vicinity of a galaxy. As such, the study of quasar absorption lines arising in extended gas associated with the great spiral galaxy in Andromeda (M31) represents a unique opportunity. M31's large extent on the sky means that many quasar sightlines should intercept its extended gas. For example, the $N_{HI} = 1.9 \times 10^{18}$ atoms cm^{-2} 21 cm emission contour around M31, as derived from the data discussed by Thilker et al. (2004), is approximately 5.0×1.5 square degrees on the sky (see Figure 5.1). We list some properties of M31 in 5.1. Quasar surveys have shown that there are as many as 18 quasars per square degree brighter than $g \sim 20$ at $z \lesssim 2.6$ (Richards et al. 2009, Abraham et al. 2012). Thus, there are likely to be on the order of 135 such quasars behind M31 within the boundaries of its observed 21 cm emission, and a factor of several more in its extended gaseous disk and halo regions. However, until now, quasar absorption lines have never been successfully used to study the extended gas of M31 because of the lack of sufficiently-bright,

*Based on observations made with the NOAO 2.1-m and the NASA/ESA *Hubble Space Telescope*

identified quasars.

Two of the most recognizable signatures of metal lines in quasar spectra are the Mg II $\lambda\lambda$2796,2803 and C IV $\lambda\lambda$1548,1550 doublets, which have been studied in numerous quasar absorption-line surveys. The first comprehensive study which demonstrated that galaxies at large impact parameters exist along the sightlines to low-redshift Mg II absorbers was by Bergeron and collaborators, e.g., Bergeron & Boissé (1991). They estimated that the average Mg II radius of a spherical gaseous envelope surrounding an L^* galaxy is $R^* \sim 3.5$ to $5.0R_H$ ($\sim$ 55 to 80 kpc) at $z \sim 0.3$ for rest equivalent widths $W_0^{\lambda 2796} \geq 0.3$ Å, where R_H is the Holmberg radius. Others had made similar estimates (e.g., Lanzetta et al. 1987, Lanzetta & Bowen 1990, Steidel 1993). The recent survey of galaxies associated with Mg II absorbers at $0.1 < z < 1.0$ by Rao et al. (2011) showed that the gaseous extent of Mg II-selected absorbing galaxies could be as large as 100 kpc. At $z < 0.5$, Chen et al. (2010) find that the mean covering fraction for Mg II absorbers with $W_0^{\lambda 2796} \geq 0.3$ Å within $\sim$130 kpc of a $2L^*$ galaxy (for $h = 0.7$) is $\sim$70%. Therefore, if cross sections have remained constant since $z \sim 0.5$, then we might expect that gas giving rise to Mg II is likely to be present in the extended gaseous regions of M31 out to a radius of $\sim$ 100 kpc or more, assuming it is a typical absorbing galaxy.

As described in §5.2, we obtained *Hubble Space Telescope (HST) - Cosmic Origins Spectrograph (COS)* spectra of ten quasars located behind M31 in order to investigate the properties of the gas in its extended disk and high velocity clouds (HVCs). We searched for Mg II, C IV, and other absorption lines to do this. In §5.3 we describe the results obtained from each spectrum. We discuss the results in §5.4 and end with a summary and conclusions in §5.5. This study indicates that M31 does not present itself as an absorbing galaxy which is *typical* of the higher-redshift galaxies inferred to give rise to moderate-strength quasar absorption lines.

Table 5.1: M31 properties

Property	Value	Reference[a]
RA (2000)	$00^{\rm h}42^{\rm m}44^{\rm s}$	1
Dec (2000)	$+41°16'08"$	1
Distance	752 ± 27 kpc	2
Inclination	$78°$	3
v_{sys}	-306 km/s	3
R^b_{opt}	22.3 kpc	4
m_B	4.16	4
L^c_B	$2.0L^*_B$	4,5
R^d_{21cm}	33 kpc	3
M_{virial}	$0.8 - 1.1 \times 10^{12} M_\odot$	6

[a] References: 1. Evans et al. (2010); 2. Riess et al. (2012); 3. Corbelli et al. (2010); 4. de Vaucouleurs et al. (1991); 5. Cool et al. (2012); 6. Tamm et al. (2012)

[b] Optical radius at B-band surface brightness $\mu_B = 25$ magnitudes per square arcsec.

[c] Assuming $M^*_B = -19.92$ (Cool et al. 2012).

[d] From the $N_{HI} = 1.9 \times 10^{18}$ atoms cm^{-2} contour (5.1).

5.2 OBSERVATIONS

5.2.1 Existing H I 21 cm Emission Observations

Since M31 is the nearest large spiral galaxy close to the Milky Way, it has been the subject of many observational studies. Specifically for this work, we will make reference to several results over the past decade from radio observational studies of M31's H I 21 cm emission. These are: the Green Bank Telescope (GBT) study of Thilker et al. (2004), which identified high-velocity clouds (HVCs) but at lower spatial resolution than later studies; the Westerbork Synthesis Radio Telescope (WSRT) study of Braun and Thilker (2004) which discovered the M31-M33 H I bridge, and of Westmeier et al. (2005), which focused on obtaining higher spatial resolution observations of HVCs; the WSRT study of Braun et al. (2009), which obtained observations over a wide field at high spatial resolution; and the study of Corbelli et al. (2010), which smoothed the data to lower spatial resolution in order to fit a tilted-ring model to M31's warped disk and study its rotation curve. At some level, all of this work was collaborative by various members of the same group, and in later studies they made use of results that could be derived from earlier data sets.

H I emission spectra were extracted from the Thilker et al. (2004) and Braun et al. (2009) datacubes along the sightlines toward our target quasars. These data, originally in units of Jy/beam, were converted to N_{HI} under the assumption of negligible H I opacity. This conventional assumption, while recently questioned by Braun et al. (2009) and Braun (2012) in the dense gaseous environment of the traditional optical disk and slightly beyond, is expected to be satisfied in the outer disk and halo environment. A more significant concern regarding the N_{HI} from observations of emission is the vastly different scale probed by the GBT and WSRT relative to COS. The maximum linear spatial resolution of the high resolution 21 cm observations is $\sim 50 - 100$ pc at the distance of M31. This scale is of order $\sim 10^5$ times larger than the linear spatial scale sampled in quasar "pencil-beam" absorption-line observations, where the pencil-beam has the scale of the UV continuum emitting region of the background quasar. Thus, N_{HI} values derived from 21 cm emission observations are averaged over a much larger spatial scale in comparison to those derived

from quasar absorption-line spectra. Nevertheless, using 21 cm observations to derive average N_{HI} values along our sightlines, and noting the velocity range of detected emission, provides some important information.

As an aside, we note that it would be interesting if N_{HI} results derived from M31's 21 cm emission data could someday be compared with N_{HI} determinations from Lyman series absorption seen in the UV spectra of background quasars. One could then get an H I column density measurement averaged over less than a milli-parsec region in M31, in comparison to the $\sim$ 50 pc linear spatial scale offered by the radio observations. This would provide information on the homogeneity and size scale of H I absorbing regions in M31.

5.2.2 Optical Discovery Spectra of Quasars behind M31

We started this project by developing a list of quasars in especially desirable locations (see below) relative to M31. These were initially quasar candidates, since existing catalogs generally did not include quasars behind M31. The quasar candidates were selected from special plates of the SDSS, which were obtained specifically to find quasars behind the extended regions of M31 (Adelman-McCarthy et al. 2006). Of the 219 candidates, 108 were confirmed as quasars. Twenty-three of the 108 were spectroscopically confirmed during our October 2003 NOAO 2.1 m Gold Camera run at Kitt Peak. To make follow-up observations with HST-COS (§5.2.3 and §5.3) more feasible, we concentrated on finding brighter quasars. We also focused our search behind M31's extended major axis to probe possible disk gas that could sample its outer rotation curve. See Figures 5.1 and 5.2, and Tables 5.1 and 5.2, for information on their locations relative to M31 and the discovery spectra. Quasars labeled 1 through 4 would sample any extended disk gas (or possibly halo gas) that is undetected in 21 cm emission; quasars 5, 6, 8, and 9 lie near the edge of detected 21 cm emission; the sightline towards quasar 7 passes through a high velocity cloud (HVC) in the circumgalactic environment of M31; and quasar 10 lies behind the 21 cm emission H I disk as well as two other HVCs. Importantly, owing to M31's systemic velocity of -306 km s^{-1} (Corbelli et al. 2010) and its direction of rotation, absorption originating on the southwest side of M31 will not be confused with Galactic absorption. Consequently, quasars 1 through 4 offer the

best opportunities for observing extended disk gas and measuring M31's rotation curve much farther out than possible with 21 cm emission observations. Unfortunately, while obtaining information on M31's rotation curve at large galactocentric distance was one of the primary motivations for observing quasars 1 through 4, no M31 absorption near the expected velocity was detected in their UV spectra (§5.2.3 and §5.3). We note, however, that higher quality observations might yet be able to detect gas at these locations. Observing quasars on the extended northeast side of M31 was avoided because of potential confusion with Galactic absorption.

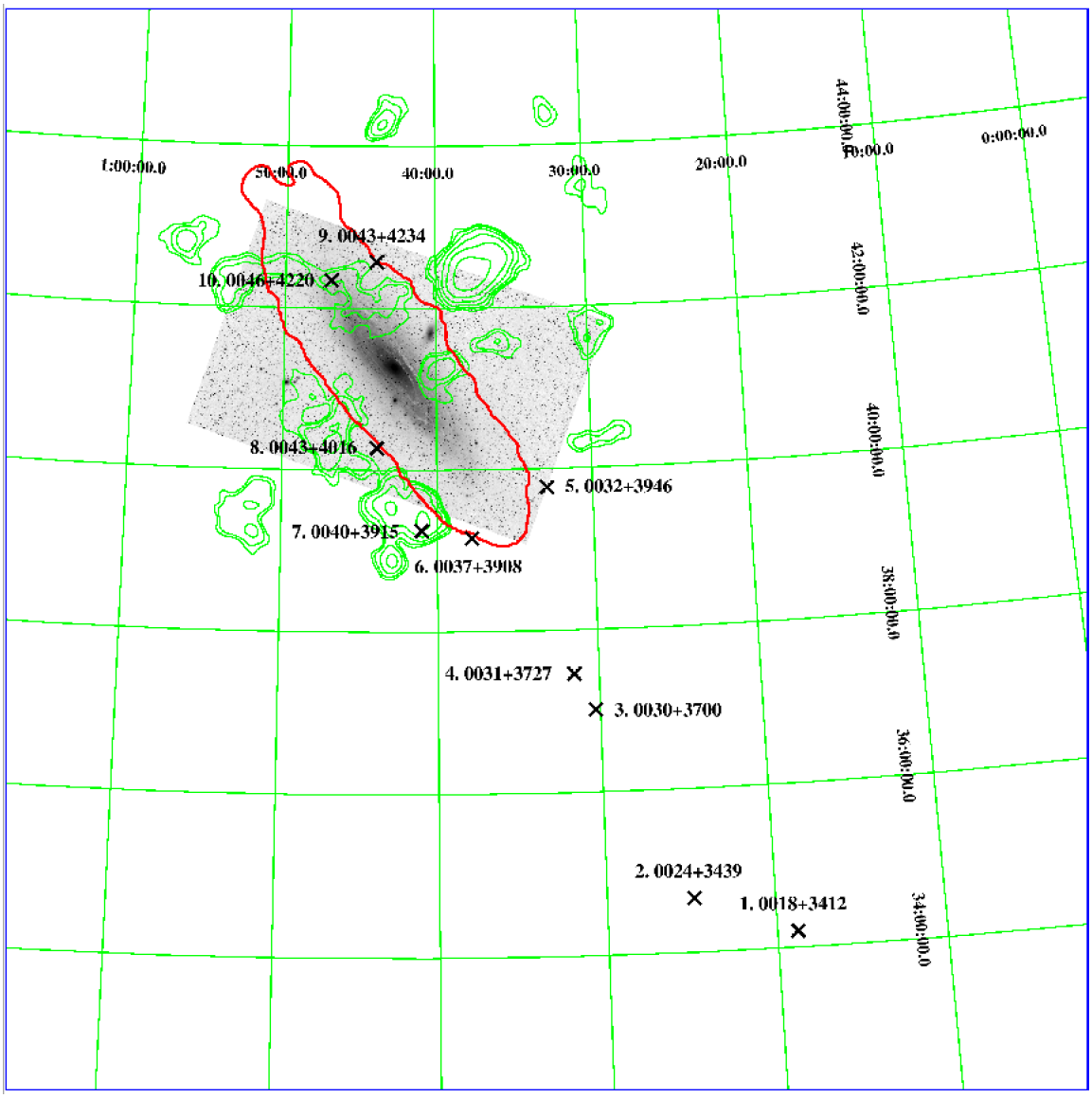

Figure 5.1: Location of the ten quasars that were observed with *HST-COS*. An optical image of M31 is shown in the background along with 21 cm emission maps showing the disk gas and HVCs. The red contour is 21 cm emission at 1 Jy km/s, or an H I column density of $N_{HI} = 1.9 \times 10^{18}$ cm^{-2}. Higher column density contours interior to this are not shown. High velocity cloud contours from Thilker et al. (2004) are shown in green. The scale at the distance of M31 is 13.2 kpc deg^{-1}. The innermost (8. 0043+4016) and outermost (1. 0018+3412) quasars are at projected distances (impact parameters) of $b = 13.4$ kpc and $b = 111.9$ kpc from M31's center. See Tables 5.1 and 5.2.

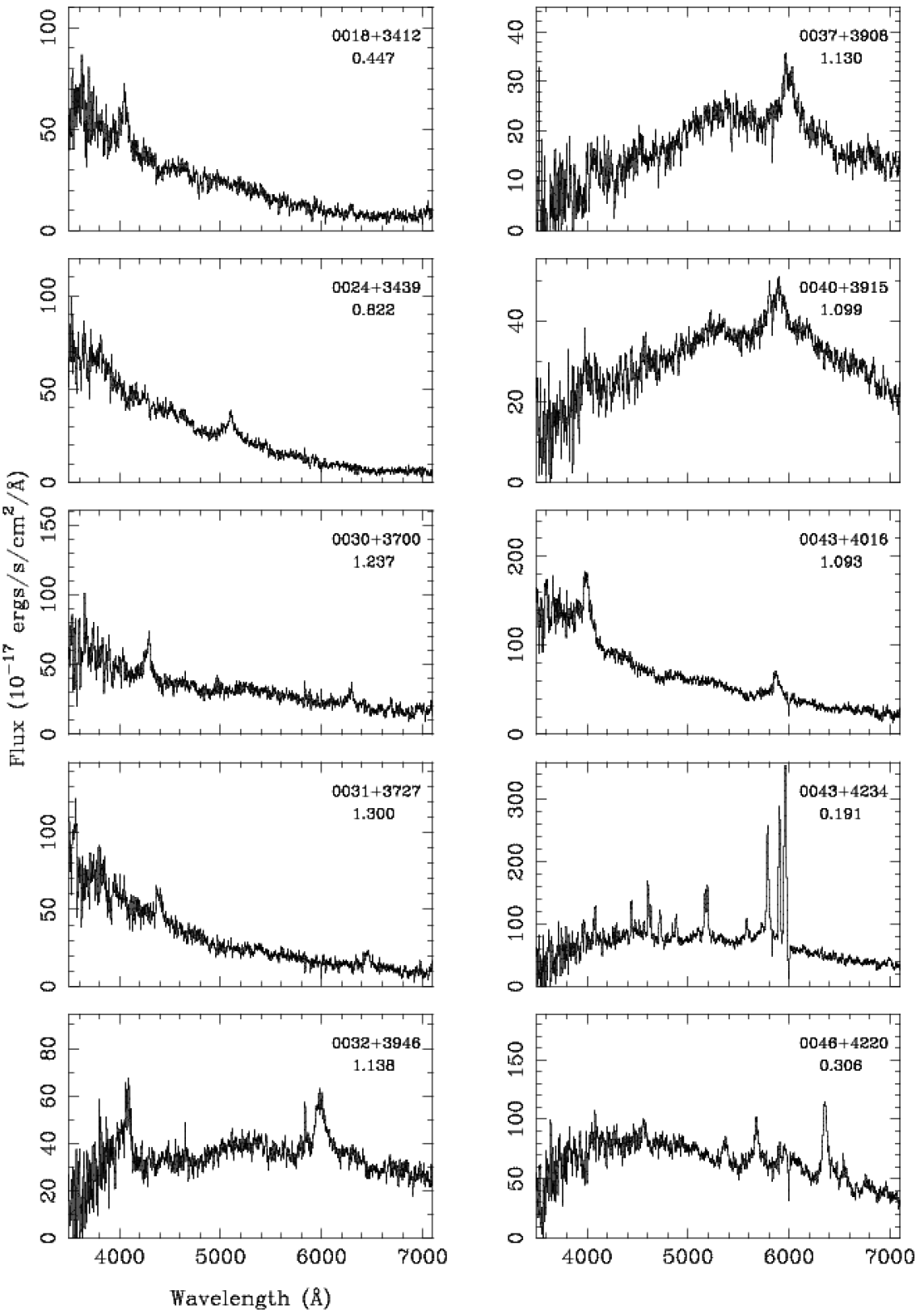

Figure 5.2: KPNO 2.1m Gold Camera discovery spectra of the ten quasars that were observed with HST-COS. The quasar name and emission redshift are noted in each panel.

Table 5.2: Quasars observed with HST-COS

Quasar	RA (2000)	Dec (2000)	Map	z_{em}	SDSS u	b	COS G140L	COS G230L	Sightline notes[c]
	h m s	° ′ ″	ID[a]		mag	(kpc)[b]	Exp time (s)	Exp time (s)	
0018+3412	00 18 47.45	+34 12 09.6	1	0.447	17.7	111.9	3446	5646	extended disk
0024+3439	00 24 50.05	+34 39 42.8	2	0.822	18.1	98.6	···	5092	extended disk
0030+3700	00 30 17.43	+37 00 54.3	3	1.237	17.5	64.4	4054	3191	extended disk
0031+3727	00 31 32.37	+37 27 51.8	4	1.300	18.5	57.6	4455	2246	extended disk
0032+3946	00 32 55.70	+39 46 19.3	5	1.138	18.6	31.5	···	10324	edge of 21 cm disk
0037+3908	00 37 48.00	+39 08 58.7	6	1.130	18.4	30.5	···	10354	edge of 21 cm disk
0040+3915	00 40 59.03	+39 15 12.3	7	1.099	18.5	26.9	6293	11101	HVC + 21 cm disk edge
0043+4016	00 43 52.45	+40 16 29.4	8	1.093	18.2	13.4	7073	5537	edge of 21 cm disk
0043+4234	00 43 54.98	+42 34 30.4	9	0.191	18.0	17.4	3555	6137	edge of 21 cm disk
0046+4220	00 46 55.52	+42 20 50.1	10	0.306	18.1	17.5	2572	5217	2 HVCs + 21 cm disk

[a] Quasar IDs in order of increasing RA.
[b]Projected distance from galactic center assuming that the center of M31 is at ($00^{\rm h}42^{\rm m}44^{\rm s}$, $+41^{\circ}16'08''$) and that the distance to M31 is 752 kpc. See Table 5.1.
[c] See Figure 5.1.

5.2.3 *HST-COS* UV Spectroscopy

The *HST-COS* spectroscopic data were obtained during the period July-October 2010. Table 5.2 gives details of the quasars and the HST-COS observations. We decided to make a broad initial absorption-line survey in order to maximize the observed number of metal-line transitions we could reasonably cover within our allocation of 39 HST orbits.[1] The aim was to reach a signal-to-noise ratio which would enable us to detect Mg II and C IV absorption rest equivalent widths commonly seen in prior, large moderate-resolution quasar absorption-line surveys. Therefore, we did not use higher-resolution COS gratings. However, it would indeed be worthwhile to perform follow-up spectroscopy of a number of our detections at higher spectral resolution and signal-to-noise ratios.

The COS gratings used in this study along each sightline are specified in Table 5.2. The near ultraviolet (NUV) G230L grating has a resolution of 2 pixels or $\sim$ 0.82 Å at the wavelength of the Mg II $\lambda\lambda$2796,2803 doublet, which corresponds to $\sim$ 87 km s^{-1} on a velocity scale. The far ultraviolet (FUV) G140L grating has a resolution of 7 pixels or $\sim$ 0.55 Å at the wavelength of the C IV $\lambda\lambda$1548,1550 doublet, which corresponds to $\sim$ 106 km s^{-1}. Given the redshifts of the quasars, we should note that in certain wavelength regions there is the possibility of contamination by Lyα forest absorption. For example, Lyα forest absorption would potentially be visible near any Galactic or M31 Mg II absorption when the quasar's redshift is higher than $z_{em} \sim 1.3$ (i.e., in quasar 4) and near any Galactic or M31 C IV absorption when the quasar's redshift is higher than $z_{em} \sim 0.27$ (i.e., in all quasars except quasar 9). However, according to Weymann et al. (1998), the incidence of Lyα forest absorption lines with rest equivalent widths $\geq$ 0.24 Å at these relatively low redshifts is typically only about one line per 30 Å (about one line per 3200 km s^{-1}), so we did not necessarily anticipate too much confusion due to overlapping Lyα forest absorption. There might also be overlapping absorption due to unidentified metal-line systems. In §5.3 we note instances where Lyα forest absorption or other overlapping unidentified absorption appears to be a confusing factor.

Seven quasars were observed with both the NUV and FUV gratings, while three were

[1] Parallel imaging data were also obtained. These will be discussed in Thilker et al. (in prep.).

targeted with the NUV grating alone. These three had low FUV fluxes based on the *GALaxy Evolution eXplorer (GALEX)* telescope measurements, and so they were not observed. The NUV grating covers Fe II, Mn II, Mg II and Mg I transitions, while the FUV grating covers C IV, Si IV and several lower-ion transitions, as described in §5.3.

Pipeline flux-calibrated and wavelength-calibrated spectra were used for all the measurements, and no additional calibrations or re-calibrations were carried out. The wavelength scale is heliocentric, and measured velocity offsets relative to a transition of interest are made on this scale. Before making absorption-line measurements, the FUV spectra were re-binned to two pixels per resolution element and all spectra were normalized using an interactive algorithm which fitted splines to a quasar's observed continuum plus broad emission lines to derive a pseudo-continuum. We used the pipeline-provided standard deviation in flux to calculate the 1σ error in the normalized flux. When reporting errors in equivalent width measurements, we do not include (propagate) any errors that might arise during the process of defining a pseudo-continuum.

5.3 RESULTS

Figures 5.3–5.12 show the pseudo-continuum-normalized spectra near the predicted locations of metal lines along the ten sightlines, and Table 5.3a gives the measured metal-line absorption rest equivalent widths or upper limits for both M31 and Galactic lines. To make these measurements, heliocentric velocity locations for the absorbing gas had to be determined. The procedure for this is discussed below and the results on velocity offsets are given in Table 5.4.

For the low-ion transitions, the narrow Mn II lines (when present) allow for a more accurate determination of the velocity centroid of Galactic gas since they are well-fitted by single Gaussians. Therefore, the velocity offsets of low-ion Galactic absorption lines are defined by the centroids of Galactic Mn II λ2576 absorption for sightlines 2, 8, 9, and 10[2].

[2]The sightline 10 Galactic component is heavily blended with the M31 disk component, as described in the discussion of sightline 10.

The centroids of Galactic Mg II λ2796 are used to define the velocity offsets of absorption along other sightlines. The wavelength interval covered by the *COS-FUV* spectra includes transitions due to Si II, O I, C II, C II*, Fe II, and Al II. The centroids of these low-ion lines were fixed at the velocities determined from either the Mn II λ2576 line or Mg II λ2796 as indicated above. In the panels for each figure, dash-dot vertical lines are drawn at the determined velocity offsets of M31 and Galactic gas.

The only high-ion transitions detected in our spectra are due to C^{3+} and Si^{3+}. The velocity centroids of Gaussians fitted to the C IV λ1548 lines were allowed to vary since low-ion and high-ion absorption lines are not *a priori* required to have the same velocity centroids or line widths. The C IV λ1550 line and Si IV lines were then constrained to have the same velocity locations and widths as the C IV λ1548 line, within the uncertainties and resolution of the data. Inspection of the final fits suggests that this was a reasonable constraint.

The 1σ error in the normalized flux is shown in the figures as a black dotted line. M31 and Galactic absorption transitions that are identified at a level of significance $> 2\sigma$ are indicated in the figures by red profiles. A $> 2\sigma$ rest equivalent width detection threshold is an appropriate criterion for identifying absorption because we already know the approximate velocity location of M31 absorption (e.g., from M31's 21 cm emission). We also searched for significant absorption in a wider velocity window. Gaussian profiles are fitted to detected absorption. If more than one Gaussian is required to fit the data, we show the individual Gaussians as red dashed profiles, visible above the solid red profile. In the absence of multiple Gaussians, the red solid profile will lie on top of the red dashed profile, and the red dashed profile will not be visible. However, the measurements indicated by the red dashed profiles are what we report in Tables 5.3a and 5.4. As noted earlier, the positions of most low-ion lines are fixed by the centroid of either the Mn II λ2576 or the Mg II λ2796 line; however, their widths are allowed to vary in order to obtain the best fit. In a few cases, even the velocity offsets had to be allowed to vary up to one resolution element in order to obtain a satisfactory fit. Also, while performing the fits, we identified some absorption in the spectra which were likely blends resulting from a real M31 or Galactic absorption line plus overlapping or nearby absorption due to, for example, Lyα forest absorption, some other unrelated absorption, or even related absorption such as C II λ1334.5 and C II* λ1335.7. When this happened, we

fitted Gaussians to these nearby absorption components in order to better isolate the M31 and Galactic absorption transition of interest. We refer to this as deblending. However, when we report results in Tables 5.3a and 5.4, as noted earlier, only absorption taken to be due to the designated transition of interest in M31 or the Galaxy is reported and shown on the figures. Other nearby absorption lines which were fitted in order to isolate M31 and Galactic gas are shown as green dashed Gaussian profiles. The identifications and measurements of M31 and Galactic lines in the presence of confusing overlapping or nearby absorption should be considered less secure.

When a line is not detected (i.e., the detection is $< 2\sigma$) at its expected velocity offset, or nearby absorption not due to the transition of interest appears to be present, a red dotted Gaussian profile with FWHM equal to the spectrograph resolution (i.e., ~ 0.82 Å or ~ 87 km s^{-1} for the NUV lines and ~ 0.55 Å or ~ 106 km s^{-1} for the FUV lines) is shown on the figures to indicate the reported upper limit. If no overlapping or nearby confusing absorption is present, this is just the 2σ upper limit on equivalent width generated from the error in normalized flux. However, if overlapping or nearby absorption is present, the upper limit is determined from the strength of this overlapping or nearby absorption. Lacking evidence that a low-oscillator-strength transition should be present along a particular sightline, we would attribute any significant detected absorption as due to overlapping absorption, and list it as an upper limit.

In cases where the velocity of an M31 absorption line overlaps with the velocity of a different Galactic absorption line, for example, the M31 C IV λ1550 and the Galactic C IV λ1548 lines, or the M31 Si II λ1304 and the Galactic O I λ1302 lines along sightlines 1, 3, and 4 (Figures 5.3, 5.5, and 5.6), we assign the absorption to the Galactic absorption system. The measurement is listed in Table 5.3a only for the Galactic absorption line.

The bottom panels for sightlines 5 through 10 (Figures 5.7–5.12) show H I 21 cm emission profiles extracted from the GBT data of Thilker et al. (2004). The intensities are scaled to accentuate the very weak emission signal from M31. The dash-dot horizontal line drawn in each 21 cm panel marks the location of zero intensity. The H I 21 cm emission disk of M31 extends out to ~ 33 kpc as determined from the $N_{HI} = 1.9 \times 10^{18}$ cm^{-2} column density contour (5.1), and no H I 21 cm measurements exist at the positions of quasars 1 through

4. Therefore, to estimate equivalent width upper limits for these four sightlines, we have assumed that M31's 21 cm rotation curve is flat at large galactocentric distances and we extrapolate the sightline 21 cm emission velocity out to the positions of quasars 1 through 4 to predict a probable velocity location of absorbing gas. Note that M31 is nearly edge-on and inclined ~ 78 deg on the plane of the sky. Thus a very small inclination correction is needed since $\sin(78) = 0.978$. Then the assumption of a flat rotation curve suggests that if metal-line absorption is present in M31's outer regions, we might find it near a heliocentric velocity location of ~ -525 km s^{-1}. This is where we determine M31 equivalent width upper limits for sightlines 1 through 4. We note that the choice of where to measure potential absorption in the four outer sightlines is purely an algorithmic decision given that flat rotation curves exist. We also considered the Tamm et al. (2012) study which derives a rotation curve out to a galactocentric radius of ~ 500 kpc. They employ, among other diagnostics, observations of stellar streams (Fardal et al. 2006) and satellite galaxies (Tollerud et al. 2012) which yield rotational velocities of ~ 160 km s^{-1} near the position of our outermost sightline. This translates to a heliocentric velocity of -466 km s^{-1} since our outer sightlines lie on the approaching, SW, side of M31. This is well within one resolution element (§2.3) of our assumed velocity location of -525 km s^{-1}. Therefore, we are confident that we have not missed any absorption from gas in M31 along the outer four sightlines that is above our detection limits.

Tables 5.3a and 5.4 summarize all of the measurements and upper limits, both for M31 and the Milky Way Galaxy. A discussion of individual sightlines follows (see Figures 5.3–5.12), with emphasis on what they reveal about M31 gas. The discussions are presented in order of increasing sightline right ascensions. This ordering generally follows decreasing impact parameter, b, except for the last three sightlines which all have $13 < b < 18$ kpc. At the beginning of each discussion we indicate the maximum wavelength at which Lyα forest absorption might cause blending and confusion, $\lambda_{forest} \sim 1216(1 + z_{em})$ Å.

1. **0018+3412 ($b = 111.9$ kpc, $\lambda_{forest} < 1760$ Å, Fig. 5.3):** No significant M31 absorption is detected along this sightline, and H I 21 cm emission maps of M31 do not extend this far out. Therefore, rest equivalent width upper limits on absorption were measured at -525 km s^{-1} as described earlier. At this velocity location, the red dotted Gaussian

lines show the velocity positions and rest equivalent widths of hypothetical unresolved absorption lines with 2σ levels of significance, and these are the upper limits reported in Table 5.3a. Galactic absorption is clearly present. Suspected confusion (blending) due to overlapping Lyα forest absorption is apparent for the Si II λ1260, Si II λ1304, O I λ1302, C II λ1334, and C IV λ1550 Galactic absorption lines. The method we used to measure such cases was discussed above.

2. **0024+3439 ($b = 98.6$ kpc, $\lambda_{forest} < 2216$ Å, Fig. 5.4):** As in the previous sightline, no significant M31 absorption is detected, and H I 21 cm emission maps do not extend this far out, so upper limits were measured at a velocity location of -525 km s^{-1}. Only NUV spectra of this quasar were obtained. Therefore, for example, the C IV region was not observed. A Galactic MnII λ2576 line is detected at a level of significance of $\sim 3\sigma$, however the two weaker members of the triplet are not detected at $> 2\sigma$. Galactic Mg II and Fe II absorption are clearly detected.

3. **0030+3700 ($b = 64.4$ kpc, $\lambda_{forest} < 2720$ Å, Fig. 5.5):** Again, no significant absorption lines from M31 are detected at or near -525 km s^{-1}, and the 21 cm emission maps do not extend out this far. Among the significant Galactic absorption lines that are detected, the measurements of Si II λ1260, Si IV λ1393, C IV λ1548 and Fe II λ2586 were made in the presence of overlapping unrelated absorption using the method described earlier. While only the stronger members of the Galactic Si IV and C IV doublets are detected, the rest equivalent width upper limits of the weaker members of these doublets are consistent with their expected strengths based on $f\lambda$ values. In addition to the detected Galactic metal absorption lines, at least two partial Lyman limit absorption systems are present in the spectrum. One at $z \sim 0.5$ is clearly visible in the FUV observation (not shown). Based on the difference in flux level between the FUV and NUV observations, and the presence of some strong Lyα forest absorption near and just shortward of the Lyα broad emission line, at least one other Lyman limit absorption system is likely to be present at $1.21 < z < 1.24$. However, it is not directly visible in our observations because it falls in the wavelength gap between the FUV and NUV spectra.

4. **0031+3727 ($b = 57.6$ kpc, $\lambda_{forest} < 2797$ Å, Fig. 5.6):** As with the first three sightlines, no significant absorption lines from M31 gas are seen, and the 21 cm emission

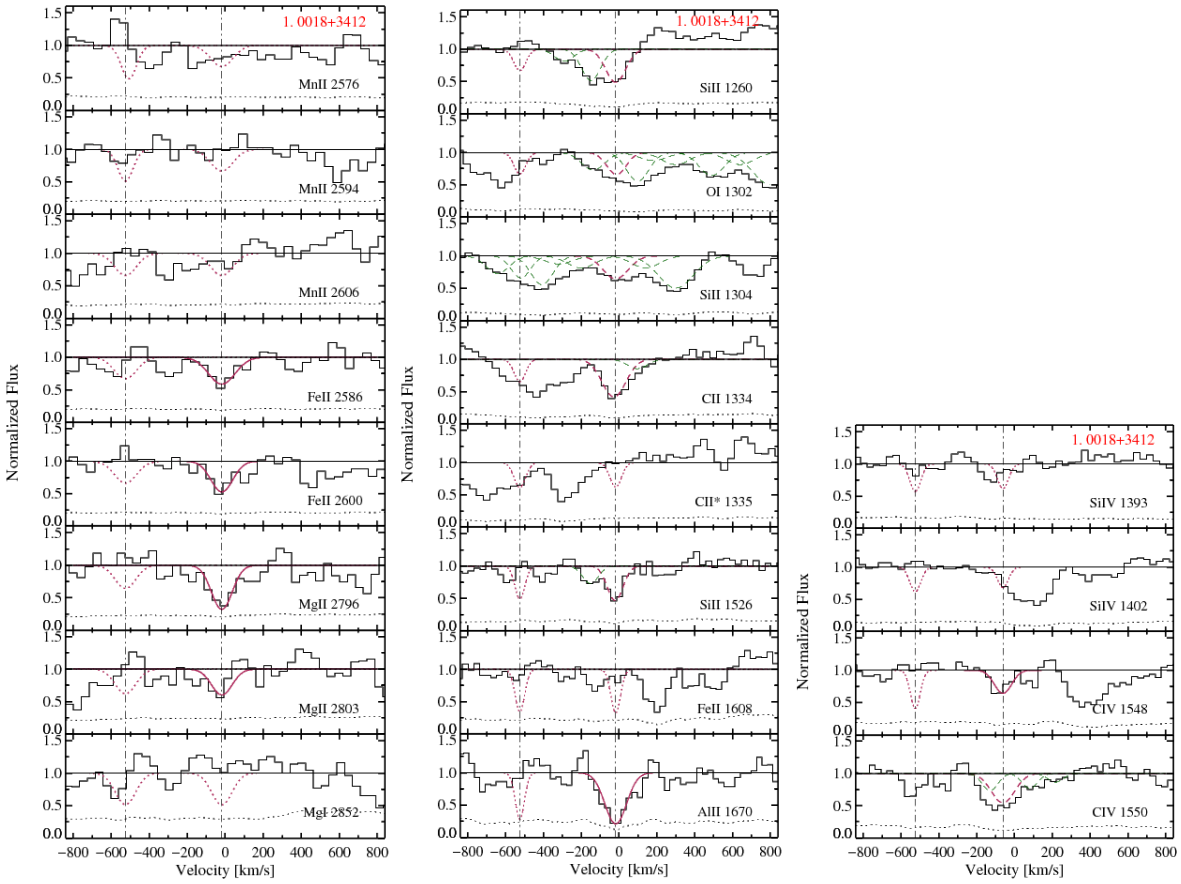

Figure 5.3: Normalized spectra versus velocity for the labeled transitions in the spectra of 0018+3412. The black dotted line is the 1σ error spectrum. All velocities are heliocentric. The vertical dot-dashed lines are Milky Way (near 0 km s^{-1}) and M31 detected or assumed velocities. See Table 5.4. Fits to M31 and Galactic absorption lines detected at a significance $> 2\sigma$ are shown as heavy dashed (if part of a blend) or solid red lines. See text. Dotted red lines indicate 2σ upper limits. Green dashed lines are components within a blend that are unrelated to M31 or Galactic absorption.

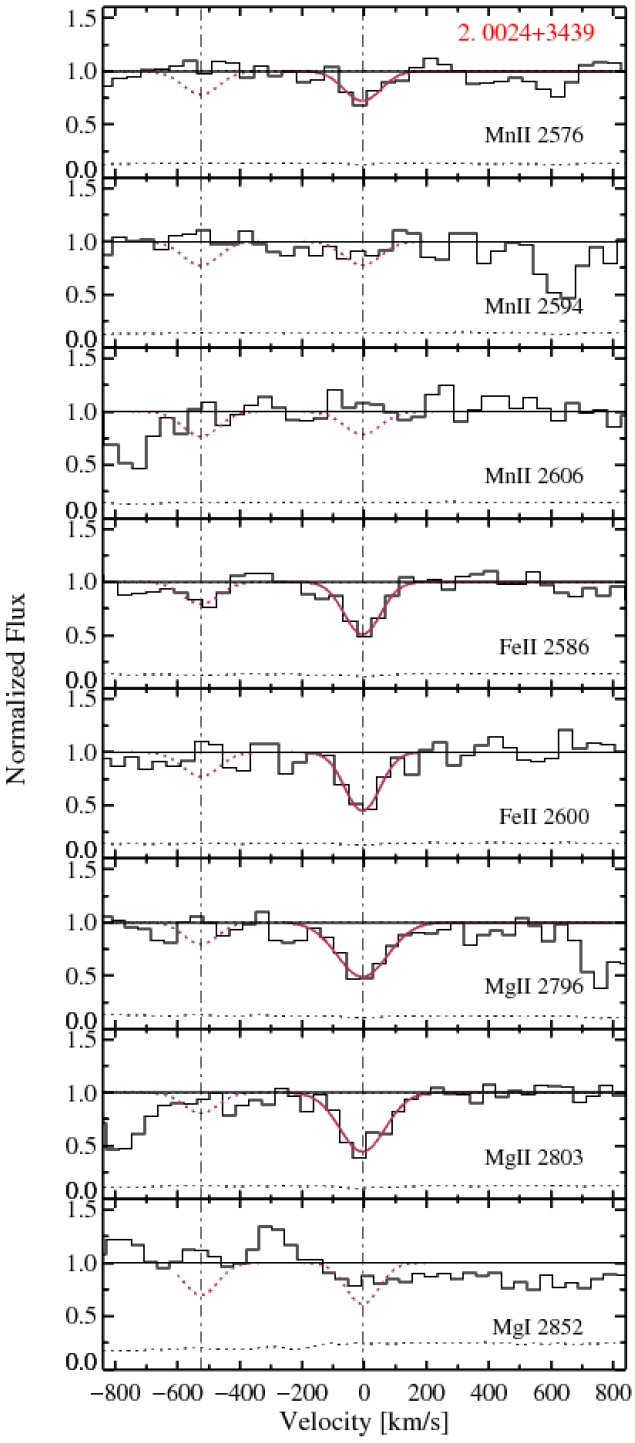

Figure 5.4: Same as Figure 5.4, but for 0024+3439. No FUV spectra of this quasar were obtained.

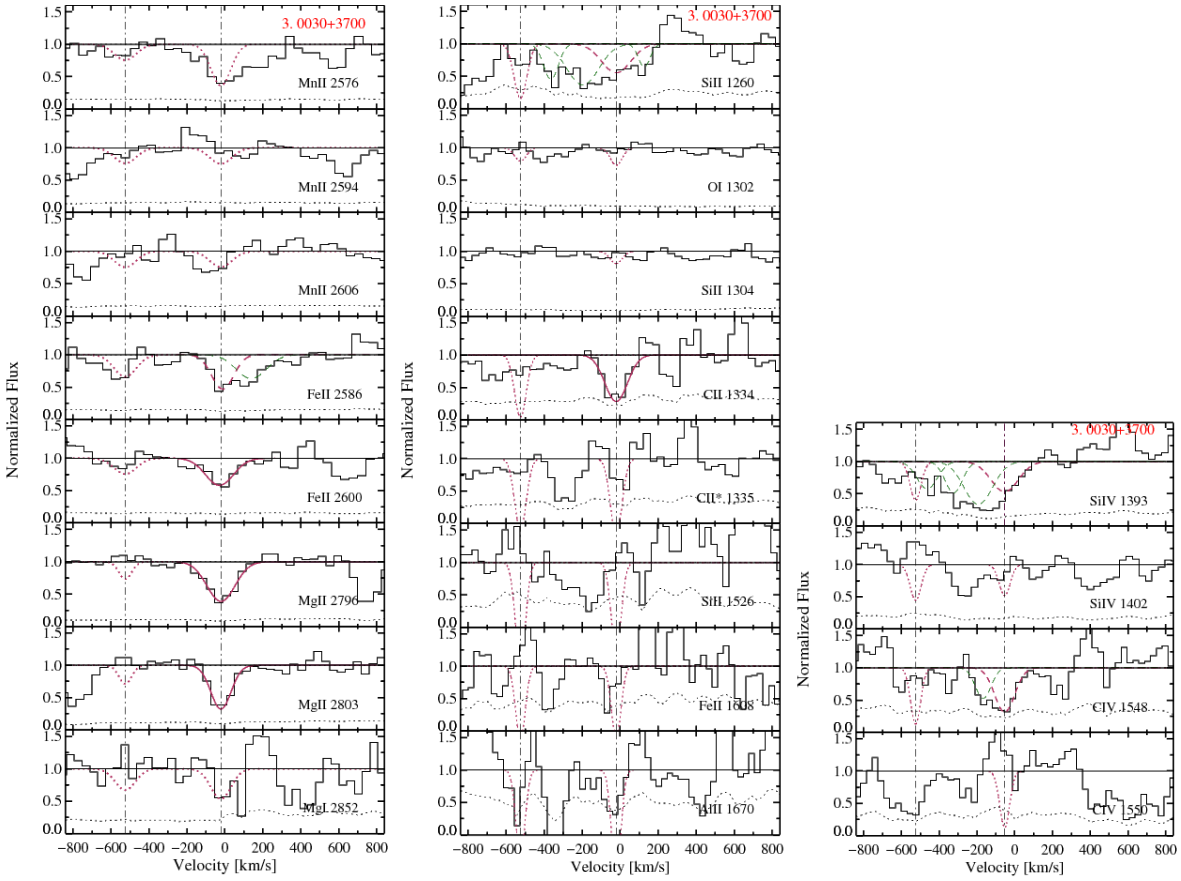

Figure 5.5: Same as Figure 5.3, but for 0030+3700.

map does not extend out this far. M31 upper limits were estimated at -525 km s^{-1} for both the high and low ions. Galactic absorption is clearly detected for some transitions, but the measurements of Si II λ1260, C II λ1334, Si II λ1526, Fe II λ1608, and Fe II λ2600 required deblending due to the presence of unrelated overlapping absorption.

5. **0032+3946 (b = 31.5 kpc, $\lambda_{forest} < 2600$ Å, Fig. 5.7):** Only NUV spectra were obtained for this quasar. An M31 Mg II λ2796 absorption line with a significance of 2σ at a heliocentric velocity of -453 km s^{-1} appears to be present (see Table 5.3a), however a corresponding 2-pixel-wide absorption feature near the expected position of Mg II λ2803 has a significance $< 2\sigma$. If present, this absorption may originate at the southwest edge of M31's disk (see Figure 5.1). Apart from strong Galactic emission, the GBT 21 cm data along this sightline (bottom panel of Figure 5.7) shows evidence for M31 emission between -509 and -459 km s^{-1}. Although the resolution of the NUV spectrum is ~ 0.82 Å (~ 87 km s^{-1}) at the position of Mg II, the centroid of the absorption line can be estimated with an uncertainty of ~ 6 km s^{-1} (see §5.4). Thus, the identified Mg II λ2796 feature at -453 km s^{-1} is near the maximum velocity of observed 21 cm emission. Keeping in mind the limitations of using H I 21 cm emission observations to determine H I column densities (§5.2.1), we find $N_{HI} \approx 2.5 \times 10^{18}$ atoms cm^{-2} along this sightline. Very significant Galactic Mg II and Fe II absorption is detected along this sightline, but the Galactic Fe II λ2586 line was deblended to separate it from unrelated nearby absorption.

6. **0037+3908 (b = 30.5 kpc, $\lambda_{forest} < 2590$ Å, Fig. 5.8):** Only NUV spectra were obtained for this quasar. Absorption from M31 gas is not detected. However, apart from the strong Galactic emission, the GBT data along this sightline reveal M31 21 cm emission between -542 and -475 km s^{-1} (bottom panel of Figure 5.8), with an integrated column density of $N_{HI} = 2.5 \times 10^{18}$ atoms cm^{-2} (see §5.2.1). The 2σ upper limits on M31 absorption are made at the central velocities predicted by the observed M31 21 cm emission. Very significant Galactic Mg II and Fe II absorption is detected along this sightline. The Galactic Fe II λ2586 and Fe II λ2600 lines were deblended to separate them out from unrelated nearby absorption.

7. **0040+3915 (b = 26.9 kpc, $\lambda_{forest} < 2552$ Å, Fig. 5.9):** Only the velocity profiles

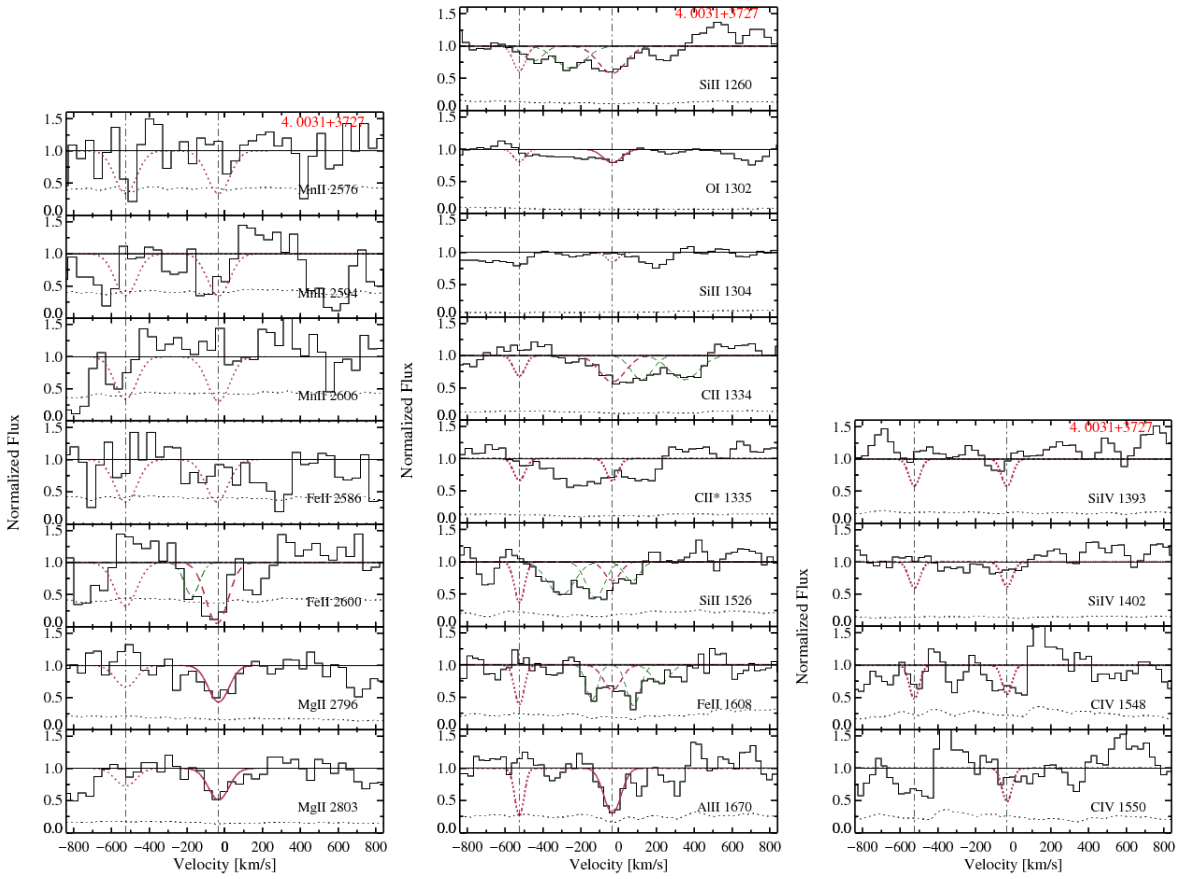

Figure 5.6: Same as Figure 5.3, but for 0031+3727.

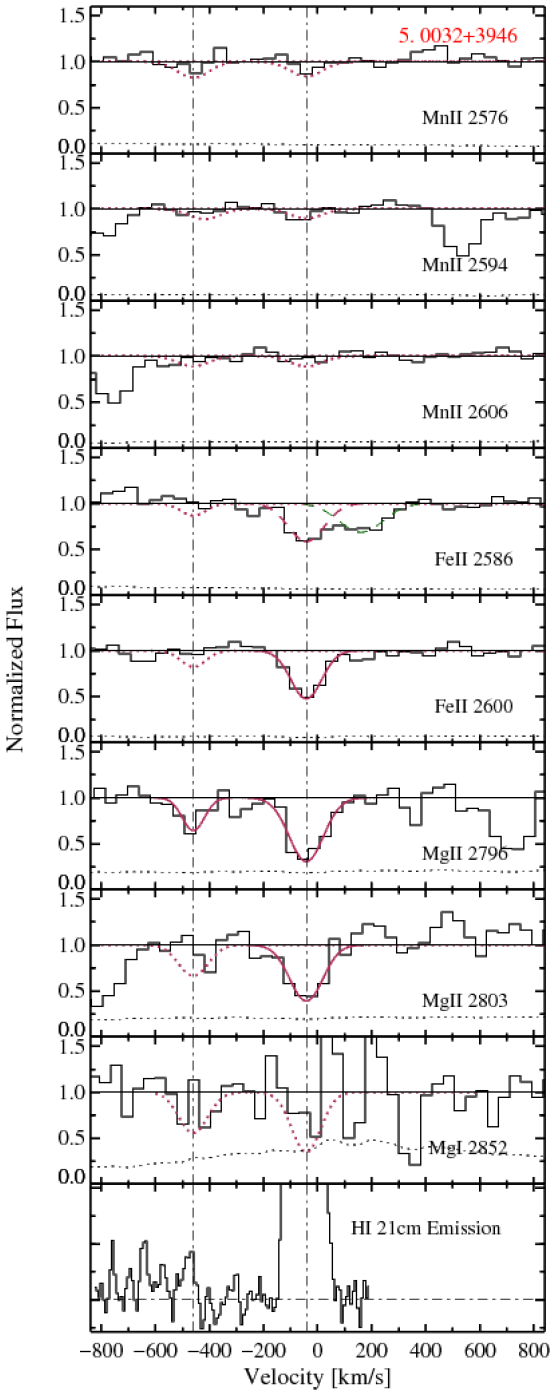

Figure 5.7: Same as Figure 5.3, but for 0032+3946. In addition, the H I 21 cm emission profile extracted from the GBT data of Thilker et al. (2004) is shown in the bottom panel. The intensities are scaled to accentuate the very weak emission signal from M31. The dash-dot horizontal line drawn in the 21 cm panel marks the location of zero intensity. No FUV spectra of this quasar were obtained.

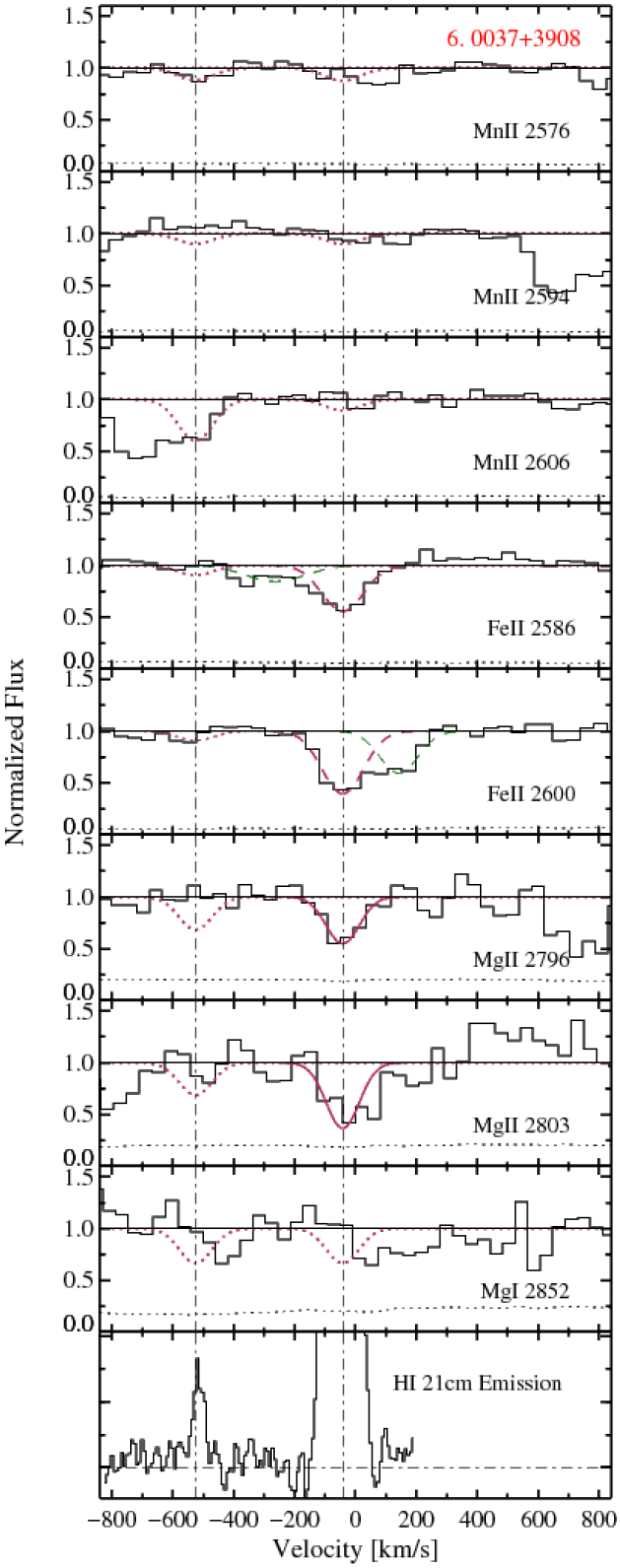

Figure 5.8: Same as Figure 5.7, but for 0037+3908. No FUV spectra were obtained for this quasar.

in the vicinity of Mg II and Mg I are visible in our observations for two reasons. First, the quasar spectrum exhibits intrinsic broad absorption lines (BALs) and the N V BAL trough overlaps the Mn II and Fe II absorption-line regions. This prevents useful measurements of M31 and Galactic lines in those regions. Second, the FUV spectrum shows no useful continuum flux, possibly due to strong shorter-wavelength BALs and/or overlapping intervening Lyman limit absorption. Mg II λ2796 due to M31 gas appears as two absorption components in the NUV spectrum. The noise characteristics of the spectrum are worse in the corresponding Mg II λ2803 region, and two absorption components are not seen (a single Gaussian was fitted to the absorption), but we give this lower weight due to the higher noise. The two vertical dash-dot lines at -389 km s^{-1} and -513 km s^{-1} mark the velocity positions of the two M31 Mg II λ2796 absorption components. The sightline passes through an HVC (see Figure 5.1), whose 21 cm emission profile can clearly be seen in the bottom panel of the figure peaking at ~ -500 km s^{-1}. The GBT data reveal that this 21 cm emission extends between -542 and -442 km s^{-1}. Thus, the two Mg II absorption components at -389 km s^{-1} and -513 km s^{-1} may correspond to M31 halo gas and HVC gas, respectively, with the halo component showing no apparent 21 cm emission. From the WSRT 21 cm emission data, the integrated H I column density in the HVC is estimated to be $N_{HI} = 9.5 \times 10^{19}$ atoms cm^{-2} (see §5.2.1). Very significant Galactic Mg II absorption is present along this sightline.

8. 0043+4016 ($b = 13.4$ kpc, $\lambda_{forest} < 2545$ Å, Fig. 5.10): This is the lowest impact parameter sightline. M31 low-ion absorption from Si II λ1260 and C II λ1334 is detected, and high-ion absorption from C IV λ1548 is detected, but the Si II λ1260 and C IV λ1548 lines had to be deblended from overlapping unrelated absorption. Given that the 21 cm emission extends over a large range in velocity, we cannot rule out that all the absorption features within the C IV λ1548 blend are due to C IV λ1548 absorption over a wide velocity range. Confirmation would require a higher signal-to-noise spectrum; here, we identify the lowest velocity component with the M31 C IV λ1548 absorption line. The low-ions are centered at ~ -336 km s^{-1} and the high-ions are centered at ~ -340 km s^{-1}. However, Mg II and Fe II absorption lines from M31 gas were not detected. The GBT data show that 21 cm emission from M31 exists along this sightline between -559

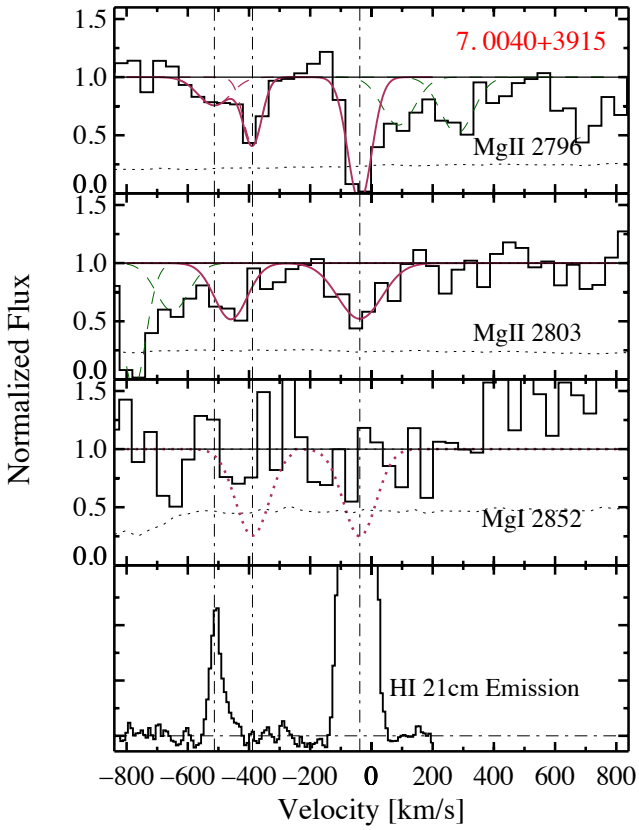

Figure 5.9: Same as Figure 5.7, but for 0040+3915. The M31 HVC that is detected in 21 cm at −513 km/s, is also detected in the Mg IIλ2796 line. The two Mg IIλ2803 components are too weak to be resolved with these data. The FUV data are not shown because the spectrum had no flux presumably due to an intervening Lyman limit system.

km s^{-1} and -326 km s^{-1}, with a total integrated column density of $N_{HI} = 1.2 \times 10^{19}$ atoms cm^{-2}. We note that the absorption-line velocities are coincident with the peak in the 21 cm emission-line spectrum (bottom panels of Figure 5.10). Many significant Galactic absorption lines are present. Galactic Si II λ1260 and C IV λ1550 had to be deblended to separate them out from unrelated overlapping absorption.

9. **0043+4234 ($b = 17.4$ kpc, $\lambda_{forest} < 1448$ Å, Fig. 5.11):** The sightline to this quasar passes "above" the H I 21 cm emission disk of M31 on the receding, northwest, side (see Figure 5.1). Due to the location of the sightline, the detected M31 and Galactic absorption lines needed to be deblended from each other. We used two-component Gaussian fits with fixed velocity components to do this. Measurements of the Si II λ1260, C II λ1334.5 (and C II* λ1335.7), Si IV λ1393, and Al II λ1670 absorption lines are further complicated by other overlapping absorption. For low-ion absorption the velocity centroid for the Galactic lines was fixed using Mn II λ2576, while allowing the position of the M31 low-ion velocity centroid to vary until the best least-squares solution was found. Deblending indicates that the detected M31 low-ion gas, which gives rise to transitions of Si II, C II, Al II, Fe II and Mg II, is located at -234 km s^{-1}, and the Galactic low-ion gas is located at -73 km s^{-1}. It is notable that along this sightline there is a detection of Galactic C II* λ1335.7. The M31 high-ion gas, which gives rise to transitions of Si IV λ1393 and C IV λ1548, are also members of a multi-component blend with Galactic lines. Using a procedure similar to the one used for the low-ions, we find that the M31 high-ion gas is at -191 km s^{-1} and the Galactic high-ion gas is at -1 km s^{-1}. GBT data reveal M31 21 cm emission between -259 km s^{-1} and -93 km s^{-1}, with a total integrated column density of $N_{HI} = 8 \times 10^{18}$ cm^{-2} (see §5.2.1). The higher velocity edge of the M31 21 cm emission is uncertain since it may overlap with Galactic 21 cm emission.

10. **0046+4220 ($b = 17.5$ kpc, $\lambda_{forest} < 1588$Å, Fig. 5.12):** To infer what gaseous structures exist along this sightline we are guided by the observed GBT H I 21 cm emission velocity profile, which is shown in the bottom panels of Figure 5.12. An inset in the bottom left panel shows the entire 21 cm profile. Most notably, the weaker 21 cm peak near -5 km s^{-1} represents Galactic emission, while the stronger 21 cm emission peak near -55 km s^{-1} represents M31's disk; however, such a velocity separation cannot be

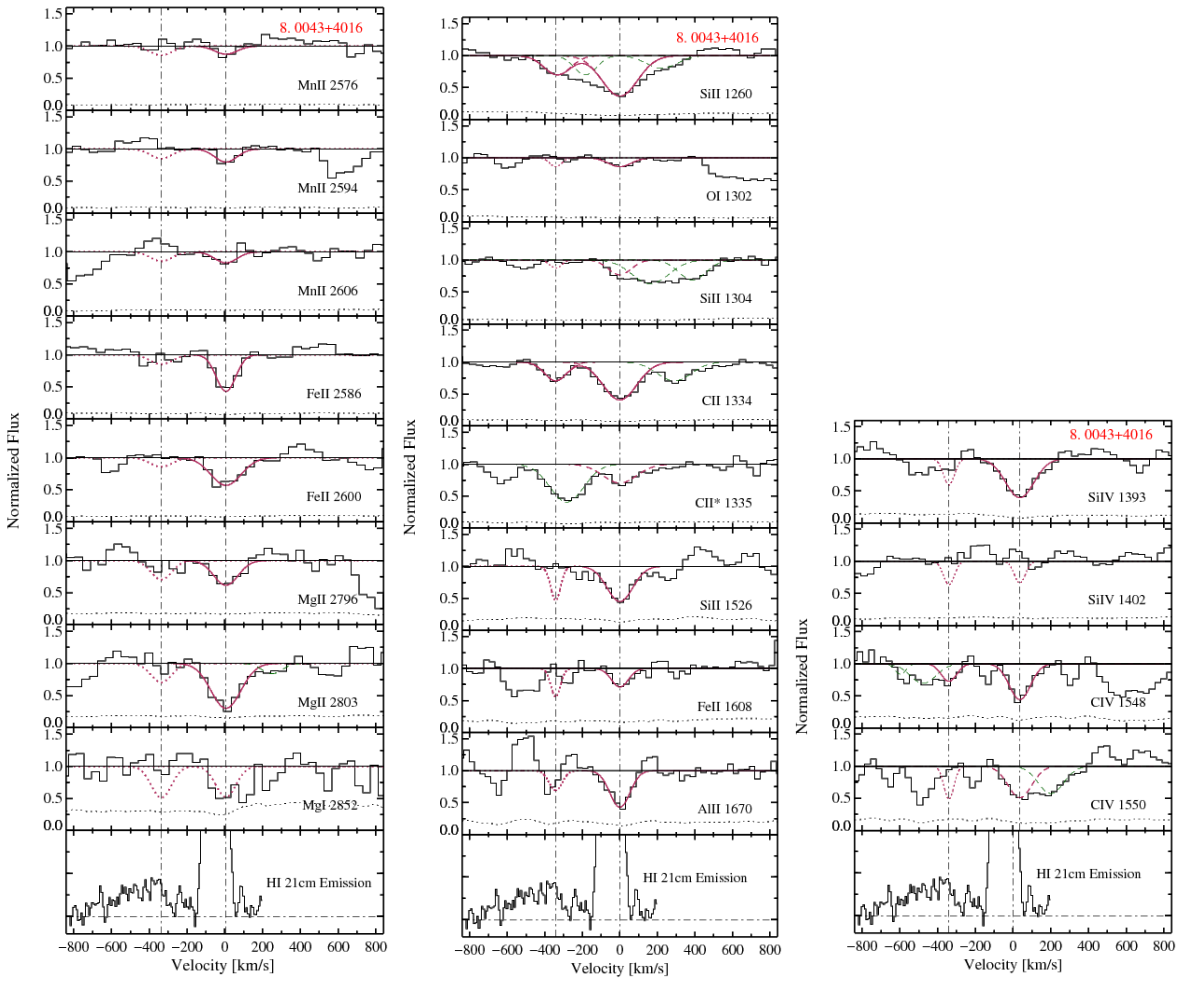

Figure 5.10: Same as Figure 5.7, but for 0043+4016. FUV data obtained for this quasar are also shown.

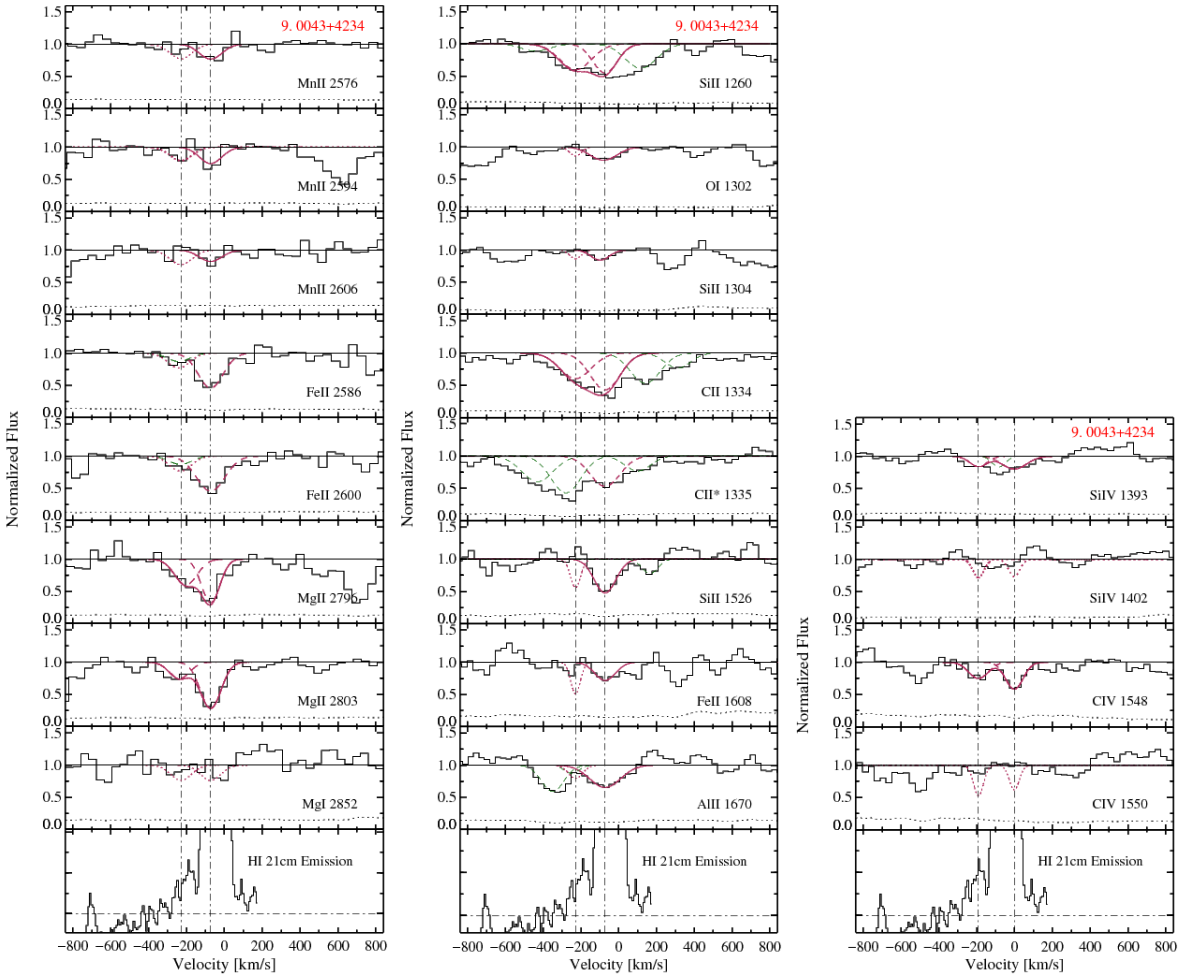

Figure 5.11: Same as Figure 5.7, but for 0043+4234. FUV data obtained for this quasar are also shown.

distinguished in the COS G140L and G230L absorption-line spectra. More generally, the entire 21 cm velocity profile and the detected low-ion absorption lines have allowed us to infer the existence of five gaseous structures along this sightline: one near −5 km s^{-1} (Galactic gas), one near −55 km s^{-1} (M31 disk gas), one near −195 km s^{-1} (M31 halo gas), one near −334 km s^{-1} (a M31 HVC), and one near −409 km s^{-1} (a second M31 HVC). As with sightline 9, detected Galactic and M31 absorption lines needed to be deblended from each other, but the blending along this sightline is more severe. In particular, the low-ion absorption detected near −40 km s^{-1} must be a blend of Galactic gas and M31 disk gas, with most of the absorption being due to M31 disk gas. This Galactic+M31 blended component is included under the heading of "Milky Way Absorption Lines" in Table 5.3a but with a footnote. Absorption due to C II* λ1335.7 is among the many transitions detected in this component (see Table 5.3a). A weak (barely significant) blended Galactic and M31 high-ion absorption component is located near −35 km s^{-1}. The 21 cm emission profile allows us to estimate that the Galactic component peaking near −5 km s^{-1} has $N_{HI} = 4.0 \times 10^{20}$ atoms cm^{-2} and the M31 disk component peaking near −55 km s^{-1} has $N_{HI} = 1.5 \times 10^{21}$ atoms cm^{-2}. Aside from this first blended absorption component, a second low-ion absorption component is seen displaced toward lower velocities by ∼ 155 km s^{-1}, close to the edge of the H I 21 cm emission profile, which we take as evidence for halo gas. However, measurements of the Si II λ1260, O I λ1302, Si II λ1304, C II λ1334.5 (and C II* λ1335.7), Si II λ1526, C IV λ1548, and Al II λ1670 absorption lines are complicated by overlapping or nearby absorption. Deblending indicates that the M31 low-ion halo gas component is near −195 km s^{-1}, and this gives rise to absorption due to Si II, O I, C II, Al II, Fe II, and Mg II. Deblending also indicates that a high-ion absorption component is located near −152 km s^{-1}; it is clearly present in C IV but possibly not Si IV. The 21 cm emission allows us to estimate that the M31 halo component peaking near −195 km s^{-1} has $N_{HI} = 7 \times 10^{19}$ atoms cm^{-2}. The velocity locations of the above described absorption components for the low ions and high ions are shown as vertical dot-dashed lines in the panels, including the lower left inset panel. In addition, the GBT 21 cm observations also reveal gas from two M31 HVCs near −334 km s^{-1} (between −342 km s^{-1} and −326 km s^{-1}), and near −409 km s^{-1} (between −426

km s^{-1} and -392 km s^{-1}). The total integrated column densities along the sightlines to these HVCs are $N_{HI} = 2 \times 10^{18}$ atoms cm^{-2} and $N_{HI} = 2.5 \times 10^{18}$ atoms cm^{-2}, respectively. We do not detect metal-line absorption near the velocities of these HVCs, so we have not used vertical lines to mark their velocity locations in Figure 5.12. Thus, using standard quasar absorption line jargon, we conclude that, given the estimated N_{HI} values for the four detected M31 velocity components, we have detected a DLA system (M31 disk gas), a sub-DLA system (M31 halo gas), and two Lyman limit systems (two M31 HVCs).

Finally, we point out that the blended low-ion absorption near -40 km s^{-1} in sightline 10 is the only system which reaches DLA H I column densities (i.e., $N_{HI} \geq 2 \times 10^{20}$ atoms cm^{-2}). As described above, it is due to a blend of Galactic gas and M31 disk gas. DLAs are the quasar absorption-line systems used to track the evolution of neutral gas in the Universe at low (Rao et al. 2006) and high (e.g., Noterdaeme et al. 2012) redshift. The strength of the Mg II λ2796 and Fe II λ2600 absorption lines in this component are consistent with criteria used in Mg II-selected DLA searches (Rao et al. 2006).

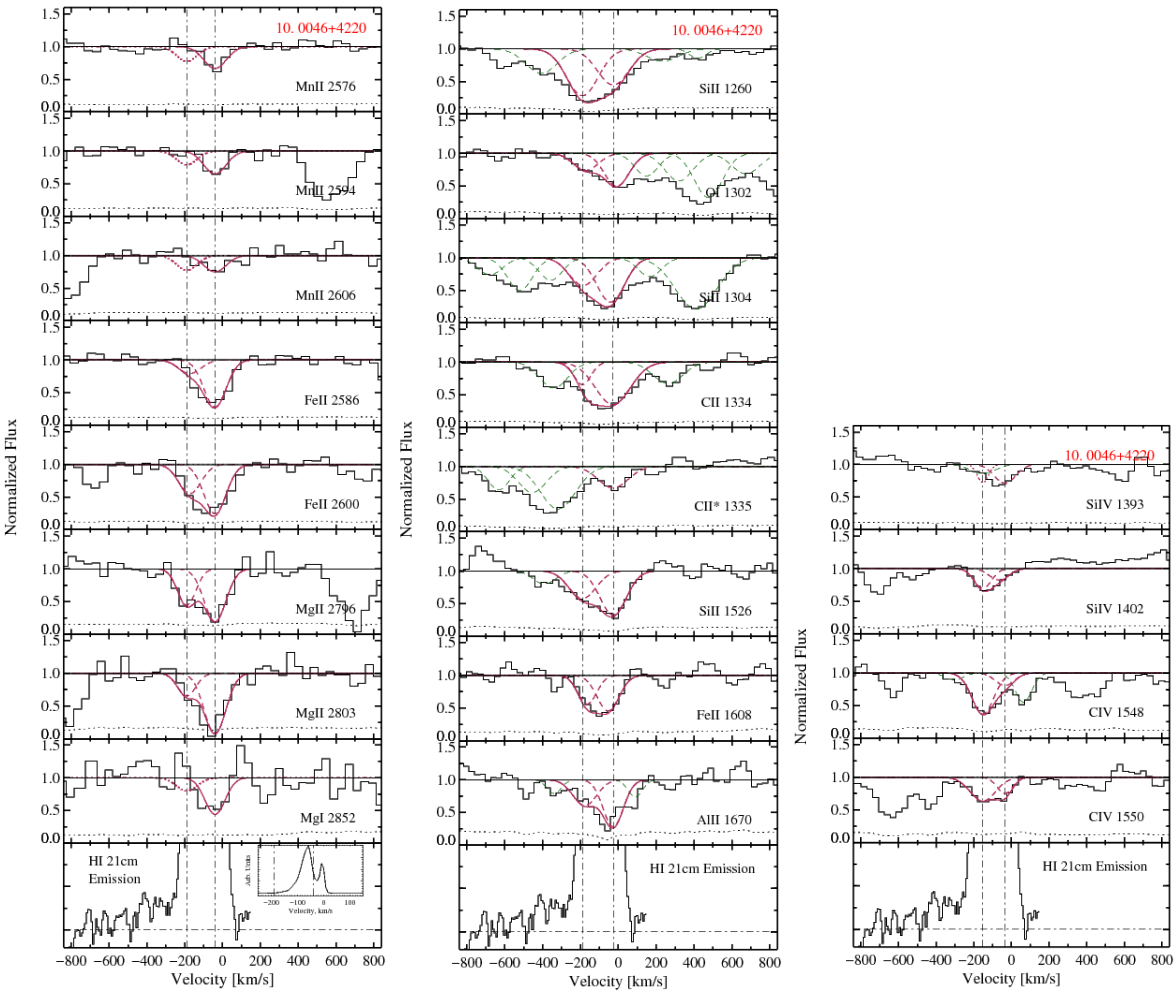

Figure 5.12: Same as Figure 5.7, but for 0046+4220. FUV data obtained for this quasar are also shown.

Table 5.3a: Rest Equivalent Width Measurements[a]

Line	1. 0018+3412 REW (Å)	2. 0024+3439 REW (Å)	3. 0030+3700 REW (Å)	4. 0031+3727 REW (Å)	5. 0032+3946 REW (Å)	6. 0037+3908 REW (Å)	7. 0040+3915 REW (Å)	8. 0043+4016 REW (Å)	9. 0043+4234 REW (Å)	10. 0046+4220[b] REW (Å)
M31 Absorption Lines										
SiII 1260	≤ 0.113	···	≤ 0.300	≤ 0.132	···	···	···	0.225 ± 0.042	0.259 ± 0.054	0.544 ± 0.042
OI 1302	≤ 0.113	···	≤ 0.093	≤ 0.065	···	···	···	≤ 0.048	≤ 0.048	0.187 ± 0.047
SiII 1304	···	···	···	···	···	···	···	≤ 0.043	≤ 0.046	0.341 ± 0.036
CII 1334	≤ 0.106	···	≤ 0.303	≤ 0.121	···	···	···	0.192 ± 0.042	0.318 ± 0.039	0.234 ± 0.044
CII* 1335	≤ 0.131	···	≤ 0.373	≤ 0.118	···	···	···	···	···	···
SiIV 1393	≤ 0.145	···	≤ 0.205	≤ 0.143	···	···	···	≤ 0.139	0.085 ± 0.042	≤ 0.095
SiIV 1402	≤ 0.131	···	≤ 0.188	≤ 0.137	···	···	···	≤ 0.125	≤ 0.098	0.156 ± 0.065
SiII 1526	≤ 0.173	···	≤ 0.523	≤ 0.214	···	···	···	≤ 0.180	≤ 0.152	0.386 ± 0.066
FeII 1608	≤ 0.223	···	≤ 0.384	≤ 0.209	···	···	···	≤ 0.151	≤ 0.168	0.267 ± 0.076
AlII 1670	≤ 0.244	···	≤ 0.453	≤ 0.253	···	···	···	≤ 0.194	≤ 0.110	0.258 ± 0.087
CIV 1548	≤ 0.202	···	≤ 0.298	≤ 0.180	···	···	···	0.146 ± 0.061	0.167 ± 0.087	0.651 ± 0.098
CIV 1550	···	···	···	···	···	···	···	≤ 0.175	≤ 0.161	0.320 ± 0.070
Milky Way Absorption Lines										
SiII 1260	0.289 ± 0.054	···	0.358 ± 0.081	0.320 ± 0.053	···	···	···	0.636 ± 0.048	0.689 ± 0.044	0.479 ± 0.056
OI 1302	0.189 ± 0.086	···	≤ 0.071	0.113 ± 0.042	···	···	···	0.107 ± 0.021	0.162 ± 0.032	0.358 ± 0.050
SiII 1304	0.258 ± 0.033	···	≤ 0.065	≤ 0.050	···	···	···	0.154 ± 0.029	0.084 ± 0.032	0.545 ± 0.045
CII 1334	0.410 ± 0.095	···	0.448 ± 0.128	0.309 ± 0.048	···	···	···	0.594 ± 0.034	0.592 ± 0.036	0.669 ± 0.032
CII* 1335	≤ 0.129	···	≤ 0.401	≤ 0.115	···	···	···	0.295 ± 0.044	0.413 ± 0.044	0.288 ± 0.039
SiIV 1393	≤ 0.131	···	0.396 ± 0.121	≤ 0.144	···	···	···	0.533 ± 0.036	0.149 ± 0.056	0.189 ± 0.095
SiIV 1402	≤ 0.108	···	≤ 0.163	≤ 0.130	···	···	···	≤ 0.116	≤ 0.104	0.133 ± 0.065
SiII 1526	0.286 ± 0.046	···	≤ 0.462	0.155 ± 0.097	···	···	···	0.483 ± 0.062	0.706 ± 0.093	0.761 ± 0.092
FeII 1608	≤ 0.231	···	≤ 0.372	0.243 ± 0.092	···	···	···	0.175 ± 0.076	0.119 ± 0.060	0.424 ± 0.078
AlII 1670	0.634 ± 0.063	···	≤ 0.557	0.443 ± 0.102	···	···	···	0.427 ± 0.082	0.274 ± 0.066	0.440 ± 0.099
CIV 1548	0.213 ± 0.077	···	0.471 ± 0.261	≤ 0.155	···	···	···	0.270 ± 0.110	0.252 ± 0.078	0.264 ± 0.079
CIV 1550	0.365 ± 0.074	···	≤ 0.299	≤ 0.177	···	···	···	0.378 ± 0.095	≤ 0.128	0.132 ± 0.066

[a] 2σ upper limits are tabulated for non-detections.
[b] In sightline 10, Milky Way absorption lines are blended with M31 disk gas. See the description in §3.
[c] The two measurements are M31 HVC and disk components, respectively. See Figure 5.9.

Table 5.3b: *Continued from Table 5.3a.*

Line	1. 0018+3412 REW (Å)	2. 0024+3439 REW (Å)	3. 0030+3700 REW (Å)	4. 0031+3727 REW (Å)	5. 0032+3946 REW (Å)	6. 0037+3908 REW (Å)	7. 0040+3915 REW (Å)	8. 0043+4016 REW (Å)	9. 0043+4234 REW (Å)	10. 0046+4220[b] REW (Å)
M31 Absorption Lines										
MnII 2576	≤ 0.447	≤ 0.274	≤ 0.307	≤ 0.829	≤ 0.218	≤ 0.150	···	≤ 0.181	≤ 0.285	≤ 0.243
MnII 2594	≤ 0.422	≤ 0.283	≤ 0.302	≤ 0.815	≤ 0.139	≤ 0.123	···	≤ 0.187	≤ 0.263	≤ 0.257
MnII 2606	≤ 0.428	≤ 0.291	≤ 0.311	≤ 0.829	≤ 0.138	≤ 0.498	···	≤ 0.182	≤ 0.285	≤ 0.259
FeII 2586	≤ 0.421	≤ 0.254	≤ 0.435	≤ 0.847	≤ 0.178	≤ 0.120	···	≤ 0.187	≤ 0.289	0.266 ± 0.115
FeII 2600	≤ 0.430	≤ 0.291	≤ 0.313	≤ 0.865	≤ 0.133	≤ 0.114	···	≤ 0.183	≤ 0.291	0.571 ± 0.112
MgII 2796	≤ 0.459	≤ 0.261	≤ 0.211	≤ 0.433	0.341 ± 0.171	≤ 0.405	0.304 ± 0.220[c]	≤ 0.379	0.554 ± 0.111	0.627 ± 0.112
···	···	···	···	···	···	···	0.412 ± 0.256[c]	···	···	···
MgII 2803	≤ 0.484	≤ 0.248	≤ 0.226	≤ 0.354	≤ 0.430	≤ 0.399	0.606 ± 0.208	≤ 0.377	0.285 ± 0.117	0.390 ± 0.122
MgI 2852	≤ 0.619	≤ 0.387	≤ 0.419	···	≤ 0.565	≤ 0.428	≤ 0.981	≤ 0.624	≤ 0.301	≤ 0.260
Milky Way Absorption Lines										
MnII 2576	≤ 0.417	0.356 ± 0.106	≤ 0.722	≤ 0.849	≤ 0.205	≤ 0.150	···	0.135 ± 0.067	0.297 ± 0.112	0.427 ± 0.093
MnII 2594	≤ 0.428	≤ 0.285	≤ 0.317	≤ 0.838	≤ 0.133	≤ 0.123	···	0.222 ± 0.074	0.325 ± 0.104	0.448 ± 0.100
MnII 2606	≤ 0.438	≤ 0.273	≤ 0.310	≤ 0.884	≤ 0.143	≤ 0.136	···	0.190 ± 0.082	0.226 ± 0.113	0.319 ± 0.100
FeII 2586	0.627 ± 0.222	0.626 ± 0.126	0.667 ± 0.163	≤ 0.838	0.602 ± 0.142	0.659 ± 0.078	···	0.632 ± 0.077	0.767 ± 0.147	0.919 ± 0.092
FeII 2600	0.591 ± 0.162	0.676 ± 0.139	0.671 ± 0.172	1.209 ± 0.312	0.646 ± 0.062	0.897 ± 0.131	···	0.755 ± 0.104	0.888 ± 0.186	0.965 ± 0.094
MgII 2796	0.869 ± 0.179	0.968 ± 0.146	1.058 ± 0.115	0.726 ± 0.133	1.025 ± 0.215	0.569 ± 0.199	0.977 ± 0.293	0.580 ± 0.194	0.764 ± 0.107	1.096 ± 0.122
MgII 2803	0.508 ± 0.198	0.947 ± 0.135	0.846 ± 0.110	0.624 ± 0.117	0.870 ± 0.220	1.038 ± 0.248	0.089 ± 0.288	1.294 ± 0.211	0.920 ± 0.096	1.249 ± 0.120
MgI 2852	≤ 0.626	≤ 0.493	≤ 0.595	···	≤ 0.833	≤ 0.428	≤ 0.959	≤ 0.608	≤ 0.304	0.846 ± 0.117

[a] 2σ upper limits are tabulated for non-detections.
[b] In sightline 10, Milky Way absorption lines are blended with M31 disk gas. See the description in §3.
[c] The two measurements are M31 HVC and disk components, respectively. See Figure 5.9.

5.4 SUMMARY AND DISCUSSION OF RESULTS FOR M31

5.4.1 Overview on the Detection of Low-Ion and High-Ion Absorption Lines

The detections of M31 gas presented in the previous section and reported in Tables 5.3a and 5.4 can be summarized as follows.

Low-ion Mg II absorption due to M31 gas is detected along four of the 10 observed sightlines (5, 7, 9, and 10). These sightlines have impact parameters ranging between $b \approx 17$ and 32 kpc. We also detect other low-ion gas (e.g., due to Si II, O I, C II, Fe II, or Al II) along three of the four sightlines with Mg II detections; sightline 5 was not observed in the FUV, where most of these transitions occur. In addition, we detect C II absorption at M31 velocities along sightline 8 ($b = 13.4$ kpc). Sightline 6 ($b = 30.5$ kpc) is the only "inner" sightline which does not show evidence for M31 low-ion absorption ($W_0^{\lambda 2796} < 0.41$ Å); however, no FUV spectra were obtained along this sightline. Among these "inner" sightlines, except for the blended Galactic and M31 line in sightline 10, the Mg II rest equivalent widths ranged between $W_0^{\lambda 2796} \approx 0.34$ and 0.71 Å, with the strongest detection being a two-component absorber with $W_0^{\lambda 2796} \approx 0.30$ and 0.41 Å. The four outer sightlines (1 through 4), with impact parameters $b \approx 57$ to 112 kpc, do not show Mg II absorption down to 2σ rest equivalent upper limits ranging between $W_0^{\lambda 2796} \approx 0.21$ and 0.46 Å.

High-ion C IV absorption due to M31 gas is detected along three of six sightlines (8, 9, and 10) which have usable FUV spectra. These three detections are all in "inner" sightlines, with impact parameters ranging between $b \approx 13$ and 18 kpc, and rest equivalent widths ranging between $W_0^{\lambda 1548} \approx 0.17$ and 0.65 Å. Some Si IV absorption and low-ion absorption is also detected along these three "inner" sightlines. The three C IV non-detections are in outer sightlines (1, 3, and 4), with impact parameters ranging between $b \approx 57$ and 112 kpc, and with 2σ rest equivalent width upper limits ranging between $W_0^{\lambda 1548} \approx 0.18$ and 0.30 Å.

We should point out that many of the detections summarized above were near the limit of our sensitivity threshold, despite the fact that our rest equivalent width upper limits are typical of those in large optical quasar absorption-line surveys. Another concern is confusion from overlapping or nearby absorption, but we believe we have dealt with this appropriately.

Also, Rich et al. (private communication) has observed three sightlines in the halo of M31 with COS. They do not cover the Mg II region, but detect C IV from M31 in some of these sightlines. There are other HST archival observations in the M31 halo, but these do not show any detections.

5.4.2 Implications

As elaborated further in §5.4.3, a clear picture does emerge. The absorption lines that arise in M31 gas are found to be relatively weak in comparison to those often identified in optical quasar absorption-line surveys, and even more so in comparison to absorption lines which arise in the ISM of the Milky Way Galaxy (e.g., Table 5.3a). Moreover, none of the detected M31 absorption lines are found at large impact parameters. This could also be viewed as unexpected since the bulk of intervening low- to moderate-redshift metal-line absorbers seen in quasar spectra are identified with large-impact-parameter galaxies in followup imaging studies (e.g., Rao et al. 2011, Chen et al. 2010). However, all of the large-impact-parameter sightlines we observed were generally along M31's major axis, so one scenario which might explain the lack of absorption in those cases would be to hypothesize that extended gaseous absorption originates in galactic fountains and preferentially avoids extended regions along the direction of the disk (e.g., Bordoloi et al. 2011, Bouché et al. 2012). Using the observed distribution of HVCs around the Milky Way and M31, Richter (2012) finds an exponential decline in the mean filling factor of HVCs with a characteristic radial extent of ~ 50 kpc. If HVCs alone are responsible for absorption lines, then one would not expect to find any absorption along our four outer sightlines. Alternatively, M31 may simply be typical of a class of luminous galaxies that don't possess large gaseous cross sections which are capable of giving rise to moderate-strength quasar absorption lines. Our findings for M31 may in some way be connected to the observed relative decrease in the incidence of stronger Mg II systems with decreasing redshift (e.g., Nestor et al. 2005).

In the past several years there has been speculation that M31 is a galaxy that lies in the "green valley" (e.g., Mutch et al. 2011, Davidge et al. 2012). The idea is that it exhibits properties that put it between the red cloud and blue cloud populations that have been

identified in large galaxy surveys. Such galaxies may be in a stage of transition and their star formation may nearly cease in less than 5 Gyrs. While this may be the case for M31, we note that the data we have discussed here should not be taken to offer any clues about this. For example, our data do not allow us to draw any conclusions about the strength of star formation or even the column densities of metal-line absorption. This is because the lines we have identified are likely to be mostly saturated. Thus, the weakness of the metal-line absorption in M31 most likely indicates that the effective gas velocity spread is low; it may either be truly low relative to the spectral resolution and/or there may be a small number of velocity components within the spectral resolution element.

5.4.3 Mg II Rest Equivalent Width ($W_0^{\lambda 2796}$) versus Impact Parameter (b)

Figure 5.13 is a plot of M31 Mg II λ2796 rest equivalent width ($W_0^{\lambda 2796}$) detections (or 2σ upper limits) versus sightline impact parameter (b). The measurement shown for sightline 7, which has $b = 26.9$ kpc, was made by fitting a single Gaussian to both absorption components reported in Table 5.3a, i.e., it is not a simple sum of the results from the two individual Gaussian fits reported in Table 5.3a. Since the impact parameters of sightlines 9 and 10 are very similar, they are displaced from each other in the figure for clarity. Note that the upper limits are 2σ upper limits, while the error bars are the 1σ uncertainties. The four outermost data points are suggestive of an overall decrease of $W_0^{\lambda 2796}$ with increasing impact parameter. Quasar absorption line studies of large samples of absorber-galaxy pairs have shown this to be true as well (Chen et al. 2010; Rao et al. 2011).

For comparison, Figure 5.14 includes results from the Rao et al. (2011) sample of absorbing galaxies which have been identified for Mg II-selected DLAs, subDLAs, and Lyman limit systems (LLSs). The mean redshift of the Rao et al. sample is $z \sim 0.5$, with redshifts in the range $0.1 \lesssim z \lesssim 1.0$. The identified absorbing galaxies in the Rao et al. sample also have a range of luminosities, mostly $0.1 \lesssim L \lesssim 1.0L^*$, but there is not a significant correlation between luminosity and impact parameter. Rao et al. found only a marginal (1.8σ) correlation between $W_0^{\lambda 2796}$ and b. The solid black circles in Figure 5.14 are DLAs and the open circles are subDLAs and LLSs. The data from this current M31 study are in

red. Sightlines 5 through 10 have averaged integrated 21 cm emission H I column densities in the subDLA regime, with the exception of the Galactic and M31 blended component along sightline 10. (See §3.) H I 21 cm emission maps are not available as far out as the four outermost sightlines, but since the $N_{HI} = 1.9 \times 10^{18}$ cm^{-2} edge of the H I disk of M31 is at $b \approx 33$ kpc (5.1), these sightlines are not expected to have averaged integrated H I column densities in the DLA or subDLA regime.

Thus, as noted in §5.4.1 and §5.4.2, it is clear that the sightlines passing near M31, or through its gaseous disk seen in 21 cm emission, do not give rise to the moderate-to-strong Mg II absorption lines which are often identified in moderate- to high-redshift quasar absorption-line surveys. For comparison, all of the Galactic detections reported in Table 5.3a have $W_0^{\lambda 2796} > 0.5$ Å, and 4 of the Galactic sightlines have $W_0^{\lambda 2796} \sim 1$ Å (sightline 10 is a blend of Galactic and M31 gas). In the HST Key Project sample of Galactic sightlines (Savage et al. 2000) the median value is $W_0^{\lambda 2796} = 1.17$ Å, and the strongest line has $W_0^{\lambda 2796} = 2.2$ Å.

Of course, our sightlines through M31 are biased sightlines in the context of traditional absorption line surveys, in that the galaxy was pre-selected in order to study the properties of its low-ion and high-ion gas. Therefore, for M31 the probability of occurrence of Mg II absorption as a function of $W_0^{\lambda 2796}$ is not properly estimated from the observed incidence of Mg II absorption in unbiased quasar absorption-line surveys. Instead, however, this experiment does show that a gas-rich, $\sim 2L^*$, spiral galaxy like M31 need not give rise to moderate-to-strong Mg II absorption along sightlines which pass through its H I 21 cm emission disk, or even through a putative extended gaseous halo.

5.4.4 Comparison of 21 cm Emission and Absorption-Line Velocities

The range of velocities that exhibit 21 cm emission for sightlines 5 through 10 are shown as cyan and orange vertical bars as a function of impact parameter in Figure 5.15. Cyan bars correspond to 21 cm emission velocities from M31 gas and orange bars represent HVC velocities. Also plotted are the velocities of the low-ion (red stars) and high-ion (blue triangles) absorption lines from Table 5.4. The Galactic and M31 blended low-ion absorption line

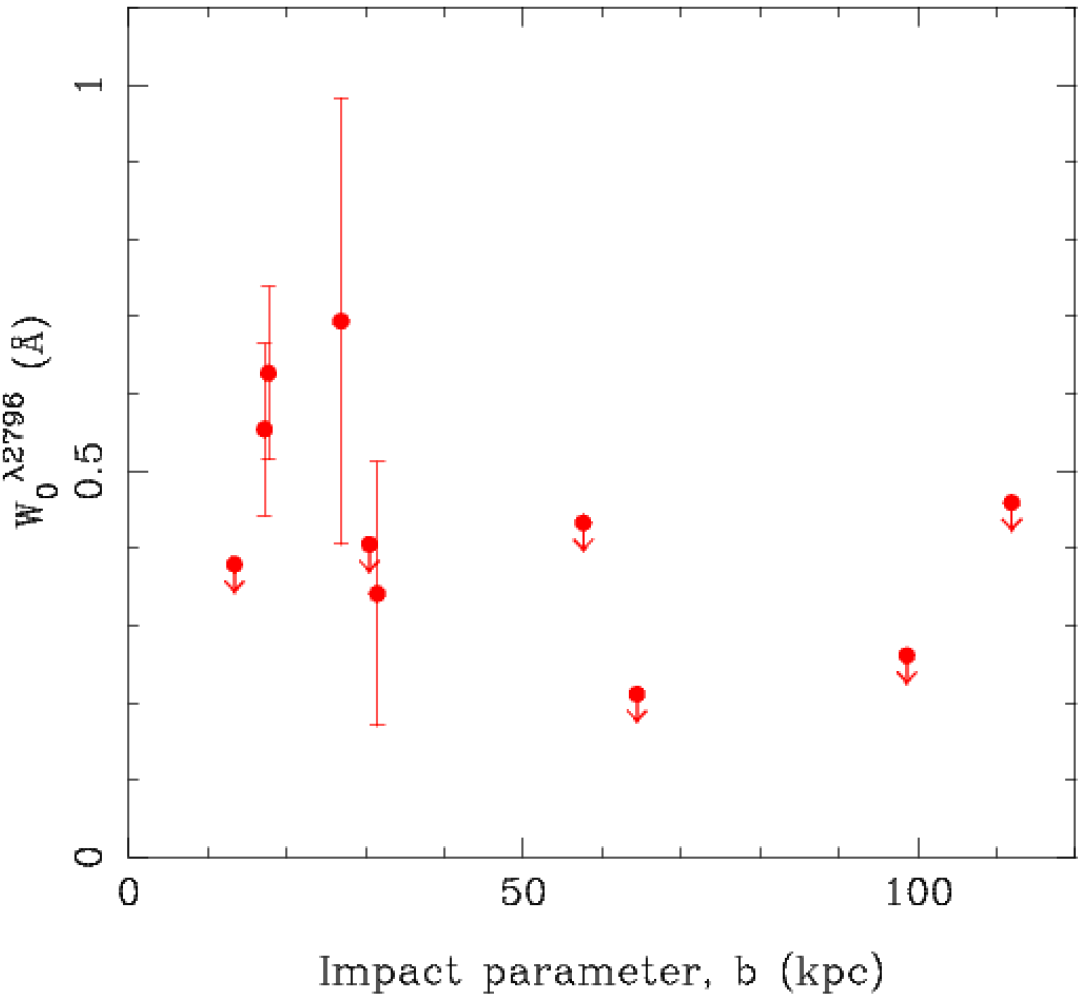

Figure 5.13: Mg II λ2796 rest equivalent width, $W_0^{\lambda 2796}$, vs. impact parameter, b, for M31 measurements from Table 5.3a. Detections have 1σ error bars and arrows indicate 2σ upper limits for the non-detections. For sightline 7, which is the data point at 26.9 kpc, a single Gaussian fit solution to the HVC and M31 components is shown. It has $W_0^{\lambda 2796} = 0.694 \pm 0.289$ Å. The two points at $b \sim 17.5$ kpc have been displaced for clarity. The blended Galactic and M31 absorption along sightline 10 with $W_0^{\lambda 2796} = 1.096 \pm 0.122$ Å has been excluded.

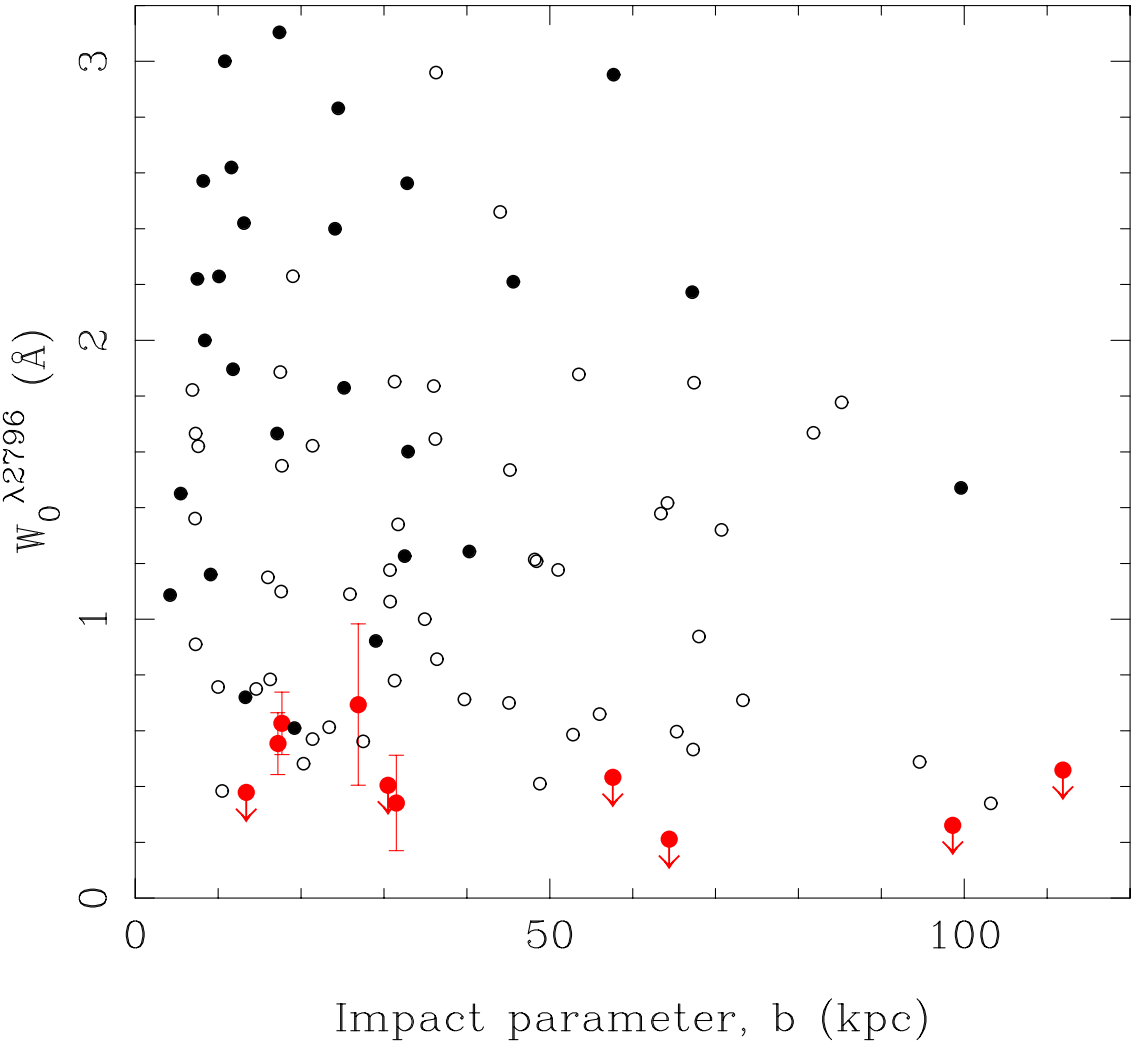

Figure 5.14: Same as Figure 5.13, but data points from Rao et al. (2011) have been added. These represent identified galaxy impact parameters for Mg II systems with H I column density measurements at $z \sim 0.5$. Solid black circles are the DLAs as measured in UV spectra (Rao, Turnshek, & Nestor 2006) and open black circles are subDLAs and LLSs.

along sightline 10 is shown as the encircled star. For the two inner disk sightlines (9 and 10 at $\approx$ 17.5 kpc), it appears that the velocity of the high-ion absorption is better correlated with the 21 cm emission velocity range. Along sightline 8, the low and high-ion absorption lie at an outer velocity edge of where 21 cm emission is detected. As noted in §5.3, this velocity corresponds to the peak in 21 cm emission along this sightline. For sightlines 7 (at $b = 26.9$ kpc) and 5 (at $b = 31.5$ kpc), the low-ion gas again coincides with the peak of 21 cm emission which is near near the edge of the 21 cm profile (see Figures 5.7 and 5.9). Thus, in nearly all cases, the low ions occur near the edge of the 21 cm profiles (two are near the low velocity edge and three are near the high velocity edge), and for sightlines 5, 7, and 8, are coincident with the peak in 21 cm emission.

Given the resolution of the NUV and FUV data ($\sim$ 87 km s^{-1} at $\sim$ 2800 Å and $\sim$ 106 km s^{-1} at $\sim$ 1550 Å), one might question if these differences are significant. However, it is well-known that in data with sufficient signal-to-noise, a Gaussian fit to an absorption line can be used to determine the centroid location of the line to an accuracy much better than the line's FWHM. In order to determine how accurately absorption-line locations can be determined, we ran 10,000 realizations of lines with equivalent widths drawn from the data. Figure 5.16 shows the distributions of equivalent widths. Noise was added to the Gaussian profiles generated with these equivalent widths so that the resulting signal-to-noise ratios matched the data. Line centroids were then estimated by refitting Gaussian profiles to the noised-up absorption lines. The resulting distributions of centroid velocities relative to the input values are shown in Figure 5.17. For both the original as well as the simulated data, the spectra were rebinned to two pixels per resolution element before measurements were made. The signal-to-noise ratios of NUV spectra were, in general, higher than in FUV spectra. Thus, the accuracy with which the line centroids can be measured is higher for the Mg II lines. Specifically, the centroid standard deviation of the Mg II distribution is $\sim$ 6 km s^{-1} compared to $\sim$ 16 km s^{-1} for C IV. These uncertainties indicate that the separations in velocities of the low and high ions are significant towards sightlines 9 and 10 at approximately the 2σ level.

The 21 cm emission studies of M31 (e.g., §5.2.1) show that for this nearly edge-on galaxy, the sightline velocities of gas giving rise to 21 cm emission can span a large range (e.g., see

Table 5.4: Heliocentric velocity offsets of low- and high-ion absorption lines[a]

Quasar	M31		Milky Way	
	Low ion	High ion	Low ion	High ion
	(km s^{-1})	(km s^{-1})	(km s^{-1})	(km s^{-1})
1. 0018+3412	···	···	−18	−61
2. 0024+3439	···	···	−6	···
3. 0030+3700	···	···	−21	−53
4. 0031+3727	···	···	−33	···
5. 0032+3946	−453	···	−42	···
6. 0037+3908	−508	···	−42	···
7. 0040+3915	−513,−389[b]	···	−38	···
8. 0043+4016	−336	−340	6	42
9. 0043+4234	−234	−191	−73	−1
10. 0046+4220	−195, −40[c]	−152, −35[c]	−40	−35

[a] The velocity centroid of the Milky Way absorption system is determined from the Mn II λ2576 line, if detected, or from the Mg II λ2796 line if no Mn II is present, or from the C II λ1334 if neither is present in the spectrum. The velocity centroid of the C IV λ1548 line was determined independent of the low-ion velocity, and was used to constrain the positions of the high-ionization lines. The uncertainties in the low- and high-ion velocities are 6 km s^{-1} and 16 km s^{-1}, respectively.
[b] The two measurements are M31 HVC and halo components, respectively. See Figure 5.9.
[c] The two measurements are M31 halo and disk components, respectively. The disk component is blended with the Milky Way line.

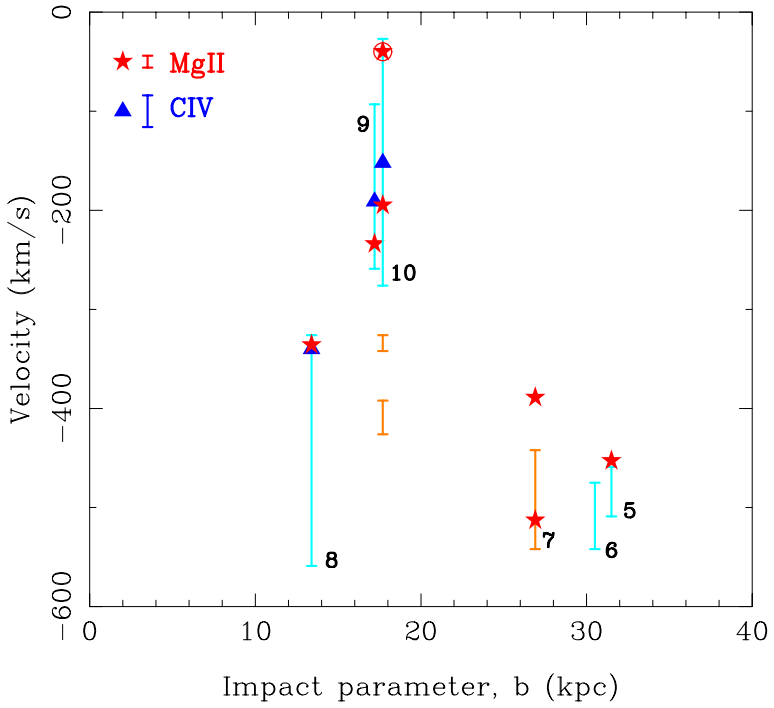

Figure 5.15: Velocities of detected lines in M31 as a function of impact parameter. Cyan and orange vertical bars represent velocity ranges of 21 cm emission from M31's disk and HVCs, respectively. (See the bottom panels of Figures 5.7−5.12 for an indication of the velocity regimes which contain the most gas.) Red stars are low-ion (Mn II, Mg II, or C II) line centroids, and blue triangles are high-ion (C IV) line centroids from Table 5.4. The uncertainty in the velocity measurement is shown as the vertical bar in the upper left corner. Sightlines 9 and 10 are displaced for clarity. Three distinct velocity ranges are apparent towards sightline 10; the wide component arises in M31, and is partly blended with Milky Way gas. The encircled star at -40 km s^{-1} is the blended Galactic and M31 disk absorption-line velocity centroid, and the red star at -195 km s^{-1} is from M31's halo. (See description of sightline 10 in §3.) The two narrower orange components originate in M31 HVCs. No metal lines are detected at these velocities. The two red stars along sightline 7 are the two components of the Mg II line shown in Figure 5.9. 21 cm emission is detected only from the HVC along this sightline but not at the velocity of the Mg II component at -389 km s^{-1}. We therefore surmise that this gas resides in the halo and not in the disk of M31. We caution that the velocities plotted in this figure are not a measurement of M31's rotation curve since, except for sightline 10, the inner sightlines, i.e., 5-9, do not lie along the major axis of M31. See Figure 5.1.

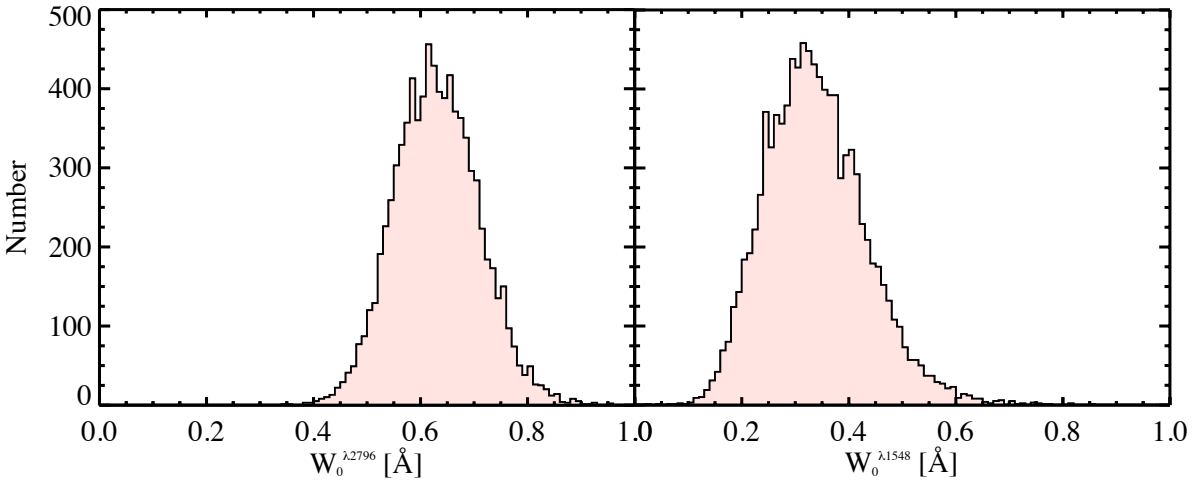

Figure 5.16: Distribution of rest equivalent widths, Mg II $W_0^{\lambda2796}$ (left) and C IV $W_0^{\lambda1548}$ (right), from 10,000 realizations of the data.

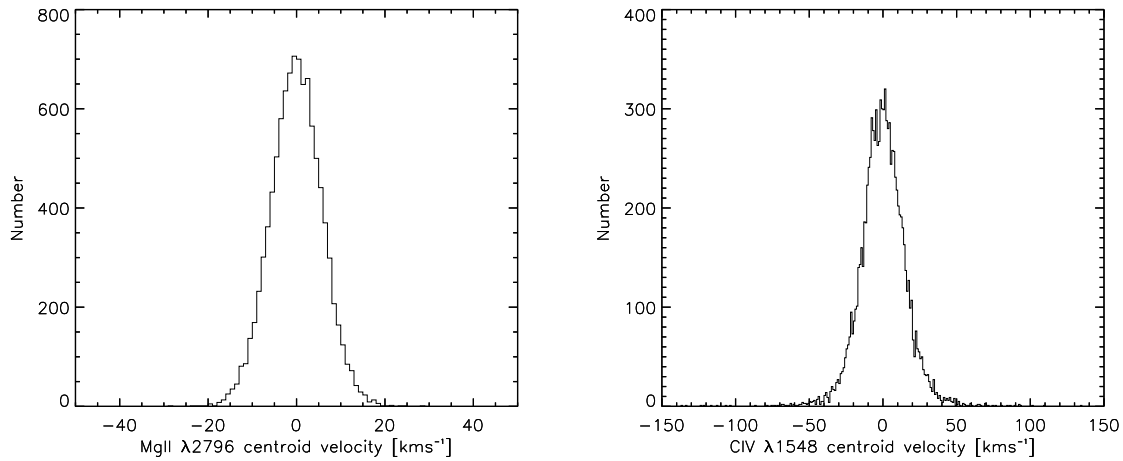

Figure 5.17: Distribution of line centroid velocity offsets measured from 10,000 realizations of the data. Gaussian profiles with rest equivalent widths sampled from measured values were generated, to which noise was added to match the signal-to-noise ratio of the data. Centroid velocities of these simulated lines were measured, and the offsets from input values are shown here. We report the standard deviation of this distribution as the uncertainty in the centroid velocity measurement, i.e., the Mg II $\lambda2796$ and C IV $\lambda1548$ line centroids can be measured with an accuracy of 6 km s^{-1} and 16 km s^{-1}, respectively.

the lower panels in Figures 5.7 - 5.12). Corbelli et al. (2010) fitted a tilted ring model to M31's H I 21 cm emission data from 8 to 37 kpc to study the details of its rotation, finding that M31's disk warps beyond galactocentric distances of $\sim$ 25 kpc and that it becomes more inclined with respect to our sightline. As we have shown above, the Mg II absorption regions are almost always at the peak of the 21 cm emission profile, which occurs near the edge of the 21 cm emission velocity range. Thus, when detected, the low-ion gas appears to trace the 21 cm gas. Interestingly, neither low- nor high-ion absorption lines are detected at the 21 cm velocity locations of the HVCs along sightline 10 ($b = 17.5$ kpc). Low-ion absorption is also not detected at the 21 cm disk velocity location along sightline 6 ($b = 30.5$ kpc). However, the observed low-ion absorption along sightline 7 originates in the HVC detected in 21 cm emission, but at the velocity location of the other absorption component, there is no detected 21 cm emission. This component, at -389 km s^{-1}, is likely to be M31 halo gas. Thus, it appears that the sightlines through M31 are passing through very different physical and kinematic conditions within its ISM.

5.5 CONCLUSIONS

A conventional study relating quasar absorption-lines to the galaxies that cause them begins with the detection of an intervening absorption-line system in a spectrum followed by imaging work to identify the galaxy. The experiment with M31 described here is a quasar absorption-line survey conducted in reverse. We probed ten sightlines with vastly different impact parameters through a single spiral galaxy with a luminosity of $\sim 2L^*$. As summarized in §5.4.1, we detected some type of absorption from M31 gas in five of the six inner sightlines ($13 < b < 32$ kpc), but no absorption in any of the four outer sightlines ($57 < b < 112$ kpc). We also reported the first detection of metals in a M31 HVC.

In §4 5.4.3 we compared our M31 results to the findings in the conventional Rao et al. (2011) survey. Rao et al. found only a marginal anticorrelation between $W_0^{\lambda 2796}$ and b, and indeed we find the same qualitative trend in M31, but the values of $W_0^{\lambda 2796}$ are far smaller in M31 (Figure 5.14). And while Rao et al. found that there were fewer systems with

moderate-to-strong $W_0^{\lambda 2796}$ at large-b ($b > 50$ kpc), we found none arising in M31. In §5.4.4 we compared the velocity locations of low-ion and high-ion gas in M31 to that of M31's 21 cm emission and found that the high-ion gas is better aligned with the velocities of observed 21 cm emission along two of three sightlines where it is detected. The velocity of the low-ion gas is correlated with the peak of 21 cm emission and is often near the edge of the 21 cm emission velocity range. In one case Mg II is detected at a velocity location that shows no 21 cm emission.

Broadly, our results indicate that:

1. Despite the fact that M31 is a gas-rich, $\sim 2L^*$ spiral galaxy, it produces relatively weak Mg II and C IV absorption lines in comparison to those found in moderate-to-high redshift quasar absorption-line surveys. For Mg II, this may indicate that M31 is typical of a class of luminous galaxies that don't possess gaseous cross sections capable of giving rise to moderate-strength quasar absorption lines even at impact parameters $b \lesssim 32$ kpc. This finding might also be related to the observed relative decrease in the incidence of stronger Mg II systems with decreasing redshift.
2. M31 appears not to possess an extensive large gaseous cross section at impact parameters $b > 57$ kpc that is capable of giving rise to moderate-strength quasar absorption lines (e.g., with $W_0^{\lambda 1548} > 0.2$ Å or $W_0^{\lambda 2796} > 0.3$ Å), at least not along the direction of its major axis.
3. For the relatively weak absorption that we did detect at $b \lesssim 32$ kpc, we found the low-ion gas to be associated with the peak in the 21 cm emission profile, near one edge of the 21 cm emission velocity range. Two of three sightlines showed high-ion gas to be centrally located within the 21 cm emission profile, with the third being coincident with an edge. It is also likely that we have detected low-ion halo gas through two of the sightlines.

Future UV spectroscopy of quasars behind M31 can build on these findings by: (1) acquiring higher signal-to-noise data to probe down to weaker rest equivalent width values, (2) acquiring higher resolution data to better study the velocity locations of the gas relative to 21 cm emission velocities, and/or (3) probing a larger number of sightlines including ones in M31's extended halo region.

It would be interesting if N_{HI} results derived from M31's 21 cm emission data could be compared with N_{HI} determinations from Lyman series absorption seen in the UV spectra of background quasars. One could then get an H I column density measurement averaged over less than a milli-parsec region in M31, in comparison to the $\sim$ 50 pc linear spatial scale offered by the radio observations. This would provide information on the homogeneity and size scale of H I absorbing regions in M31.

6.0 SUMMARY, CONCLUSIONS, AND FUTURE WORK

After providing a brief introduction (Chapter 1), we presented quasar absorption-line spectroscopy results to study the low-redshift Universe. This thesis consisted of two separate projects. The first project (Chapters 2-4) dealt with studies of Ca II absorbers along quasar sightlines, which probed the redshift regime $z_{abs} < 1.34$, equivalent to a cosmic lookback time of 8.5 Gyrs. This was done by identifying the Ca II $\lambda\lambda$ 3934,3969 resonance doublet transition of singly-ionized calcium in a quantitative search of $\sim 95,000$ background SDSS quasar spectra, and resulted in a catalog of 435 intervening absorbers, which is the largest ever assembled for Ca II. The analysis described the absorbers statistical properties, their chemical and dust properties, and the galaxies that are associated with them. The second project of this thesis (Chapter 5) presented results on using, for the first time, an unprecedented ten quasar sightlines to study the extended gaseous disk, halo, and high velocity clouds (HVCs) of the Great Spiral Galaxy in Andromeda, M31. This now serves as an important $z = 0$ benchmark for the study of intervening quasar absorbers. The results from each endeavor described in Chapters 2-4 are briefly summarized below. Following this we present comments on some of the needed future work directly related to this thesis.

6.1 SUMMARY AND CONCLUSIONS

In Chapter 2 we presented the results of a survey for Ca II $\lambda\lambda 3934, 3969$ absorption-line systems culled from $\sim 95,000$ Sloan Digital Sky Survey (SDSS) Data Release 7 and Data Release 9 quasar spectra. With 435 doublets identified in the catalog, this list is the largest Ca II catalog compiled to date, spanning redshifts $z < 1.34$, which corresponds to the most re-

cent 8.5 Gyrs of the history of the Universe. We derived statistics on the Ca II rest equivalent width distribution and incidence. We found that the λ3934 rest equivalent width ($W_0^{\lambda3934}$) distribution cannot be described by a single exponential function. A double exponential function is required to produce a satisfactory description. The function can be written as a sum of weak and strong components: $\partial n/\partial W_0^{\lambda3934} = (N^\star_{wk}/W^\star_{wk})exp(-W_0^{\lambda3934}/W^\star_{wk}) + (N^\star_{str}/W^\star_{str})exp(-W_0^{\lambda3934}/W^\star_{str})$. A maximum likelihood fit to the unbinned data indicates: $N^\star_{wk} = 0.140\pm0.029$, $W^\star_{wk} = 0.165\pm0.020$ Å, $N^\star_{str} = 0.024\pm0.020$, and $W^\star_{str} = 0.427\pm0.101$ Å. This suggests that the Ca II absorbers are composed of at least two distinct populations. The incidence of the overall Ca II absorber population does not show evidence for evolution in the standard cosmology. The normalization of the no-evolution curve, i.e., the value of the Ca II incidence extrapolated to redshift $z = 0$, for $W_0^{\lambda3934} \geq 0.3$ Å, is $n_0 = 0.017 \pm 0.001$. In comparison to Mg II surveys, we found that only 3% of Mg II systems in the SDSS have Ca II, confirming that Ca II systems are rare. We also reported on some preliminary investigations of the nature of the two populations of Ca II absorbers, and showed that they can likely be distinguished using their Mg II properties.

In Chapter 3 we presented measurements of element abundance ratios and dust in Ca II absorbers identified in SDSS DR7+DR9. As described in Chapter 2, we formed a statistical sample of 435 Ca II absorbers and postulated that their statistical properties might be representative of at least two populations of absorbers. Here in Chapter 3, we showed that if the absorbers are roughly divided into two subsamples with Ca II rest equivalent widths larger and smaller than $W_0^{\lambda3934} = 0.7$ Å, they are then representative of two physically different populations. Comparisons of abundance ratios between the two Ca II absorber populations indicate that the weaker $W_0^{\lambda3934}$ absorbers have properties consistent with halo-type gas, while the stronger absorbers have properties intermediate between halo- and disk-type gas. We also showed that, on average, the dust extinction properties of the overall sample is consistent with a LMC or SMC dust law, and the stronger absorbers are nearly 6 times more reddened than their weaker counterparts. The absorbed-to-unabsorbed composite flux ratio at $\lambda_{rest} = 2200$ Å is $\mathcal{R} \approx 0.73$ and $E(B-V) \approx 0.046$ for the stronger Ca II absorbers ($W_0^{\lambda3934} \geq 0.7$ Å), and $\mathcal{R} \approx 0.95$ and $E(B-V) \approx 0.011$ for the weaker Ca II absorbers ($W_0^{\lambda3934} < 0.7$ Å).

In Chapter 4 we used SDSS imaging data to study galaxies associated with Ca II absorbers in the redshift interval $z_{abs} = [0.02, 0.65]$. The Ca II absorbers were identified in our survey for Ca II $\lambda\lambda 3934, 3969$ absorption-line systems in SDSS DR7+DR9 quasar spectra. First, we discussed four cases where we identified galaxies with SDSS spectroscopic redshifts that match that of the Ca II absorbers. The four galaxies, three of which are star-forming, have redshifts between $0.04 - 0.24$, impact parameters between $5 - 25$ kpc, and luminosities between $\sim$ 0.1-1 $L_r^\star$. We then specifically considered the question of whether a sample of Ca II absorbers separated above and below $W_0^{\lambda 3934} = 0.7$ Å showed different associated galaxy properties. This rest equivalent width value was motivated by Ca II $\lambda 3934$ absorption-line properties described in Chapters 2 and 3. This was investigated statistically by stacking and forming composite images. We then inferred associated galaxy properties by assuming that any excess galaxy light above the background is due to associated galaxies at $z = z_{abs}$. We found that galaxies associated with Ca II absorbers above and below $W_0^{\lambda 3934} = 0.7$ Å have significantly different statistical properties. The stronger Ca II absorbers have a more concentrated and steeper light profile than the weaker Ca II absorbers, with average luminosity-weighted impact parameters of ≈ 26 kpc and ≈ 48 kpc, respectively. The results from our overall study of Ca II absorbers in the SDSS give rise to a consistent picture, with the various derived observables (impact parameters, metal abundance ratios, dust) qualitatively correlated as might be expected. However, the fact that Ca II absorbers, which are often known to contain significant columns of neutral and molecular gas, can exist at large impact parameters from any associated galaxy needs to be theoretically explained. The results most likely provide important clues about inflows, outflows, and chemical enrichment in the extended circumgalactic regions surrounding both luminous and under-luminous galaxies.

In Chapter 5, we presented *Hubble Space Telescope - Cosmic Origins Spectrograph* spectra of ten quasars located behind M31, selected to investigate the properties of gas associated with its extended disk, halo, and HVCs. The sightlines have impact parameters ranging between $b = 13$ kpc and 112 kpc. No absorption is detected in the four sightlines selected to sample any extended disk (or halo) gas that might be present in the outer regions of M31 beyond an impact parameter of $b > 57$ kpc. Of the six remaining sightlines, all of which lie at $b < 32$ kpc and within the $N_{HI} = 2 \times 10^{18}$ cm^{-2} boundary of the H I disk

of M31, we detected low-ionization absorption at M31 velocities along four of them (three of which include Mg II absorption). We also detected Mg II absorption from a HVC. This HVC sightline does not pass through the 21 cm disk of M31, but we detected additional Mg II absorption at velocities distinct from the HVC that presumably arises in the halo. We found that along sightlines where both are detected, the velocity location of the low-ion gas tracks the peak in 21 cm emission. High-ionization absorption is detected along the three inner sightlines, but not along the three outer sightlines for which C IV data exist. As inferred from high-resolution 21 cm emission line maps of M31's disk and extended regions, only one of the sightlines may be capable of harboring a damped Lyα system, i.e., with $N_{HI} \geq 2 \times 10^{20}$ cm^{-2}. This sightline has impact parameter $b = 17.5$ kpc, and we detected both low- and high-ion absorption lines associated with it. The impact parameters of our observed sightlines through M31 are similar to the impact parameters of galaxies identified with Mg II absorbers at redshifts $0.1 < z < 1.0$ in a 2011 study by Rao *et al.* However, even if we only count cases where absorption due to M31 is detected, the Mg II λ2796 rest equivalent width values are significantly smaller. In comparison, moderate-to-strong Mg II absorption from Milky Way gas is detected along all ten sightlines. Thus, this study indicates that M31 does not present itself as an absorbing galaxy which is *typical* of higher-redshift galaxies inferred to give rise to moderate-strength quasar absorption lines. M31 also appears not to possess an extensive large gaseous cross section, at least not along the direction of its major axis.

6.2 FUTURE WORK

There are a myriad of ways through which we can explore galaxy formation and evolution using QALs. One direction, which is a natural extension of the work discussed in Chapter 4, involves the individual identification of galaxies associated with Ca II absorbers. A proposal to obtain candidate galaxies' redshifts and ultimately identify the galaxies associated with Ca II absorbers was approved for queue observations for the Semester 2014B and Semester 2015A cycles of the Gemini-North Observatory using the Multi-Object Spectro-

graph (GMOS-N). For this project, we proposed to observe 15 of the lowest redshift fields, with $z_{abs} < 0.08$. At the very low-redshifts, the goal is to identify all galaxies down to SDSS r-band luminosity of 0.01L* in the vicinity of Ca II absorbing regions seen in background quasar spectra. As the presence of Ca II absorption is likely indicative of cool neutral gas that may contain molecules and dust, studying the association between cool, metal-rich gas and galaxies down to very low luminosity will lead to important constraints on the overall existence and extent of such gas around galaxies, which in turn constrains models of inflows, outflows, star formation, feedback, chemical enrichment, and cooling. The Gemini program is designed to find all galaxies, including very faint dwarfs, within ∼100 kpc of the quasar sightlines, enabling us to constrain just how far these absorbing gaseous regions are from galaxies. A common criticism of this type of work at high redshift is that a galaxy could be hidden under the surrounding glare of a quasar's PSF; however, due to the low absorber redshifts, interference from the glare of the quasar will be negligible. In total over 260 galaxy candidates along 15 sightlines could be observed. At present, observations for the five Semester 2014B program fields are complete. The remaining ten Semester 2015A fields are currently being observed.

Also in the context of finding galaxies associated with Ca II absorption, one could extend the results of this thesis even more by using HST images to study the nature of several Ca II absorbers, such as the absorber in quasar SDSS1532+0613 with $z_{abs} = 0.05$. This absorber is particularly remarkable because, despite its low redshift and the relative ease of finding galaxies at this redshift, there is apparently no candidate galaxy within 100 kpc that is identifiable in the SDSS images. A follow-up observation using the ACS/WFC on the HST is an appropriate match to the goal of imaging the absorber environment in much greater detail. The capabilities of the ACS will allow the field to be imaged down to $r = 24.8$, corresponding to $0.001L^\star$ at $z_{abs} = 0.05$. Such a project would contribute to an improved understanding of the environments which give rise to Ca II absorbers and their properties in the context of the CGM and the intergalactic medium (IGM). Improved ground-based images will likely be needed before an allocation of HST time is likely.

Finally, since Ca II absorbers are quite rare, there is limited information on the neutral gas column densities for this class of absorber. Hence, it would be worthwhile to conduct

a future UV study using HST to specifically target these quasars to measure their neutral hydrogen column densities. Such a study would be important for clarifying the nature of these rare absorbers and how the strength of Ca II relates to the neutral hydrogen gas column density (e.g., to sort out whether a particular Ca II absorber should be classified as a DLA, a sub-DLA, or a LLS). Measurements of the neutral hydrogen gas column densities in Ca II absorbers will also be crucial for properly characterizing individual values for their dust-to-gas contents, molecular hydrogen properties, the low-ionization and high-ionization metals associated with them, and their neutral-gas-phase chemical abundances (not just abundance ratios).

APPENDIX

THE Ca II ABSORBER DATA

Table A1: The Ca II Absorber Sample

Quasar	**SDSS g mag**	z_{em}	z_{abs}	$W_0^{\lambda 3934}$ (Å)	$\sigma(W_0^{\lambda 3934})$ (Å)	$W_0^{\lambda 3969}$ (Å)	$\sigma(W_0^{\lambda 3969})$ (Å)
J001214.19-095922.9	1.262	0.6901	19.44	0.773	0.137	0.412	0.112
J001444.02-000018.5	1.550	0.0277	17.95	0.326	0.056	0.201	0.055
J002025.22+154054.6	2.023	0.0963	17.65	0.382	0.065	0.167	0.067
J002940.02+010528.5	1.388	0.3732	17.83	0.302	0.059	0.213	0.060
J004130.97+024222.5	2.308	0.7095	18.81	0.720	0.143	0.370	0.120
J004800.50+022514.9	2.160	0.5982	18.96	0.594	0.101	0.297	0.096
J005355.15-000309.3	1.703	1.2503	18.57	0.395	0.072	0.270	0.062
J005408.46-094638.1	2.125	0.4779	18.01	0.427	0.071	0.250	0.070
J010332.30+133233.6	1.663	1.0485	18.96	1.150	0.151	0.887	0.147
J010759.23+092256.7	1.574	0.6048	18.89	1.126	0.125	0.753	0.096
J012327.61+131947.4	2.100	0.2061	19.03	0.715	0.123	0.762	0.163

Continued on next page

Table A1 – *Continued from previous page*

Quasar	**SDSS g mag**	z_{em}	z_{abs}	$W_0^{\lambda 3934}$ (Å)	$\sigma(W_0^{\lambda 3934})$ (Å)	$W_0^{\lambda 3969}$ (Å)	$\sigma(W_0^{\lambda 3969})$ (Å)
J012412.47-010049.7	2.827	1.2942	18.65	0.233	0.037	0.244	0.034
J012412.47-010049.7	2.827	1.1321	18.65	0.243	0.043	0.180	0.054
J014354.48+115913.3	3.143	0.3233	19.40	0.459	0.088	0.359	0.080
J014717.77+125808.7	1.495	1.0388	18.39	0.484	0.065	0.253	0.062
J015144.31+040248.7	0.414	0.3954	18.98	0.578	0.103	0.289	0.091
J015318.19+000911.4	0.838	0.7717	17.83	0.519	0.069	0.375	0.070
J015701.02+135503.2	0.960	0.4837	20.38	1.760	0.184	1.599	0.318
J022015.14+025025.3	2.334	0.1005	19.38	0.698	0.107	0.534	0.111
J022111.33-081308.7	1.840	0.7890	19.08	0.657	0.118	0.366	0.099
J022322.73-005248.5	1.365	0.2992	18.94	0.281	0.051	0.137	0.054
J024736.85+035835.3	1.103	0.6155	19.71	0.472	0.094	0.478	0.080
J025248.15+015303.6	2.645	0.4694	18.63	0.573	0.069	0.263	0.076
J025316.45+010759.8	1.031	0.6317	19.11	0.783	0.138	0.518	0.149
J072810.13+393027.9	2.725	1.0780	19.35	0.451	0.085	0.306	0.086
J072912.26+410551.4	0.103	0.0394	17.25	0.643	0.128	0.645	0.124
J073128.46+290242.0	1.607	0.8228	19.04	1.109	0.134	0.678	0.147
J073306.63+462517.5	0.541	0.7735	18.23	0.428	0.065	0.234	0.085
J073306.63+462517.5	0.541	0.3070	18.23	0.660	0.116	0.347	0.122
J074054.05+332006.5	0.886	0.4912	17.43	0.205	0.041	0.142	0.039
J074356.39+434842.9	2.006	0.6127	18.78	0.818	0.143	0.521	0.113
J074500.47+341731.1	3.688	0.5366	20.64	1.784	0.201	1.009	0.130
J074707.62+305415.0	0.974	0.7651	18.67	0.917	0.093	0.644	0.103
J074816.97+422509.2	1.107	0.5575	17.15	0.314	0.036	0.148	0.030

Continued on next page

Table A1 – *Continued from previous page*

Quasar	**SDSS g mag**	z_{em}	z_{abs}	$W_0^{\lambda 3934}$ (Å)	$\sigma(W_0^{\lambda 3934})$ (Å)	$W_0^{\lambda 3969}$ (Å)	$\sigma(W_0^{\lambda 3969})$ (Å)
J074938.96+513124.6	2.351	0.1769	19.58	1.335	0.200	1.024	0.159
J074942.51+171512.1	2.157	0.0434	19.02	1.618	0.322	1.102	0.345
J075031.39+192754.5	0.425	0.1804	17.83	0.437	0.084	0.447	0.098
J075048.32+471732.5	1.411	0.7725	18.92	0.803	0.105	0.741	0.094
J075131.00+502654.5	2.282	0.5931	18.30	0.275	0.051	0.212	0.045
J075934.16+530505.7	2.255	0.9813	19.12	1.080	0.206	0.648	0.150
J075948.30+510539.0	2.386	1.1679	19.18	0.380	0.073	0.247	0.076
J080000.05+152326.1	0.274	0.2315	19.38	0.943	0.173	0.838	0.161
J080002.25+351243.3	2.255	0.2695	18.98	0.531	0.103	0.481	0.066
J080106.51+415753.4	1.892	0.1041	18.14	0.499	0.095	0.379	0.092
J080623.70+200631.8	1.537	0.5736	19.25	0.960	0.178	0.584	0.130
J080735.97+304743.8	1.259	0.9690	18.98	0.698	0.139	0.612	0.117
J081039.80+345730.8	3.766	0.8214	19.88	0.914	0.072	0.605	0.071
J081053.95+352224.6	1.305	0.8769	18.75	0.509	0.074	0.254	0.078
J081059.27+283658.6	0.329	0.2847	18.70	0.358	0.069	0.253	0.072
J081225.08+501845.6	2.607	0.2628	18.30	0.445	0.088	0.422	0.065
J081336.05+481302.9	0.870	0.4368	18.17	0.619	0.042	0.290	0.047
J081443.66+343141.2	1.995	0.8366	19.17	1.040	0.133	0.543	0.157
J081649.00+391223.9	2.383	0.2200	18.68	0.730	0.139	0.544	0.151
J081739.19+453228.3	1.510	0.7487	18.63	0.751	0.084	0.396	0.069
J081930.35+480825.8	1.999	0.9032	18.17	0.947	0.065	0.434	0.062
J081954.89+423636.3	1.687	0.6537	20.01	0.844	0.127	0.498	0.108
J082039.66+372137.3	4.276	0.8263	21.95	0.755	0.142	0.639	0.165

Continued on next page

Table A1 – *Continued from previous page*

Quasar	**SDSS g mag**	z_{em}	z_{abs}	$W_0^{\lambda 3934}$ (Å)	$\sigma(W_0^{\lambda 3934})$ (Å)	$W_0^{\lambda 3969}$ (Å)	$\sigma(W_0^{\lambda 3969})$ (Å)
J082103.50+400903.3	1.229	0.5989	18.55	0.362	0.066	0.251	0.068
J082153.82+503120.4	2.124	0.1833	17.95	0.296	0.054	0.165	0.054
J082159.58+402236.3	3.770	1.0102	20.33	0.809	0.098	0.520	0.123
J082206.66+344806.0	2.284	0.3441	19.69	0.915	0.178	0.678	0.146
J082226.81+475059.1	1.126	0.1796	17.32	0.163	0.028	0.107	0.029
J082312.13+264415.7	1.857	0.2533	18.59	0.633	0.103	0.383	0.102
J082324.39+513950.2	2.477	1.0498	19.14	0.649	0.088	0.565	0.068
J082341.08+241805.4	1.812	0.6192	17.49	0.886	0.091	0.394	0.069
J082716.26+395742.4	2.827	0.5588	19.13	1.257	0.129	0.586	0.103
J082736.21+270532.6	2.614	0.1615	19.22	0.489	0.086	0.393	0.088
J082803.82+362915.2	2.277	0.1168	19.51	0.818	0.161	0.808	0.139
J082918.09+113341.7	1.257	0.7424	17.45	0.230	0.034	0.134	0.041
J082958.13+150157.2	1.206	0.2860	18.23	0.759	0.091	0.251	0.092
J083036.17+255240.2	1.242	0.4168	19.11	0.900	0.157	0.496	0.147
J083137.24+235352.8	0.430	0.3827	19.28	0.717	0.143	0.535	0.148
J083247.21+150744.6	1.394	0.2038	18.62	0.680	0.133	0.731	0.133
J083553.63+154139.5	1.400	0.5313	18.68	1.064	0.106	0.726	0.117
J083559.15+142716.6	1.766	0.7129	19.41	0.697	0.117	0.466	0.127
J083937.84+223940.6	1.308	0.4466	16.71	0.607	0.079	0.405	0.063
J084106.79+031206.8	1.837	1.3427	16.48	0.225	0.033	0.133	0.029
J084244.84+201215.2	1.229	0.3820	18.22	0.960	0.097	0.358	0.102
J084442.74+385358.8	2.430	1.2514	18.84	0.549	0.080	0.308	0.063
J084650.44+052946.0	1.050	0.7429	17.82	0.435	0.063	0.264	0.053

Continued on next page

Table A1 – *Continued from previous page*

Quasar	**SDSS g mag**	z_{em}	z_{abs}	$W_0^{\lambda 3934}$ (Å)	$\sigma(W_0^{\lambda 3934})$ (Å)	$W_0^{\lambda 3969}$ (Å)	$\sigma(W_0^{\lambda 3969})$ (Å)
J084730.45+103327.2	1.058	0.8048	18.77	0.512	0.067	0.337	0.073
J084804.73+212441.1	1.753	0.7707	19.67	1.214	0.225	0.968	0.165
J085010.26+593118.2	1.718	0.2821	16.82	0.279	0.043	0.160	0.044
J085045.44+563618.7	2.467	0.2253	18.24	0.532	0.071	0.219	0.073
J085135.39+015601.9	3.205	0.9112	20.25	1.467	0.168	0.514	0.165
J085223.93+565725.7	1.547	0.3003	18.64	0.672	0.133	0.504	0.131
J085245.09+010239.4	2.533	0.2019	18.71	0.498	0.089	0.234	0.074
J085313.54+042257.2	2.288	0.4095	19.02	1.271	0.202	0.616	0.161
J085905.54+310522.9	0.742	0.3282	18.10	0.442	0.070	0.202	0.072
J085917.59+105509.2	0.296	0.1830	17.84	0.920	0.108	0.431	0.115
J090130.79+631117.8	1.859	0.8175	18.38	0.812	0.086	0.343	0.088
J090208.63+514352.6	1.972	0.7594	19.33	0.787	0.114	0.310	0.076
J090231.46+172841.2	1.412	0.3101	19.06	0.838	0.157	0.605	0.169
J090334.92+502819.2	3.564	0.6462	21.55	1.623	0.236	0.900	0.284
J090757.59+421823.6	0.809	0.2215	18.30	0.469	0.085	0.306	0.118
J090809.20+041326.2	0.948	0.7585	18.43	1.414	0.092	0.744	0.120
J090902.22+345926.5	0.575	0.4617	17.92	0.492	0.080	0.511	0.116
J091333.65-004250.9	0.426	0.2807	17.67	0.496	0.080	0.317	0.107
J091510.01+475658.8	3.342	0.4519	18.16	0.456	0.089	0.254	0.094
J091727.16+282302.3	1.312	0.9727	19.88	1.938	0.326	1.191	0.308
J091815.92+481135.5	1.270	0.6626	18.53	0.465	0.080	0.318	0.085
J091958.24+111152.3	1.928	0.1818	18.91	1.105	0.212	0.720	0.168
J092525.17+202139.0	0.459	0.4453	18.78	0.858	0.169	0.502	0.149

Continued on next page

Table A1 – *Continued from previous page*

Quasar	**SDSS g mag**	z_{em}	z_{abs}	$W_0^{\lambda 3934}$ (Å)	$\sigma(W_0^{\lambda 3934})$ (Å)	$W_0^{\lambda 3969}$ (Å)	$\sigma(W_0^{\lambda 3969})$ (Å)
J092837.98+602521.0	0.295	0.1538	17.24	0.307	0.048	0.288	0.049
J092908.67+563556.7	0.897	0.2746	17.52	0.359	0.063	0.275	0.064
J093035.07+464408.4	2.034	0.6212	18.69	0.526	0.096	0.325	0.100
J093508.36+271648.6	0.940	0.6559	19.46	0.611	0.099	0.323	0.108
J093556.91+002255.6	3.739	1.2825	19.81	0.900	0.071	0.368	0.073
J093738.03+562838.8	1.800	0.9784	19.76	1.311	0.153	0.847	0.173
J093743.93+004130.6	2.580	0.4099	19.44	0.838	0.115	0.351	0.123
J093945.62+511327.2	1.935	0.6738	17.29	0.421	0.080	0.212	0.065
J094109.66+050114.6	2.601	0.7743	19.48	0.785	0.158	0.415	0.125
J094145.03+303503.6	1.225	0.9378	18.69	1.118	0.095	0.872	0.104
J094158.74+352329.7	2.062	1.2092	17.58	0.310	0.037	0.267	0.053
J094229.86+614652.2	0.643	0.1992	19.46	0.828	0.153	0.488	0.175
J094613.97+133441.2	2.470	0.1152	17.58	0.393	0.058	0.229	0.064
J094636.86+323949.6	1.307	0.7982	17.34	0.600	0.062	0.279	0.067
J094806.59+045811.7	1.738	0.9017	19.00	0.527	0.102	0.268	0.077
J094927.67+314110.0	0.309	0.3055	16.88	1.779	0.056	1.065	0.062
J095031.63+432908.4	1.771	0.7308	17.33	0.820	0.037	0.536	0.043
J095046.94+041451.3	1.864	0.6264	19.02	0.667	0.108	0.443	0.114
J095221.58+235248.3	2.545	0.2369	18.43	0.449	0.088	0.187	0.075
J095352.70+080103.6	1.718	1.0232	17.89	0.470	0.071	0.337	0.084
J095624.74+355604.5	2.804	0.8148	18.32	0.427	0.052	0.200	0.050
J095737.14+255546.9	1.520	0.7811	17.88	0.391	0.049	0.202	0.049
J095808.06+500055.3	1.312	0.8088	18.16	0.493	0.069	0.334	0.098

Continued on next page

Table A1 – *Continued from previous page*

Quasar	**SDSS g mag**	z_{em}	z_{abs}	$W_0^{\lambda 3934}$ (Å)	$\sigma(W_0^{\lambda 3934})$ (Å)	$W_0^{\lambda 3969}$ (Å)	$\sigma(W_0^{\lambda 3969})$ (Å)
J095829.88+182528.1	2.363	0.5045	18.52	0.842	0.125	0.485	0.126
J100000.85+514416.6	1.236	0.9070	18.97	0.896	0.168	0.660	0.216
J100033.85+132410.8	1.355	0.6984	16.85	0.318	0.043	0.194	0.053
J100102.75+500421.9	2.150	1.1488	19.19	1.479	0.287	0.659	0.210
J100125.06+072329.1	3.140	0.4090	18.99	1.401	0.191	0.728	0.175
J100145.14+594008.6	1.186	0.9001	18.36	0.452	0.087	0.225	0.073
J100237.22+270056.5	1.976	0.7536	17.61	0.525	0.055	0.298	0.053
J100523.73+115712.4	1.655	0.8345	18.16	0.777	0.080	0.634	0.103
J100544.53+520903.3	3.140	0.5849	18.33	0.609	0.112	0.341	0.088
J100625.17+302611.7	0.747	0.7157	18.53	0.540	0.095	0.280	0.101
J100629.14+682126.0	1.044	0.4346	18.06	0.632	0.070	0.339	0.058
J100713.68+285348.4	1.045	0.8839	20.09	1.411	0.109	0.931	0.129
J100734.64+155751.8	2.049	0.6707	18.94	0.666	0.111	0.334	0.102
J100937.13+291606.5	2.226	0.2894	17.96	0.380	0.072	0.262	0.077
J100940.65+123010.3	0.611	0.5054	17.98	0.541	0.097	0.382	0.099
J100943.55+052953.8	0.942	0.3862	17.17	0.424	0.031	0.225	0.034
J101030.54+255949.5	0.511	0.2446	16.53	0.386	0.048	0.214	0.038
J101145.10+422617.1	2.258	0.2220	18.68	0.652	0.129	0.440	0.103
J101209.65+484839.4	1.518	0.7767	18.34	0.463	0.080	0.232	0.075
J101252.58+474708.6	2.606	0.8312	18.51	0.554	0.094	0.522	0.110
J101358.73+011928.4	1.995	0.6696	19.29	0.906	0.108	0.344	0.109
J101748.68+222659.2	1.993	0.5362	18.60	0.583	0.091	0.336	0.091
J101847.31+445145.6	1.962	0.4357	17.87	0.332	0.049	0.180	0.055

Continued on next page

Table A1 – *Continued from previous page*

Quasar	**SDSS g mag**	z_{em}	z_{abs}	$W_0^{\lambda 3934}$ (Å)	$\sigma(W_0^{\lambda 3934})$ (Å)	$W_0^{\lambda 3969}$ (Å)	$\sigma(W_0^{\lambda 3969})$ (Å)
J102653.65+251540.4	3.160	0.6503	18.28	0.452	0.060	0.534	0.071
J102928.64+310623.4	1.062	0.4042	17.60	0.435	0.072	0.254	0.078
J102935.19-012138.3	1.058	0.2899	18.68	0.351	0.067	0.208	0.055
J103024.18+561832.8	1.293	1.0001	18.14	0.727	0.147	0.459	0.091
J103410.41+233657.7	2.352	0.7323	18.43	0.517	0.084	0.524	0.098
J103451.42+233435.4	2.654	0.3324	17.12	0.378	0.049	0.326	0.076
J103546.02+110546.4	2.358	0.3328	17.65	0.466	0.074	0.416	0.090
J103708.76-004402.3	2.470	0.3524	19.58	0.673	0.132	0.306	0.082
J104304.88+464953.4	2.895	0.6518	19.83	2.023	0.326	0.885	0.330
J104448.52+160041.1	1.715	0.0652	19.28	0.778	0.149	0.765	0.133
J104547.50+365655.3	2.395	0.5443	18.67	0.567	0.089	0.398	0.089
J104702.22+173410.0	1.779	0.8243	18.38	0.737	0.071	0.462	0.107
J104837.40-002813.6	4.033	0.7924	19.25	0.661	0.132	0.296	0.117
J104923.94+012224.6	1.947	0.4715	17.80	0.582	0.054	0.236	0.057
J105042.27+160056.1	1.267	0.7418	18.40	0.688	0.097	0.443	0.087
J105106.07+100923.6	0.897	0.7643	17.85	0.557	0.080	0.386	0.081
J105640.55+013941.9	2.366	0.3478	19.88	1.318	0.213	0.749	0.185
J105709.91+381859.5	2.974	0.9077	19.75	0.712	0.143	0.719	0.144
J105714.82+440323.8	3.311	0.6561	18.03	0.376	0.063	0.139	0.051
J105853.11+370314.1	1.688	0.0473	18.23	0.619	0.076	0.249	0.060
J105930.93+403956.6	1.208	0.4469	18.16	0.776	0.095	0.484	0.129
J110608.13+592559.0	1.147	0.7776	18.79	1.380	0.134	0.969	0.111
J110729.03+004811.2	1.392	0.7405	17.62	0.347	0.065	0.240	0.055

Continued on next page

Table A1 – *Continued from previous page*

Quasar	**SDSS g mag**	z_{em}	z_{abs}	$W_0^{\lambda 3934}$ (Å)	$\sigma(W_0^{\lambda 3934})$ (Å)	$W_0^{\lambda 3969}$ (Å)	$\sigma(W_0^{\lambda 3969})$ (Å)
J110834.54+411900.9	2.453	0.1014	19.12	1.453	0.151	0.872	0.131
J111109.65+144238.2	3.097	0.6539	19.16	0.940	0.182	0.492	0.195
J112012.12+671115.9	1.493	0.5800	18.88	0.384	0.077	0.179	0.072
J112053.85+623106.3	1.130	1.0723	17.85	0.491	0.068	0.395	0.068
J112602.80+003418.2	1.800	0.7247	18.54	0.363	0.057	0.209	0.063
J112642.95+434949.8	1.296	0.8091	17.95	0.407	0.067	0.351	0.071
J112932.71+020422.8	1.192	0.9649	17.64	0.632	0.051	0.489	0.063
J113148.44+383811.6	2.108	0.5945	19.45	1.359	0.173	0.635	0.190
J113324.63+250249.2	1.566	0.6444	18.57	0.701	0.099	0.415	0.090
J113653.03+482812.9	1.659	0.7383	19.46	0.855	0.123	0.619	0.109
J113709.49+390723.4	1.029	0.7191	18.13	0.571	0.093	0.249	0.077
J113853.35+230739.6	1.495	0.7427	20.08	0.784	0.129	0.562	0.147
J114006.15+013731.8	3.864	0.9327	21.66	1.240	0.212	0.904	0.106
J114107.43+522818.6	1.264	0.5937	17.16	0.384	0.056	0.150	0.044
J114114.62-032623.9	0.755	0.4378	17.72	0.375	0.055	0.190	0.048
J114339.86+073105.7	1.305	0.1891	17.98	0.632	0.098	0.462	0.080
J114502.90+645725.8	1.972	0.6902	19.39	1.049	0.147	0.915	0.160
J114534.27+493559.0	2.987	0.7999	18.88	0.860	0.146	0.488	0.131
J114557.84+080029.0	2.363	0.8695	18.54	0.607	0.084	0.353	0.107
J114658.29+395834.2	1.088	0.9004	18.65	0.381	0.042	0.137	0.045
J114719.89+522923.1	2.000	0.0475	19.11	0.973	0.166	0.601	0.173
J114751.16+205347.6	1.459	0.1806	18.78	1.477	0.266	1.033	0.190
J114856.57+525425.3	1.632	0.8309	16.91	0.400	0.051	0.255	0.042

Continued on next page

Table A1 – *Continued from previous page*

Quasar	**SDSS g mag**	z_{em}	z_{abs}	$W_0^{\lambda 3934}$ (Å)	$\sigma(W_0^{\lambda 3934})$ (Å)	$W_0^{\lambda 3969}$ (Å)	$\sigma(W_0^{\lambda 3969})$ (Å)
J114907.14+004104.3	2.292	0.6663	18.22	0.436	0.073	0.349	0.055
J115244.06+571202.1	1.604	0.8476	18.83	0.516	0.103	0.368	0.094
J115337.56+320046.2	2.418	0.2801	19.19	0.431	0.083	0.322	0.086
J115413.10+340942.0	1.768	0.6768	18.06	0.737	0.057	0.503	0.064
J115718.31+561135.4	1.636	0.8308	18.44	0.549	0.071	0.414	0.075
J115830.96+631004.2	2.925	0.2604	19.58	1.634	0.325	1.175	0.285
J120008.69-015736.2	2.986	0.7414	19.55	1.626	0.186	0.720	0.202
J120200.93+523753.1	3.051	0.6988	19.39	0.905	0.126	0.581	0.161
J120301.01+063441.5	2.178	0.8619	19.74	1.378	0.171	0.960	0.179
J120342.24+102831.8	1.894	0.7461	17.88	0.655	0.122	0.365	0.082
J120554.32+531648.6	1.798	0.6705	19.79	1.576	0.280	1.040	0.258
J120802.65+630328.8	2.579	0.3361	17.48	0.627	0.068	0.483	0.056
J121020.17+225920.1	0.573	0.5605	19.37	1.499	0.235	0.871	0.328
J121320.98+050601.7	2.427	0.3546	19.23	1.150	0.179	0.499	0.176
J121442.30+280329.1	1.973	0.6778	17.80	0.538	0.075	0.334	0.058
J121454.11+120030.1	0.873	0.7195	19.02	0.824	0.126	0.545	0.148
J121604.72+584333.2	1.452	0.7247	18.20	0.528	0.066	0.226	0.063
J121753.03+050030.8	0.632	0.5410	18.52	0.542	0.104	0.444	0.154
J121911.23-004345.5	2.288	0.4484	17.89	0.400	0.060	0.325	0.048
J121930.77+494052.3	2.699	1.0453	17.09	0.295	0.049	0.187	0.068
J122043.87+011122.1	2.627	0.9191	18.46	0.615	0.052	0.448	0.079
J122108.73+184847.9	2.178	0.5962	18.36	0.945	0.165	0.556	0.103
J122151.96+110223.5	1.887	0.2035	19.21	1.132	0.200	0.472	0.185

Continued on next page

Table A1 – *Continued from previous page*

Quasar	**SDSS g mag**	z_{em}	z_{abs}	$W_0^{\lambda 3934}$ (Å)	$\sigma(W_0^{\lambda 3934})$ (Å)	$W_0^{\lambda 3969}$ (Å)	$\sigma(W_0^{\lambda 3969})$ (Å)
J122756.34+425632.3	1.311	1.0449	17.47	0.359	0.063	0.244	0.053
J122831.53+041424.8	1.355	0.6116	18.71	0.726	0.108	0.422	0.110
J122930.94+230331.5	1.586	0.9910	19.11	0.843	0.165	0.626	0.165
J123401.23+002437.3	2.147	0.1125	19.49	0.518	0.097	0.519	0.097
J123413.61+292212.9	1.611	0.7066	19.21	0.791	0.093	0.520	0.098
J123600.33+561444.0	2.313	0.2528	18.44	0.822	0.165	0.593	0.131
J124011.15+003203.9	3.028	0.3690	19.81	1.211	0.157	0.516	0.129
J124300.47+204246.8	1.980	0.2769	18.62	1.488	0.126	1.034	0.101
J124347.60+374512.5	2.146	0.7176	18.42	0.552	0.103	0.302	0.088
J124349.61+191537.7	2.311	0.4320	19.08	1.196	0.156	0.652	0.194
J124722.49+342727.0	2.494	1.0379	18.14	0.695	0.129	0.329	0.104
J124753.19-014712.2	3.670	0.7900	20.24	0.776	0.112	0.249	0.082
J124910.19+623847.3	1.457	0.6169	18.74	0.564	0.097	0.245	0.097
J124924.43-011617.6	2.219	0.7554	19.82	0.880	0.156	0.421	0.147
J124949.65+593216.9	2.052	0.7063	18.24	0.429	0.070	0.347	0.072
J125244.53+642103.3	1.399	0.5124	17.58	1.099	0.096	0.696	0.076
J125314.72+380911.3	1.815	0.9896	18.16	0.447	0.078	0.301	0.049
J125348.77+340243.4	1.269	0.8902	19.79	0.494	0.096	0.490	0.092
J125419.07+362750.4	2.985	0.2702	18.50	0.533	0.099	0.446	0.088
J125431.89+210315.9	3.281	0.4338	20.46	2.235	0.386	1.322	0.486
J130028.53+283010.1	0.647	0.2228	16.95	0.429	0.069	0.259	0.061
J130153.78-011410.9	1.718	1.2436	17.92	0.822	0.137	0.318	0.066
J130537.33+283007.0	1.141	0.7279	17.93	0.616	0.059	0.395	0.066

Continued on next page

Table A1 – *Continued from previous page*

Quasar	**SDSS g mag**	z_{em}	z_{abs}	$W_0^{\lambda 3934}$ (Å)	$\sigma(W_0^{\lambda 3934})$ (Å)	$W_0^{\lambda 3969}$ (Å)	$\sigma(W_0^{\lambda 3969})$ (Å)
J130811.95+113609.2	2.098	0.3486	18.38	1.068	0.121	0.815	0.119
J130846.76-005046.8	2.091	0.2107	19.05	0.400	0.077	0.369	0.084
J131058.14+010822.1	1.395	0.8621	18.86	0.874	0.069	0.434	0.059
J131204.43+361814.5	1.429	0.3285	18.10	0.798	0.094	0.527	0.098
J131232.07+392023.8	1.509	0.4014	19.59	0.793	0.150	0.533	0.157
J131446.65+040609.4	2.360	0.9817	18.91	0.903	0.154	0.546	0.131
J131630.46+005125.5	2.401	0.1544	18.23	1.123	0.176	0.835	0.166
J132323.78-002155.2	1.391	0.7162	18.44	0.896	0.050	0.518	0.043
J132657.45+405018.9	2.711	0.6108	17.97	0.723	0.080	0.548	0.078
J132657.46+405018.9	1.727	0.6112	17.97	0.852	0.115	0.386	0.096
J132736.15+152450.7	2.566	0.2771	18.35	0.546	0.093	0.296	0.099
J132752.04+103627.2	1.901	0.5985	19.18	1.910	0.257	1.094	0.218
J132803.43+352152.2	2.350	0.5324	19.51	0.679	0.095	0.439	0.096
J133008.08+145357.0	3.028	0.5243	19.50	1.597	0.251	0.699	0.225
J133317.74+353750.1	0.769	0.0938	19.33	0.351	0.070	0.364	0.073
J133404.15+195930.1	2.464	0.3514	19.30	1.671	0.168	0.759	0.102
J133526.01-010028.1	0.671	0.1731	17.28	0.303	0.061	0.185	0.049
J133550.37+284808.7	1.066	0.8491	17.41	0.478	0.074	0.356	0.075
J133658.54+100808.2	0.356	0.1796	17.82	0.766	0.060	0.287	0.084
J133719.25+074728.4	1.392	0.8594	17.57	0.501	0.083	0.258	0.056
J134246.25-003543.7	0.787	0.5383	18.23	0.596	0.099	0.271	0.079
J134317.34+635444.9	1.139	0.7095	17.56	0.777	0.065	0.470	0.053
J134804.80+072439.6	2.496	0.2425	18.86	0.539	0.105	0.447	0.139

Continued on next page

Table A1 – *Continued from previous page*

Quasar	**SDSS g mag**	z_{em}	z_{abs}	$W_0^{\lambda 3934}$ (Å)	$\sigma(W_0^{\lambda 3934})$ (Å)	$W_0^{\lambda 3969}$ (Å)	$\sigma(W_0^{\lambda 3969})$ (Å)
J135406.12+104220.9	0.318	0.3186	19.05	1.550	0.303	1.123	0.280
J135547.63+071241.1	0.348	0.3019	19.55	0.841	0.157	0.642	0.174
J135639.93-012321.8	2.207	0.9370	20.20	0.957	0.151	0.478	0.123
J135721.40+164213.1	2.246	0.8183	19.70	0.831	0.129	0.678	0.146
J135828.74+005811.4	3.921	0.7067	20.84	1.055	0.198	0.665	0.184
J140056.06+021825.8	0.196	0.1547	19.22	1.825	0.295	1.544	0.319
J140059.27+073339.9	2.346	0.2988	18.93	0.724	0.107	0.303	0.085
J140134.90+533714.2	1.971	0.8280	18.97	0.471	0.093	0.383	0.131
J140215.79+341533.3	2.079	0.5548	18.69	0.815	0.096	0.424	0.094
J140444.19+551637.0	1.588	1.0708	19.42	1.374	0.233	0.501	0.195
J140448.80+144940.6	2.192	0.7532	19.43	0.601	0.116	0.419	0.113
J140602.17+590443.2	2.364	0.6762	18.63	0.673	0.092	0.675	0.092
J140703.55+243137.0	2.144	0.1168	18.56	0.735	0.105	0.521	0.133
J140717.90+170709.5	1.794	0.8369	18.30	1.355	0.101	0.685	0.113
J140744.20+140620.8	2.175	0.2111	19.01	0.962	0.187	0.464	0.179
J140945.23+494119.5	1.230	0.3343	19.28	1.166	0.221	0.984	0.232
J141108.45+285551.7	0.540	0.1350	19.18	1.536	0.303	0.973	0.287
J141615.71+365537.3	1.827	1.2035	18.30	0.696	0.086	0.396	0.063
J141723.73+285522.6	1.808	0.2243	19.42	1.750	0.281	0.709	0.240
J141746.03+162512.2	1.720	0.2415	17.79	0.603	0.110	0.479	0.092
J142119.39+313219.6	2.921	0.7044	20.25	1.371	0.141	1.109	0.130
J142536.12-001702.2	2.679	0.2197	18.83	1.111	0.094	0.515	0.079
J142543.32+540619.3	3.260	0.3791	18.12	0.487	0.086	0.268	0.076

Continued on next page

Table A1 – *Continued from previous page*

Quasar	**SDSS g mag**	z_{em}	z_{abs}	$W_0^{\lambda 3934}$ (Å)	$\sigma(W_0^{\lambda 3934})$ (Å)	$W_0^{\lambda 3969}$ (Å)	$\sigma(W_0^{\lambda 3969})$ (Å)
J143040.83+014939.9	2.113	1.2419	17.81	0.301	0.039	0.130	0.043
J143113.14-005238.4	1.635	0.0292	20.11	1.370	0.219	0.819	0.161
J143218.94+134145.6	1.204	0.3383	19.24	1.148	0.213	0.923	0.213
J143517.71+634259.2	0.528	0.0329	17.93	0.397	0.076	0.185	0.072
J143614.14+105905.6	1.240	0.4775	17.48	0.833	0.121	0.551	0.107
J143712.49+613519.2	1.783	0.5477	18.54	1.142	0.186	0.769	0.141
J143841.95+034110.3	1.737	0.2943	18.50	0.441	0.089	0.233	0.088
J144030.18+160012.3	2.010	0.3174	18.25	0.668	0.086	0.413	0.094
J144047.39+093809.0	1.201	0.9016	18.08	0.497	0.086	0.229	0.081
J144107.90+392329.8	1.351	0.6785	19.13	1.007	0.167	0.672	0.162
J144314.18-024722.1	0.677	0.6503	17.35	0.524	0.057	0.357	0.050
J144335.16+334859.8	3.606	0.5646	19.58	0.583	0.086	0.202	0.067
J144342.21-025430.6	0.775	0.7627	19.61	2.573	0.222	1.114	0.241
J144446.73+591047.4	0.277	0.2333	18.70	0.598	0.114	0.350	0.104
J144617.43+163707.0	1.687	0.7866	19.51	0.697	0.133	0.534	0.136
J145012.13+302551.5	1.219	0.6035	18.22	0.371	0.067	0.177	0.059
J145048.95+191430.6	0.790	0.4772	18.58	0.578	0.095	0.590	0.102
J145306.70+123902.4	0.541	0.4078	18.98	0.994	0.151	0.575	0.162
J145322.45+053448.4	2.207	0.7389	19.28	0.439	0.085	0.286	0.086
J145943.07+135758.3	0.800	0.0624	18.85	1.305	0.222	0.602	0.215
J150917.22+341026.2	1.936	0.8020	18.69	0.489	0.090	0.428	0.069
J151144.82+184511.0	1.535	0.7776	19.14	0.644	0.110	0.524	0.110
J151247.48+573843.5	2.125	1.0444	19.26	1.040	0.182	0.692	0.195

Continued on next page

Table A1 – *Continued from previous page*

Quasar	**SDSS g mag**	z_{em}	z_{abs}	$W_0^{\lambda 3934}$ (Å)	$\sigma(W_0^{\lambda 3934})$ (Å)	$W_0^{\lambda 3969}$ (Å)	$\sigma(W_0^{\lambda 3969})$ (Å)
J151424.94+370413.5	1.061	0.5106	18.65	0.715	0.143	0.440	0.118
J151507.84+612411.9	2.181	0.5216	17.88	0.369	0.069	0.233	0.089
J151617.79+265525.0	3.107	0.9429	21.88	1.542	0.109	0.839	0.118
J151958.12+502919.2	2.095	0.5193	19.07	1.123	0.205	0.669	0.194
J152046.36+610511.3	2.176	0.4234	19.21	1.192	0.223	1.191	0.186
J152340.18+094651.7	1.432	0.5139	18.31	0.876	0.133	0.536	0.103
J152531.76+151238.2	1.492	0.2757	18.35	0.473	0.080	0.406	0.081
J152552.40+111706.7	2.039	0.6878	18.37	0.497	0.092	0.272	0.093
J152607.22+292903.6	2.734	1.2192	19.41	0.490	0.090	0.439	0.088
J152609.38+071829.3	2.417	1.1321	19.64	1.148	0.187	1.234	0.227
J152652.76+405126.6	3.717	0.6507	19.90	1.394	0.222	1.096	0.159
J152726.97+263637.5	3.481	0.7200	20.04	0.946	0.145	0.591	0.177
J152740.66+063218.5	2.924	0.4454	19.56	0.606	0.114	0.283	0.105
J152800.29+535223.8	1.391	0.3160	17.47	0.541	0.056	0.325	0.080
J152918.02+324841.8	1.650	0.0636	17.75	0.238	0.046	0.259	0.048
J152934.79+275416.3	1.374	0.2399	18.85	0.878	0.134	0.453	0.140
J152941.57+254815.9	3.646	0.5403	20.48	0.466	0.082	0.351	0.081
J153043.23+210743.2	1.338	0.3594	18.36	0.493	0.068	0.321	0.055
J153043.23+210743.3	1.337	0.3595	18.36	0.510	0.087	0.385	0.087
J153209.51+061356.1	0.842	0.0533	17.37	0.506	0.102	0.262	0.081
J153338.11+023320.9	0.870	0.8425	17.91	0.425	0.078	0.301	0.075
J153400.58+025615.8	0.430	0.3986	17.50	0.333	0.064	0.251	0.067
J153503.43+311832.1	1.511	0.9042	18.12	0.524	0.045	0.387	0.044

Continued on next page

Table A1 – *Continued from previous page*

Quasar	**SDSS g mag**	z_{em}	z_{abs}	$W_0^{\lambda 3934}$ (Å)	$\sigma(W_0^{\lambda 3934})$ (Å)	$W_0^{\lambda 3969}$ (Å)	$\sigma(W_0^{\lambda 3969})$ (Å)
J153717.86+432752.9	2.186	0.3678	17.97	0.375	0.075	0.263	0.074
J153731.01+335836.7	1.023	0.9136	17.57	0.451	0.070	0.412	0.079
J154052.05-001822.5	1.862	0.2004	19.66	1.683	0.290	1.392	0.387
J154207.66+191525.6	2.505	0.6074	18.84	0.357	0.053	0.228	0.055
J154317.71+302921.3	1.053	0.8049	19.03	0.480	0.093	0.415	0.100
J154348.98+232910.2	2.383	0.0930	19.27	0.841	0.144	0.480	0.120
J154550.38+554346.2	2.155	0.5443	17.71	0.471	0.055	0.523	0.056
J154836.39+174941.9	1.170	0.6933	18.43	0.661	0.125	0.446	0.104
J154929.89+113743.3	0.681	0.3528	19.35	0.520	0.103	0.558	0.100
J155121.13+071357.7	0.675	0.3290	16.85	0.197	0.035	0.147	0.036
J155328.49+095102.0	0.192	0.1577	16.60	0.212	0.036	0.130	0.036
J155331.55+122039.1	2.162	1.0450	18.53	0.578	0.073	0.204	0.062
J155412.48+144533.0	0.780	0.3667	17.49	0.427	0.050	0.315	0.052
J155434.56+200845.8	2.048	0.5661	19.43	1.430	0.243	0.612	0.183
J155453.30+245622.5	1.029	0.5996	20.31	0.618	0.100	0.512	0.091
J155744.01+330231.1	3.146	0.4422	18.61	0.524	0.087	0.489	0.083
J155752.31+342140.0	1.265	0.1140	18.56	0.598	0.102	0.628	0.168
J155924.08+094431.3	3.030	0.4408	19.70	1.022	0.163	0.536	0.146
J155948.17+065727.6	2.895	0.5325	18.98	0.909	0.169	0.427	0.132
J160202.39+401301.3	2.096	0.8452	18.38	0.310	0.048	0.233	0.050
J160212.46+334954.0	1.966	0.8396	19.24	0.707	0.133	0.261	0.091
J160224.86+024220.5	1.401	0.5713	18.23	0.395	0.065	0.224	0.080
J160335.78+453656.3	3.031	0.6119	19.79	1.198	0.193	0.795	0.224

Continued on next page

Table A1 – *Continued from previous page*

Quasar	**SDSS g mag**	z_{em}	z_{abs}	$W_0^{\lambda 3934}$ (Å)	$\sigma(W_0^{\lambda 3934})$ (Å)	$W_0^{\lambda 3969}$ (Å)	$\sigma(W_0^{\lambda 3969})$ (Å)
J160343.18+244836.4	2.263	0.6564	20.37	1.170	0.157	0.575	0.138
J160500.70+203511.3	1.362	0.6461	19.30	1.390	0.112	0.844	0.089
J160637.57+173516.2	2.313	0.5947	18.50	0.286	0.050	0.265	0.054
J160843.90+071508.6	2.864	1.3206	16.78	0.308	0.034	0.209	0.034
J160932.94+462613.3	2.372	0.9655	18.76	0.985	0.161	0.381	0.153
J160943.67+533041.0	1.329	0.7940	18.99	0.884	0.076	0.527	0.077
J161018.39+042631.6	2.612	0.3626	18.55	0.293	0.054	0.225	0.055
J161033.12+202420.1	0.627	0.1585	17.59	0.536	0.067	0.358	0.071
J161206.04+320516.3	1.839	1.1425	18.84	0.749	0.140	0.318	0.113
J161644.75+211907.4	1.322	0.6207	19.57	1.041	0.191	0.527	0.188
J161649.42+415416.3	0.440	0.3212	16.95	0.397	0.067	0.226	0.054
J161808.79+192325.7	1.496	0.5841	18.87	0.640	0.120	0.395	0.097
J161833.54+335826.0	2.951	0.4923	19.18	0.721	0.141	0.369	0.136
J161907.54+211114.3	2.423	0.3256	18.29	0.598	0.116	0.330	0.107
J161925.53+513029.6	1.301	0.6497	18.31	0.664	0.074	0.290	0.088
J161953.10+071621.0	1.846	0.1105	20.20	1.439	0.241	0.742	0.128
J162044.77+125629.8	1.339	0.3949	18.05	0.232	0.047	0.175	0.048
J162537.74+352022.3	0.662	0.5259	19.17	0.971	0.133	0.514	0.121
J162548.79+264658.7	2.522	0.1432	17.32	0.535	0.083	0.332	0.088
J162558.00+313911.3	1.207	0.9056	18.90	0.813	0.156	0.332	0.130
J162904.96+361512.1	0.363	0.2583	17.74	0.533	0.082	0.452	0.069
J162933.60+253200.6	1.339	0.6545	19.65	0.897	0.171	0.522	0.146
J162957.80+423051.4	1.187	0.3783	19.26	0.734	0.146	0.498	0.148

Continued on next page

Table A1 – *Continued from previous page*

Quasar	**SDSS g mag**	z_{em}	z_{abs}	$W_0^{\lambda 3934}$ (Å)	$\sigma(W_0^{\lambda 3934})$ (Å)	$W_0^{\lambda 3969}$ (Å)	$\sigma(W_0^{\lambda 3969})$ (Å)
J163101.91+141037.3	2.355	0.2440	19.31	0.521	0.077	0.299	0.079
J163513.26+145938.3	1.643	0.6538	19.20	0.521	0.103	0.359	0.109
J163513.47+132305.8	2.857	0.6867	18.96	0.843	0.114	0.367	0.111
J163556.84+110907.7	2.172	0.6684	19.53	0.858	0.171	0.369	0.145
J163638.18+211255.5	1.803	0.8001	19.42	0.432	0.058	0.308	0.061
J163923.07+161041.8	2.511	0.3622	18.98	0.577	0.073	0.352	0.068
J164042.18+175334.2	2.744	0.2154	19.75	0.667	0.111	0.492	0.118
J164105.35+403651.7	2.444	0.2446	18.69	0.608	0.114	0.332	0.117
J164447.09+171154.3	2.970	0.9240	18.96	0.897	0.087	0.610	0.148
J165118.61+400124.8	0.357	0.3356	17.22	0.244	0.035	0.126	0.042
J165621.66+415524.4	2.901	0.3296	18.92	1.321	0.171	0.913	0.182
J165743.05+221149.1	1.779	0.2659	18.38	1.642	0.221	1.546	0.158
J165749.66+345149.0	1.643	0.7694	19.03	0.881	0.140	0.485	0.109
J170428.65+242917.9	1.788	1.3129	16.94	0.316	0.059	0.190	0.057
J170700.46+591041.2	1.834	0.5184	18.71	0.760	0.145	0.490	0.139
J171712.86+640344.7	2.101	0.1799	19.03	1.321	0.253	0.710	0.193
J172739.03+530229.1	1.444	0.9452	18.44	0.590	0.094	0.422	0.112
J173257.40+325121.6	3.236	0.6950	18.60	0.469	0.089	0.442	0.073
J173559.98+573106.0	1.827	0.8725	18.87	0.995	0.163	0.723	0.140
J205455.16-052511.5	0.831	0.7016	20.43	1.152	0.159	1.165	0.166
J205601.68-001613.2	0.521	0.4687	18.05	0.863	0.164	0.591	0.167
J210757.66-062010.6	1.899	0.2321	17.48	0.747	0.080	0.503	0.063
J210803.84+010217.2	2.441	0.3187	19.74	0.624	0.115	0.487	0.101

Continued on next page

Table A1 – *Continued from previous page*

Quasar	**SDSS g mag**	z_{em}	z_{abs}	$W_0^{\lambda 3934}$ (Å)	$\sigma(W_0^{\lambda 3934})$ (Å)	$W_0^{\lambda 3969}$ (Å)	$\sigma(W_0^{\lambda 3969})$ (Å)
J211443.95-005532.8	3.442	0.5066	19.44	1.742	0.085	1.086	0.097
J212110.54+035501.4	2.680	0.3087	19.72	0.673	0.082	0.389	0.091
J212258.85+034309.5	3.250	0.7794	19.77	0.749	0.115	0.499	0.120
J212727.19+082724.6	0.745	0.4393	18.87	0.535	0.104	0.456	0.089
J212916.60+003756.7	2.955	0.2918	17.89	0.200	0.040	0.163	0.039
J213235.95-001350.6	2.506	0.9886	18.96	0.803	0.146	0.542	0.126
J213408.11+043611.4	2.215	1.1182	18.67	0.804	0.085	0.426	0.089
J213613.74+005825.9	0.528	0.3257	19.65	0.488	0.063	0.197	0.065
J213617.71+084007.6	2.266	0.8685	18.79	0.893	0.149	0.539	0.118
J213623.52-003410.9	2.224	1.2213	18.40	1.616	0.248	0.536	0.172
J214037.59+100351.1	2.227	1.0724	18.47	0.430	0.060	0.298	0.054
J214704.08-002600.1	1.803	0.7409	20.13	1.141	0.176	0.851	0.158
J214730.00+104830.8	2.107	0.6995	18.47	0.549	0.081	0.318	0.084
J220249.76-003441.4	2.565	0.8341	20.94	1.772	0.233	1.329	0.384
J221608.88-005708.5	2.400	1.3428	17.61	0.378	0.056	0.255	0.061
J221945.06+003708.1	3.531	0.4809	20.01	1.900	0.139	1.228	0.150
J222733.20+003449.0	0.307	0.2419	18.83	0.815	0.157	0.432	0.152
J223848.23+133926.8	2.223	0.0655	19.27	1.122	0.206	0.529	0.199
J224511.27+130904.0	1.547	0.8612	19.05	1.279	0.162	0.849	0.231
J224728.80-004417.5	1.140	0.4697	18.39	0.392	0.047	0.163	0.050
J225800.02-084143.7	1.493	0.7311	17.69	0.306	0.057	0.278	0.058
J225913.74-084419.6	1.291	0.5295	18.61	0.697	0.137	0.488	0.110
J230048.95+023320.6	2.346	0.5546	18.82	0.487	0.092	0.282	0.074

Continued on next page

Table A1 – *Continued from previous page*

Quasar	**SDSS g mag**	z_{em}	z_{abs}	$W_0^{\lambda 3934}$ (Å)	$\sigma(W_0^{\lambda 3934})$ (Å)	$W_0^{\lambda 3969}$ (Å)	$\sigma(W_0^{\lambda 3969})$ (Å)
J230951.18-094016.3	1.574	0.6780	19.60	0.776	0.124	0.558	0.112
J231930.38+004330.9	0.969	0.7517	18.22	0.746	0.050	0.570	0.051
J232820.38+002238.1	1.307	0.6519	17.83	0.212	0.036	0.142	0.037
J233112.65-100758.0	1.322	0.3584	16.97	0.338	0.055	0.136	0.045
J233212.46-093301.9	1.425	0.2446	18.94	0.800	0.154	0.423	0.136
J233728.39+004533.7	2.722	0.3159	19.63	0.888	0.150	0.723	0.148
J233917.86-002943.5	1.344	0.9667	18.80	0.475	0.095	0.439	0.111
J234002.76-005242.1	2.254	0.2827	18.79	0.866	0.084	0.447	0.140
J234009.92-090921.3	0.519	0.0368	18.82	1.591	0.298	0.810	0.244
J234340.34+011254.4	1.954	0.1585	19.01	1.288	0.243	0.814	0.226

BIBLIOGRAPHY

[AAA+06] J. K. Adelman-McCarthy, M. A. Agüeros, S. S. Allam, K. S. J. Anderson, S. F. Anderson, J. Annis, N. A. Bahcall, I. K. Baldry, J. C. Barentine, A. Berlind, M. Bernardi, M. R. Blanton, W. N. Boroski, H. J. Brewington, J. Brinchmann, J. Brinkmann, R. J. Brunner, T. Budavári, L. N. Carey, M. A. Carr, F. J. Castander, A. J. Connolly, I. Csabai, P. C. Czarapata, J. J. Dalcanton, M. Doi, F. Dong, D. J. Eisenstein, M. L. Evans, X. Fan, D. P. Finkbeiner, S. D. Friedman, J. A. Frieman, M. Fukugita, B. Gillespie, K. Glazebrook, J. Gray, E. K. Grebel, J. E. Gunn, V. K. Gurbani, E. de Haas, P. B. Hall, F. H. Harris, M. Harvanek, S. L. Hawley, J. Hayes, J. S. Hendry, G. S. Hennessy, R. B. Hindsley, C. M. Hirata, C. J. Hogan, D. W. Hogg, D. J. Holmgren, J. A. Holtzman, S.-i. Ichikawa, Ž. Ivezić, S. Jester, D. E. Johnston, A. M. Jorgensen, M. Jurić, S. M. Kent, S. J. Kleinman, G. R. Knapp, A. Y. Kniazev, R. G. Kron, J. Krzesinski, N. Kuropatkin, D. Q. Lamb, H. Lampeitl, B. C. Lee, R. F. Leger, H. Lin, D. C. Long, J. Loveday, R. H. Lupton, B. Margon, D. Martínez-Delgado, R. Mandelbaum, T. Matsubara, P. M. McGehee, T. A. McKay, A. Meiksin, J. A. Munn, R. Nakajima, T. Nash, E. H. Neilsen, Jr., H. J. Newberg, P. R. Newman, R. C. Nichol, T. Nicinski, M. Nieto-Santisteban, A. Nitta, W. O'Mullane, S. Okamura, R. Owen, N. Padmanabhan, G. Pauls, J. Peoples, Jr., J. R. Pier, A. C. Pope, D. Pourbaix, T. R. Quinn, G. T. Richards, M. W. Richmond, C. M. Rockosi, D. J. Schlegel, D. P. Schneider, J. Schroeder, R. Scranton, U. Seljak, E. Sheldon, K. Shimasaku, J. A. Smith, V. Smolčić, S. A. Snedden, C. Stoughton, M. A. Strauss, M. SubbaRao, A. S. Szalay, I. Szapudi, P. Szkody, M. Tegmark, A. R. Thakar, D. L. Tucker, A. Uomoto, D. E. Vanden Berk, J. Vandenberg, M. S. Vogeley, W. Voges, N. P. Vogt, L. M. Walkowicz, D. H. Weinberg, A. A. West, S. D. M. White, Y. Xu, B. Yanny, D. R. Yocum, D. G. York, I. Zehavi, S. Zibetti, and D. B. Zucker. The Fourth Data Release of the Sloan Digital Sky Survey. *ApJS*, 162:38–48, January 2006.

[AAA+09] K. N. Abazajian, J. K. Adelman-McCarthy, M. A. Agüeros, S. S. Allam, C. Allende Prieto, D. An, K. S. J. Anderson, S. F. Anderson, J. Annis, N. A. Bahcall, and et al. The Seventh Data Release of the Sloan Digital Sky Survey. *ApJS*, 182:543–558, June 2009.

[AAA+12] C. P. Ahn, R. Alexandroff, C. Allende Prieto, S. F. Anderson, T. Anderton, B. H. Andrews, É. Aubourg, S. Bailey, E. Balbinot, R. Barnes, and et al. The Ninth

Data Release of the Sloan Digital Sky Survey: First Spectroscopic Data from the SDSS-III Baryon Oscillation Spectroscopic Survey. *ApJS*, 203:21, December 2012.

[AEPS05] C. J. Akerman, S. L. Ellison, M. Pettini, and C. C. Steidel. Zn and Cr abundances in damped Lyman alpha systems from the CORALS survey. *A&A*, 440:499–509, September 2005.

[AGSS09] M. Asplund, N. Grevesse, A. J. Sauval, and P. Scott. The Chemical Composition of the Sun. *ARA&A*, 47:481–522, September 2009.

[APK+12] S. Abraham, N. S. Philip, A. Kembhavi, Y. G. Wadadekar, and R. Sinha. A photometric catalogue of quasars and other point sources in the Sloan Digital Sky Survey. *MNRAS*, 419:80–94, January 2012.

[BA96] E. Bertin and S. Arnouts. SExtractor: Software for source extraction. *AApS*, 117:393–404, June 1996.

[BB91] J. Bergeron and P. Boissé. A sample of galaxies giving rise to Mg II quasar absorption systems. *A&A*, 243:344–366, March 1991.

[BC03] G. Bruzual and S. Charlot. Stellar population synthesis at the resolution of 2003. *MNRAS*, 344:1000–1028, October 2003.

[BHV+12] N. Bouché, W. Hohensee, R. Vargas, G. G. Kacprzak, C. L. Martin, J. Cooke, and C. W. Churchill. Physical properties of galactic winds using background quasars. *MNRAS*, 426:801–815, October 2012.

[Bla88] J. C. Blades. QSO Absorption Lines: Probing the Universe. Proceedings of the QSO Absorption Line Meeting held May 19-21, 1987, in Baltimore, MD USA. In J. C. Blades, D. A. Turnshek, and C. A. Norman, editors, *QSO Absorption Lines: Probing the Universe*, pages 147–177, Cambridge, 1988. Cambridge Univ. Press.

[BLK+11] R. Bordoloi, S. J. Lilly, C. Knobel, M. Bolzonella, P. Kampczyk, C. M. Carollo, A. Iovino, E. Zucca, T. Contini, J.-P. Kneib, O. Le Fevre, V. Mainieri, A. Renzini, M. Scodeggio, G. Zamorani, I. Balestra, S. Bardelli, A. Bongiorno, K. Caputi, O. Cucciati, S. de la Torre, L. de Ravel, B. Garilli, K. Kovač, F. Lamareille, J.-F. Le Borgne, V. Le Brun, C. Maier, M. Mignoli, R. Pello, Y. Peng, E. Perez Montero, V. Presotto, C. Scarlata, J. Silverman, M. Tanaka, L. Tasca, L. Tresse, D. Vergani, L. Barnes, A. Cappi, A. Cimatti, G. Coppa, C. Diener, P. Franzetti, A. Koekemoer, C. López-Sanjuan, H. J. McCracken, M. Moresco, P. Nair, P. Oesch, L. Pozzetti, and N. Welikala. The Radial and Azimuthal Profiles of Mg II Absorption around $0.5 < z < 0.9$ zCOSMOS Galaxies of Different Colors, Masses, and Environments. *ApJ*, 743:10, December 2011.

[BLW+13] C. L. Bennett, D. Larson, J. L. Weiland, N. Jarosik, G. Hinshaw, N. Odegard, K. M. Smith, R. S. Hill, B. Gold, M. Halpern, E. Komatsu, M. R. Nolta, L. Page, D. N. Spergel, E. Wollack, J. Dunkley, A. Kogut, M. Limon, S. S. Meyer, G. S. Tucker, and E. L. Wright. Nine-year Wilkinson Microwave Anisotropy Probe (WMAP) Observations: Final Maps and Results. *ApJS*, 208:20, October 2013.

[BMT+12] A. J. Battisti, J. D. Meiring, T. M. Tripp, J. X. Prochaska, J. K. Werk, E. B. Jenkins, N. Lehner, J. Tumlinson, and C. Thom. The First Observations of Low-redshift Damped Lyα Systems with the Cosmic Origins Spectrograph: Chemical Abundances and Affiliated Galaxies. *ApJ*, 744:93, January 2012.

[Bow91] D. V. Bowen. Interstellar CA II in the galactic halo and in QSO absorption systems. *MNRAS*, 251:649–663, August 1991.

[BPPB91] D. V. Bowen, M. Pettini, M. V. Penston, and C. Blades. A survey of interstellar CA II absorption in the haloes of low-redshift galaxies. *MNRAS*, 249:145–158, March 1991.

[BPS+94] J. Bergeron, P. Petitjean, W. L. W. Sargent, J. N. Bahcall, A. Boksenberg, G. F. Hartig, B. T. Jannuzi, S. Kirhakos, B. D. Savage, D. P. Schneider, D. A. Turnshek, R. J. Weymann, and A. M. Wolfe. The Hubble Space Telescope quasar absorption line key project. 6: Properties of the metal-rich systems. *ApJ*, 436:33–43, November 1994.

[BR07] M. R. Blanton and S. Roweis. K-Corrections and Filter Transformations in the Ultraviolet, Optical, and Near-Infrared. *AJ*, 133:734–754, February 2007.

[BRS09] G. D. Becker, M. Rauch, and W. L. W. Sargent. High-Redshift Metals. I. The Decline of C IV at z ¿ 5.3. *ApJ*, 698:1010–1019, June 2009.

[BRWM08] N. Ben Bekhti, P. Richter, T. Westmeier, and M. T. Murphy. Ca II and Na I absorption signatures from extraplanar gas in the halo of the Milky Way. *A&A*, 487:583–594, August 2008.

[BT98] T. A. Barlow and D. Tytler. The Metallicity of Low-Redshift Lyalpha Forest Clouds. *AJ*, 115:1725–1736, May 1998.

[BTWC09] R. Braun, D. A. Thilker, R. A. M. Walterbos, and E. Corbelli. A Wide-Field High-Resolution H I Mosaic of Messier 31. I. Opaque Atomic Gas and Star Formation Rate Density. *ApJ*, 695:937–953, April 2009.

[CBC+13] N. H. M. Crighton, J. Bechtold, R. F. Carswell, R. Davé, C. B. Foltz, B. T. Jannuzi, S. L. Morris, J. M. O'Meara, J. X. Prochaska, J. Schaye, and N. Tejos. A high molecular fraction in a subdamped absorber at z = 0.56. *MNRAS*, 433:178–193, July 2013.

[CBGM05] J. Cui, J. Bechtold, J. Ge, and D. M. Meyer. Molecular Hydrogen in the Damped Lyα Absorber of Q1331+170. *ApJ*, 633:649–663, November 2005.

[CEK+12] R. J. Cool, D. J. Eisenstein, C. S. Kochanek, M. J. I. Brown, N. Caldwell, A. Dey, W. R. Forman, R. C. Hickox, B. T. Jannuzi, C. Jones, J. Moustakas, and S. S. Murray. The Galaxy Optical Luminosity Function from the AGN and Galaxy Evolution Survey. *ApJ*, 748:10, March 2012.

[CHG+10] H.-W. Chen, J. E. Helsby, J.-R. Gauthier, S. A. Shectman, I. B. Thompson, and J. L. Tinker. An Empirical Characterization of Extended Cool Gas Around Galaxies Using Mg II Absorption Features. *ApJ*, 714:1521–1541, May 2010.

[CKS+13] K. L. Cooksey, M. M. Kao, R. A. Simcoe, J. M. O'Meara, and J. X. Prochaska. Precious Metals in SDSS Quasar Spectra. I. Tracking the Evolution of Strong, $1.5 < z < 4.5$ C IV Absorbers with Thousands of Systems. *ApJ*, 763:37, January 2013.

[CLW+10] E. Corbelli, S. Lorenzoni, R. Walterbos, R. Braun, and D. Thilker. A wide-field H I mosaic of Messier 31. II. The disk warp, rotation, and the dark matter halo. *A&A*, 511:A89, February 2010.

[Cra92] I. A. Crawford. High-resolution observations of the interstellar 3302-wavelength NA I doublet and a discussion of the resulting NA I/Ca II ratios. *MNRAS*, 259:47–62, November 1992.

[CSK05] C. Churchill, C. Steidel, and G. Kacprzak. Mg II Absorbing Galaxies: Morphologies and Kinematics. In R. Braun, editor, *Extra-Planar Gas*, volume 331 of *Astronomical Society of the Pacific Conference Series*, page 387, June 2005.

[DB06] A. Dekel and Y. Birnboim. Galaxy bimodality due to cold flows and shock heating. *MNRAS*, 368:2–20, May 2006.

[ddC+91] G. de Vaucouleurs, A. de Vaucouleurs, H. G. Corwin, Jr., R. J. Buta, G. Paturel, and P. Fouqué. *Third Reference Catalogue of Bright Galaxies. Volume I: Explanations and references. Volume II: Data for galaxies between 0^h and 12^h. Volume III: Data for galaxies between 12^h and 24^h.* 1991.

[DFO11] R. Davé, K. Finlator, and B. D. Oppenheimer. Galaxy evolution in cosmological simulations with outflows - II. Metallicities and gas fractions. *MNRAS*, 416:1354–1376, September 2011.

[DHKW99] R. Davé, L. Hernquist, N. Katz, and D. H. Weinberg. The Low-Redshift Lyα Forest in Cold Dark Matter Cosmologies. *ApJ*, 511:521–545, February 1999.

[DKHW02] R. Davé, N. Katz, L. Hernquist, and D. Weinberg. Group Scaling Relations From a Cosmological Hydrodynamic Simulation: No Pre-heating Required? In S. Borgani, M. Mezzetti, and R. Valdarnini, editors, *Tracing Cosmic Evolution with*

Galaxy Clusters, volume 268 of *Astronomical Society of the Pacific Conference Series*, page 236, 2002.

[DMF+12] T. J. Davidge, A. W. McConnachie, M. A. Fardal, J. Fliri, D. Valls-Gabaud, S. C. Chapman, G. F. Lewis, and R. M. Rich. The Recent Stellar Archeology of M31−The Nearest Red Disk Galaxy. *ApJ*, 751:74, May 2012.

[DOF11] R. Davé, B. D. Oppenheimer, and K. Finlator. Galaxy evolution in cosmological simulations with outflows - I. Stellar masses and star formation rates. *MNRAS*, 415:11–31, July 2011.

[DPD02] M. Dessauges-Zavadsky, J. X. Prochaska, and S. D'Odorico. New detections of Mn, Ti and Mg in damped Lyalpha systems: Toward reconciling the dust/nucleosynthesis degeneracy. *A&A*, 391:801–807, September 2002.

[DPK+03] M. Dessauges-Zavadsky, C. Péroux, T.-S. Kim, S. D'Odorico, and R. G. McMahon. A homogeneous sample of sub-damped Lyman α systems - I. Construction of the sample and chemical abundance measurements. *MNRAS*, 345:447–479, October 2003.

[Dra11] B. T. Draine. *Physics of the Interstellar and Intergalactic Medium*. Princeton University Press, 2011.

[DSA+13] K. S. Dawson, D. J. Schlegel, C. P. Ahn, S. F. Anderson, É. Aubourg, S. Bailey, R. H. Barkhouser, J. E. Bautista, A. Beifiori, A. A. Berlind, V. Bhardwaj, D. Bizyaev, C. H. Blake, M. R. Blanton, M. Blomqvist, A. S. Bolton, A. Borde, J. Bovy, W. N. Brandt, H. Brewington, J. Brinkmann, P. J. Brown, J. R. Brownstein, K. Bundy, N. G. Busca, W. Carithers, A. R. Carnero, M. A. Carr, Y. Chen, J. Comparat, N. Connolly, F. Cope, R. A. C. Croft, A. J. Cuesta, L. N. da Costa, J. R. A. Davenport, T. Delubac, R. de Putter, S. Dhital, A. Ealet, G. L. Ebelke, D. J. Eisenstein, S. Escoffier, X. Fan, N. Filiz Ak, H. Finley, A. Font-Ribera, R. Génova-Santos, J. E. Gunn, H. Guo, D. Haggard, P. B. Hall, J.-C. Hamilton, B. Harris, D. W. Harris, S. Ho, D. W. Hogg, D. Holder, K. Honscheid, J. Huehnerhoff, B. Jordan, W. P. Jordan, G. Kauffmann, E. A. Kazin, D. Kirkby, M. A. Klaene, J.-P. Kneib, J.-M. Le Goff, K.-G. Lee, D. C. Long, C. P. Loomis, B. Lundgren, R. H. Lupton, M. A. G. Maia, M. Makler, E. Malanushenko, V. Malanushenko, R. Mandelbaum, M. Manera, C. Maraston, D. Margala, K. L. Masters, C. K. McBride, P. McDonald, I. D. McGreer, R. G. McMahon, O. Mena, J. Miralda-Escudé, A. D. Montero-Dorta, F. Montesano, D. Muna, A. D. Myers, T. Naugle, R. C. Nichol, P. Noterdaeme, S. E. Nuza, M. D. Olmstead, A. Oravetz, D. J. Oravetz, R. Owen, N. Padmanabhan, N. Palanque-Delabrouille, K. Pan, J. K. Parejko, I. Pâris, W. J. Percival, I. Pérez-Fournon, I. Pérez-Ràfols, P. Petitjean, R. Pfaffenberger, J. Pforr, M. M. Pieri, F. Prada, A. M. Price-Whelan, M. J. Raddick, R. Rebolo, J. Rich, G. T. Richards, C. M. Rockosi, N. A. Roe, A. J. Ross, N. P. Ross, G. Rossi, J. A. Rubiño-Martin, L. Samushia, A. G. Sánchez, C. Sayres, S. J. Schmidt, D. P.

Schneider, C. G. Scóccola, H.-J. Seo, A. Shelden, E. Sheldon, Y. Shen, Y. Shu, A. Slosar, S. A. Smee, S. A. Snedden, F. Stauffer, O. Steele, M. A. Strauss, A. Streblyanska, N. Suzuki, M. E. C. Swanson, T. Tal, M. Tanaka, D. Thomas, J. L. Tinker, R. Tojeiro, C. A. Tremonti, M. Vargas Magaña, L. Verde, M. Viel, D. A. Wake, M. Watson, B. A. Weaver, D. H. Weinberg, B. J. Weiner, A. A. West, M. White, W. M. Wood-Vasey, C. Yeche, I. Zehavi, G.-B. Zhao, and Z. Zheng. The Baryon Oscillation Spectroscopic Survey of SDSS-III. *AJ*, 145:10, January 2013.

[EPG+10] I. N. Evans, F. A. Primini, K. J. Glotfelty, C. S. Anderson, N. R. Bonaventura, J. C. Chen, J. E. Davis, S. M. Doe, J. D. Evans, G. Fabbiano, E. C. Galle, D. G. Gibbs, II, J. D. Grier, R. M. Hain, D. M. Hall, P. N. Harbo, X. (Helen He, J. C. Houck, M. Karovska, V. L. Kashyap, J. Lauer, M. L. McCollough, J. C. McDowell, J. B. Miller, A. W. Mitschang, D. L. Morgan, A. E. Mossman, J. S. Nichols, M. A. Nowak, D. A. Plummer, B. L. Refsdal, A. H. Rots, A. Siemiginowska, B. A. Sundheim, M. S. Tibbetts, D. W. Van Stone, S. L. Winkelman, and P. Zografou. The Chandra Source Catalog. *ApJS*, 189:37–82, July 2010.

[EPKW95] B. Edvardsson, B. Pettersson, M. Kharrazi, and B. Westerlund. Abundance analysis and origin of the ζ SCULPTORIS open cluster. *A&A*, 293:75–86, January 1995.

[FBGG06] M. A. Fardal, A. Babul, J. J. Geehan, and P. Guhathakurta. Investigating the Andromeda stream - II. Orbital fits and properties of the progenitor. *MNRAS*, 366:1012–1028, March 2006.

[FCB88] C. B. Foltz, F. H. Chaffee, Jr., and J. H. Black. Molecules at early epochs. IV - Confirmation of the detection of H2 toward PKS 0528 - 250. *ApJ*, 324:267–278, January 1988.

[Fie74] G. B. Field. Interstellar abundances: gas and dust. *ApJ*, 187:453–459, February 1974.

[Fit99] E. L. Fitzpatrick. Correcting for the Effects of Interstellar Extinction. *PASP*, 111:63–75, January 1999.

[FMC+04] P. François, F. Matteucci, R. Cayrel, M. Spite, F. Spite, and C. Chiappini. The evolution of the Milky Way from its earliest phases: Constraints on stellar nucleosynthesis. *A&A*, 421:613–621, July 2004.

[FMPY10] S. Frank, S. Mathur, M. Pieri, and D. G. York. A Survey of Metal Lines at High Redshift. II. SDSS Absorption Line Studies-O VI Line Density, Space Density, and Gas Metallicity at z $_{abs}$ ~ 3.0. *AJ*, 140:835–843, September 2010.

[FPLS07] A. J. Fox, P. Petitjean, C. Ledoux, and R. Srianand. Hot halos around high redshift protogalaxies. Observations of O VI and N V absorption in damped Lyman-α systems. *A&A*, 465:171–184, April 2007.

[GCM+03] K. D. Gordon, G. C. Clayton, K. A. Misselt, A. U. Landolt, and M. J. Wolff. A Quantitative Comparison of the Small Magellanic Cloud, Large Magellanic Cloud, and Milky Way Ultraviolet to Near-Infrared Extinction Curves. *ApJ*, 594:279–293, September 2003.

[GSP+09] N. Gupta, R. Srianand, P. Petitjean, P. Noterdaeme, and D. J. Saikia. A complete sample of 21-cm absorbers at z ˜ 1.3: Giant Metrewave Radio Telescope survey using MgII systems. *MNRAS*, 398:201–220, September 2009.

[HPD+06] S. Herbert-Fort, J. X. Prochaska, M. Dessauges-Zavadsky, S. L. Ellison, J. C. Howk, A. M. Wolfe, and G. E. Prochter. The Metal-strong Damped Lyα Systems. *PASP*, 118:1077–1097, August 2006.

[HW07] P. C. Hewett and V. Wild. K-band imaging of strong CaII-absorber host galaxies at z ˜ 1. *MNRAS*, 379:738–754, August 2007.

[JW96] E. B. Jenkins and G. Wallerstein. Hubble Space Telescope Observations of Interstellar Lines in Three High-Latitude Stars. *ApJ*, 462:758, May 1996.

[KDS+01] L. J. Kewley, M. A. Dopita, R. S. Sutherland, C. A. Heisler, and J. Trevena. Theoretical Modeling of Starburst Galaxies. *ApJ*, 556:121–140, July 2001.

[KFL+05] V. P. Kulkarni, S. M. Fall, J. T. Lauroesch, D. G. York, D. E. Welty, P. Khare, and J. W. Truran. Hubble Space Telescope Observations of Element Abundances in Low-Redshift Damped Lyα Galaxies and Implications for the Global Metallicity-Redshift Relation. *ApJ*, 618:68–90, January 2005.

[Kir79] T. B.L. Kirkwood. Geometric Means and Measures of Dispersion. *Biometrics*, 35:908–909, December 1979.

[KKF+09] D. Kereš, N. Katz, M. Fardal, R. Davé, and D. H. Weinberg. Galaxies in a simulated ΛCDM Universe - I. Cold mode and hot cores. *MNRAS*, 395:160–179, May 2009.

[KSD+11] E. Komatsu, K. M. Smith, J. Dunkley, C. L. Bennett, B. Gold, G. Hinshaw, N. Jarosik, D. Larson, M. R. Nolta, L. Page, D. N. Spergel, M. Halpern, R. S. Hill, A. Kogut, M. Limon, S. S. Meyer, N. Odegard, G. S. Tucker, J. L. Weiland, E. Wollack, and E. L. Wright. Seven-year Wilkinson Microwave Anisotropy Probe (WMAP) Observations: Cosmological Interpretation. *ApJS*, 192:18, February 2011.

[KSE+06] N. Kanekar, R. Subrahmanyan, S. L. Ellison, W. M. Lane, and J. N. Chengalur. HI 21 cm absorption at z ˜ 2.347 towards PKS B0438-436. *MNRAS*, 370:L46–L50, July 2006.

[KT97] D. Kirkman and D. Tytler. The Detection of Highly Ionized Gas via O VI Absorption toward QSO HS 1422+2309. *ApJ*, 489:L123, November 1997.

[KT99] D. Kirkman and D. Tytler. The Detection of Two Distinct High Ionization States in a QSO Lyman-Limit Absorption System: Evidence for Hierarchical Galaxy Formation at Z ˜ 3? *ApJ*, 512:L5–L8, February 1999.

[KYRa13] A. Kramida, Yu. Ralchenko, J. Reader, and and NIST ASD Team. NIST Atomic Spectra Database (ver. 5.1), [Online]. Available: `http://physics.nist.gov/asd` [2014, April 7]. National Institute of Standards and Technology, Gaithersburg, MD., 2013.

[LAD+15] D. B. Lee-Brown, B. J. Anthony-Twarog, C. P. Deliyannis, E. Rich, and B. A. Twarog. Spectroscopic Abundances in the Open Cluster NGC 6819. *AJ*, 149:121, April 2015.

[LB90] K. M. Lanzetta and D. Bowen. Intermediate-redshift galaxy halos - Results from QSO absorption lines. *ApJ*, 357:321–325, July 1990.

[LBP02] C. Ledoux, J. Bergeron, and P. Petitjean. Dust depletion and abundance pattern in damped Lyalpha systems: A sample of Mn and Ti abundances at z ¡ 2.2. *A&A*, 385:802–815, April 2002.

[LCB+07] P. Lah, J. N. Chengalur, F. H. Briggs, M. Colless, R. de Propris, M. B. Pracy, W. J. G. de Blok, S. S. Fujita, M. Ajiki, Y. Shioya, T. Nagao, T. Murayama, Y. Taniguchi, M. Yagi, and S. Okamura. The HI content of star-forming galaxies at z = 0.24. *MNRAS*, 376:1357–1366, April 2007.

[Lid07] A. R. Liddle. Information criteria for astrophysical model selection. *MNRAS*, 377:L74–L78, May 2007.

[LOF+14] N. Lehner, J. M. O'Meara, A. J. Fox, J. C. Howk, J. X. Prochaska, V. Burns, and A. A. Armstrong. Galactic and Circumgalactic O VI and its Impact on the Cosmological Metal and Baryon Budgets at $2 < z <\tilde{} 3.5$. *ApJ*, 788:119, June 2014.

[LPB+98] C. Ledoux, P. Petitjean, J. Bergeron, E. J. Wampler, and R. Srianand. On the kinematics of damped Lyman-alpha systems. *A&A*, 337:51–63, September 1998.

[LPS03] C. Ledoux, P. Petitjean, and R. Srianand. The Very Large Telescope Ultraviolet and Visible Echelle Spectrograph survey for molecular hydrogen in high-redshift damped Lyman α systems. *MNRAS*, 346:209–228, November 2003.

[LSB+96] L. Lu, W. L. W. Sargent, T. A. Barlow, C. W. Churchill, and S. S. Vogt. Abundances at High Redshifts: The Chemical Enrichment History of Damped Ly alpha Galaxies. *ApJS*, 107:475, December 1996.

[LSB+11] C. Lintott, K. Schawinski, S. Bamford, A. Slosar, K. Land, D. Thomas, E. Edmondson, K. Masters, R. C. Nichol, M. J. Raddick, A. Szalay, D. Andreescu,

P. Murray, and J. Vandenberg. Galaxy Zoo 1: data release of morphological classifications for nearly 900 000 galaxies. *MNRAS*, 410:166–178, January 2011.

[LSP02] C. Ledoux, R. Srianand, and P. Petitjean. Detection of molecular hydrogen in a near Solar-metallicity damped Lyman-alpha system at $z_{abs} \sim 2$ toward Q 0551-366 ≈ 2. *A&A*, 392:781–789, September 2002.

[LTW87] K. M. Lanzetta, D. A. Turnshek, and A. M. Wolfe. An absorption-line survey of 32 QSOs at red wavelengths - Properties of the MG II absorbers. *ApJ*, 322:739–769, November 1987.

[LTWY96] J. T. Lauroesch, J. W. Truran, D. E. Welty, and D. G. York. QSO Absorption Line Systems and Early Chemical Evolution. *PASP*, 108:641, August 1996.

[LWT95] K. M. Lanzetta, A. M. Wolfe, and D. A. Turnshek. The IUE Survey for Damped Lyman- alpha and Lyman-Limit Absorption Systems: Evolution of the Gaseous Content of the Universe. *ApJ*, 440:435, February 1995.

[MCP11] S. J. Mutch, D. J. Croton, and G. B. Poole. The Mid-life Crisis of the Milky Way and M31. *ApJ*, 736:84, August 2011.

[ML04] M. T. Murphy and J. Liske. Dust-reddening and gravitational lensing of SDSS QSOs due to foreground damped Lyman α systems. *MNRAS*, 354:L31–L36, October 2004.

[MMCV98] P. Mazzotta, G. Mazzitelli, S. Colafrancesco, and N. Vittorio. Ionization balance for optically thin plasmas: Rate coefficients for all atoms and ions of the elements H to NI. *A&AS*, 133:403–409, December 1998.

[MMP83] J. S. Mathis, P. G. Mezger, and N. Panagia. Interstellar radiation field and dust temperatures in the diffuse interstellar matter and in giant molecular clouds. *A&A*, 128:212–229, November 1983.

[MMT11] N. Murray, B. Ménard, and T. A. Thompson. Radiation Pressure from Massive Star Clusters as a Launching Mechanism for Super-galactic Winds. *ApJ*, 735:66, July 2011.

[MP09] A. D. Montero-Dorta and F. Prada. The SDSS DR6 luminosity functions of galaxies. *MNRAS*, 399:1106–1118, November 2009.

[MPSP03] A. H. Maller, J. X. Prochaska, R. S. Somerville, and J. R. Primack. Damped Lyman alpha systems and galaxy formation models - II. High ions and Lyman-limit systems. *MNRAS*, 343:268–278, July 2003.

[MSBP12] S. Muzahid, R. Srianand, J. Bergeron, and P. Petitjean. A high-resolution study of intergalactic O VI absorbers at z$\sim$ 2.3. *MNRAS*, 421:446–467, March 2012.

[MYJ86] D. C. Morton, D. G. York, and E. B. Jenkins. Extent of ionized calcium in the outer parts of galaxies. *ApJ*, 302:272–279, March 1986.

[NLPS08] P. Noterdaeme, C. Ledoux, P. Petitjean, and R. Srianand. Molecular hydrogen in high-redshift damped Lyman-α systems: the VLT/UVES database. *A&A*, 481:327–336, April 2008.

[NPC+12] P. Noterdaeme, P. Petitjean, W. C. Carithers, I. Pâris, A. Font-Ribera, S. Bailey, E. Aubourg, D. Bizyaev, G. Ebelke, H. Finley, J. Ge, E. Malanushenko, V. Malanushenko, J. Miralda-Escudé, A. D. Myers, D. Oravetz, K. Pan, M. M. Pieri, N. P. Ross, D. P. Schneider, A. Simmons, and D. G. York. Column density distribution and cosmological mass density of neutral gas: Sloan Digital Sky Survey-III Data Release 9. *A&A*, 547:L1, November 2012.

[NPH+08] D. B. Nestor, M. Pettini, P. C. Hewett, S. Rao, and V. Wild. Measurements of CaII absorption, metals and dust in a sample of z ˜= 1 DLAs and subDLAs. *MNRAS*, 390:1670–1682, November 2008.

[NPL+10] P. Noterdaeme, P. Petitjean, C. Ledoux, S. López, R. Srianand, and S. D. Vergani. A translucent interstellar cloud at z = 2.69. CO, H_2, and HD in the line-of-sight to SDSS J123714.60+064759.5. *A&A*, 523:A80, November 2010.

[NRTV03] D. B. Nestor, S. M. Rao, D. A. Turnshek, and D. Vanden Berk. Damped Lyα Gas Metallicities at Redshifts z=0.9-2.0 from Sloan Digital Sky Survey Spectra. *ApJL*, 595:L5–L8, September 2003.

[NS09] B. B. Nath and J. Silk. Starburst-driven galactic outflows. *MNRAS*, 396:L90–L94, June 2009.

[NTR05] D. B. Nestor, D. A. Turnshek, and S. M. Rao. Mg II Absorption Systems in Sloan Digital Sky Survey QSO Spectra. *ApJ*, 628:637–654, August 2005.

[NTR06] D. B. Nestor, D. A. Turnshek, and S. M. Rao. MMT Survey for Intervening Mg II Absorption. *ApJ*, 643:75–80, May 2006.

[PAA+15] Planck Collaboration, P. A. R. Ade, N. Aghanim, M. Arnaud, M. Ashdown, J. Aumont, C. Baccigalupi, A. J. Banday, R. B. Barreiro, J. G. Bartlett, and et al. Planck 2015 results. XIII. Cosmological parameters. *ArXiv e-prints*, February 2015.

[PBH90] M. Pettini, A. Boksenberg, and R. W. Hunstead. Metal enrichment, dust, and star formation in galaxies at high redshifts. I - The Z = 2.3091 absorber toward PHL 957. *ApJ*, 348:48–56, January 1990.

[PCB06] J. X. Prochaska, H.-W. Chen, and J. S. Bloom. Dissecting the Circumstellar Environment of γ-Ray Burst Progenitors. *ApJ*, 648:95–110, September 2006.

[PDD+03] C. Péroux, M. Dessauges-Zavadsky, S. D'Odorico, T.-S. Kim, and R. G. McMahon. A homogeneous sample of sub-damped Lyman α systems - II. Statistical, kinematic and chemical properties. *MNRAS*, 345:480–496, October 2003.

[PESB99] M. Pettini, S. L. Ellison, C. C. Steidel, and D. V. Bowen. Metal Abundances at z <1.5: Fresh Clues to the Chemical Enrichment History of Damped Lyα Systems. *ApJ*, 510:576–589, January 1999.

[Pet98] P. Petitjean. QSO Absorption Line Systems. *ArXiv Astrophysics e-prints*, October 1998.

[PFM+10] M. M. Pieri, S. Frank, S. Mathur, D. H. Weinberg, D. G. York, and B. D. Oppenheimer. A Search for Oxygen in the Low-density Lyα Forest using the Sloan Digital Sky Survey. *ApJ*, 716:1084–1094, June 2010.

[PFW+10] M. M. Pieri, S. Frank, D. H. Weinberg, S. Mathur, and D. G. York. The Composite Spectrum of Strong Lyα Forest Absorbers. *ApJL*, 724:L69–L73, November 2010.

[PGW+03] J. X. Prochaska, E. Gawiser, A. M. Wolfe, J. Cooke, and D. Gelino. The ESI/Keck II Damped Lyα Abundance Database. *ApJS*, 147:227–264, August 2003.

[PLNS06] P. Petitjean, C. Ledoux, P. Noterdaeme, and R. Srianand. Metallicity as a criterion to select H_2-bearing damped Lyman-α systems. *A&A*, 456:L9–L12, September 2006.

[PPA+12] I. Pâris, P. Petitjean, É. Aubourg, S. Bailey, N. P. Ross, A. D. Myers, M. A. Strauss, S. F. Anderson, E. Arnau, J. Bautista, D. Bizyaev, A. S. Bolton, J. Bovy, W. N. Brandt, H. Brewington, J. R. Browstein, N. Busca, D. Capellupo, W. Carithers, R. A. C. Croft, K. Dawson, T. Delubac, G. Ebelke, D. J. Eisenstein, P. Engelke, X. Fan, N. Filiz Ak, H. Finley, A. Font-Ribera, J. Ge, R. R. Gibson, P. B. Hall, F. Hamann, J. F. Hennawi, S. Ho, D. W. Hogg, Ž. Ivezić, L. Jiang, A. E. Kimball, D. Kirkby, J. A. Kirkpatrick, K.-G. Lee, J.-M. Le Goff, B. Lundgren, C. L. MacLeod, E. Malanushenko, V. Malanushenko, C. Maraston, I. D. McGreer, R. G. McMahon, J. Miralda-Escudé, D. Muna, P. Noterdaeme, D. Oravetz, N. Palanque-Delabrouille, K. Pan, I. Perez-Fournon, M. M. Pieri, G. T. Richards, E. Rollinde, E. S. Sheldon, D. J. Schlegel, D. P. Schneider, A. Slosar, A. Shelden, Y. Shen, A. Simmons, S. Snedden, N. Suzuki, J. Tinker, M. Viel, B. A. Weaver, D. H. Weinberg, M. White, W. M. Wood-Vasey, and C. Yèche. The Sloan Digital Sky Survey quasar catalog: ninth data release. *A&A*, 548:A66, December 2012.

[PSKH97] M. Pettini, L. J. Smith, D. L. King, and R. W. Hunstead. The Metallicity of High-Redshift Galaxies: The Abundance of Zinc in 34 Damped Lyα Systems from z = 0.7 to 3.4. *ApJ*, 486:665–680, September 1997.

[PSL00] P. Petitjean, R. Srianand, and C. Ledoux. Molecular hydrogen and the nature of damped Lyman-alpha systems. *A&A*, 364:L26–L30, December 2000.

[PT09] Jason X Prochaska and Jason Tumlinson. Baryons: What, when and where? In *Astrophysics in the Next Decade*, pages 419–456. Springer, 2009.

[PW02] J. X. Prochaska and A. M. Wolfe. The UCSD HIRES/Keck I Damped Lyα Abundance Database. II. The Implications. *ApJ*, 566:68–92, February 2002.

[PWC+11] J. X. Prochaska, B. Weiner, H.-W. Chen, J. Mulchaey, and K. Cooksey. Probing the Intergalactic Medium/Galaxy Connection. V. On the Origin of Lyα and O VI Absorption at z < 0.2. *ApJ*, 740:91, October 2011.

[QNT+11] A. M. Quider, D. B. Nestor, D. A. Turnshek, S. M. Rao, E. M. Monier, A. N. Weyant, and J. R. Busche. The Pittsburgh Sloan Digital Sky Survey Mg II Quasar Absorption-line Survey Catalog. *AJ*, 141:137, April 2011.

[RBT+11] S. M. Rao, M. Belfort-Mihalyi, D. A. Turnshek, E. M. Monier, D. B. Nestor, and A. Quider. A ground-based imaging study of galaxies causing damped Lyman α (DLA), sub-DLA and Lyman limit system absorption in quasar spectra. *MNRAS*, 416:1215–1249, September 2011.

[RC93] J. P. Rousseeuw and C. Croux. Alternatives to the Median Absolute Deviation. *JASA*, 88:1273–1283, December 1993.

[RFV12] A. G. Riess, J. Fliri, and D. Valls-Gabaud. Cepheid Period-Luminosity Relations in the Near-infrared and the Distance to M31 from the Hubble Space Telescope Wide Field Camera 3. *ApJ*, 745:156, February 2012.

[Ric12] P. Richter. Cold Gas Accretion by High-velocity Clouds and Their Connection to QSO Absorption-line Systems. *ApJ*, 750:165, May 2012.

[Rim07] L. G. Rimoldini. *Strong magnesium(II) absorbers and their relation to galaxies*. PhD thesis, University of Pittsburgh, August 2007.

[RKF+11] P. Richter, F. Krause, C. Fechner, J. C. Charlton, and M. T. Murphy. The neutral gas extent of galaxies as derived from weak intervening Ca II absorbers. *A&A*, 528:A12, April 2011.

[RLPB05] P. Richter, C. Ledoux, P. Petitjean, and J. Bergeron. The sub-damped Ly α system toward HE 0001-2340: galaxy formation at z $\sim$ 2. *A&A*, 440:819–829, September 2005.

[RMG+09] G. T. Richards, A. D. Myers, A. G. Gray, R. N. Riegel, R. C. Nichol, R. J. Brunner, A. S. Szalay, D. P. Schneider, and S. F. Anderson. Efficient Photometric Selection of Quasars from the Sloan Digital Sky Survey. II. ˜1,000,000 Quasars from Data Release 6. *ApJS*, 180:67–83, January 2009.

[RS52] P. M. Routly and L. Spitzer, Jr. A Comparison of the Components in Interstellar Sodium and Calcium. *ApJ*, 115:227, March 1952.

[RTN06] S. M. Rao, D. A. Turnshek, and D. B. Nestor. Damped Lyα Systems at z<1.65: The Expanded Sloan Digital Sky Survey Hubble Space Telescope Sample. *ApJ*, 636:610–630, January 2006.

[SAK+03] J. Schaye, A. Aguirre, T.-S. Kim, T. Theuns, M. Rauch, and W. L. W. Sargent. Metallicity of the Intergalactic Medium Using Pixel Statistics. II. The Distribution of Metals as Traced by C IV. *ApJ*, 596:768–796, October 2003.

[SBD+07] D. N. Spergel, R. Bean, O. Doré, M. R. Nolta, C. L. Bennett, J. Dunkley, G. Hinshaw, N. Jarosik, E. Komatsu, L. Page, H. V. Peiris, L. Verde, M. Halpern, R. S. Hill, A. Kogut, M. Limon, S. S. Meyer, N. Odegard, G. S. Tucker, J. L. Weiland, E. Wollack, and E. L. Wright. Three-Year Wilkinson Microwave Anisotropy Probe (WMAP) Observations: Implications for Cosmology. *ApJS*, 170:377–408, June 2007.

[SBE+07] D. J. Schlegel, M. Blanton, D. Eisenstein, B. Gillespie, J. Gunn, P. Harding, P. McDonald, R. Nichol, N. Padmanabhan, W. Percival, G. Richards, C. Rockosi, N. Roe, N. Ross, D. Schneider, M. Strauss, D. Weinberg, and M. White. SDSS-III: The Baryon Oscillation Spectroscopic Survey (BOSS). In *American Astronomical Society Meeting Abstracts*, volume 39 of *Bulletin of the American Astronomical Society*, page 132.29, December 2007.

[SCS+13] E. N. Seyffert, K. L. Cooksey, R. A. Simcoe, J. M. O'Meara, M. M. Kao, and J. X. Prochaska. Precious Metals in SDSS Quasar Spectra. II. Tracking the Evolution of Strong, $0.4 < z < 2.3$ Mg II Absorbers with Thousands of Systems. *ApJ*, 779:161, December 2013.

[SDM+97] C. C. Steidel, M. Dickinson, D. M. Meyer, K. L. Adelberger, and K. R. Sembach. Quasar Absorbing Galaxies at z $<\tilde{}$ 1: Deep Imaging and Spectroscopy in the Field of 3C 336. *ApJ*, 480:568–588, May 1997.

[SDP94] C. C. Steidel, M. Dickinson, and S. E. Persson. Field galaxy evolution since Z approximately 1 from a sample of QSO absorption-selected galaxies. *ApJ*, 437:L75–L78, December 1994.

[SGU+13] S. A. Smee, J. E. Gunn, A. Uomoto, N. Roe, D. Schlegel, C. M. Rockosi, M. A. Carr, F. Leger, K. S. Dawson, M. D. Olmstead, J. Brinkmann, R. Owen, R. H. Barkhouser, K. Honscheid, P. Harding, D. Long, R. H. Lupton, C. Loomis, L. Anderson, J. Annis, M. Bernardi, V. Bhardwaj, D. Bizyaev, A. S. Bolton, H. Brewington, J. W. Briggs, S. Burles, J. G. Burns, F. J. Castander, A. Connolly, J. R. A. Davenport, G. Ebelke, H. Epps, P. D. Feldman, S. D. Friedman, J. Frieman, T. Heckman, C. L. Hull, G. R. Knapp, D. M. Lawrence, J. Loveday, E. J. Mannery, E. Malanushenko, V. Malanushenko, A. J. Merrelli, D. Muna, P. R. Newman, R. C. Nichol, D. Oravetz, K. Pan, A. C. Pope, P. G. Ricketts,

A. Shelden, D. Sandford, W. Siegmund, A. Simmons, D. S. Smith, S. Snedden, D. P. Schneider, M. SubbaRao, C. Tremonti, P. Waddell, and D. G. York. The Multi-object, Fiber-fed Spectrographs for the Sloan Digital Sky Survey and the Baryon Oscillation Spectroscopic Survey. *AJ*, 146:32, August 2013.

[SKB+11] K. R. Stewart, T. Kaufmann, J. S. Bullock, E. J. Barton, A. H. Maller, J. Diemand, and J. Wadsley. Observing the End of Cold Flow Accretion Using Halo Absorption Systems. *ApJ*, 735:L1, July 2011.

[SKD+14] J. T. Stocke, B. A. Keeney, C. W. Danforth, D. Syphers, H. Yamamoto, J. M. Shull, J. C. Green, C. Froning, B. D. Savage, B. Wakker, T.-S. Kim, E. V. Ryan-Weber, and G. G. Kacprzak. Absorption-line Detections of 10^5-10^6 K Gas in Spiral-rich Groups of Galaxies. *ApJ*, 791:128, August 2014.

[SKW+14] B. D. Savage, T.-S. Kim, B. P. Wakker, B. Keeney, J. M. Shull, J. T. Stocke, and J. C. Green. The Properties of Low Redshift Intergalactic O VI Absorbers Determined from High S/N Observations of 14 QSOs with the Cosmic Origins Spectrograph. *ApJS*, 212:8, May 2014.

[SN12] M. Sharma and B. B. Nath. The Roles of Radiation and Ram Pressure in Driving Galactic Winds. *ApJ*, 750:55, May 2012.

[SPL+05] R. Srianand, P. Petitjean, C. Ledoux, G. Ferland, and G. Shaw. The VLT-UVES survey for molecular hydrogen in high-redshift damped Lyman α systems: physical conditions in the neutral gas. *MNRAS*, 362:549–568, September 2005.

[SRH+10] D. P. Schneider, G. T. Richards, P. B. Hall, M. A. Strauss, S. F. Anderson, T. A. Boroson, N. P. Ross, Y. Shen, W. N. Brandt, X. Fan, N. Inada, S. Jester, G. R. Knapp, C. M. Krawczyk, A. R. Thakar, D. E. Vanden Berk, W. Voges, B. Yanny, D. G. York, N. A. Bahcall, D. Bizyaev, M. R. Blanton, H. Brewington, J. Brinkmann, D. Eisenstein, J. A. Frieman, M. Fukugita, J. Gray, J. E. Gunn, P. Hibon, Ž. Ivezić, S. M. Kent, R. G. Kron, M. G. Lee, R. H. Lupton, E. Malanushenko, V. Malanushenko, D. Oravetz, K. Pan, J. R. Pier, T. N. Price, III, D. H. Saxe, D. J. Schlegel, A. Simmons, S. A. Snedden, M. U. SubbaRao, A. S. Szalay, and D. H. Weinberg. The Sloan Digital Sky Survey Quasar Catalog. V. Seventh Data Release. *AJ*, 139:2360, June 2010.

[SRS+11] Y. Shen, G. T. Richards, M. A. Strauss, P. B. Hall, D. P. Schneider, S. Snedden, D. Bizyaev, H. Brewington, V. Malanushenko, E. Malanushenko, D. Oravetz, K. Pan, and A. Simmons. A Catalog of Quasar Properties from Sloan Digital Sky Survey Data Release 7. *ApJS*, 194:45, June 2011.

[SS74] R. S. Siluk and J. Silk. On the velocity dependence of the interstellar Na I/Ca II ratio. *ApJ*, 192:51–57, August 1974.

[SS96] B. D. Savage and K. R. Sembach. Interstellar Abundances from Absorption-Line Observations with the Hubble Space Telescope. *ARAA*, 34:279–330, 1996.

[Ste90] C. C. Steidel. A high-redshift extension of the survey for C IV absorption in the spectra of QSOs - The redshift evolution of the heavy element absorbers. *ApJS*, 72:1–39, January 1990.

[Ste93] C. C. Steidel. The Properties of Absorption-Line Selected High-Redshift Galaxies. In J. M. Shull and H. A. Thronson, editors, *The Environment and Evolution of Galaxies*, volume 188 of *Astrophysics and Space Science Library*, page 263, 1993.

[STR14] G. M. Sardane, D. A. Turnshek, and S. M. Rao. Ca II absorbers in the Sloan Digital Sky Survey: statistics. *MNRAS*, 444:1747–1758, October 2014.

[STR15] G. M. Sardane, D. A. Turnshek, and S. M. Rao. Ca II absorbers in the Sloan Digital Sky Survey: element abundances and dust. *MNRAS*, 452:3192–3208, September 2015.

[SWJ+00] B. D. Savage, B. Wakker, B. T. Jannuzi, J. N. Bahcall, J. Bergeron, A. Boksenberg, G. F. Hartig, S. Kirhakos, E. M. Murphy, W. L. W. Sargent, D. P. Schneider, D. Turnshek, and A. M. Wolfe. The Hubble Space Telescope Quasar Absorption Line Key Project. XV. Milky Way Absorption Lines. *ApJS*, 129:563–610, August 2000.

[TBG+12] E. J. Tollerud, R. L. Beaton, M. C. Geha, J. S. Bullock, P. Guhathakurta, J. S. Kalirai, S. R. Majewski, E. N. Kirby, K. M. Gilbert, B. Yniguez, R. J. Patterson, J. C. Ostheimer, J. Cooke, C. E. Dorman, A. Choudhury, and M. C. Cooper. The SPLASH Survey: Spectroscopy of 15 M31 Dwarf Spheroidal Satellite Galaxies. *ApJ*, 752:45, June 2012.

[TBW+04] D. A. Thilker, R. Braun, R. A. M. Walterbos, E. Corbelli, F. J. Lockman, E. Murphy, and R. Maddalena. On the Continuing Formation of the Andromeda Galaxy: Detection of H I Clouds in the M31 Halo. *ApJ*, 601:L39–L42, January 2004.

[TC08] C. Thom and H.-W. Chen. A STIS Survey for O VI Absorption Systems at $0.12 < z <\tilde{} 0.5$. I. The Statistical Properties of Ionized Gas. *ApJ*, 683:22–32, August 2008.

[TSB+08] T. M. Tripp, K. R. Sembach, D. V. Bowen, B. D. Savage, E. B. Jenkins, N. Lehner, and P. Richter. A High-Resolution Survey of Low-Redshift QSO Absorption Lines: Statistics and Physical Conditions of O VI Absorbers. *ApJS*, 177:39–102, July 2008.

[TTT+12] A. Tamm, E. Tempel, P. Tenjes, O. Tihhonova, and T. Tuvikene. Stellar mass map and dark matter distribution in M 31. *A&A*, 546:A4, October 2012.

[TTW+11] J. Tumlinson, C. Thom, J. K. Werk, J. X. Prochaska, T. M. Tripp, D. H. Weinberg, M. S. Peeples, J. M. O'Meara, B. D. Oppenheimer, J. D. Meiring, N. S.

Katz, R. Davé, A. B. Ford, and K. R. Sembach. The Large, Oxygen-Rich Halos of Star-Forming Galaxies Are a Major Reservoir of Galactic Metals. *Science*, 334:948–, November 2011.

[TWL+89] D. A. Turnshek, A. M. Wolfe, K. M. Lanzetta, F. H. Briggs, R. D. Cohen, C. B. Foltz, H. E. Smith, and B. J. Wilkes. Damped Lyman-alpha absorption by disk galaxies with large redshifts. III - Intermediate-resolution spectroscopy. *ApJ*, 344:567–596, September 1989.

[VCBH01] G. Vladilo, M. Centurión, P. Bonifacio, and J. C. Howk. Ionization Properties and Elemental Abundances in Damped Lyα Systems. *ApJ*, 557:1007–1020, August 2001.

[Ver99] D. A. Verner. The Atomic Data for Astrophysics Database. *PhST*, 83:174–176, 1999.

[VFKY96] D. A. Verner, G. J. Ferland, K. T. Korista, and D. G. Yakovlev. Atomic Data for Astrophysics. II. New Analytic FITS for Photoionization Cross Sections of Atoms and Ions. *ApJ*, 465:487, July 1996.

[Vie95] S. M. Viegas. Abundances at high redshift: ionization correction factors. *MNRAS*, 276:268–272, September 1995.

[Vla02] G. Vladilo. Chemical abundances of damped Ly alpha systems:. A new method for estimating dust depletion effects. *A&A*, 391:407–415, August 2002.

[VPW08] G. Vladilo, J. X. Prochaska, and A. M. Wolfe. The color excess of quasars with intervening DLA systems. Analysis of the SDSS data release five. *A&A*, 478:701–715, February 2008.

[VRB+01] D. E. Vanden Berk, G. T. Richards, A. Bauer, M. A. Strauss, D. P. Schneider, T. M. Heckman, D. G. York, P. B. Hall, X. Fan, G. R. Knapp, S. F. Anderson, J. Annis, N. A. Bahcall, M. Bernardi, J. W. Briggs, J. Brinkmann, R. Brunner, S. Burles, L. Carey, F. J. Castander, A. J. Connolly, J. H. Crocker, I. Csabai, M. Doi, D. Finkbeiner, S. Friedman, J. A. Frieman, M. Fukugita, J. E. Gunn, G. S. Hennessy, Ž. Ivezić, S. Kent, P. Z. Kunszt, D. Q. Lamb, R. F. Leger, D. C. Long, J. Loveday, R. H. Lupton, A. Meiksin, A. Merelli, J. A. Munn, H. J. Newberg, M. Newcomb, R. C. Nichol, R. Owen, J. R. Pier, A. Pope, C. M. Rockosi, D. J. Schlegel, W. A. Siegmund, S. Smee, Y. Snir, C. Stoughton, C. Stubbs, M. SubbaRao, A. S. Szalay, G. P. Szokoly, C. Tremonti, A. Uomoto, P. Waddell, B. Yanny, and W. Zheng. Composite Quasar Spectra from the Sloan Digital Sky Survey. *AJ*, 122:549–564, August 2001.

[WBT05] T. Westmeier, R. Braun, and D. Thilker. Westerbork H I observations of high-velocity clouds near M 31 and M 33. *A&A*, 436:101–115, June 2005.

[WC10] D. E. Welty and P. A. Crowther. Interstellar TiII in the Milky Way and Magellanic Clouds. *MNRAS*, 404:1321–1348, May 2010.

[WH05] V. Wild and P. C. Hewett. Evidence for dust reddening in damped Lyα absorbers identified through CaII (H&K) absorption. *MNRAS*, 361:L30–L34, July 2005.

[WHL+99] D. E. Welty, L. M. Hobbs, J. T. Lauroesch, D. C. Morton, L. Spitzer, and D. G. York. The Diffuse Interstellar Clouds toward 23 Orionis. *ApJS*, 124:465–501, October 1999.

[WHP06] V. Wild, P. C. Hewett, and M. Pettini. Selecting damped Lyman α systems through CaII absorption - I. Dust depletions and reddening at z˜ 1. *MNRAS*, 367:211–230, March 2006.

[WHP07] V. Wild, P. C. Hewett, and M. Pettini. The star formation rate of CaII and damped Lyman α absorbers at 0.4 $<$ z $<$ 1.3. *MNRAS*, 374:292–304, January 2007.

[WJL+98] R. J. Weymann, B. T. Jannuzi, L. Lu, J. N. Bahcall, J. Bergeron, A. Boksenberg, G. F. Hartig, S. Kirhakos, W. L. W. Sargent, B. D. Savage, D. P. Schneider, D. A. Turnshek, and A. M. Wolfe. The Hubble Space Telescope Quasar Absorption Line Key Project. XIV. The Evolution of Lyα Absorption Lines in the Redshift Interval z = 0-1.5. *ApJ*, 506:1–18, October 1998.

[WLB+01] D. E. Welty, J. T. Lauroesch, J. C. Blades, L. M. Hobbs, and D. G. York. Unusual Depletions toward the SMC Star SK 155-Differences in Dust Composition in the SMC Interstellar Medium? *ApJL*, 554:L75–L79, June 2001.

[WMH96] D. E. Welty, D. C. Morton, and L. M. Hobbs. A High-Resolution Survey of Interstellar Ca II Absorption. *ApJS*, 106:533, October 1996.

[WP00] A. M. Wolfe and J. X. Prochaska. Ionized Gas in Damped Lyα Protogalaxies. I. Model-independent Inferences from Kinematic Data. *ApJ*, 545:591–602, December 2000.

[WPP+85] K. A. West, M. Pettini, M. V. Penston, J. C. Blades, and D. C. Morton. The interstellar spectrum of the bright Seyfert galaxy NGC 3783 - Evidence for an extragalactic origin of high-velocity clouds. *MNRAS*, 215:481–497, August 1985.

[WPT+14] J. K. Werk, J. X. Prochaska, J. Tumlinson, M. S. Peeples, T. M. Tripp, A. J. Fox, N. Lehner, C. Thom, J. M. O'Meara, A. B. Ford, R. Bordoloi, N. Katz, N. Tejos, B. D. Oppenheimer, R. Davé, and D. H. Weinberg. The COS-Halos Survey: Physical Conditions and Baryonic Mass in the Low-Redshift Circumgalactic Medium. *ArXiv e-prints*, March 2014.

[WTSC86] A. M. Wolfe, D. A. Turnshek, H. E. Smith, and R. D. Cohen. Damped Lyman-alpha absorption by disk galaxies with large redshifts. I - The Lick survey. *ApJS*, 61:249–304, June 1986.

[YAA+00] D. G. York, J. Adelman, J. E. Anderson, Jr., S. F. Anderson, J. Annis, N. A. Bahcall, J. A. Bakken, R. Barkhouser, S. Bastian, E. Berman, W. N. Boroski, S. Bracker, C. Briegel, J. W. Briggs, J. Brinkmann, R. Brunner, S. Burles, L. Carey, M. A. Carr, F. J. Castander, B. Chen, P. L. Colestock, A. J. Connolly, J. H. Crocker, I. Csabai, P. C. Czarapata, J. E. Davis, M. Doi, T. Dombeck, D. Eisenstein, N. Ellman, B. R. Elms, M. L. Evans, X. Fan, G. R. Federwitz, L. Fiscelli, S. Friedman, J. A. Frieman, M. Fukugita, B. Gillespie, J. E. Gunn, V. K. Gurbani, E. de Haas, M. Haldeman, F. H. Harris, J. Hayes, T. M. Heckman, G. S. Hennessy, R. B. Hindsley, S. Holm, D. J. Holmgren, C.-h. Huang, C. Hull, D. Husby, S.-I. Ichikawa, T. Ichikawa, Ž. Ivezić, S. Kent, R. S. J. Kim, E. Kinney, M. Klaene, A. N. Kleinman, S. Kleinman, G. R. Knapp, J. Korienek, R. G. Kron, P. Z. Kunszt, D. Q. Lamb, B. Lee, R. F. Leger, S. Limmongkol, C. Lindenmeyer, D. C. Long, C. Loomis, J. Loveday, R. Lucinio, R. H. Lupton, B. MacKinnon, E. J. Mannery, P. M. Mantsch, B. Margon, P. McGehee, T. A. McKay, A. Meiksin, A. Merelli, D. G. Monet, J. A. Munn, V. K. Narayanan, T. Nash, E. Neilsen, R. Neswold, H. J. Newberg, R. C. Nichol, T. Nicinski, M. Nonino, N. Okada, S. Okamura, J. P. Ostriker, R. Owen, A. G. Pauls, J. Peoples, R. L. Peterson, D. Petravick, J. R. Pier, A. Pope, R. Pordes, A. Prosapio, R. Rechenmacher, T. R. Quinn, G. T. Richards, M. W. Richmond, C. H. Rivetta, C. M. Rockosi, K. Ruthmansdorfer, D. Sandford, D. J. Schlegel, D. P. Schneider, M. Sekiguchi, G. Sergey, K. Shimasaku, W. A. Siegmund, S. Smee, J. A. Smith, S. Snedden, R. Stone, C. Stoughton, M. A. Strauss, C. Stubbs, M. SubbaRao, A. S. Szalay, I. Szapudi, G. P. Szokoly, A. R. Thakar, C. Tremonti, D. L. Tucker, A. Uomoto, D. Vanden Berk, M. S. Vogeley, P. Waddell, S.-i. Wang, M. Watanabe, D. H. Weinberg, B. Yanny, N. Yasuda, and SDSS Collaboration. The Sloan Digital Sky Survey: Technical Summary. *AJ*, 120:1579–1587, September 2000.

[YKV+06] D. G. York, P. Khare, D. Vanden Berk, V. P. Kulkarni, A. P. S. Crotts, J. T. Lauroesch, G. T. Richards, D. P. Schneider, D. E. Welty, Y. Alsayyad, A. Kumar, B. Lundgren, N. Shanidze, T. Smith, J. Vanlandingham, B. Baugher, P. B. Hall, E. B. Jenkins, B. Menard, S. Rao, J. Tumlinson, D. Turnshek, C.-W. Yip, and J. Brinkmann. Average curves and relative abundances for quasi-stellar object absorption-line systems at 1 $z \leq_{abs} < 2$. *MNRAS*, 367:945–978, April 2006.

[ZM13] G. Zhu and B. Ménard. The JHU-SDSS Metal Absorption Line Catalog: Redshift Evolution and Properties of Mg II Absorbers. *ApJ*, 770:130, June 2013.

[ZMHP09] B. J. Zych, M. T. Murphy, P. C. Hewett, and J. X. Prochaska. Dust depletion, chemical uniformity and environment of CaII H&K quasar absorbers. *MNRAS*, 392:1429–1450, February 2009.

[ZMN+07] S. Zibetti, B. Ménard, D. B. Nestor, A. M. Quider, S. M. Rao, and D. A. Turnshek. Optical Properties and Spatial Distribution of Mg II Absorbers from SDSS Image Stacking. *ApJ*, 658:161–184, March 2007.

[ZMP+07] B. J. Zych, M. T. Murphy, M. Pettini, P. C. Hewett, E. V. Ryan-Weber, and S. L. Ellison. The host galaxies of strong CaII quasar absorption systems at z < 0.5. *MNRAS*, 379:1409–1422, August 2007.